DESIGN AND ANALYSIS OF MULTILAYERED ORGANIC SOLAR CELL FOR BIOMEDICAL APPLICATION

A Thesis Submitted

In Partial Fulfillment of the Requirements

for the Degree of

DOCTOR OF PHILOSOPHY

by

PARITOSH CHAMOLA

(2K19/PHDEC/08)

Under the Supervision of

Prof. POORNIMA MITTAL

Department of Electronics and Communication Engineering

DELHI TECHNOLOGICAL UNIVERSITY

(Formerly Delhi College of Engineering)

Shahbad Daulatpur, Main Bawana Road

Delhi-110042. India

October, 2023

CERTIFICATE

Certified that **Paritosh Chamola (2K19/PHDEC/08)** has carried out their research work presented in this thesis entitled **"Design and Analysis of Multilayered Organic Solar Cell for Biomedical Application"** for the award of **Doctor of Philosophy** from Delhi Technological University, Delhi, under my supervision. The thesis embodies results of original work, and studies are carried out by the student himself and the contents of the thesis do not form the basis for the award of any other degree to the candidate or to anybody else from this or any other University/Institution.

Date: 04-10-2023

Prof. POORNIMA MITTAL

Supervisor

Department of ECE

Delhi Technological University

Delhi, India

CANDIDATE'S DECLARATION

I, **Paritosh Chamola** (**Roll No. 2K19/PHDEC/08)** student of Ph.D., hereby declare that the Dissertation titled "**Design and Analysis of Multilayered Organic Solar Cell for Biomedical Application**" which is submitted by me to the Department of Electronics and Communication Engineering, Delhi Technological University, Delhi in partial fulfillment of the requirement for the award of the degree of **Doctor of Philosophy**, is original and not copied from any source without proper citation. This work has not previously formed the basis for the award of any Degree, Diploma Associateship, Fellowship or other similar title or recognition.

Place: DTU, Delhi **PARITOSH CHAMOLA**

Date: 04-10-2023 **(Roll No. 2K19/PHDEC/08)**

ABSTRACT

The present work delves into the research, development, and optimization of solar cell technology for energy harvesting and biomedical applications. This research focuses on two key areas: improving solar cell efficiency and integrating solar cells into biomedical devices. The goal is to improve the performance of solar cells and investigate their potential in healthcare challenges.

The work analyses the use of Sb (Antimony) and Sn (Tin) doped Zinc Telluride (ZnTe) thin films as absorber layers in multi-layered solar cells. The films are synthesised using a low-cost melt-quenching technique and then analysed using X-ray diffraction (XRD). The electrical characteristics and parameters for ZnTe, SbZnTe and SnZnTe materials are analysed. Further, based on the extracted properties, these materials are utilized as the absorber layer in the solar cell. Additionally, the performance of SbZnTe and SnZnTe based solar cells is compared against the ZnTe material based solar cell. Illustrating the behaviour of absorber layer materials internally, these solar cells are analysed through horizontal and vertical cut-lines, wherein, it is observed that SnZnTe cell has reasonably higher hole and electron carrier concentrations.

The current density for SnZnTe based solar cell is obtained higher by 2.3 and 2.6 times than that of SbZnTe and ZnTe based cells, respectively at the thickness of 1.5 μm. The Fill Factor for SnZnTe cell is obtained as 84.66%, which is also reasonably higher than the fill factor of 59.66% obtained for SbZnTe and 56.66% for ZnTe based solar cell. Further the efficiency with 17.8% is highest for SnZnTe, which is followed by SbZnTe with 10.6%. The efficiency of 9.2% is lowest for ZnTe. The current density of SbZnTe and SnZnTe solar cells is significantly higher than that of ZnTe solar cell, with enhancements of 1.1 and 2.6 times, respectively, at 1.5 μm absorber thickness. Furthermore, a comparison of the different solar cell layers shows that SnZnTe demonstrates superior performance due to its lowest band gap and higher charge carrier generation. Hence, it is found that the SnZnTe material is best suits as the absorber material. Therefore, the absorber layer is found instrumental in improving the device performance without increasing the dimensions of the device.

The focus of the work further moves towards optimization and efficiency enhancement of organic solar cells. The P3HT: PCBM bilayer organic solar cell is analysed internally to determine carrier concentration, electric field distribution, and electron/hole current density in

the constituent layers. The effect of donor and acceptor layer thicknesses on the solar cell performance is investigated, and an optimised efficiency of 0.90% is obtained. To further enhance the efficiency, the donor layer material is changed from P3HT (poly(3-hexylthiophene-2,5-diyl)) to PTB7 (Poly[[4,8-bis[(2-ethylhexyl)oxy]benzo[1,2-b:4,5-b']dithiophene-2,6-diyl][3-fluoro-2-[(2-ethylhexyl)carbonyl]thieno[3,4-b]thiophenediyl]], which increases the efficiency to 1.33 %. Furthermore, a Poly(3,4-ethylenedioxythiophene)-poly(styrenesulfonate) (PEDOT: PSS) hole transport layer (HTL) is added for efficiency enhancement up to 1.55%. It is followed by an addition of Poly [(9,9-bis(3'-(N,N-dimethylamino)propyl-2,7-fluorene)-alt-2,7-(9,9-dioctylfluorene)] (PFN) electron transport layer (ETL) which enhanced the efficiency to 1.91%. Subsequently, an inverted structure for the modified solar cell is analysed, which further enhanced the efficiency to 2.08%.

Further, a comparative study for conventional and inverted structure of solar cell is executed. The solar cell performs optimum at a donor and acceptor thickness of 40 nm and 50 nm respectively. Addition of HTL and ETL increases the performance of solar cell significantly so does the change of donor material from P3HT to PTB7, a low band gap material. Further, using the conventional and inverted structure of the solar cell revels that inverted structure is the best performing among all the other structures with a highest Power Conversion Efficiency (PCE) of 2.08%. This efficiency is 1.6 times higher than the 0.78 % PCE achieved for the experimental solar cell. Thus, the findings of present work represent strategies for increasing the efficiencies and can be extremely useful for the design and development of high efficiency solar cells.

This work additionally addresses the necessity for non-invasive biomedical sensing technology, particularly for haemoglobin detection. A low-cost, portable haemoglobin detector device is proposed, using organic solar cells and LED light sources. The device uses haemoglobin's optical absorption properties to assess blood haemoglobin levels in a non-invasive manner, providing a simple, biocompatible, and flexible method of screening populations for anaemia.

Further, the present work showcased a non-invasive method of haemoglobin detection comprising of an organic photovoltaic cell and three LED's sources i.e., blue, green and red. These are used with their respective radiation spectral range of 450-495 nm, 495-570 nm and 620-750 nm to illuminate an area of the skin on finger. This transmitted light after interacting with tissues is detected by an arrangement of Coumarin 30: C_{60}/NN'-QA/ZnPc active layer based organic solar cell.

The Coumarin 30: C_{60}/NN'-QA/ZnPc based multilayer organic photovoltaic solar cell is made up of three organic photodetector layers individually sensitive towards the blue, green, and red colour lights, which are arranged in a stack one above the other. The proposed multilayer photovoltaic cell has shown an excellent selectivity of the spectrum and also demonstrated separation of the colours in the photovoltaic cell. This excellent capability to separate the colours makes this organic photovoltaic cell to further utilise as a photodetector to realise a haemoglobin detector device by combining it with blue, green, and red colour LEDs. The photodetector detects the haemoglobin present in RBC owing to the optical property of haemoglobin not to absorb or to reflect the red colour. This transmitted red colour wavelengths are absorbed by the ZnPc layer of the multilayer structure producing a photosensitivity of 0.02 A/W.

Thus, the method used in this work presents a simple, low-cost, non-invasive, biocompatible, and flexible means for assessing blood haemoglobin level by utilizing an multi spectral optical processing method. The method developed herein can further integrate to wearable electronic devices. This method will be extremely useful for checking anaemia anywhere and will be vital primarily for children and women suspected to be anaemic.

Furthermore, the incorporation of solar cells into biomedical implants is explored, especially for powering cardiac pacemakers. Current pacemakers rely on batteries that must be replaced surgically, posing risks and complications. The work explores the feasibility of powering a modern cardiac pacemaker with a subdermal PPV-PCBM bulk heterojunction organic photovoltaic cell. Power yield analyses are performed for different skin tones and implantation depths. Thus, in the present work, subdermal PPV–PCBM [poly(2-methoxy-5-{3′,7′-dimethyloctyloxy}-p-phenylene vinylene) and {6,6}-phenyl C61-butyric acid methyl ester] active layer-based bulk heterojunction (BHJ) organic photovoltaic cell is analysed to power a modern pacemaker.

A power output of 2.1 mW, 0.45 mW and 0.05 mW for Caucasian, Asian and African skin types is obtained at 2 mm implantation depth, respectively, which is adequate to run modern pacemakers requiring power in the range of (~10) microwatts. Further, the results also specifically show that the higher output power is produced under brighter and thinner skin.

The photovoltaic cell used in this work allows for sufficient energy harvesting to electrically charge an energy storing accumulator in six (6) minutes when exposed to daylight. This energy

accumulator can run a medical pacemaker for a total of twenty-four (24) hours. This analysis shows promising results and thus applicability of sub-dermal PV device for powering cardiac pacemaker. The sub-dermally implanted organic PV cell could increases the lifespan of cardiac pacemaker therefore, dropping the number of complex surgeries essential for replacement of the implants. Subsequently, this has also reduced the size of bio-medical implant and thus increasing the comfort level of patients. Additionally, such organic photovoltaic cell can be used to power up other bio-medical similar types of implants.

In summary, this work contributes to the advancements in solar cell technology for biomedical applications and energy harvesting. The findings demonstrate that Sb and Sn doped ZnTe thin films have the potential to increase solar cell efficiency. The organic solar cell integration into biomedical devices opened the possibilities for non-invasive diagnostics and self-powered implants. The findings emphasise the need of optimising absorber layer materials and device designs to improve solar cell performance. Furthermore, the utilisation of organic solar cells in biomedical applications has the potential to transform healthcare technology that too with contributing to sustainable energy solutions.

ACKNOWLEDGEMENTS

I would like to express my deepest gratitude and sincere appreciation to all those who have contributed in the completion of my doctoral thesis. Their guidance, support, and encouragement have been invaluable throughout this journey.

First and foremost, I am immensely grateful to my supervisor, Prof. Poornima Mittal, Professor, Department of Electronics and Communication Engineering, Delhi Technological University, Delhi, India. I am greatly thankful for her unwavering commitment, patience, and expertise. Madam's guidance and insightful feedback have been instrumental in shaping the direction of my research and enhancing the quality of my work. I am truly fortunate to have such a dedicated mentor who consistently challenged and inspired me to reach new heights.

I express my gratitude towards the distinguished faculty members who have time and again helped us at different avenues. I extend my sincere regards to HoD sir, for his constant support. I wish to express my gratitude towards the DRC chairperson, the distinguished DRC members. Their expertise, constructive criticism, and valuable suggestions have significantly contributed to the refinement of my thesis. I am deeply grateful for the time and effort they invested in reviewing and evaluating my work.

I am indebted to the esteemed faculty members of Department of Electronics and Communication Engineering, DTU, Delhi, who provided me with a rich academic environment and facilitated my intellectual growth. I express my deepest regards for Prof. Brijesh Kumar, Department of Information Technology, Indira Gandhi Delhi Technical University, Delhi, India, for providing insightful remarks. I am also grateful to Prof. D. K. Dwivedi, Department of Physics and Material Science, for experimental support in the Amorphous Semiconductor Research Laboratory at Madan Mohan Malviya Universuty of Technology, Gorakhpur, India.

I am also grateful to all my colleagues and seniors of the Electronics and Communication Department, especially Mr. Sachin Tyagi, Mr. Mohit Tyagi, Mr. Ashish Raturi, Ms. Bhawna Rawat, Ms. Sugandha, Ms. Yogita Chopra, Mr. Ayush, and Ms. Bharti. I am thankful to them as they have generously contributed their time and shared their insights, without whom my study would not have been possible. Their willingness to participate and engage in meaningful

discussions enriched my research and provided me with valuable data. I also express my thanks all the staff members of the department for their continuous support in our academic activities.

Lastly, I would like to thank my family for their kindness, support, and patience thought my journey. Their belief in me has kept my spirits and motivation high during this process. Their understanding, love, and encouragement have been a constant source of motivation, and I am truly grateful for their presence in my life.

Finally, I would like to acknowledge the financial support provided by Delhi Technological University, Delhi. Their assistance enabled me to carry out my research effectively and ensured that I had the necessary resources to complete my thesis.

To all those who have directly or indirectly contributed to my doctoral thesis, I extend my deepest gratitude. Your support, whether big or small, has played a significant role in shaping my academic and personal growth. I am profoundly grateful for your presence in my life and for the impact you have had on my journey as a researcher.

PARITOSH CHAMOLA
(Roll No. 2K19/PHDEC/08)

Table of Contents

List of Figures

List of Tables

List of Abbreviations

Symbol/Abbreviation	Full Form
a-Si	Amorphous Silicon
BHJ	Bulk heterojunction
BTI	Bithiophene imide
CdTe	Cadmium Telluride
CuPc	Copper(II) Phthalocyanine
C60	Fullerene
EBL	Electron Blocking Layer
ETL	Electron Transport Layer
FF	Fill Factor
FET	Field Effect Transistors
HBL	Hole Blocking Layer
HOMO	Highest Occupied Molecular Orbital
HTL	Hole Transport Layer
ICBA	Indene-C60 Bisadduct
I_{SC}	Short circuit current
ITO	Indium Tin Oxide
J_{SC}	Short circuit current density
LED	Light Emitting Diode
LUMO	Lowest Unoccupied Molecular Orbital
MDMO-PPV	Poly(2-methoxy-5-(3,7-dimethyloctyloxy)-1,4-phenylene-vinylene)
mW	Microwatt
NFA	Non-Fullerene Acceptors
NDI	Naphthalene diimide
nm	Nanometer
QD	Quantum Dots
OLED	Organic Light Emitting Diodes
OSC	Organic Solar Cells
PCE	Power Conversion Efficiency
PEDOT:PSS	Poly(3,4-ethylenedioxythiophene):poly(styrene

	sulfonate)
PLD	Pulsed Laser Deposition
PDI	Perylene diimide
PCBM	Phenyl-C61-butyric acid methyl ester
PffBT4T-2OD	Poly[(5,6-difluoro-2,1,3-benzothiadiazol-4,7-diyl)-alt-[3,3'-(4,4-bis(2-octyldodecyl)-4H-silolo[3,2-b:4,5-b']dithiophene-2,6-diyl)]]
P3HT	Poly(3-hexylthiophene)
PTB7	Poly[[4,8-bis[(2-ethylhexyl)oxy]benzo[1,2-b:4,5-b']dithiophene-2,6-diyl][3-fluoro-2-[(2-ethylhexyl)carbonyl]thieno[3,4-b]thiophenediyl]]
PTB7-Th	Poly[[4,8-bis[(2-ethylhexyl)oxy]benzo[1,2-b:4,5-b']dithiophene-2,6-diyl][3-fluoro-2-[(2-ethylhexyl)carbonyl]thieno[3,4-b]thiophenediyl]]
PTCBI	Phenyl-C61-butyric acid 3,4,9,10-tetracarboxylic acid bisimide
PV	Photovoltaic
QD	Quantum Dots
RBC	Red Blood Cells
Si	Silicon
Sb	Antimony
Sn	Tin
SnZnTe	Tin doped Zinc Telluride
V	Volts
VOC	Open circuit voltage
W	Watt
XRD	X-ray diffraction
ZnTe	Zinc Telluride

CHAPTER – 1

INTRODUCTION

Solar energy is a rapidly growing field of renewable energy that has received significant attention in recent years as a potential alternative to fossil fuels. This chapter, introduces the fundamental concepts, performance parameters, and functioning processes of solar cells. The chapter includes the intermediate band gap thin film solar cells and organic solar cells, highlighting their unique characteristics. The chapter aims to provide a thorough introduction of solar cell technology while highlighting the emerging biomedical applications of organic solar cells.

This chapter is divided into eight different sections, including introduction as section 1.1. It is followed by section 1.2 describing basics and performance parameter of a solar cell. In section 1.3 basics of organic electronics is detailed. The section 1.4 represents organic photovoltaic cell and their biomedical applications. Further, section 1.5 describes the problem statement identified. Thereafter, in section 1.6 objectives are formulated to address the identified issues. The section 1.7 explains the methodology used to achieve each desired objective. Finally in section 1.8, thesis organisation is summarized.

1.1 INTRODUCTION

The photovoltaic (PV) cell, is an electronic device based on semiconductor materials that operates on the principle of photoelectric effect, converting sunlight into electric current [1,2]. The solar cells can revolutionize electricity generation as an alternative source. The solar cell technology offers a renewable and environment friendly approach in comparison to the fossil fuels that contribute to pollution and greenhouse gas emissions. The innovation and development of high performance and economical PV cells are crucial factors for the solar cell technology to become commercially successful. By transitioning to a green or carbon free economy, solar cells can play a vital role in mitigating the effects of climate change and global warming.

Organic solar cells, also called organic photovoltaic cells (OPV), use organic materials such as small molecules or carbon-based polymers in their photoactive layer [3]. These OPVs have lower cost and are flexible. Due to their mechanically flexibility, they can be shaped into

various forms [4]. Additionally, the use of printing methods for instance roll to roll and inkjet enables the fabrication of large area OPVs, contributing to their affordability, making the OPVs an appealing for renewable energy production.

The field of OPVs has witnessed remarkable advancements over past two decades. With the introduction of new materials and innovative device designs, these organic solar cells have attained higher efficiencies and improved stability [5]. However, there are still challenges required to be overcome, such as increasing power conversion efficiencies, optimizing device structure, and developing accurate and reliable simulation models. These efforts are crucial for predicting the OPV device behaviour and properties, as well as understanding their internal device physics. Through careful analysis the above-mentioned aspects, it becomes feasible to efficiently design and optimize the OPV devices [6].

1.2 STRUCTURE AND PERFORMANCE PARAMETERS OF SOLAR CELL

The basic structure of a solar cell is often made up of multiple layers of semiconductor materials. Material such as silicon gallium arsenide and cadmium telluride are utilized [2, 7]. Primary components are absorber layer, semiconductor layers, and contacts. The absorber layer is responsible for absorbing photons from sunlight. When photons strike the absorber layer, transfer of energy promotes electrons to higher energy levels [8]. The p-n junctions in the solar cell are critical in the separation and transport of electrons and holes. Metal contacts are placed on top and bottom layers to allow electron collection and current flow. In comparison of bottom the top contact is usually a thin structure that allows sunlight to reach the absorber layer. To maximise light absorption, an anti-reflection coating is frequently applied to solar cell's front surface.

Photons striking the solar cell, excite electrons of the absorber layer, resulting in the electron-hole pairs [9]. The built-in field then separates the electrons and holes, resulting in voltage across PV cell. Efficiency of a solar cell is a measure of how effectively it converts sunlight into electrical energy. The material properties, cell design, and incident sunlight intensity all have an impact on the efficiency. Higher efficiency solar cells are desirable since they can generate more electricity for a given amount of sunlight. The Figs. 1 (a) and (b) represents the cross section and current-voltage plot of PV cell respectively.

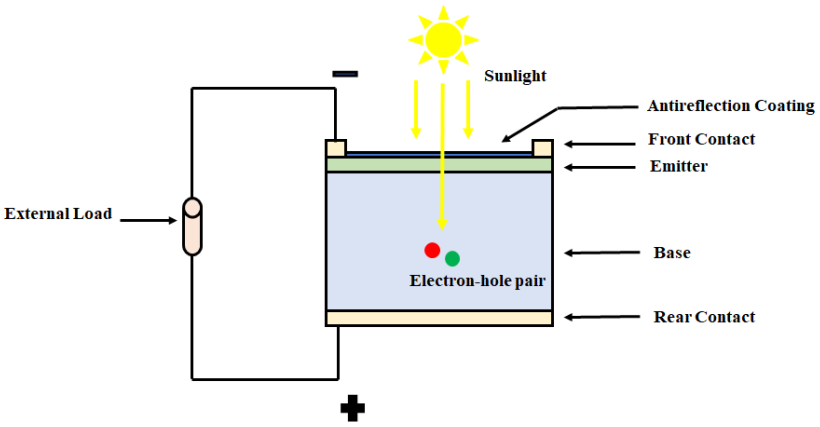

(a)

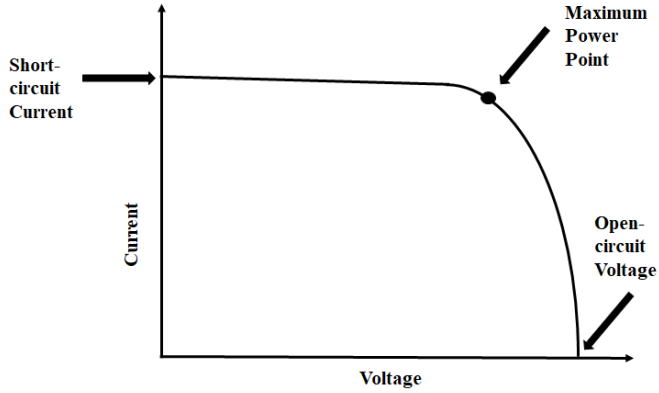

(b)

Fig. 1.1 (a) Structure and (b) Current-voltage curve of a solar cell.

Efficiency and suitability of solar cell for diverse applications are determined by fundamental characteristics parameters. A solar cell's primary performance parameters are efficiency (η), Open circuit voltage (V_{OC}), Short circuit current (I_{SC}) and Fill Factor (FF). The efficiency measures how effectively PV cell transforms sunlight into electrical current. It represents proportion of produced power to incident solar power. Higher efficiency better the PV cell. The V_{OC} is maximum voltage that PV cell generates without external load connected. The V_{OC} depends on the energy levels of the materials utilised and semiconductor's bandgap [10. The J_{SC} depends on incident sunlight and the PV cell's surface area. The fill factor is the ratio of solar cell's maximum power to the product of its V_{OC} and J_{SC}. A higher FF suggests better power conversion efficiency. These performance parameters are critical for determining a solar cell's performance. These parameters assist researchers and users in comparing various kinds of PV cells, optimizing their performance, and determining their suitability for specific applications.

The Intermediate band solar cells have states in the host atom's band gap, which decreases the required power to excite an electron from valance to conduction band. This occurs due to inclusion of the intermediate band [11]. The creation of intermediate band requires alloys of mismatched elements and the host. They offer distinct and remarkable characteristics and properties making them apt for solar energy harvesting. Different elements are blended in fixed ratios to form intermediate band solar cells enabling them to demonstrate extensive range of band-gap energies, thereby facilitating them to absorb the incoming irradiance efficiently throughout a wider spectrum.

The utilization of intermediate band solar cells facilitates bandgap customization that align with the solar spectrum, enhancing sunlight absorption Thus, using intermediate band cells provides an enhanced efficiency for particular application. Further, these solar cells have illustrated encouraging cost saving and power conversion efficiency hence, making them irresistible contenders for solar energy harvesting technologies.

The progress of photovoltaic cells based upon the intermediate band solar cells is a dynamic field of research with persistent endeavours emphasising on enhancing efficiency and scalability of PV cells. These innovations and developments focusing on performance enhancement and viability of intermediate band cells lead to advancement of the sustainable energy technologies.

1.3 ORGANIC ELECTRONICS

The field of organic electronics uses organic materials, as active components in electronic systems. The materials generally used are carbon-based polymers or small organic molecules. These materials have distinct electronic and mechanical characteristics, making them apt for electronics applications. The organic materials offer numerous advantages over inorganic materials.

Applications of organic electronics include Organic Light-Emitting Diodes (OLED) displays, photovoltaics, transistors, printed electronics and bioelectronics. OLEDs are utilized in displays and lighting, producing vibrant colours. OLED displays are utilised in smartphones, televisions, and wearable devices [12]. The Organic photovoltaic cells are utilised to convert solar energy to electrical current. OPVs have advantages such as lightweight, flexible, and ability to integrate into variety of surfaces. They can be used in portable electronics, integrated

photovoltaics, and off grid power generation. Organic transistors or organic field effect transistors (OFETs), are utilised in electronic amplification and switching. Elastic displays, RFID tags, and smart sensors can all benefit from them.

Organic electronics allows for the realization of printed electronic components, in which electronic circuits and devices are directly printed onto the substrates. This allows for the fabrication of flexible electronic products including smart packaging, electronic labels, and wearable sensors. The significant aspect of organic electronic materials is their capability to interact or interface with biological process and systems. Unlike inorganic materials, organic electronic materials are nontoxic within the body and are biocompatible. This property allows an extensive range of bioelectronics and biosensor applications, including biomedical sensing devices, drug delivery systems, and implantable electronics. Therefore, organic electronic materials offer exciting prospects for the advancement of lightweight, flexible, and affordable electronic devices and are capable of breakthroughs in various industries such as displays, energy harvesting, and healthcare.

1.4 ORGANIC SOLAR CELLS AND THEIR BIOMEDICAL APPLICATION

Organic solar cells (OSCs) operate on photoelectric effect. Wherein, photons produce electron-hole pairs. Its active layer is made up of organic semiconductor materials, a donor material (electron donor) and acceptor material (electron acceptor). In OPVs inbound solar radiation is converted to electricity in four steps (a) incoming sunlight produces excitons (b) diffusion of exciton (c) exciton dissociation leading to charge separation (d) charge transportation to electrodes. The effective charge transportation is desired to minimize charge recombination and maximize the generation of electrical current. In general, OPVs consist of active layer.

Organic solar cells are indeed highly promising candidates for various biomedical applications owing to their exceptional properties, including high mechanical flexibility, transparency, and biocompatibility. Their flexibility and biocompatibility allow seamless integration with biological tissues, enabling them to serve as self-sustainable power sources for implanted medical devices such as pacemakers, neurotransmitters, and drug delivery systems. Additionally, their lightweight and flexible nature makes them ideal for wearable biomedical electronic equipment, such as fitness trackers. In biosensing applications, OSCs can be utilized to monitor physiological parameters like glucose levels, biomarker identifiers and pH sensing

among other applications. Given their ability of convert light into electrical signals, they can be used in biomedical imaging techniques, including optoelectronic retinal prostheses. Ongoing research efforts continue to discover innovative possibilities for utilizing OSCs in healthcare.

1.4.1 Organic solar cell for disease detection

Detection of conditions such as anaemia, a grave complication indicating deficiency of iron and can lead to death, presently relies on invasive methods for determining the haemoglobin, by taking sample from patient and then analyse it. This causes patient discomfort while collecting the blood sample moreover, it does not allow a real time monitoring of the patient. In comparison to the present method of measuring haemoglobin, a non-invasive method will allow for pain free, immediate, and reliable measurement without any risk of infection.

The main rationale for the use of non-invasive method is that it can increase testing at low cost by providing on the spot results without any requirement of large setup. It is accurate, and is highly reliable as the physical conditions cannot tamper with it. The non-invasive approach is also environment friendly as it creates no biohazardous waste and is also reusable.

1.4.2 Bulk heterojunction organic solar cell for medical implants

Living tissue are complex mixture of biomolecules and are very soft. In contrast, inorganic materials are rigid. The organic polymers possess exceptional characteristics in terms of their composition and flexibility. These features make them ideal candidates for interfaces between tissues and electronic equipment, which are essential for bio-medical implants. Present medical implants such as pacemakers are driven by batteries which are required to be changed. This procedure requires surgical operation and is expensive, with associated risks. The organic solar cells can provide constant energy, eliminating the need for battery replacement. This can considerably extend the pacemaker’s lifespan. As these cells are made up of organic ingredients, they are biocompatible and non-toxic, essential for medical implantation. Further, they pose no risk of chemical reaction or leakage inside the body, assuring patient’s safety.

1.5 PROBLEM STATEMENT

Efficiency is a crucial aspect for improving solar cells overall performance. Traditional single bandgap solar cells have a narrow absorption spectrum, resulting in lower conversion efficiency. Additionally, they suffer from thermalization loss, where photons with energy levels

above the bandgap are lost, inefficient charge separation, and poor carrier transport, leading to high recombination losses. In comparison, third-generation cells with intermediate bands have the potential to achieve higher efficiency as they can utilize a wider solar spectrum range, absorbing both high and low-energy photons through intermediate energy levels within their bandgap. Their tunable intermediate bandgaps also allow for fine-tuning their performance. Consequently, intermediate bandgap solar cells address several limits of traditional cells.

The OSCs are known to have lower efficiencies in comparison to their inorganic counterparts. This lower efficiency restricts the commercialization of these cells. Therefore, it is required to investigate various factors and develop strategies to enhance their efficiency. Optimizing acceptor and donor layers, finding efficient absorber material, and developing device structures is indispensable. Further, analysis of the internal device physics for understanding the processes governing excitation generation, recombination and charge separation is important for identifying and mitigating the efficiency limiting mechanisms.

The absence of proper diagnostic facilities, particularly in developing countries poses a significant challenge and leads to incorrect treatment, increased morbidity, and mortality rates. The absence of proper diagnosis facilities also has significant economic implications, such as increased cost of healthcare. This economic burden extends beyond the healthcare system to society, leading decreased productivity and overall well-being. The organic cells have lower fabrication prices. Anaemia, a disorder marked by a decrease in volume of haemoglobin, is a significant public health concern worldwide. The existing methods for assessing haemoglobin levels, often require invasive procedures and expensive equipment, restricting their widespread use and accessibility. To address this problem, a portable, low-cost, and non-invasive haemoglobin detection technology capable of offering reliable and continuous information is required. The usage of organic materials in advancement of this technology offers several advantages, including simpler manufacturing processes resulting in reduced material and equipment expense. Thus, making them suitable for widespread adoption especially in resource-limited settings.

The cardiac pacemakers have transformed the treatment of cardiac disorders and enhanced the quality of life for millions of patients worldwide. However, modern cardiac pacemakers still face several challenges and limitations affecting their effectiveness and patient outcomes. The present-day cardiac pacemakers are reliant on batteries that must be replaced periodically through invasive surgeries. This not only puts patients at risk and causes discomfort but it also

adds to the healthcare costs and inconvenience associated with frequent device replacements. The size of traditional cardiac pacemakers might be an issue, especially for pediatric patients with limited anatomical room for the device installation causing discomfort and limiting physical activities. Furthermore, the surgical procedures for pacemaker insertion carries inherent risks and complications, such as infections, bleeding, or tissue damage. To address these challenges, an innovative approach based on organic photovoltaic cells, capable of producing enough power to operate a cardiac pacemaker is explored. This innovative approach aims to significantly extending life of a pacemaker and eliminate the need for complex replacement surgeries, thereby increasing patient comfort and convenience.

Therefore, the overall problem addressed in this work is synthesis and characterization of new intermediate solar cell, performance optimization of multi-layer solar cells, development of a non-invasive haemoglobin detection method using organic solar cells, and analysis of organic solar cells as power source for cardiac pacemakers.

1.6 OBJECTIVES

The main objective of this work is to design, analyze, characterize, and investigate the third-generation cells primarily amorphous thin-film and organic cells for biomedical applications. The designed organic solar cells consist of multilayer device, including bilayer and bulk heterojunction cells. Moreover, in addition to the design, internal device physics analysis is conducted to gain a comprehensive understanding of the device physics of these organic cells. The novel design for these multilayer cells is proposed for biomedical applications mainly for haemoglobin detection and for powering a modern cardiac pacemaker.

To accomplish the proposed work, the following objectives are framed:

Objective 1:

Synthesis and characterisation of absorber layer material and analysis of amorphous absorber material based thin film solar cell.

Objective 2:

Design and analysis of organic materials based solar cell and further performance improvement using multi organic layers for carrier enhancement.

Objective 3:

RBC Light scattering analysis to detect compounds present in the blood for identification of disease and further utilization of organic solar cell for blood flow monitoring.

Objective 4:

Performance optimization of fully organic and biocompatible solar cell for subdermal implants and to supply sustainable energy to pacemaker.

The detailed methodology to achieve above objectives is explained in the subsequent section.

1.7 OBJECTIVE-WISE METHODOLOGY

The methodology employed to attain the set objectives concerning the synthesis of ZnTe thin films, optimization of organic solar cells and their biomedical applications is as follows -

Methodology for Objective 1

The first step involves the synthesis of required material for absorber layer of intermediate band solar cell. This process is carried out under controlled conditions and using appropriate synthesis techniques. Thin films are prepared utilising deposition technique followed by synthesis of absorber layer material. The resulting thin films are characterised using X-ray diffraction (XRD) to find their crystalline structure and quality. Electrical characteristics of the solar cell are analyzed including measurements of J_{SC}, V_{OC} and FF. These measurements reveal insights about the device's performance. The objective is to find best absorber material for the PV cell.

Methodology for Objective 2

The structure of bilayer organic photovoltaic device includes acceptor and donor materials. Specific acceptor and donor materials are determined by the solar cell's intended characteristics and performance requirements. To understand the complex device physics of the organic solar cell, internal cut-line analysis is performed. The donor and acceptor layer thickness has a major effect on cell efficiency. Thus, an analysis is executed to analyse the effect of modifying thicknesses of these layers on solar cell's performance. This work correspondingly investigates effect of using different donor materials. Additionally, results of adding transport layers into device structure is explored with the purpose of determining their impact on the overall

performance of OPV cell. Further, focus is also on comparing the cell performance in both conventional and inverted configurations.

Methodology for Objective 3

A thorough analysis of the existing invasive haemoglobin detection techniques is performed. This analysis seeks to comprehend their limitations, benefits, and places for improvement. The next step is to explore various techniques that utilize the interaction between human blood and light for disease detection. It entails determining haemoglobin's absorption and reflection properties. Additionally, materials utilised in photoactive layer is examined to determine their compatibility and potential for haemoglobin detection. Further, based on the examination of current techniques and understanding of haemoglobin's optical properties, the device requirements for a non-invasive haemoglobin detector are finalised. These requirements include selecting appropriate organic materials for photoactive layer, selecting light sources, and designing the detecting device.

Methodology for Objective 4

The objective is to design bulk heterojunction (BHJ) solar cell that is specifically designed to power a modern cardiac pacemaker. This involves selecting appropriate materials, optimising the device design, and considering variables such as; efficiency, stability, and pacemaker's compatibility. The examination of skin properties (absorption and scattering coefficients), determination of optimal skin depth contributes to ensure the successful implementation of the solar cell and efficient power generation. The optimal skin depth is determined by considering factors such as; light penetration, optimum solar radiation absorption, and minimising interference with the pacemaker's functionality. The generated power of the designed BHJ organic solar cell is analyzed for various skin types and lighting conditions. This analysis aids in finding the performance of cell once exposed to different levels of sunlight and diverse types of skin tones.

1.8 THESIS ORGANIZATION

The complete thesis is arranged in seven chapters. Primarily, a brief introduction based on the issues concerned is included. The concise objective of each chapter is discussed with subsequent details.

Chapter 1

This chapter includes basic information on solar cells, organic materials, OSCs. It puts forward the operating principle of traditional and organic cells. It includes motivation for work, problem statement and the objectives. The chapter concludes with organization of complete thesis work.

Chapter 2

This chapter presents an extensive literature review in relation to the different solar cells. It discusses the recent advancement in different solar cells generations specially focusing on third generation organic cells. It makes available an outline of diverse layers, device structures, electrical characteristics. It also reviews the diverse types of OPVs and potential biomedical applications of organic cells. Subsequently, various technical gaps are identified based on the literature review.

Chapter 3

This chapter details experimental procedures for sample preparation via melt quench method. It also details the Sb and Sn doped ZnTe thin film preparation using thermal evaporation method. These films are characterized through XRD patterns to determine their crystal structure. Furthermore, the Sb and Sn doped ZnTe are explored as absorber-layer material and examined through cut-line analysis to explore internal processes. Subsequently a comparative analysis among ZnTe, SnZnTe and SbZnTe is performed to determine the best performing absorb layer material.

Chapter 4

This chapter includes the analysis of bilayer organic solar cell consisting of P3HT - PCBM. The solar device is modelled and analyzed on J-V characteristics. Also, all the major performance parameters are optimized. The OSC is further examined through vertical cut-line analysis to understand the internal device physics of organic solar cell. It also details effect of different layers on solar cell efficiency. Furthermore, electron and hole transport layers are added to bilayer cell to enhance its efficiency. Additionally, conventional and inverted structures are mapped for the best possible efficiency output.

Chapter 5

This chapter proposes a non-invasive method of haemoglobin detection utilizing the interaction of light and RBCs. The non-invasive method comprises of an Coumarin 30: C60/NN'-QA/ZnPc active layer based organic solar cell and three LED's sources. An in-depth analysis to understand optical properties of haemoglobin is carried out, as it is the absorption spectrum of haemoglobin which plays a vital role in the proposed method. Subsequently, analysis of spectral photo-response of OSC is executed to establish that different values of photosensitivity relate to different colour wavelengths absorbed. This concept of photosensitivity is applied to detect haemoglobin in RBCs.

Chapter 6

In this chapter, a PPV-PCBM bulk heterojunction cell is investigated and its fundamental parameters are extracted to get an insight to the solar cell's performance. Subsequently feasibility of subdermal PPV-PCBM active layer based BHJ organic solar cell to power a modern pacemaker is investigated.

Chapter 7

This chapter summarizes important results obtained from the proposed work. It presents the comprehensive discussion and outcomes of the methods proposed. Additionally, it the ongoing investigations and potential applications, which may help scientists to explore different origins related to solar cell.

The thesis ends with the complete bibliography of earlier research work that enlightened us with numerous vital facts regarding behaviour and applications of solar cells and helped in finding novel directions to accomplish the proposed work. Afterwards, our publications based on the present research work are included as well.

CHAPTER-2

LITERATURE REVIEW

The present chapter emphases on the current development in domain of organic photovoltaic cells. Solar cells play a vital role for electricity production by converting sunlight to electric current. This chapter presents an exhaustive literature review and advancements in field of OPVs. The solar cells, as a substitute to fossil fuels are at the forefront in vide range of research field and applications. The organic solar cells efficiency and operational lifespan made outstanding advancement throughout the past decades by refining materials of the photoactive layer and presenting new inter-layers. The functioning of organic solar cell is centred on photoinduced electron transfer. Organic solar cell technology has immense potential owing to lower production cost and flexible characteristics. The latest advancement in the material engineering and sophisticated device structure have significantly improved the solar cells commercial feasibility. This chapter, highlights the research and advancements for organic bioelectronics in powering numerous bio-medical electronic devices. The important challenges, engineering result and forthcoming prospects driving the progress of OSCs are explored.

This chapter is structured into thirteen different sections. It begins with an introduction in section 2.1, followed by section 2.2 focussing first-generation of solar cells. In the next section 2.3 second generation cells are described, while section 2.4 focuses on third generation solar cells. The section 2.5 details the thin film technology and section 2.6 covers the various deposition techniques for the ZnTe material. The influence of doping on ZnTe properties is elaborated in section 2.7. The section 2.8 delves into organic solar cell, while sections 2.9 and 2.10 focus on the acceptor and donor materials used in organic cells, respectively. The lifetime of organic cells is discussed in section 2.11, and section 2.12 details their applications. Finally, the section 2.13 addresses the identified technical gaps based on the literature review.

2.1 INTRODUCTION

Solar energy is large quantity of thermal energy available as radiation. It is limitless and is completely free [13, 14]. Utilization of fossil fuels to produce electricity leads to increase in greenhouse gases and pollutants causing environmental concerns. Renewable technologies have great potential to significantly reduce pollution. Thin film solar cell technologies [15]

which are identified as second-generation solar cell technologies are primarily dependent on in-organic semiconductor materials. These inorganic materials have a higher absorption capacity compared to silicon material and includes amorphous silicon, chalcogenides like CIGS, CIS, and II-VI semiconductors like CdTe, CdS. Though second-generation photovoltaics have high efficiencies manufacturing second-generation solar cell is a remains a great challenge.

In the past two decades [16-23] the engineering and science of organic-materials have progressed steadily resulting in a range of device demonstration and optimization such as photodiodes [23], organic light emitting diodes (OLEDs), and field effect transistors (FETs) [24-26]. The first-generation organic cells were fabricated as a single photoactive layer squeeze amid dissimilar work function electrodes. Tang [27], in 1986 developed single heterojunction bilayer OSC and reported an efficiency of 1%. Yu *et al*. [28] in 1995 presented OSC with a mixture of donor and acceptor layer which serves as photoactive layer. The BHJ OSC enhances donor-acceptor interface and decreases exciton diffusion distance which improves device performance, the OSCs based on BHJ have reported efficiencies of over 18%. Further, low-temperature processing of organic materials limits the variety of substrates on which inorganic materials could be deposited. Moreover, low-temperature processing also reduces the energy used during manufacturing and the ability of organic materials to tune its physical properties by tuning its chemical structure attracts the research and commercial interest in OSCs.

Cells built using organic materials with more than one p-n junction are denoted as third-generation of solar cells. These include (i) multijunction cell based on group IV and III-V semiconductors [29] (ii) dye sensitized solar cells [30, 31] (iii) hybrid approaches such as in-organic quantum dots doped in semiconductor polymer or merging in-organic material TiO_2 with organic materials [32-34] (iv) completely organic approach. Arena of OSCs has progressed immensely in past years with efficiencies over 10% even reaching up to 20%. This high efficiency could be credited to the advancement of novel light-absorbing materials. Additionally, new device structures, for instance tandem and ternary organic photovoltaic cells have gained increased attention. Substantial advancement has also been achieved in other essential components of OSCs such as interlayers and electrodes. A major difference in physics of in-organic and organic photovoltaic cell is in the character of excited state. In organic solar cells the photon absorption does not immediately generate free electrons and holes to produce

electric current like their inorganic counterparts but generates excitons. These created excitons separate to produce electric current. The Fig. 2.1 presents different solar cell generations.

2.2 FIRST GENERATION SOLAR CELLS

The silicon wafer is utilized for construction of first-generation photovoltaics. The high-power conversion efficiencies achieved have made the first-generation solar cells widespread photovoltaic technology [35]. First-generation photovoltaic cells are further classified into two subcategories or classes [36].

(i) Monocrystalline silicon photovoltaic cell
(ii) Polycrystalline photovoltaic cell

2.2.1 Monocrystalline photovoltaic cell

In manufacturing of monocrystalline photovoltaic cell Czochralski process is utilized [37, 38]. In the Czochralski process massive size ingots are produced from which silicon crystals are sliced. In manufacturing of this large size ingot an extremely precise control in the whole process is required which makes this process very expensive. Efficiency of monocrystalline general varies from 14% to 18% and some leading solar cell manufacturing companies have attained efficiencies up-to 20%.

2.2.2 Polycrystalline photovoltaic cell

In making of polycrystalline silicon photovoltaic cells different types of crystals are simultaneously mixed. This process of manufacturing is more economical that for the monocrystalline solar cells due to the graphite mould processing. These polycrystalline cells are the most popular solar cell at present as they are inexpensive to manufacture. In comparison to the monocrystalline photovoltaic cells these cells have an efficiency in range of 12% to 14% [39]. Further, efficiencies of these photovoltaic cells are impacted substantially by temperature variations [40].

2.3 SECOND-GENERATION PHOTOVOLTAIC CELLS

Second-generation cells are primarily dependent on the thin films, consisting of three key families of solar cells i.e., CdTe cells, CIGS photovoltaic cells, and amorphous / micromorph (μc-Si) silicon solar cells. The photoactive layers in these photovoltaic cells are 1 μm [41] in thickness, possessing a bandgap of ~ 1.45 eV [42]. Also, these cells are inexpensive to fabricate.

Trapping of light and back surface passivation helps these second-generation thin film photovoltaic cells to attain efficiencies in the upwards of ~19% [43].

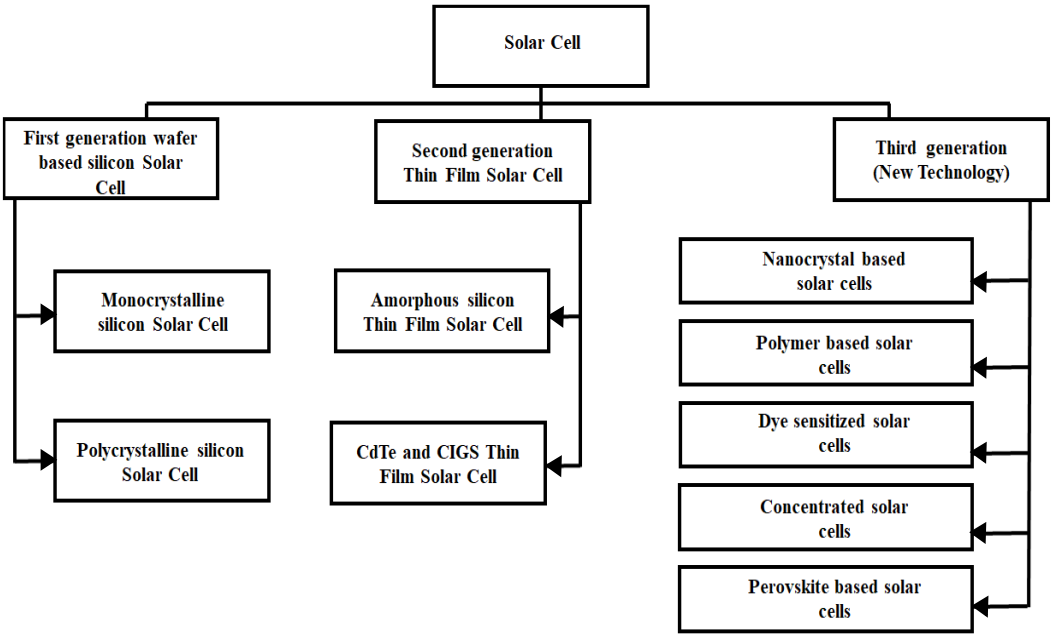

Fig. 2.1 Generation wise categorization for solar cells technology.

2.3.1 Amorphous silicon thin film (a-Si) photovoltaic cell

The a-Si photovoltaics are processed at low-temperatures and utilizes inexpensive polymer and other substrates of flexible nature. In fabrication process the substrates backside is covered with silicon material. The amorphous silicon photovoltaic solar cells posses' silverish colour on their conducting side and brown colour on their reflecting side. The key constraint of these photovoltaic cells is their uneven efficiency. The general efficiencies for these photovoltaics lie in range of 5.9% to 9%.

2.3.2 Cadmium Telluride thin film photovoltaic cells

CdTe is an inexpensive and feasible thin film photovoltaic cell (44, 45). Efficiency of CdTe typically ranges 9.5% to 11% [44, 46]. However, toxic character of cadmium poses environmental concerns, including accumulation in animals, humans, and plants, besides challenges in recycling and disposal. Previous studies have reported efficiencies of around 15% to 16% [47, 48], with the highest efficiency achieved by First Solar (2011) at 17.3% [49]. The manufacturing process involves synthesizing CdTe solar cell from polycrystalline materials, on a glass substrate, and depositing multiple layers onto the substrate.

2.3.3 CIGS (Copper Indium Gallium Selenide) photovoltaic cell

The semiconductor CIGS is composed of four elements: Copper, Indium, Gallium, and Selenium [36, 50]. CIGS cells have reached efficiencies of approximately 10% - 12%, making them among the prominent thin film technologies known for their high-power conversion efficiency. One of the significant strengths of CIGS technology is its non-degrading nature and long lifespan [51, 52]. Various techniques, including electrochemical coating, electron beam deposition, sputtering, and evaporation, are utilized for processing of CIGS photovoltaic cells [53]. The Table 2.1. summarizes different PV cell technologies.

Table 2.1. Generation wise different solar cell technologies

Solar cell Type	Cost	Details	References
First-generation			
Monocrystalline	Expensive in comparison to thin films solar cells	Oldest technology but widely used.	[44, 54]
Polycrystalline	More expensive when compared to thin films solar cells but cheaper than mono-crystalline solar cells	Economic solar cells	[55]
Second-generation			
a-Si (amorphous silicon)	Inexpensive than crystalline silicon	More installation time required	[56]
CdTe	Most cost effective	Toxic due to Cd	[46]
CIGS	Inexpensive than crystalline silicon	Achieved efficiencies up to 20%	[57]
Third generation			
Nano crystals	Inexpensive than crystalline inorganic silicon cell	Requires significant room	[58]
Polymer	Low-cost with respect to silicon solar cell	Requires lesser time for installation	[59]
Dye-sensitised	Cheaper than crystalline silicon	Requires small room	[60]
Concentrated	50% Inexpensive compared to conventional silicon	Needs large space	[61]
Perovskite	Inexpensive compared to crystalline silicon	Up-to-date technology	[62]

2.4 THIRD-GENERATION PHOTOVOLTAIC CELLS

The photovoltaic cell technologies that are still in the demonstration and investigation phase include concentrating PV (CPV) and organic PV cells. These emerging technologies are part of third-generation photovoltaic cells, as mentioned by Choubey *et al.* [1] in 2012. These

include solar cells based on nanocrystals, polymers, dye sensitization, and concentration techniques. These technologies hold promise for further advancements in solar energy conversion.

2.4.1 Nano crystal based photovoltaic cells

The Quantum Dots (QD), are characterised by their nano crystal size. These cells composed of semiconductors belonging to the transition group, and their nanocrystals typically have a size ranging from few nanometers [58]. The presence of centrifugal force enables rapid rotation of these nanocrystals [63].

2.4.2 Polymer based photovoltaic cells

Polymer photovoltaics are known for their flexibility, thanks to their polymer substrate. These solar cells consist of thin layers which are sequentially interconnected and coated with ribbon and polymer foil [64]. Similar to other cells, polymer photovoltaic cells operate on photovoltaic effect, converting solar energy into electrical current [65]. Through significant parameter optimization, researchers have achieved efficiencies of more than 3% for polymer photovoltaic cells [66].

2.4.3 Dye-sensitised photovoltaic cells

In dye-sensitised photovoltaics, dye molecules are situated between the different electrodes. The first dye-sensitised photovoltaic cell was pioneered by Michel Gratzel [67]. These cells consist of four main components a semiconductor electrode, a counter electrode, a redox mediator, and a dye sensitiser [68].

Dye sensitised solar cells are appealing due to their simple conventional processing methodologies, for instance printing techniques, as well as their transparency, flexibility, and lower cost [36]. Efficiency of dye synthesised cells could be improved to greater than 10% by utilizing nano-grained TiO_2 [56]. However, challenges such as deterioration and stability issues need to be addressed in dye synthesized technology.

2.4.4 Concentrated photovoltaic cells

The concentrated photovoltaic cells represent a newly developed technology that aims to gather a significant amount of solar energy and focus it onto a small area. These photovoltaic cells are categorized into low, medium, and high concentration systems [69]. One of the advantages of

concentrated photovoltaic technology is that it does not have any moving parts or thermal mass. These solar cells generate significant amount of heat energy to produce electricity.

2.4.5 Perovskite photovoltaic cells

The perovskite photovoltaic cells present a newly developed research group in area of photovoltaic cells and offer several advantages over thin film and conventional silicon photovoltaic cells. Perovskite compounds are characterised by the formula ZYX_3, wherein X represents a halogen and Z and Y are cations of diverse sizes. Park *et al.* [70] in 2015, initially reported perovskite photovoltaic cells with a high efficiency of up to 9.7%. However, Jacobsson *et al*. [71] 2016 observed a performance drop of up to 25%, as temperature is rises from -80^0 - 80^0 C. Perovskite photovoltaics have the potential to attain efficiencies up to 31% [72].

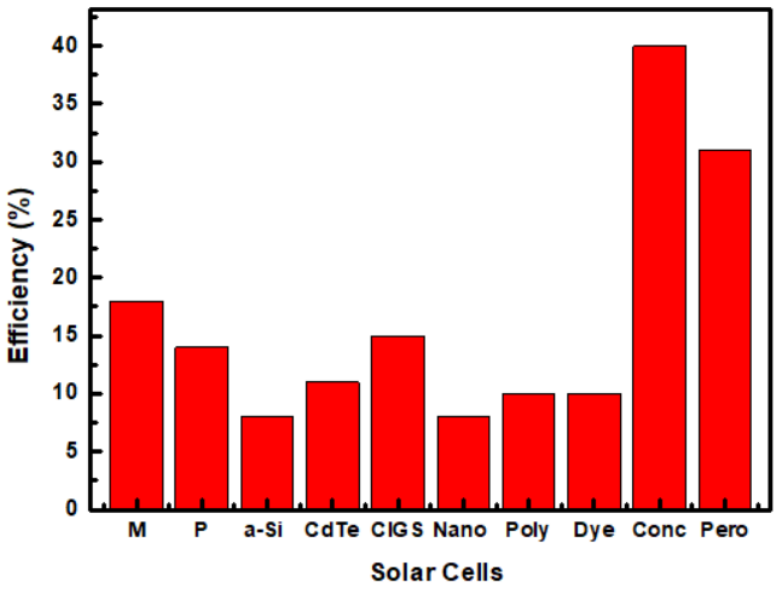

Fig. 2.2 Comparison of efficiency for various types of photovoltaic cells. (M: monocrystalline; P: polycrystalline; a-Si: amorphous silicon; CdTe: Cadmium Telluride; CIGS: Copper Indium Gallium Selenide; Nano: nanocrystal; Poly: polymer; Dye: dye-sensitised; Conc: concentrated; Pero: perovskite)

Different solar cell generations have distinct advantages and disadvantages, and PV performance is influenced by characteristics of their materials and the conditions under which they are fabricated. The Fig. 2.2 presents the comparison the efficiencies of various types of photovoltaic cells, from the figure is it evident that third generation solar cells present a significant improvement over their first- or second-generation counterparts, and introduce several key advancements that enhance their applicability. One of the notable advantages is their enhanced efficiency, which helps them achieve higher power conversion efficiency.

Another crucial advantage is their lightweight and flexible nature. These cells are designed to be lighter, enabling their integration to large range of applications making them suitable for portable devices, wearable electronics, and building-integrated photovoltaics. These solar cells are capable of absorbing wide spectrum making them suitable for electricity generation even under low light or indoor conditions. Further, these cells have inexpensive fabrication costs and are more environment friendly, and have reduced ecological footprint. Therefore, these third-generation cells can revolutionise the solar energy harvesting.

2.5. THIN FILM TECHNOLOGY

Thin film cells have garnered significant interest as it offers a cost-effective approach through efficient utilization of constituent materials via optimizing layer thickness and additional parameters. This technology holds potential in photovoltaics worldwide owing to its adaptability in device fabrication and design options. A comprehensive understanding and information of thin film deposition procedures are crucial for realizing high-performance solar cells. The compounds with semiconducting properties are formed by elements belonging to II (metals) and VI (chalcogens) group of periodic tables. Amongst these elements, II and VI group compounds such as ZnTe, ZnSe, ZnS, ZnO, CdTe, CdSe, CdS, and CdO are extensively utilized in photovoltaic cell applications. The ZnTe solar cells have gained widespread usage due to the unique properties of ZnTe as an emerging material. These properties include bandgap 2.26 eV, high stability, and a considerable coefficient of light absorption.

As per the reported work, ZnTe is a significant and environmentally friendly semiconductor material, that falls under the II-VI group. It possesses lower electron affinity making it appropriate for solar cell devices. ZnTe is primarily found in crystalline cubic structure. Owing to its favourable properties, ZnTe is a prominent material with extensive prospective applications in various solid-state electronics devices. These applications include solar cells, integrated circuits, laser diodes, solar panel displays, LEDs, solar panel displays, switching devices, nano-sensors, gas sensors, tandem solar cells, and photodetectors.

In case of ZnTe thin films, enhanced performance can be accomplished through processes like doping, annealing, and post-deposition actions on diverse substrates. Detailed assessment of the effect of several parameters on ZnTe film properties are described herein. Adding to its properties mentioned earlier, ZnTe offers the advantage of tunable band-gap within the visible electromagnetic spectrum (1.7-3.0 eV). These characteristics makes ZnTe a promising

contender for opto-electronic applications. Moreover, ZnTe exhibits potential advantages for instance lower costs, environmental stability, and effortlessness of manufacturing, further enhancing its appeal [73, 74].

The synthesis of ZnTe thin films employs numerous methods that could be broadly categorized into two kinds - physical and chemical deposition techniques. Physical deposition techniques encompass thermal evaporation, closed space sublimation, e-beam evaporation, other similar methods. On the other hand, chemical deposition techniques include electrodeposition, brush plating, spin coating, and related approaches.

2.6 DEPOSITION TECHNIQUES for ZnTe MATERIAL

Physical deposition techniques employ thermodynamic, mechanical, or electromechanical methods to deposit films, which are of high quality. Similarly, chemical deposition techniques involve development films through chemical transformation. These techniques enable deposition of films over large areas at a lower cost. Various deposition techniques for ZnTe material are as mentioned:

2.6.1 Thermal evaporation technique

Thermal evaporation technique has been adopted by many researchers for depositing ZnTe thin films [75-80]. In this technique, material to be deposited is heated until it melts, and resulting vapours are directed towards the substrate in a vacuum (in range 10^{-3} to 10^{-5} Pa). The rate of deposition, temperature, and the thin film thickness could be regulated [75]. Deposition rate ranges from 0.5 to 5 nm/s [76, 81-84].

2.6.2 Electron-beam evaporation technique

In this technique, the material target is subjected to bombardment with a beam of electron in a high vacuum environment. The effect of beam causes target material atoms to transition to vaporous phase. These atoms then condense forming a thin film on substrate. ZnTe films have been reported to be deposited at vacuum pressures ranging from approximately 10^{-5} Pa to 10^{-4} Pa. The rate of deposition can be regulated, with documented results ranging from 0.1 to 8 nm/s [85-87].

2.6.3 Closed space sublimation technique

This technique is a fast and cost-effective method that efficiently utilizes the depositing material by minimizing distance separating source and substrate. Several researchers have utilized this technique for depositing ZnTe thin films [88-91].

2.6.4 Pulsed laser deposition technique

PLD is a physical vapor deposition method that operates on ablation process. This technique is known for its simplicity and versatility, leading to its widespread use in film formation by many researchers. ZnTe thin films with different thicknesses have been reported using the PLD technique [92, 93].

2.6.5 Sputtering technique

In the sputtering technique, energetic particles, typically gas ions, bombard a solid target material, causing particles to be ejected from the target [94]. Sputtering is an inexpensive and popular deposition technique that can be carried out at low temperatures [95]. Moreover, using sputtering technique, crystalline films with thicknesses varying from 255 to 1650 nm have been deposited [96]. The Table 2.2. presents different ZnTe deposition techniques and parameters associated with it.

2.6.6 Brush plating technique

Brush plating technique, also referred to as swab plating, selective plating, or contact plating, involves the use of a handheld portable tool for depositing thin films. Plating is applied via using a brush or swab that is saturated with a solution and attached to flexible anode cable [97].

2.6.7 Electrodeposition technique

Electrochemical deposition is an appropriate technique for depositing semiconducting thin films. The technique offers several benefits, including processing at low-temperature, control over film morphology and thicknesses, and cost-effectiveness [98]. Researchers have reported the deposition of ZnTe films ranging from 0.1 to 0.7 μm (thickness), using electrochemical deposition [99]. In addition to the stated techniques, other approaches have been documented for depositing ZnTe films for example, Chemical Vapour Deposition [100], SILAR method [101], and spray pyrolysis [102] were documented for depositing ZnTe thin films.

Table 2.2. Various deposition techniques for ZnTe material and thin film performance parameters

S. No.	Deposition pressure (Pa)	Substrate temperature (^{0}C)	Optical bandgap (eV)	Resistivity (Ω cm)	Activation Energy (eV)	Mobility (μ)	References
Thermal evaporation technique							
1.	6.6×10^{-3}	30 100 200 250 300	2.10 2.15 2.20 2.26 2.28	- - - - -	0.05 0.07 0.09 0.04 0.11	- - - - -	[84]
2.	10^{-3}	Room temperature	-	2.5×10^4 – 1.7×10^7	-	-	[75]
3.	3×10^{-2}	-123 27	2.13 2.16	32 1×10^4	- -	- -	[81]
4.	10^{-5}	27 100 200 280	- - - -	1538 709 310 287	- - - -	μ = 12.8 μ = 21.2 μ = 36.9 μ = 37.6	[82]
5.	1.3×10^{-3}	27 100 200 280	- - - 2.26	1538 709 310 287	- - - -	μ = 12.8 μ = 21.2 μ = 36.9 μ = 37.6	[103]
Electron beam evaporation technique							
6.	8×10^{-5}	8	2.265		8.6×10^{-3}		[85]
7.	8×10^{-4}	2.05			-		[86]
8.	1.3×10^{-4}	0.1	- 2.24		-		[87]
Closed space sublimation technique							
9.	10^{-2}	350	2.23	-	1.01×10^6		[88]
10.	1	400	2.24	2.71	4.5×10^6		[89]
11.	-	420	2.259	-	-		[90]
12.	1	450	2.23	2.27	2.91×10^8		[91]
Pulsed laser deposition technique							
13.	1.3×10^{-7}	248	-	2.26×10^5			[92]
14.	$<10^{-4}$	532 1064	1.25 1.32	-			[104]
15.	1.3×10^{-4}	266	-	-			[93]
Sputtering technique							
16.	1.5-1.6	N_2	1.70	-	1.4×10^4	-	[105]
17.	10^{-2}	Ar	2.26	2.55	-	0.48	[96]

Chemical deposition techniques					
18.	Brush plating technique	2.0	2.30	Resistivity = $10^3 – 10^4$ Ω cm Mobility (μ) = 5 – 60 $cm^2 V^{-1} s^{-1}$	[106]
19.	SILAR technique	10.0	2.75 – 3.15	-	[101]
20.	Electro chemical technique	2.5	2.26	-	[107]

The above-mentioned deposition techniques enable the precise growing of ZnTe films with diverse properties and thicknesses, making them suitable for various applications, for instance solar cells, optoelectronic, and semiconductor devices. The technique chosen relies on specific requirements of the applications and the desired film characteristics.

2.7 EFFECT OF DOPING ON ELECTRICAL AND OPTICAL PROPERTIES OF ZnTe THIN FILMS

Doping refers to the deliberate addition of impurities to a material to amend its various properties. The integration of impurity atoms can significantly affect crystallinity, conductivity, and the material's optical characteristics [87, 108]. Doping play's vital part in enhancing applicability of chalcogenides. For ZnTe thin films, several elemental compositions have been used for doping. Researchers have studied the impact of different dopants on the ZnTe thin films electrical, and optical properties, and their findings are summarized in Table 2.3.

Pattar *et al*. [109] in 2009, conducted a study where ZnTe was doped with Indium. The researchers observed that as the doping concentration increase, optical band-gap decrease. Lastra *et al*. [92] conducted a study where ZnTe was doped via dipping them in solutions comprising varying concentrations $Cu(NO_3)_2$-$3H_2O$ for 1 minute. The doping level influenced the improvement in mobility and carrier concentration, resulting in reduced sheet resistance and doped films resistivity. Gul *et al*. [108] doped ZnTe using the thermal evaporation technique. The band-gap declined with growing copper doping content. Copper-doped films exhibited higher refractive indices, which was attributed to improved crystallinity.

Mahmood *et al*. [88] doped ZnTe via submerging it into copper solutions of various concentrations. Optical studies showed lessening in optical band-gap due to defects caused by doping. Electrical resistivity decreases with doping so does the mobility after doping. Lee *et*

al. [93] conducted a study where ZnTe films were doped under diverse pressure of N_2 (3×10^{-3} Pa, 6.6 Pa, and 9.3 Pa). The electric findings revealed that the resistivity and mobility decreased, while the concentration of holes increased with increase in level of doping.

Mahmood *et al*. [87] conducted a study where Zn Ni Te films were deposited with dissimilar compositions. The researchers observed a gradual decline in band-gap with rise in doping concentration. Sharma *et al*. [110] performed a study where chromium doped Zn Cr Te films were deposited, with doping concentrations of x = 0.1 and 0.2. It was observed that the integration of Cr atoms led to a slight reduction in absorbance.

Rao *et al*. [103] employed a new technique for doping vacuum-deposited ZnTe thin films using nano-spheres as the dopant material. The optical band gap did not show significant changes after doping. The enhancement in carrier density was credited to the incorporation of bismuth atoms. Aqili *et al*. [89] conducted a study where ZnTe thin films were doped via submerging them in a solution comprising 1 gm of $AgNO_3$ in 1 liter of water for varying time durations (1, 5, and 30 minutes). Mahmood *et al*. [88] doped ZnTe by dipping them in a solution made up of one gm of Ag in one liter of H_2O for dissimilar periods of time. A decline in band-gap was detected because of the existence of additional defect states.

Ma *et al*. [111] utilized the laser-assisted deposition/epitaxy technique to dope ZnTe. Hossain *et al*. [86] deposited amorphous vanadium doped thin films using the e-beam evaporation technique. The study revealed activation energy reduced with growing doping. Optical results demonstrated that the band-gap declined [87-89]. However, some scholars found no effect [103] or even enhancement in the band-gap with doping [109, 111]. The Table 2.3. summarizes effect of doping on ZnTe properties.

Table 2.3. Effect of doping on electrical properties of ZnTe thin films. (E_g = Activation Energy; ε = permittivity)

S. No.	Dopant	Doping	Heat treatment	Optical band gap (eV)	Resistivity (Ω cm)	Remarks	References
1.	Indium	Undoped	127 °C, 3 h	2.37	-	Amorphous	[109]
		5 min	127 °C, 3 h	-	-	Crystalline, $\varepsilon = 3.04 \times 10^{-3}$	
		10 min	127 °C, 3 h	-	-	Crystalline $\varepsilon = 4.545 \times 10^{15}$	
						-	

		15 min immersion	127 ºC, 3 h	2.14	-		
2.	Indium	Undoped 6%	- 127 ºC, 6 h	- -	7.10×10^6 3.00×10^5	Polycrystalline, p type	[112]
3.	Copper "X" in mg	Undoped x = 6 mg x = 7 mg x = 9 mg x = 11 mg x = 13 mg x = 15 mg x = 60 mg	- 300 ºC, 10 minutes 300 ºC, 10 minutes 300 ºC, 10 minutes 300 ºC, 10 minutes 300 ºC, 10 minutes 300 ºC, 10 minutes 300 ºC, 10 minutes	- - - - - - - -	2.26×10^5 145.00 50.00 12.45 2.44 4.39 0.35 0.35	2.52×10^{10} Ω/sq. 1.60×10^7 Ω/sq. 5.80×10^6 Ω/sq. 1.6×10^6 Ω/sq. 2.70×10^5 Ω/sq. 4.88×10^5 Ω/sq. 3.90×10^4 Ω/sq. 3.90×10^4 Ω/sq.	[92]
4.	Copper	Undoped 6 % 8 % 10%	- - - -	2.24 2.00 1.84 1.64	- - - -	n = 2.39 n = 2.47 n = 3.03 n = 3.20	[108]
5.	Copper	Undoped 20 min immersion	- 350 ºC, 1 h	2.23 2.21	1.01×10^6 68.97	- -	[88]
6.	Nitrogen	Undoped 13.3 mPa 6.6 Pa 9.3 Pa	- - - -	- - - -	- - 54.90 9.32	Polycrystalline Crystallinity dec. Crystallinity dec. Crystallinity dec.	[93]
7.	Nickel	Undoped 5% 10% 15% 20%	- - - - -	2.25 - - - -	- - - - -	-	[87]
8.	Chromium	Undoped 0.1 0.2	- - -	2.57 1.84 1.47	- - -	- - -	[110]

9.	Bismuth	Undoped 0.18% 0.23% 0.32%	- - - -	2.25 2.25 2.25 2.25	1.32×10^3 1.19×10^2 0.88×10^2 0.85×10^2	$E_g = 0.89$ eV - - $E_g = 0.78$ eV	[103]
10.	Silver	Undoped 1 min 5 min 30 min	- 400 °C, 1 Pa 400 °C, 1 Pa 400 °C, 1 Pa	2.24 2.21 2.18 2.16	4.50×10^6 8.10×10^3 5.90×10^2 3.54	$E_g = 0.25$ eV - - $E_g = 0.14$ eV	[89]
11.	Silver	Undoped 20 min immersion	- 350 °C, 1h	2.23 2.19	1.01×10^6 4.00×10^4	- -	[88]
12.	Gadolinium	Undoped 3% 7% 8% 9%	- N_2, 400 °C, 30 min N_2, 400 °C, 30 min N_2, 400 °C, 30 min N_2, 400 °C, 30 min	2.26 - - 2.28 2.31	- - - - -	- - - - -	[111]
13.	Vanadium	Undoped 2.5% 5.0% 7.5% 10.0%	- - - - -	- - - - -	- - - - -	$E_g = 0.50$ eV $E_g = 0.48$ eV $E_g = 0.46$ eV $E_g = 0.42$ eV $E_g = 0.36$ eV	[86]

Therefore, ZnTe due to its wide bandgap is a good candidate for doping. The crystalline structure of ZnTe also makes it a stable structure allowing precise control over doping process. Additionally, its unique electronic properties make it an excellent host material for introducing dopant atoms, which can modify its electrical behaviour and enhance its performance in

applications such as solar cells. Further, ZnTe is relatively easy to synthesise, making it a convenient choice for doping experiments and applications in semiconductor technology.

2.8 ORGANIC SOLAR CELLS

Owing to their environmentally friendly nature, flexibility, ease of large-scale production, and cost-effectiveness, OSCs are regarded as a promising energy source for future [113]. Calculations indicates that organic solar cell (OSC) technology holds great potential and can enable cost-efficient power generation. After the discovery of photovoltaic effect in organic materials [114] and starting of the heterojunction idea in 1986 [27], performance of organic solar cells has enhanced rapidly. The effective utilization of photons through the blending of donor and acceptor into solo layer, known as bulk heterojunctions (BHJ) solar cells, has transformed the technology, and led growth of high efficiency OSC devices [28, 115-117].

Enhancement in processing conditions [118], as well as in pre and post-fabrication actions [119], along with utilization of advanced materials and novel device strategies [120, 121], have significantly contributed to the remarkable efficiency improvements in organic cells. In the past, reported efficiencies of OSCs were limited to around 1%, but today, efficiencies exceeding 7% have been achieved [115-117]. In the past, OSCs had a very short lifespan of only a few hours. However, significant advancements have been made, and now OSCs with an outdoor lifespan exceeding 15,000 hours have been successfully developed [122-124]. With ongoing improvements in efficiency, it is anticipated that OSCs will present robust alternative to traditional solar cells.

2.8.1 Bilayer solar cells

Tang, introduced donor/acceptor notion in a bi-layer OSC structure, which marked a important milestone OSCs development [27]. The bi-layer structure, also identified as a planer heterojunction, demonstrated a efficiency of approximately 1.0%. Forrest *et al*. further enhanced the efficiency to 1.8% by using CuPc and perylene tetracarboxylic dianhydride in a bi-layer configuration [125].

The fullerene (C_{60}) has superior electrical properties and superior diffusion displacement of exciton in comparison to perylene derivatives made it a preferred acceptor materials for efficient devices [136]. Other small molecule donor materials commonly utilised in photovoltaic cell applications include zinc phthalocyanine (ZnPc) [120], boron

subphthalocyanine [130,126], tin phthalocyanine [137], and others. One of the challenges faced by bilayer solar cells is exciton quenching [138]. Addressing this, Peumans *et al*. [139] presented exciton blocking layer, this addition of EBL increased the efficiency from 1.0% to 2.4%. The Table 2.4. presents the performance of important bilayer OSCs.

Table 2.4. Photovoltaic performance of important bilayer organic solar cells

Device No.	Layered Materials	J_{Sc} (mA/cm^2)	V_{OC} (V)	FF (%)	η (%)	Reference
D1.	ITO/CuPc/SubPc/C60/BPhen/Al	5.16	0.42	0.47	1.29	[126]
D2.	ITO/CuPc/PTCBI/Ag	2.3	0.45	0.65	0.95	[27]
D3.	ITO/MEH: PPV/BBL/Al	1.98	0.93	0.47	1.1	[127]
D4.	ITO/PPV/BBL/Al	2.15	1.1	0.50	1.5	[127]
D5.	ITO/CuPc/PTCDA/In	2.0	0.55	0.35	1.8	[125]
D6.	ITO/PEDOT:PSS/MDMO-PPV/PCBM/Al	0.96	0.78	0.5	0.5	[128]
D7.	ITO/NDP2/ZnPc/C60/ZnPc/C60/ZnPc /C60/ZnPc/C60/BPhen/Al	10.13	0.49	0.51	2.2	[129]
D8.	ITO/SubPc/C60/BCP/Al	3.36	0.97	0.57	2.1	[130]
D9.	ITO/Pentacene/C60/BCP/Al	15	0.36	0.50	2.7	[131]
D10.	ITO/PEDOT: PSS/Tetracene/C60/BCP/Al	7.0	0.58	0.57	2.3	[132]
D11.	ITO/PEDOT: PSS/CuPc/C60/BCP/Al	18.8	0.58	0.52	3.6	[133]
D12.	ITO/CuPc/C60/BCP/Ag	53.1	0.57	0.61	4.2	[134]
D13.	ITO/Au/p-doped Di-NPB/Di-NPB/DCV5T/C60/BPhen	10.6	0.98	0.49	3.4	[135]

Because of lower carrier mobilities and amorphous nature of organic materials, charge carriers tend to accumulate near the heterojunction after dissociation of exciton in bi-layer photovoltaic cells. These accumulates near heterojunction after dissociation of exciton in bi-layer photovoltaic cells. This accumulation creates a space charge that significantly influences the performance of the OSC. Furthermore, bound nature of the carriers through coulombic attraction and the potential for recombination via exciplex formation contribute to the limitations of bilayer photovoltaic cells. Another contributing factor is the interface area of donor and acceptor, hindering effective separation of charges and exciton dissociation. To overcome these challenges, a solution was found in the form of a single layer configuration wherein donor and acceptor are blended simultaneously. This allows for the formation of heterojunctions throughout bulk of the material, ensuring efficient and quantitative exciton dissociation. This approach maximizes interfacial area thereby improves overall solar cell performance.

2.8.2 Bulk-heterojunction solar cells

Heeger *et al*. [28] introduced concept of a bulk heterojunction (BHJ) photovoltaic cell, demonstrating PCE of approximately 1.5%. This efficiency was significantly higher than the previously reported bilayer configuration by Tang [27]. The BHJ structure involved the use of donor and acceptor, specifically MEH-PPV and PCBM, respectively. The blend of these materials exhibited phase separation because of lower entropy of mixing. The BHJ structure reduced recombination and resulted in high short circuit density (J_{SC}) [134].

Friend *et al*. [140] also adopted the BHJ approach in the same year, further contributing to the growth of efficient photovoltaic cells. To improve the performance, Shaheen *et al*. [118] used MDMO-PPV as the donor and PCBM as the acceptor, achieving an efficiency of 2.5%. Padinger *et al*. developed photovoltaic cell using P3HT and PCBM material [119]. They observed significantly improved efficiency from 0.4% to 2.5%. In 2005, Ma *et al*. [141] achieved an efficiency of 5% by utilizing P3HT and PCBM as donor and acceptor material in simple BHJ configuration.

Table 2.5. Photovoltaic performance of important bulk heterojunction organic solar cells

Device No.	Device	J_{SC} (mA/cm^2)	V_{OC} (V)	FF (%)	η (%)	References
D1.	ITO/PEDOT: PSS/PCPDTBT: PCBM/Al	16.2	0.62	0.55	5.2	[145]
D2.	ITO/PEDOT: PSS/P3HT: PCBM/Al	9.5	0.63	0.68	5.0	[141]
D3.	ITO/PEDOT: PSS/P3HT: PCBM/TiO_X/Al	11.1	0.61	0.66	5.0	[146]
D4.	ITO/PEDOT: PSS/PTB7: PCBM/Al	14.5	0.74	0.69	7.4	[143]
D5.	ITO/MEH: PCBM/Ca	2.0	0.80	0.25	1.5	[147]
D6.	ITO/PEDOT: PSS/APFO-Green5:PCBM/LiF/Al	8.88	0.59	0.42	2.2	[148]
D7.	ITO/PEDOT: PSS/MDMO-PPV: PCBM/LiF/Al	5.25	0.82	0.61	3.3	[149]
D8.	ITO/PEDOT: PSS/PFDTBT: PCBM/LiF/Al	4.66	1.04	0.46	2.2	[150]
D9.	ITO/CuPc: C60/C60/BCP/Ag	15.4	0.50	0.46	3.5	[151]
D10.	ITO/CuPc/CuPc: C60/C60/BCP/Ag	18.2	0.54	0.61	5.0	[152]

The superior regioregularity of P3HT, resulting in high mobility and enhanced photon absorption at longer wavelengths when set side by side to PPV derivatives, played a significant role in achieving this efficiency. Small molecular BHJ photovoltaic cells have also demonstrated efficiencies of approximately 3.5% [118, 121]. The nanoscale morphology is critical constraint to achieve efficient OSCs [141, 118, 142]. In polymer-based cells,

morphology is regulated via selecting suitable solvents, optimizing thickness of layer, methods of deposition, and curing processes [118, 140]. The use of mixed solvent method further proves successful in improving the morphology of photoactive layers [143, 144, 145]. The Table 2.5 represents important BHJ cells.

Yao *et al*. studied outcome of mixed solvent method on P3HT: PCBM films morphology [153]. Li *et al*. [154] introduced annealing method as a means to enhance film morphology in OSCs. By controlling solidification rate during polymer layer growth, the self-organisation of polymer chains can be influenced, leading to improved morphology. Nanoparticles derived from polymers have been utilize to manipulate the thin films morphology.

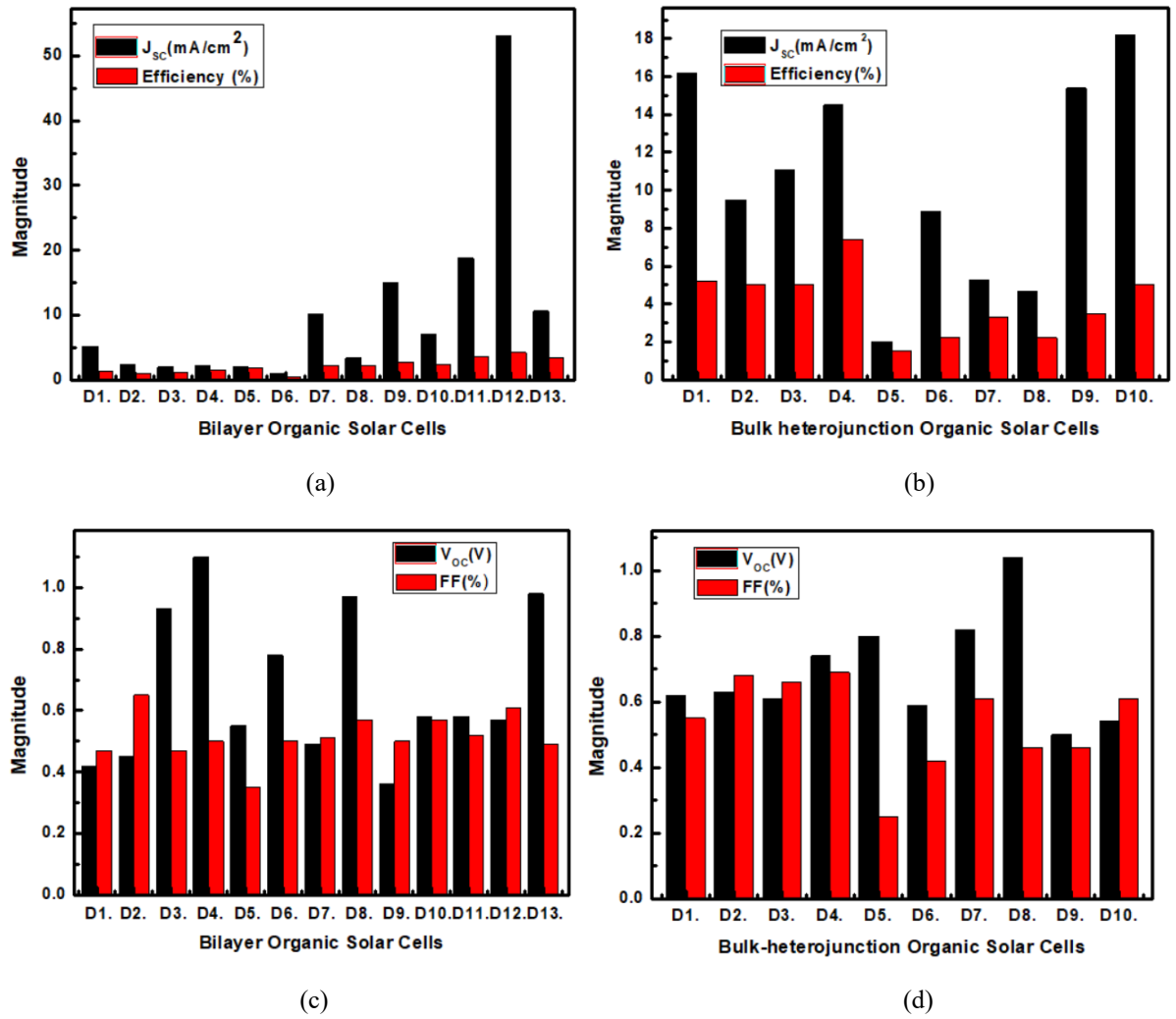

Fig. 2.3 Short-circuit current density and efficiency of (a) bilayer and (b) bulk heterojunction organic solar cells, and open circuit voltage and fill factor of (c) bilayer and (d) bulk heterojunction organic solar cells.

The Figs. 2.3 (a) and (b) presents J_{SC} and efficiency of various important organic cells respectively. From figures it could be detected that the BHJ organic cells have higher

efficiencies in contrast to bilayer. In BHJ, blend of donor and acceptor creates a large interfacial area facilitating an efficient transport and separation of charges. Therefore, BHJ can absorb broad spectrum of light, leading to higher photocurrent generation. Similarly, Figs. 3 (c) and (d) present the V_{OC} and *FF* of bilayer and bulk heterojunction cells. BHJ, achieve higher V_{OC} because more photogenerated excitons have a better chance of dissociating into free charges at the interface. Further, better energy level alignment in BHJ also leads to a higher open circuit voltage. The higher generation, better transport, and efficient collection of photocarriers reduces the number of recombination losses. Therefore, fill factor of BHJ is higher in comparison to organic bilayer solar cells. The higher efficiency and other performance parameters make the BHJ organic solar cells an excellent selection for organic solar cell applications.

2.8.3 Tandem Solar Cells

To address the limited absorption range of OSCs, researchers have proposed a tandem configuration, consisting of multiple interconnected solar cells, to enhance the overall optical density across a wider spectrum. Hiramoto *et al*. [155] introduced the tandem cell concept, which involves the series connection of two or more OSCs. Hiramoto *et al*. [155] demonstrated a tandem configuration with non-continuous metal layer, resulting in an efficiency that was more than double that of individual cells. Tandem photovoltaics have been explored advancements have been made in optimizing the interlayer design for improved performance.

Xue *et al*. [156] achieved an PCE of approximately 5.7% by stacking two CuPc/C_{60} heterojunction cells. Exciton blocking layers, PTCBI and BCP, were used for front and back cells, respectively. Tandem cell exhibited a 15% increase in efficiency compared to a single hybrid planer-mixed heterojunction photovoltaic cell. In another study, Gilot *et al*. [157] fabricated multi-junction photovoltaic cells using polymers. They employed appropriate solvent mixtures for deposition of sequential layer.

Shrotriya *et al*. [158] conducted a study where they fabricated two solar cells with different configurations. Denller *et al*. [159] conducted a study where they made tandem heterojunction cells. The tandem cell consisted of a planer-mixed heterojunction cell of ZnPc:C60 stacked on P3HT: PCBM. However, tandem cell exhibited a lower J_{SC} in comparison to the individual cell, resulting in a lower efficiency.

Similarly, Colsmann *et al*. [150] made a tandem P3HT, PCBM and CuPc/C60 cell. The efficiency of tandem solar cell was 1.2%, which was lesser than the efficiencies of reference polymer photovoltaic cell (1.5%) and the reference CuPc/C60 cell (1.1%). The Table 2.6. represents important tandem cells.

Table 2.6. Photovoltaic performance of important tandem organic solar cells

S. No.	Device	J_{SC} (mA/cm^2)	V_{OC} (V)	FF (%)	η (%)	References
1.	ITO/CuPc/CuPc: C60/C60/PTCBI/Ag/m-MTDATA: F4TCNQ/CuPc/CuPc: C60/C60/BCP/Ag	9.7	1.03	0.59	5.7	[156]
2.	ITO/p-MeO-TPD/ZnPc: C60/n-C60/Au/p-MeO-TPD/ZnPc: C60/n-C60/Al	10.8	0.99	0.47	3.8	[159]
3.	ITO/PEDOT: PSS/PCPDTBT: PCBM/TiO_X/PEDOT: PSS/P3HT: PCBM/TiO_x/Al	7.8	1.24	0.67	6.5	[161]

In order to attain PCE in OSCs, selection of active layer materials, including donor and acceptor materials, is crucial. These donor/acceptor materials should have certain properties to optimize the performance of OSCs. Specifically, they should exhibit (a) matched absorption spectrum to efficiently capture a broad range of photons, (b) accurate alignment of energy levels to facilitate efficient charge transfer, (c) nanoscale phase separation for efficient dissociation of exciton, and (d) high carrier mobility to facilitate efficient transportation of charge within the device. These properties are important considerations for designing donor-acceptor materials in OSCs.

2.9 ORGANIC SOLAR CELL ACCEPTOR MATERIALS

There have been two distinct phases of research in the development of acceptor materials for OSCs. Prior to 2015, $PC_{61}BM$ and $PC_{71}BM$ remained leading acceptors used in organic solar cells. However, in 2015, Lin and colleagues introduced a novel non-fullerene acceptor (NFA) called ITIC, which exhibited improved absorption in visible region, higher mobility of electrons, and better compatibility with donor materials compared to fullerene acceptors. This discovery sparked increased interest in NFAs, leading to significant advancements NFA-based OSCs.

2.9.1 Fullerene Derivatives as Acceptors

In 1995, Yu and colleagues introduced soluble fullerene derivative $PC_{61}BM$, which enabled formation of efficient donor-acceptor interfaces and improved separation of exciton in BHJ organic solar cell [28]. This breakthrough in using soluble fullerene derivatives significantly advanced field of OSCs.

Shaheen *et al*. [118] mixed $PC_{61}BM$ and MDMOK-PPV in OSCs which attained an PCE of 2.5%. Padinger *et al*. [119] stated 3.5% efficiency in P3HT: $PC_{61}BM$ photovoltaics under white light illumination. In 2005, Li *et al*. improved the carrier mobility and charge transport in P3HT: $PC_{61}BM$ photovoltaic cells by controlling growth rate, producing a PCE of 4.37% [154]. Further modifications, for instance thermal or vapour annealing during fabrication of the device, have pushed PCE of P3HT: $PC_{61}BM$ cells beyond 6%. Performance characteristics of organic cell established on various fullerene derivatives are compiled and presented in Table 2.7 outlining important device parameters.

Table 2.7. Characteristics of typical fullerene acceptors and corresponding device performance

Device No.	Acceptor	Donor	J_{SC} (mA/cm^2)	V_{OC} (V)	FF (%)	PCE (%)	References
D1.	$PC_{71}BM$	PTB7	14.50	0.74	68.97	7.40	[162]
D2.	$PC_{61}BM$	P3HT	8.5	0.55	60	3.5	[118]
D3.	$PC_{61}BM$	MDMO-PPV	5.25	0.82	61	2.5	[163]
D4.	$PC_{61}BM$	P3HT	10.6	0.61	67.4	4.37	[28]
D5.	$NC_{61}BM$	P3HT	9.06	0.70	64	4.09	[164]
D6.	$IC_{70}BA$	PTB7	15.4	0.79	55	6.67	[165]
D7.	ICBA	P3HT	10.61	0.84	72.7	6.48	[166]
D8.	$PC_{71}BM$	MDMO-PPV	7.6	0.77	51	3.0	[167]
D9.	$PC_{71}BM$	PffBT4T-2OD	18.2	0.77	74	10.4	[168]
D10.	F1	P3HT	10.8	0.564	60.3	3.7	[169]
D11.	Bis$PC_{61}BM$	P3HT	9.14	0.724	68	4.5	[170]
D12.	F	P3HT	10.3	0.81	63	5.25	[171]
D13.	$PC_{71}BM$	P3HT	12.2	0.61	55	4.1	[172]
D14.	ICBA	P3HT	9.67	0.84	67	5.44	[173]
D15.	$IC_{70}BM$	P3HT	11.34	0.81	63	5.79	[174]

Troshin reported efficiency of 4.1% by utilizing P3HT:PC71BM as photoactive layer of BHJ organic solar cell [175]. Yu's *et al*. stated PTB7 and $PC_{71}BM$ yielding 7.4% [176]. In 2014, Liu

et al. reported PffBT4T-2OD, a novel donor material and an efficiency of 10.4% was attained by blending it with $PC_{71}BM$ [177]. In 2008, Lenes *et al*. introduced bis$PC_{61}BM$, its use in P3HT: bis$PC_{61}BM$ solar cell resulted in PCE of 4.5% [178]. He *et al*. synthesised indene-C60 bisadduct (ICBA), organic solar cells made up of P3HT: ICBA presented an efficiency of 5.44% [179]. Zhao *et al*. improved efficiency of ICBA organic solar cells to 6.4% via device optimization [180]. The OSC made of P3HT with $IC_{70}BM$ as acceptor reported a PCE value of 5.79%.

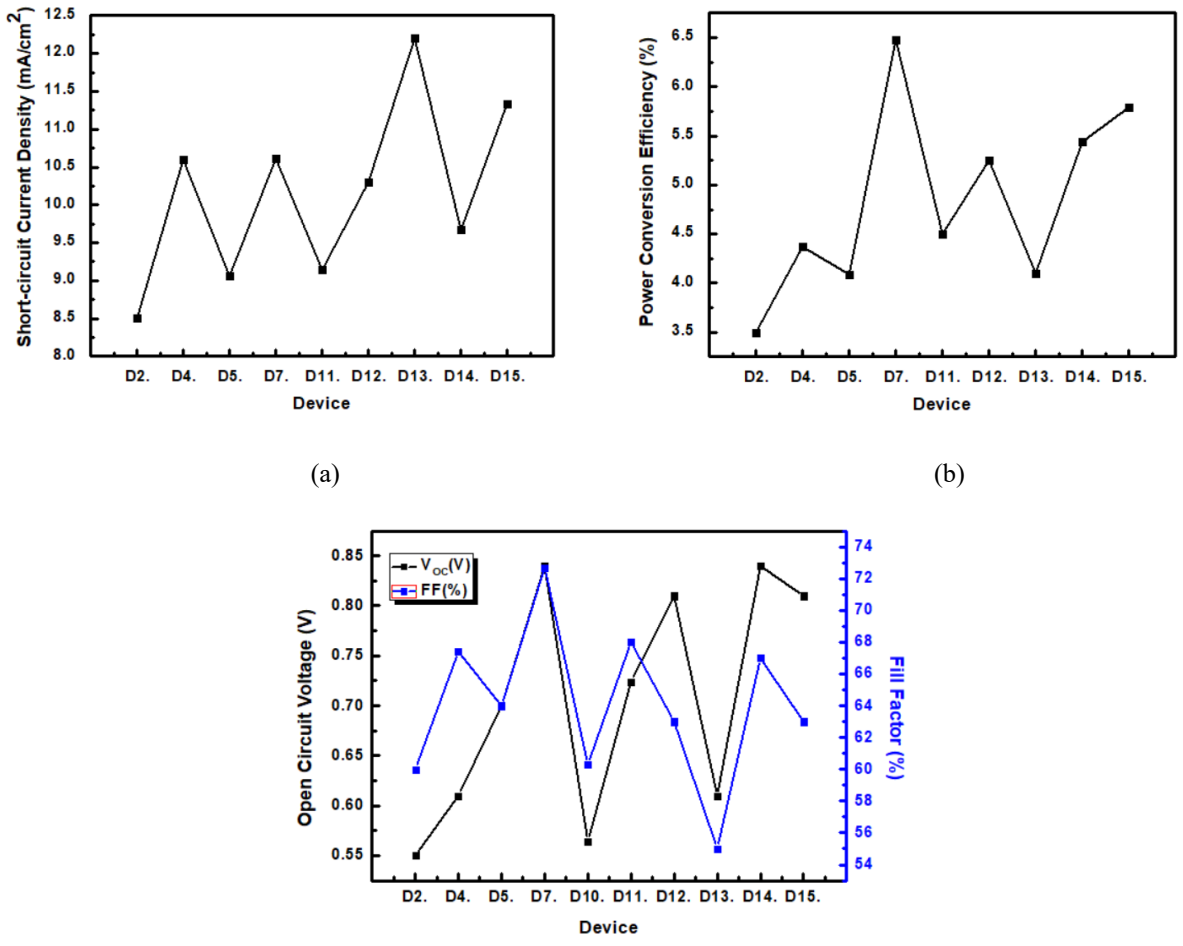

Fig. 2.4 The characteristic plots of (a) Short-circuit current density, (b) efficiency, (c) open-circuit voltage and fill factor of organic solar cells with different fullerene acceptors and same donor (P3HT) material.

The Fig. 2.4 represents the reported values of various performance parameters of organic solar cells with diverse fullerenes but same donor material (P3HT), mentioned in the Table 2.7. From the plots it can be established that the acceptor material can affect the organic cell's performance. In OSCs acceptor primarily accepts the electrons and facilitates charge separation essential for current generation. The lower magnitude of acceptor material LUMO in

comparison to donor layer facilitates efficient charge separation. Further, acceptor material significantly impacts the energy loss and morphology of the device. By carefully selecting appropriate acceptor material and optimizing its properties, researchers can enhance performance of the organic cells.

2.9.2 Small molecular Non-Fullerene Acceptors (NFA)

While fullerene acceptors were extensively studied, they have inherent limitation, primarily restricted tunability of chemical structure and low absorption in visible spectrum. These drawbacks have motivated researchers to explore NFAs as alternatives. NFAs offer advantages such as enhanced optical absorption, tunable bandgap, and higher open circuit voltage (V_{OC}) values. The Table 2.8. presents the characteristics and device performance of small molecular NFAs.

Table 2.8. Characteristics performance of small molecular NFAs

Device No.	Acceptor	Donor	J_{SC} (mA/cm^2)	V_{OC} (V)	FF (%)	PCE (%)	References
D1.	FOIC	PTB7-Th	24.0	0.743	67.1	12.0	[181]
D2.	L8-BO	PM6	26.03	0.893	80.0	18.60	[182]
D3.	BTP-eC9	PM6	26.2	0.839	81.1	17.8	[183]
D4.	ITIC	PTB7-Th	14.21	0.81	59.1	6.80	[184]
D5.	ITIC-Th	PDBT-T1	16.24	0.88	67.1	9.6	[185]
D6.	SeTIC4Cl	PM6	22.92	0.78	75	13.32	[186]
D7.	L8-BO	PM6	25.72	0.87	81.5	18.32	[187]
D8.	m-BTP-PhC6	PTQ10	25.3	0.883	79.3	17.7	[188]
D9.	Y6	PM6	25.2	0.82	76.1	15.7	[189]
D10.	BTP-4Cl	PM6	25.4	0.867	75	16.5	[190]
D11.	ITIC	PBDB-T	16.81	0.899	74.2	11.21	[191]
D12.	IT-4F	PBDB-T-SF	20.50	0.88	71.9	12.97	[192]
D13.	ITIC	PBDTS-TDZ	17.78	1.10	65.4	12.80	[193]
D14.	IDIC	FTAZ	20.8	0.84	71.8	12.5	[194]
D15.	Y6	D18	27.70	0.859	76.6	18.22	[195]
D16.	IT-M	PBDB-T	17.44	0.94	73.5	12.05	[196]
D17.	IOIC3	PTB7-Th	22.9	0.762	74.9	13.1	[197]
D18.	Y6	PM6	27.43	0.845	73.8	17.1	[198]
D19.	Y6Se	D18	27.98	0.839	75.3	17.7	[199]

The Table 2.8 provides device parameters of organic cells made of efficient small molecular NFAs. In 2016, Hou *et al*. [200] developed IT-M which lead to a high open circuit voltage of 0.94 Volts in organic solar cell, resulting in a PCE of 12.05%. They also synthesised IT-4F which exhibited improved absorption and enhanced inter/intramolecular interactions. When combined with PBDB-T-SF donor material, the OSC attained an efficiency of 12.97%.

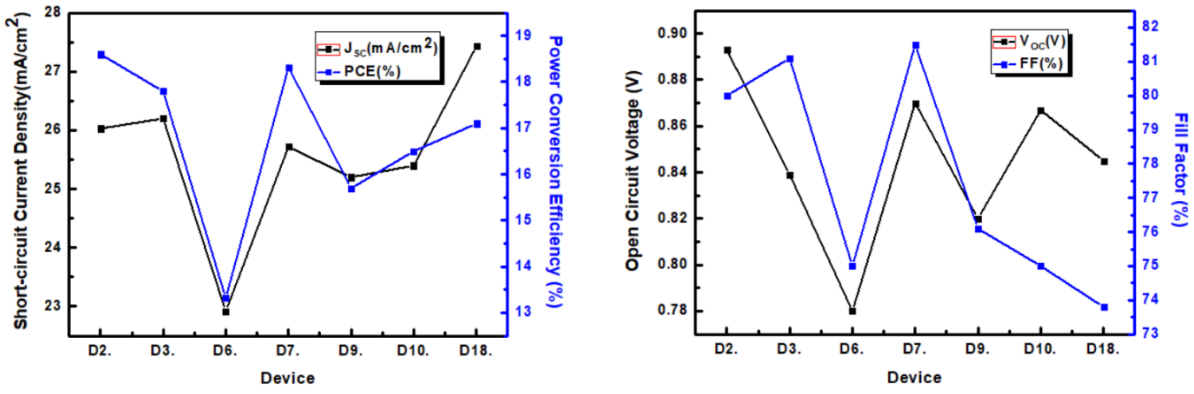

(a) (b)

Fig. 2.5 The variation plot of (a) Short-circuit current density and efficiency, (b) open-circuit voltage and fill factor of organic solar cells with different small molecule NFAs acceptors and same donor (PM6) material.

When combined with PM6, a device with structure ITO/PEDOT: PSS/PM6: Y6/PDINO/Al achieved an impressive efficiency of 15.7%. Tran *et al*. [201] demonstrated a Y6-based cells by incorporating MoO_x as HTL resulting in efficiency of 17.1%.

The Fig. 2.5. (a) represents plot of J_{SC} and efficiency, and Fig. 2.5. (b) represents the V_{OC} and *FF* of organic solar cells with different small molecule NFAs acceptors but same donor (PM6) material. From the Fig. 2.5 it can be observed that small molecule NFAs have a higher J_{SC} and efficiency in contrast to fullerene acceptor discussed in previous sub-section. This is primarily due to the broader absorption range of small molecule NFAs than fullerene acceptors. The chemical structure of NFAs is also tunable and hence can be modified to achieve better band energy alignment. Further, these solar cells have improved nanoscale morphology leading to better charge transport and reduced charge recombination, contributing to higher photocurrent and fill factor.

Non-fullerene OSCs utilizing small molecule acceptor like ITIC, Y6, and L8-BO and have demonstrated impressive efficiencies and have offered promising alternate to fullerene based organic solar cells. In the following section another notable approach for developing OSCs consisting of polymers is presented.

2.9.3 Polymeric NFAs

Polymer photovoltaic cells offer several exclusive benefits, including morphological flexibility, structural stability, and excellent mechanical properties. In the arena of all-polymer photovoltaic cells, various polymeric NFAs have been developed using Perylene diimide (PDI) [62-64], Naphthalene diimide (NDI), and Bithiophene imide (BTI) [68, 69]. The Table 2.9. provide an overview of the OSC device parameters based on polymeric NFAs.

In 2007, Zhan *et al*. [202] presented a polymeric acceptor made of Perylene diimide (PDI) in OSCs. Guo *et al*. [203] developed PDI-V, with improved electron transport properties. This led to efficiency of 7.57% in PTB7-Th: PDI-V organic solar cells. The NDI based polymer N2200 has proven to be an efficient acceptor. In 2013, Mori *et al*. fabricated a photovoltaic cell using PTQ1 and N2200 which exhibited an efficiency of 4.1% [204].

Table 2.9. Characteristics parameters based on polymeric NFAs

S. No.	Acceptor	Donor	J_{SC} (mA/cm^2)	V_{OC} (V)	FF (%)	PCE (%)	References
1.	P(BTI-BTI2)	PTB7-Th	15.66	1.01	54.01	8.61	[206]
2.	NDP-V	PTB7-Th	17.07	0.74	67	8.59	[207]
3.	N2200	PTzBI	15.17	0.849	70.36	9.16	[208]
4.	PZT-Y	PBDB-T	24.7	0.896	71.3	15.8	[209]
5.	PYT_M	PM6	21.78	0.95	66.33	13.44	[210]
6.	PYF-T	PM6	23.41	0.89	67.73	14.10	[211]
7.	PBN-12	CD1	13.39	1.17	64	10.07	[212]
8.	PY-IT	PM6	22.30	0.933	72.3	15.05	[213]
9.	PY2F-T	PM6	24.27	0.86	72.62	15.22	[214]
10.	PDI-DTT	biTV-PT	4.2	0.63	39	1.03	[215]
11.	N2200	J51	14.18	0.83	70.24	8.27	[216]
12.	N2200	PTzBI-Si	17.62	0.88	75.78	11.76	[217]
13.	L14	PM6	20.6	0.96	72.1	14.3	[218]
14.	PJ1-H	PBDB-T	22.6	0.90	71	14.4	[219]
15.	PDI-V	PTB7-Th	15.9	0.74	63	7.57	[220]
16.	N2200	PTQ1	8.85	0.84	55	4.10	[221]

Gao *et al*. [205] presented J51 as a donor material, by combining J51 with N2200 in the device design of ITO/PEDOT: PSS/J51: N2200/PDINO/Al, they achieved high efficiency of 8.27%. Appling annealing techniques to enhance the film morphology which resulted in enhanced

transport of carriers and decreased recombination. By utilizing PTzBI-Si material and N2200, they achieved a high efficiency of 11.76% for the all-polymer solar cell.

Shi *et al*. [222] synthesised P(BTI-BTI2), exhibiting high mobility (electron) of 1.23 cm^2/Vs in organic thin film transistors. When combined with PTB7-Th as donor material, resulting all-polymer photovoltaic cells attained a high efficiency of 8.61%. The PBN-12, based on BN-Py unit work as the acceptor. By carefully tuning its absorption spectrum, electron mobility, energy levels, and phase separation behaviour, the OSC based on CD1: PBN-12 showed a favourable efficiency 10.07%. Sun *et al*. [223] developed low band-gap acceptor called L14. The all-polymer photovoltaic cells made up of PM6 and L14 blend achieved a remarkable PCE of 14.3%.

A new polymeric acceptor called PZ1, showed a narrow band-gap of 1.55 eV, with high coefficient of absorption, leading to a high efficiency of 9.19% for polymer photovoltaic cells. Polymer acceptor PYT, having a band-gap of 1.42 eV, with high absorption. Blend of PM6 with PYT all polymer photovoltaic cell showed an outstanding efficiency of 13.44%. Jia *et al*. [224] presented a polymer PJ1-H. By using PBDB-T: PJ1-H as photoactive layer, they attained a efficiency of 14.4% in all-polymer solar cell.

The advancement in acceptor materials, transitioning from fullerene to non-fullerene acceptors, has significantly enhanced organic solar cells performance. The continuous efforts and research conducted by scientists in developing improved acceptor materials are expected to drive further enhancements in efficiency of solar cells.

2.10 ORGANIC SOLAR CELLS DONOR MATERIALS

In addition to high-performance acceptors, the selection of suitable donor materials is also vital for the progress of OSCs. Initially, conjugated Poly (Phenylene Vinylene) (PPV) and its derivatives garnered significant interest owing to their photoluminescent and conducting properties.

The Poly(thiophene)-based conjugate polymer, P3HT, gained significant prominence as a donor material in OSCs. This was because of its benefits for instance, good solubility, and high carrier mobility. OSCs utilizing P3HT as the donor material typically demonstrated PCEs ranging from 3% to 5%.

In 2006, Mvhlbacher *et al*. [225] introduced a new conjugated polymer called PCPDTBT as the donor in organic cells. PCPDTBT had energy-gap of approximately 1.46 eV and absorption range of 300 to 860 nm. When mixed with $PC_{71}BM$ as the acceptor, they achieved a PCE of 3.2%. A modify morphology of PCPDTBT: $PC_{71}BM$ blend film. OSC demonstrated an average efficiency of 5.5%. Polymer named PBDTTT-CF further enhances the open circuit voltage of the devices. PBDTTT-CF film indicated a band-gap value 1.61 eV. Organic cells based on PBDTTT-CF: $PC_{71}BM$ achieved an impressive PCE of 7.73% [226].

Liang *et al*. [227] introduced narrow band-gap polymer, PTB1, as the donor in OSC. It exhibited a band-gap value 1.63 eV, with higher mobility (hole). The PTB1: $PC_{71}BM$ organic solar cell achieved an impressive PCE of 5.30%. PTB4, and OSCs using PTB4: $PC_{61}BM$ blend achieved efficiency of 5.90%. Lu's group further optimized the structure and developed a novel polymer called PTB7 from PTB family. PTB7 based OSCs exhibited a high efficiency of up to 7.40%. Table 2.10. represents the donor materials in fullerene based organic cells.

Table 2.10. Parameters of donor materials in fullerene based OSCs and corresponding device efficiency

S. No.	Donor	Acceptor	J_{SC} (mA/cm^2)	V_{OC} (V)	FF (%)	PCE (%)	References
1.	PTB7	$PC_{71}BM$	14.50	0.74	68.97	7.40	[228]
2.	PBDTTT-CF	$PC_{71}BM$	15.2	0.76	66.9	7.73	[229]
3.	PffBT4T-2OD	$TC_{71}BM$	18.8	0.77	75	10.8	[230]
4.	PTB7-Th	$PC_{71}BM$	15.73	0.80	74.3	9.35	[231]
5.	P3HT	ICBA	10.61	0.84	72.7	6.48	[232]
6.	PffBT4T-C9C13	$PC_{71}BM$	20.2	0.788	74	11.7	[233]
7.	PTB1	$PC_{71}BM$	15.0	0.56	63.3	5.30	[234]
8.	PCPDTBT	$PC_{71}BM$	16.2	0.62	55	5.5	[235]
9.	PTB7-Th	$PC_{71}BM$	19.47	0.775	66.9	10.10	[236]
10.	PTB4	$PC_{61}BM$	13.0	0.74	61.4	5.90	[237]
11.	PTB7	$PC_{71}BM$	17.46	0.754	69.99	9.214	[238]

The inverted structure of ITO/ZnO-C60/PTB7-Th: $PC_{71}BM/MoO_3$/Ag, a remarkable efficiency of 9.35% was achieved. In 2014, Yan *et al*. [239] achieved high-efficiency thick film organic cell using new donor polymer called PffBT4T-2OD, it has a band gap of 1.65 eV and greater mobility in blend film with fullerene acceptor $TC_{71}BM$. As a result, these organic solar cells attained efficiency of 10.8%. Further, established eco-friendly and high-performance donor,

PffBT4T-C9C13. The organic solar cells based on PffBT4T-C9C13: $PC_{71}BM$ system displayed a high efficiency of 11.7%.

Typically, fullerene based OSCs, are used to expand the light harvesting range of photoactive layer. However, many of these donor materials may not be well suited for NFA based organic solar cells. The flexibility in donor material selection provides researchers with more options to optimize the OSC performance. A novel donor material PDBT-T1, exhibiting band-gap value 1.85 eV. When combined to $PC_{71}BM$ as acceptor, the resulting OSC achieved a respectable efficiency of 9.74%. When combined with $PC_{71}BM$ as acceptor, the resulting OSC achieved an efficiency of 9.74%. Later, blended PDBT-T1 with ITIC-Th as photoactive layer organic solar cells, leading to a PCE of 9.6% owing to balanced charge transport and complementary absorption properties. The Table 2.11. represents donor materials in NFA-based organic cells.

Table 2.11. Parameters of donor materials in NFA-based OSCs and corresponding device efficiency

S No.	Donor	Acceptor	J_{SC} (mA/cm^2)	V_{OC} (V)	FF (%)	PCE (%)	References
1.	PBDB-T-SF	IT-4F	20.88	0.88	71.3	13.10	[240]
2.	PM6	BTP-eC9	26.2	0.839	81.1	17.8	[241]
3.	J61	m-ITIC	18.03	0.984	65.54	11.63	[242]
4.	PM7	Y6	25.644	0.897	74.0	17.037	[243]
5.	D18-Cl	N3	27.85	0.859	75.7	18.13	[244]
6.	PDBT-T1	ITIC-Th	16.24	0.88	67.1	9.6	[245]
7.	PBDB-T-2F	IT-4F	20.81	0.84	76	13.2	[246]
8.	T1	IT-4F	21.5	0.899	78	15.1	[247]
9.	D16	Y6	26.61	0.85	73.8	16.72	[248]
10.	PM6	Y6	25.2	0.82	76.1	15.7	[249]
11.	PBDB-T	ITIC	16.81	0.899	74.2	11.21	[250]
12.	D18	N3	27.44	0.862	78.5	18.56	[251]
13.	J61	ITIC	17.43	0.89	61.48	9.53	[252]
14.	D18	Y6	27.70	0.859	76.6	18.22	[253]
15.	PBDB-T	Y1	22.44	0.87	69.1	13.42	[254]
16.	PBDB-T-2Cl	IT-4F	21.80	0.86	77	14.4	[255]

PBDB-T polymer as donor material in fullerene based OSCs, obtaining an efficiency of 6.67%. The PBDB-T: ITIC mixture exhibited broader absorption in comparison to PBDB-T: $PC_{71}BM$. This combination led to a significant improvement, resulting in an efficiency of 11.21%. OSCs based on PBDB-T: Y1 mixture films, the device achieved an PCE of 13.42%. This highlights

the adaptability and potential of certain donor materials in increasing efficiency of NFA-based OSCs.

PBDB-T, which led to apt energy level alignments and improved absorption, device made of PBDB-T-SF: IT-4F achieved an efficiency value 13.10%. Subsequently, two coupled materials, PBDB-T-2F and PBDB-T-2Cl, were made. OSCs based on PM7 with Y6 as acceptor achieved a finest efficiency of 17.037. OSCs made of T1: IT-4F blend films achieved an efficiency of 15%. In 2012, Li *et al*. developed J51, OSCs consisting of J51: $PC_{71}BM$ as photoactive layer showed a comparatively lower efficiency of 6% [256]. The blend film of J51: ITIC leds to an efficiency of 9.26%. Similarly, the OSC made of J61:ITIC resulted in a efficiency value 9.53%.

2.11 LIFETIME OF ORGANIC SOLAR CELL

Organic photovoltaic devices have gained central attention for their commercial and industrial applications, thanks to their flexibility, inexpensive manufacturing costs and semi-transparent nature. However, active lifetime of these OSCs remains a main apprehension. Numerous papers reported degradation of the most stable OPV devices within few years. This created an impression that OPVs have brief functional lifetime making them less attractive commercially in contrast to traditional cells, despite rapid and positive reception of OLEDs with a lifetime of million hours [257].

Table 2.12. Lifetime of organic solar cells based on different layer materials

S. No.	Front Electrode	Transport Layer 1	Active Layer	Transport Layer 2	Back Electrode	PCE (%)	Lifetime (days)	References
1.	ITO	TiO_x	P3HT: PCBM	MoO_x	Ag	3.7	198	[260]
2.	ITO	ZnO_x	P3HT: PCBM	PEDOT: PSS	Ag+Al	3.5	187	[261]
3.	ITO	ZnO_x	P3HT: PCBM	-	Ag	2.5	146	[262]
4.	Ag	PEDOT: PSS + ZnO_x	P3HT: PCBM	PEDOT: PSS	Ag	0.93	120	[163]
5.	ITO	-	P3HT: PCBM	Cs_2CO_3	Al	3.6	100	[264]
6.	ITO	ZnO_x	P3HT: PCBM	PEDOT: PSS	Multilayer electrode	1.9	96	[265]

However, Burlingame *et. al.* [258] dispelled this impression by constructing an OPV with a T_{80} of 4.9×10^7 hours, which is equivalent to 27,000 years of outdoor use. T_{80} refers to the time needed by the efficiency to attain 80% of its original performance. Xu *et. al.* [259] presented

an OSC with a T_{80} of 34,000 hours, equivalent to a lifetime of 22 years. The Table 2.12. represents OSC lifetime.

Du *et al.* [256] examined a cell with T_{80} of 11,000 hours, corresponding to a lifetime of 10 years. Krens *et. al.* [257] conducted a systematic study on PPV: PCBM bulk heterojunction lifetime. Schuller *et. al.* [268] measured PPV: PCBM bulk heterojunction lifetime. Additionally, Du *et. al.* [256] examined the T_{80} lifespan of PCBM to be 7400 hours. Furthermore, Burlingame *et. al.* [269] reported organic cells have capability for higher functional lifespans if clean materials, apt manufacturing processes, and right device structure are utilized.

2.12 APPLICATIONS OF ORGANIC SOLAR CELLS

OSCs offer distinct benefits in comparison to in-organic solar cells, especially in terms of aesthetics, flexibility, and absorption tunabilitly. OSCs show remarkable possibilities in applications such as wearable electronics, where their flexibility and lightweight properties are advantages. Additionally, they can be integrated into semi-transparent devices, allowing for energy harvesting while maintaining partial transparency in certain applications. Furthermore, OSCs have shown promise for indoor solar cells, providing a viable alternative for powering electronic devices indoors efficiently. These features demonstrate the versatility and potential of OSCs in various promising applications.

2.12.1 Semi-transparent OSCs

Semi-transparent photovoltaic cells have gained increased consideration owing to their potential applications in facilitating integrated photovoltaics, modern greenhouses, and energy saving windows. Compared to in-organic semiconductor materials, organic semiconductors offer greater tunability of the bandgap, enabling visible light transmission and infrared light absorption. Additionally, organic materials have excellent absorption coefficient allowing adequate light absorption even with a thickness of 100 nm.

Ravishanker *et al*. [270], achieved a net zero energy greenhouse by integrating semi-transparent OSCs. This led to effective replacement of shade cloths minimizing sunlight attenuation. Similarly, Wang *et al*. presented an eco-friendly semi-transparent organic solar cell for greenhouse application with an excellent PCE of 17.71% [271]. A PTB7-Th: IEICO-4F semi-transparent organic sola cell with 11% efficiency. The fabricated semi-transparent OSC has

wide potential as power producing windows for buildings and vehicles. Sun *et al*. developed heat insulating multi-functional semi-transparent polymer photovoltaic cell with 6% PCE and infrared rejection rate of 80% [272]. The results achieved by them showed that the semi-transparent OSCs can be used for heat insulation, opening a new area of OSC application which is energy saving.

This selective absorption nature OSC can be used for detection of anaemia. Presently, the invasive methods used for determining haemoglobin involve collecting a blood sample from the patient and then analysing it. This method causes patient discomfort while collecting the blood sample and, in this method, there is a significant delay between the sample collection and sample analysis, preventing a real time or continues monitoring of the patient. In comparison to the present method of measuring haemoglobin a non-invasive method presented in this chapter offers a pain free, immediate, and reliable measurement of haemoglobin without the risk of infection. Additionally, a low-cost and portable but invasive method of haemoglobin detection known as Haemoglobin colour scale method is also used for determining the haemoglobin levels, where the patient's blood is matched with a scale. However, this method suffers from high variability and inaccuracy.

The scattering of light is commonly utilized in soft, condensed, and biological material applications. In the field of biomedical applications, scattering of light offers promising opportunities for non-invasive monitoring and imaging of various medical conditions [273]. Blood, is an important and attractive fluid of biological nature, which could be used for applications that involve the scattering of sunlight. The Red Blood Cells (RBCs) remain the main constituent of the human blood and is almost 45% of the blood by volume. These RBCs contain an extremely dense solution of haemoglobin. This haemoglobin is the primary component responsible for the absorption and scattering visible light [274]. The different techniques of light scattering have already been utilized for the measurement of different RBC properties [275-277]. For instance, the light scattering has been utilised for the measurement of changes in the shape of the RBCs in case of sickle cell anaemia [278], malaria detection [275], monitoring fluctuations in the RBCs membrane [275,276] and for studying the dynamics and metabolic characteristic of the RBCs [279,280].

2.12.2 Indoor Organic Solar Cells

The rapid growth of energy efficient electronic devices propelled by the internet of things (IOT) has created possibilities for advancement of indoor organic photovoltaic cells. These devices have experienced a gradual decrease in power consumption and cost, making indoor solar cells more viable. Unlike outdoor solar cells that face challenges such as intermittent solar radiation and environmental variability, indoor photovoltaic cells offer benefits such as insensitivity to active layer thickness and series resistance, as well as functioning under milder conditions.

Indoor photovoltaic cells are expected to have a growing market size due to their compatibility with indoor light sources and low manufacturing costs. Silicon cells do not align with the spectrum range of most indoor illumination sources, and solar cells using III-V semiconductor involve high manufacturing costs. In contrast, OSC show great potential for indoor applications due to their solution processing and cost-effectiveness. Yang *et al*. presented a OSC using three different polymer/fullerene blend under indoor lighting conditions with a best PCE of 13.76% [281]. In 2015, Mori *et al*. [282] conducted a study to investigate the performance of polymer based OPV using PTB7-Th (donor) and $PC_{71}BM$ (acceptor), under indoor LED lighting conditions. They compared the findings with those of conventional silicon solar cell (c-Si-SCs). Under outdoor illumination conditions, the efficiency of c-Si-SC and OPV were found to be 13.49% and 8.43%, respectively. However, when subjected to LED illuminations the OPV exhibited a higher efficiency of 11.63% in comparison to the c-Si-Sc. Also, in 2016, Cutting *et al*. [283] documented that OPVs can surpass silicon cells under LED lighting conditions.

2.12.3 Flexible OSCs

In comparison to in-organic photovoltaic cells, one of the major advantages of OPVs is their remarkable mechanical properties, which makes them appropriate for integration into portable and wearable devices with self-powering capabilities. The inherent flexibility of organic materials has led to increased efforts in the development of flexible OSCs, especially focusing on self-powered integrated electronics utilizing flexible OSCs in bio-medical devices. Table 2.13. represents the important OSCs in bio-medical devices.

Biomedical electronic devices are essential in modern medical services, each designed to fulfil specific functions. The recent advancement in technology have facilitated in advancement of OSCs with exclusive characteristics like lightweight, flexibility, biocompatibility, and reduced size, making them appealing for bio-medical electronic device applications. This section

focuses on recent research that explores the usage of photovoltaic cells to power various types of biomedical devices.

Table 2.13. Important organic semiconductors for bio-medical devices

S. No.	Device	Active layer	V_{OC} (V)	J_{SC} (mA/cm^2)	FF (%)	PCE (%)	Functionality	References
1.	OSC/OBEI	P3HT: PCBM	0.59	9.66	0.64	3.68	Cell growth; Cell differentiation	[284]
2.	OSC/PTME	PTB7-Th: PCBM	-	-	-	-	Pressure sensor; Motion monitoring	[285]
3.	OSC/OECT	PTB7-Th: PCBM	0.785	19.17	69.7	10.49	Sensor; Cardiac signal recording	[286]

Bio-medical devices powered by solar cell continue to be area of significant research interest. Lu *et al*. [287] presented a study on transient solar cells that demonstrated full biocompatibility and biodegradability within a live rat's body over a period of 4 month. In 2009, Natcore Technology obtained a patent for their solar powered artificial retina prothesis. This implant was designed as a flat, circular disc measuring approximately 4 mm in diameter. The main purpose of implant is to transform incoming light into an electrical signal, which is then used to simulate retinal neurons, aiding in vision restoration [288].

The Italian Institute of Technology has successfully created a solar-powered artificial retina prosthesis which is entirely organic and could be implemented into the eye. This artificial retina functions as a replacement for a damaged retina [289]. The photovoltaic cell utilized in this prothesis is a multilayer structure, comprising P3HT as the active material, an intermediate conductive layer of PEDOT: PSS. Park *et al*. [290] integrated a highly efficient BHJ solar cell composed of PBDTTT-OFT organic polymer and PCBM to a flexible biosensor. This innovation has led to the creation of a self-powered heartbeat monitor that operates autonomously.

Zhang *et al*. [291] presented a device comprising of a biocompatible OSC and organic bioelectronic interface electrode, capable of generating electrical stimulations for PC12 cell. Soumeya *et al*. [292] demonstrated high efficiency flexible OSC [44]. A self-powered pressure sensor made up of flexible OSC with PTB7-Th:$PC_{71}BM$ as active layer to sense human finger motions was successfully fabricated. The Table 2.14. represents organic materials with confirmed biocompatibility.

Table 2.14. Biocompatible organic semiconductors with environment and location of implant

S. No.	Material	Environment	Implant location	References
1.	P3HT, (poly(3-hexylthiophene-2,5-diyl))	In vitro, Ex vivo	Hippocampal and retinal neuron from rat and chick embryos respectively.	[293]
2.	PPy, (Polypyrole)	Ex vivo, In vitro, In vivo	PC12 cells, chicken sciatic nerve explants, adult male Lewis rat	[294]
3.	T4, (Quaterthiophene)	In vitro	Primary dorsal root ganglion (DRG) neurons	[295]
4.	Pentacene	In vitro	Neurons from forebrain of mouse embryos	[296]
5.	PEDOT, (poly(3,4-ethylenedioxythiophene))	In vitro	Primary cortical cells, embryonic mice	[297]
6.	PPV, (poly(p-phenylenevinylene)) derivatives	In vitro	AsPC-1, HMEC-1, BV-2 cells	[298]
7.	Nafion	In vivo, In vitro	Hep-2 cells. Male ICR mice	[299]
8.	Graphene	In vitro	Brain tissue from postnatal mice	[300]
9.	BECP, (Pyrrole-thiophene based polymer)	In vivo, In vitro	Human neuroblastoma cells, subcutaneous implantation into rats	[301]
10.	PANI, (Poly(aniline))	In vivo	Subcutaneous implantation into male rats below dorsal skin	[302]
11.	PEDOT: PSS, (poly(3,4-ethylenedioxythiophene) doped with poly (styrenesulfonate))	In vivo	Male long Evans rats	[303]
12.	PAP, (PLA-b-AP-b-PLA copolymer)	In vitro	H9c2 cells	[304]
13.	PE, (Polyethlene)	In vivo	Subcutaneous implantation into male rats below dorsal skin	[305]
14.	PCBM, (phenyl-C61-butyric-acid-methyl ester)	Ex vivo	Hippocampal neuron from rat embryo.	[306]
15.	Carbon nanotubes	In vitro	Hippocampal cells from Sprague Dawley rats	[307]

Therefore, after conducting a comprehensive review of various inorganic and organic solar cells their types and their applications specifically biomedical applications, specific technical gaps have been identified. These gaps serve as the foundation for the research work proposed in this thesis.

2.13 TECHNICAL GAPS

- The first- and second-generation solar cells were completely dependent on the fabrication material properties for their functioning. While, the concept of doping a material to design solar cells was introduced in third generation cells. Most reported third generation cells used various combinations of dopants from different groups. But, based on the properties of group II-VI material, improved solar cells can be realized as, it creates an intermediate energy band that would help to improve the performance for the cell. Additionally, amorphous materials are highly required for the absorber layer of thin film solar cells.

- Various designs for bilayer organic solar cells have been reported in literature. Most of the reported designs have limited their scope to efficiency analysis and less attention is given to the internal device physics for the structure. But it is the internal device physics for the structure that determines its performance. Therefore, it is crucial to evaluate, analyse and understand the same so as to determine if any additional layers can be added to the structure for performance enhancement.

- The scope of application of solar cells have been expanded to medical domain, as they are a suitable alternative for detection of diseases. The advantage of solar cells is that they provide a non-invasive mechanism for disease detection. A major health issue amongst women is anaemia. The present methods of its detection are invasive and time consuming. Also, patients have to go to designated health centres and a trained professional is needed to carry out the tests. Thus, generating the need for designing a non-invasive solar cell-based anaemia detection method. Similarly, at present pacemakers are dependent on batteries, requiring to be replaced (~6 years) with complex surgery. Thus, realization of sub-dermally implantable BHJ organic solar cell capable of supplying power to pacemakers with higher lifetime (~25 years) will eliminate requirement of replacing batteries in pacemakers.

CHAPTER-3

SYNTHESIS AND CHARACTERISATION OF AMORPHOUS ABSORBER MATERIAL THIN FILMS FOR SOLAR CELL

The solar cells present a capable technology that has the potential to revolutionize present methods and approaches to electricity generation. The thin films solar cells, in particular, are generally lighter and elastic in comparison to traditional silicon solar cell making films apt for various applications. Additionally, they require less material for fabrication, leading to reduced manufacturing costs. Intermediate band solar cells exhibit distinct and remarkable characteristics and properties that make them apt for solar energy harvesting. By blending different elements in specific ratios, they demonstrate an extensive range of band-gap energies, enabling efficient absorption of incoming irradiance efficiently across a wider spectrum. The combination of cost saving and high-power conversion efficiency make Intermediate band solar cells irresistible contenders for solar energy harvesting technologies. Therefore, to synthesise and to attain a comprehensive understanding of the internal device analysis of Intermediate band solar cells the following objective is formed:

"Synthesis and characterisation of absorber layer material and analysis of amorphous absorber material based thin film solar cell."

The methodology used to achieve desired objective involved following steps: -

- Synthesise Sn (Tin)/Sb (Antimony) doped ZnTe (Zinc Telluride) material for the absorber layer of the solar cell.
- Prepare thin films of Sn/SbZnTe material and analyse their crystal structure.
- Analyse the electrical characteristics and internal device physics of the ZnTe solar cell.
- Analyse the electrical characteristics and internal device physics of the Sn/Sb doped ZnTe solar cell.
- Comparative analysis of ZnTe, SbZnTe and SnZnTe solar cell to determine the best (most suitable) absorber layer material for the solar cell.

This chapter is divided into six sections, including the introduction in the first section. The second section provides information on the experimental setup and procedure for Sb/Sn doped ZnTe thin films preparation. Following that, in the third section, the solar cell structure and the

materials used in different layers are presented. The performance analysis of the ZnTe based solar cell is discussed in section four. In section five, the electrical characteristics and parameters of Sn and Sb doped ZnTe solar cells, along with the internal analysis using horizontal cutline, are illustrated. Finally, the important outcomes are summarized in section six.

3.1 INTRODUCTION

Semiconductor based Solar cells are highly efficient and low-cost devices for harnessing solar energy, which is an eco-friendly and renewable source of energy. The main function of solar cell is to convert light into electricity, by utilizing photons or photo-electrons. The energy of a photon is indeed its inherent property and is not dependent on any additional energy source. Photons with higher frequencies have higher energy, while those with longer wavelengths have lower energy [308]. To design the solar cell, numerical models have turned out to be the tools of great importance in understanding the cell operation and optimize their performance for high-end future applications [309,310]. Solar cells based on the elements of II–VI groups are frontrunners in realization of low-cost photovoltaic cells [311].

First-generation cells were built using a single crystal structure and implemented using wafers. Second generation cells are characterised by thin film deposition of semiconductor material on a glass or metal substrate. In these semiconductors based solar cells, the photons with energy lower and higher than the energy band gap of absorber layer material are not absorbed, and are lost, resulting in wastage of energy. Further, the intermediate band solar cell represents the third generation of solar cells. These types of cells have additional states within the host atom's band gap, which lowers the required energy to move an electron from valance to conduction band due to the presence intermediate band. The creation of intermediate band requires alloys of mismatched elements and the host [312, 313].

Undoped Zinc Telluride (ZnTe) material naturally exhibits p-type conductivity. Generally, ZnTe is doped with group I, V, and rear earth elements. The addition of Sn (Tin) and Sb (Antimony) as dopants enhances the characteristics of ZnTe and improves its properties for solar cell applications. The doping of Zinc Telluride with Sb substitutes the Zn (Zinc) atoms. On the other hand, doping with Sn sets a donor source, which leads to the generation of states within the band gap, resulting in band gap energy reduction [314].

The doping of Sb/Sn in ZnTe results in a highly mismatched alloy. This has an advantage of achieving low band gap energy in visible spectrum, making Sn doped ZnTe alloy a suitable choice for optoelectronic applications [315, 316]. However, Zinc Telluride (ZnTe) material is not an ideal choice as an absorber material in solar cells, as its efficiency is less due to its large bandgap of 2.25 eV. As per the Shockley-Queisser limit, which defines maximum power conversion efficiency of a solar cell, the theoretical efficiency peaks at around 1.4–1.5 eV bandgap.

The purpose of comparing the performance of solar cell with undoped and Sb/Sn doped ZnTe material is to assess the impact of doping on properties of ZnTe material. In previous studies, researchers such as Bayad *et al.* [317], Olusola *et al.* [318], Tanaka *et al.* [319, 320] and Sharma *et al.* [321] have explored homojunction and heterojunction solar cells, using ZnTe as the absorber material. Based on the findings from these earlier reports, the present analysis focuses on undoped and Sb/Sn doped ZnTe thin films to evaluate their suitability as an absorber material in PV cells. Here, Sn doped ZnTe material is observed to be a favourable choice for the absorber layer owing to its smaller band gap compared to undoped and Sb doped ZnTe.

In this chapter, the synthesis and characterization of Sn/Sb doped Zinc Telluride thin film is carried out. These films are prepared using a vapour deposition process, and the obtained parameters are utilized for analysing solar cell using the Silvaco-ATLAS numerical device simulator [322]. Further, these cells are compared on different absorber layer thicknesses by means of various performance parameters. These parameters include open circuit voltage (V_{OC}), short circuit current density (J_{SC}) and Fill Factor (FF). These three solar cells are further analyzed in-depth using horizontal and vertical cut-lines, enabling examination of hole/electron current density, charge carrier concentration, recombination rate, potential distribution, and band energy. These internal analyses are very helpful in providing valuable insight into the behaviour of PV device and are essential to comprehend device behaviour in more practical and comprehensive manner.

3.2 EXPERIMENTAL SETUP FOR THIN FILM PREPARATION

The Sn/Sb doped ZnTe alloys are prepared through melt quenching, which is a low-cost technique. The elements are accurately weighted on an electronic balance (LIBROR, AEG-120) with a precise least count of 10^{-4} gm. A quartz ampoule (L = 5 cm, Dia =8 mm) is first cleaned with acetone and evacuated at a pressure of 10^{-5} Torr (approx.) to make it

contamination free before sealing the materials inside the ampoule. Further, the quartz ampoule is placed in the furnace and heated to 800º C for a duration of 12 hours. The growth rate of temperature is observed as 3–4º C per minute. The ampoule needs to be rocked repeatedly throughout the heating process, to ensure a homogeneous alloy. The process of rocking in the furnace (performed to get a uniform reaction) is immediately followed by quenching of the ampoule containing the melt in cold water. This process of melt quenching helps in achieving a well-mixed and homogeneous Sn/Sb doped ZnTe alloy.

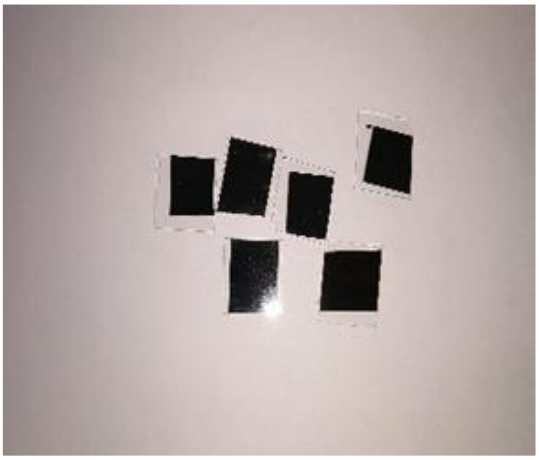

Fig. 3.1. Sb (Antimony) and Sn (Tin) doped ZnTe thin films.

The quenching process is performed to prevent the undesired low temperature developments, such as phase transformations. It can also reduce the crystal grain size and increase the hardness of materials. After quenching, the ampoule is broken and the sample is finely grinded. The vacuum-evaporation-technique is used to prepare the thin films of SbZnTe and SnZnTe materials, wherein, respective alloys are placed in a molybdenum boat and heated till the evaporation is achieved. During the evaporation process, first the rotary pump is tuned with the pirani gauge (measure thermal conductivity of the gas sample), this is further followed by backing at 120-130 milli bar pressure. Afterwards, the differential pump is turned on and pressure is maintained at 10^{-5} Torr (approx.). Subsequently, the cooling process takes place to reduce the temperature of heater.

The entire process is carried out without the working chamber. Afterwards, the working chamber is placed, and roughing is performed (after 5 min) followed by backing process at 10^{-5} Torr pressure. Finally, the high vacuum valve is opened to create the vacuum level for evaporation process. The films of SbZnTe and SnZnTe, as demonstrated in Fig. 3.1, are prepared on glass substrate, which is kept at a pressure of 10^{-6} Torr at room temperature. The

deposition rate depends upon the vapor pressure of the individual elements present in the material and here Zn has very high vapor pressure, which would lead to a significant change in the deposition over time. However, deposition of ZnTe thin films have been successfully carried out by many researchers using thermal evaporation technique [323]. During thin film deposition by vacuum thermal evaporation, following factors were taken care off, which may impact nature and charecteristics of the evaporated films.

To ensure a straight-line path for the evaporated molecule, pressure in the order of 10^{-5} torr and the distance between source and substrate was maintained at 12 cm. The film quality depends on the temperature, structure, and cleaning of substrate [324]. Since, thin film readily adheres to a clean insulating surface. Here, cleaning of the substrate involves three steps, first step is to remove any dust impurities, visible grease, and oil; soap solution cleaning was done by scrubbing the substrate in the soap solution, then rinsed carefully with triple distilled ionized water. This procedure was repeated four to five times for cleaning single substrate. The second step is to get rid of organic impurities from substrate surface, vapour cleaning procedure was done by acetone. The third step is the removal of inorganic impurities, methanol was used.

If the evaporated material is impure then there will always be a possibility of contaminations in the deposited thin film. In this experiment, precise amounts of high purity elemental substance of Zn, Te, Sb and Sn were taken to prepare glassy alloy [325–327]. To increase mean free path, high vacuum is essential during thin film deposition. Also, to reduce surface as well as bulk impurities and to defend vapour source from oxidation and corrosion, high vacuum is needed. In this work up to 10^{-6} torr pressure was achieved using a diffusion pump.

The deposition rate for thin films was preserved at ~ 12 Å/s with ±2 Å/s variation. Thin film thickness of all samples is 450 nm evaluated by crystal monitor, situated at the same height as of substrate under vacuum-chamber. The deposited thin films were kept in vacuum- chamber for 12 hours. Further, to find the parameters of lattice and the structure of crystal, the XRD (X-ray diffraction) examination is applied. XRD patterns of films are obtained with X-ray diffractometer with scanning angles ranged from 10° to 80°. The diffraction pattern is a product of the unique crystal structure of a material. The interatomic distance determines the positions of the diffraction peaks, and the atom types with atom positions determine peak intensities.

Further, XRD analysis can be used to determine the crystal structure, residual strain, and phase composition of a sample. These patterns depict the structural changes in ZnTe material on applying doping. The X-ray diffraction patterns of prepared chalcogenide Sb/Sn doped ZnTe

thin films at room temperature are shown in Figs. 3.2 (a) and (b) for SbZnTe and SnZnTe thin films, respectively. These XRD patterns show no sharp peaks and the absence of peaks illustrates the amorphous nature of SbZnTe and SnZnTe samples. These results are in good agreement with earlier reported work [315, 328, 329].

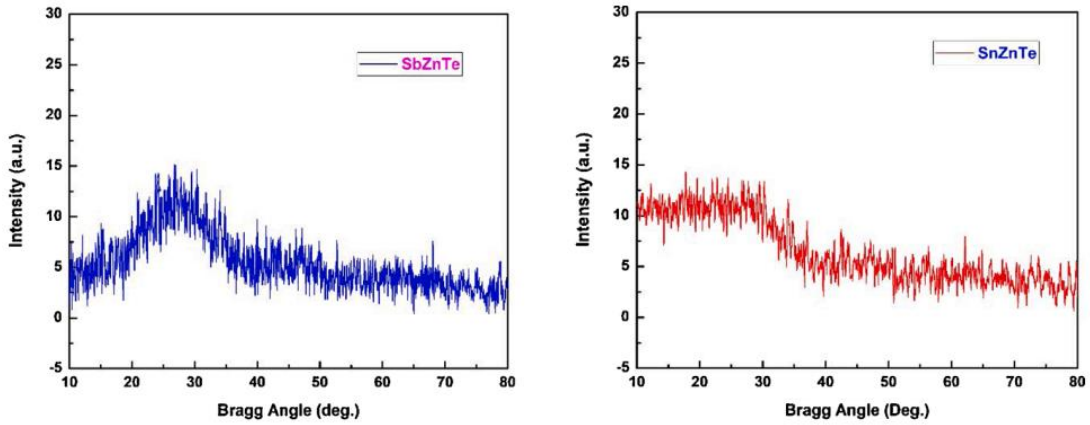

(a) (b)

Fig. 3.2. XRD patterns of (a) SbZnTe and (b) SnZnTe thin films.

In general, amorphous material contain background noise, and there are no sharp peaks. In our research work also, noise does not confirm the crystalline nature of material. The two stepped humps are seen at different angular positions which are because of amorphous glass substrates used for study. Cost-effective deposition techniques enable the fabrication of amorphous materials in thin film structure. Therefore, the layered architecture of Sb and Sn doped ZnTe based solar cells are designed and analyzed in the subsequent sections.

3.3 ELECTRICAL CHARACTERISTIC OF ZnTe SOLAR CELL

Analytical models-based simulators have been proven crucial to envisage and optimize the device performance before their actual realization. In present section, focus is on understanding performance of a PV cell by utilizing undoped and Sb/Sn doped ZnTe materials as absorber layer materials. To gain an understanding of internal operation of the devices, the proposed PV cells are analysed using benchmarked industry standard Silvaco Atlas 2-D numerical device simulator [322]. This simulator allows user defined materials and structures with a variety of model parameters including Shockley-Read Hall and Poole-Frenkel mobility models. Further, meshing is incorporated to model the calculations, wherein, a high meshing density leads to an improved accuracy and precision in the simulation results.

The accuracy of electrical characteristics of solar cell in Silvaco Atlas is achieved through a combination of different optical propagation models, which are very robust in nature. The Silvaco-Atlas has built-in public domain AM0 and AM1.5 solar spectra that can be directly accessed by specifying the BEAM statement. Additionally, ray tracing propagation model is also used. It automatically traces the precise number of rays to entirely resolve any discontinuity at the surface and throughout the device structure. Further, there are multiple models in Silvaco Atlas to simulate the generation-recombination mechanism to achieve equilibrium state, which is an important aspect of semiconductor behaviour. In semiconductors, the equilibrium state can be expressed as:

$$n_0 p_0 = n_i^2 \tag{3.1}$$

where, n_0 and p_0 correspond to electron and hole concentration at equilibrium state and n_i is the intrinsic carrier concentration. When light falls on the surface of solar cell, the electron-hole pairs are generated that results in a significant augmentation in the minority carrier concentration. This generation of electron-hole pair is followed by the recombination process leading to restoration of equilibrium. The R_{SRH} is the Shockley-Read-Hall recombination rate of the electrons (holes) per unit of volume. This can be obtained using Shockley-Read-Hall recombination model as:

$$R_{SRH} = \frac{pn - n_{ie}^2}{TAUP0\left[n + n_{ie}\exp\left(\frac{ETRAP}{kT_L}\right)\right] + TAUN0\left[p + n_{ie}\exp\left(\frac{-ETRAP}{kT_L}\right)\right]} \tag{3.2}$$

where, *ETRAP* denotes the energy difference between trap and intrinsic fermi level. T_L symbolizes for lattice temperature in degrees Kelvin. Further, *TAUP0* and *TAUN0* are hole and electron lifetimes, respectively, while n_{ie} represents effective intrinsic carrier concentration. This model can be activated by specifying SRH parameter in the MODELS statement. The device structure of solar cell is presented in Fig. 3.3 (a).

Here, CdS material is used as the buffer layer. For window layer, ZnO material is used, which is forming a heterojunction with CdS buffer layer. These materials' combination demonstrates a high lateral conductivity with generation of textures for enhanced light trapping. Numerous advantages including: high efficiency, point defect passivation and good hetero partner are associated with CdS material when used as the buffer layer [330, 331]. The ZnO layers are

often used as window layers in solar cell structures due to their low cost and extensive availability [332]. A combination of ZnO with band gap of 3.3 eV, CdS with band-gap of 2.4 eV and absorber material with band gap of 1.5 eV approx. shows a good band alignment.

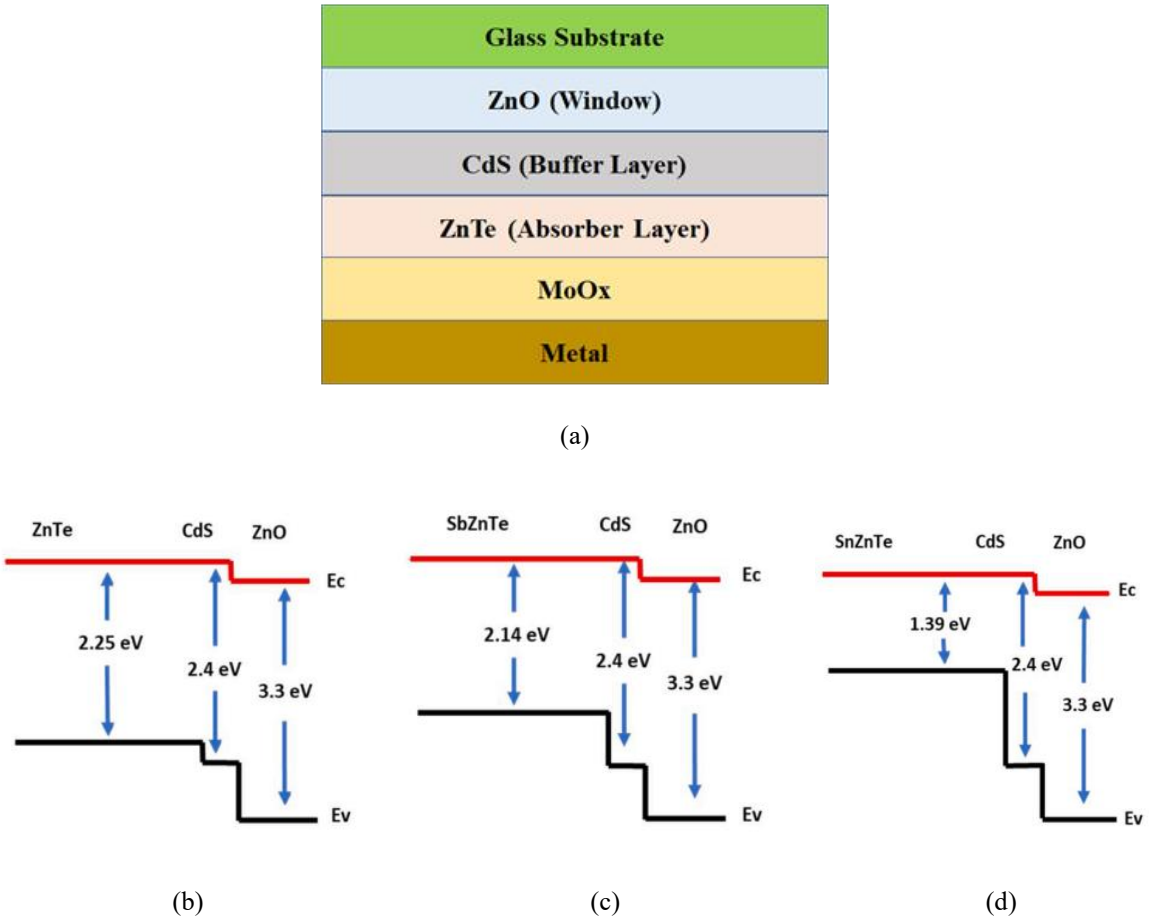

Fig. 3.3. (a) Device structure of multi-layered solar cell and energy band illustration for (b) ZnTe, (c) SbZnTe and (d) SnZnTe solar cells.

The band alignment is one of the most imperative parameters that impacts the photogenerated carriers-transport and functionality of the solar cells. Energy band diagrams are illustrated in Figs. 3.3 (b) to (d), respectively for ZnTe, SbZnTe and SnZnTe absorber material based solar cells [330]. The window and buffer layers are kept same for all three cells. The band gap for the ZnTe and CdS materials are of 2·25 and 2·4 eV respectively. Therefore, band bending of 0·15 eV occurs at the junction of these materials. Similarly, this band bending is of 0·26 eV at SbZnTe/CdS interface and 1·01 eV at SnZnTe/CdS interface. Further, a band bending of 0·9 eV occurs at the interface of CdS and ZnO layers in all three cells due to the band gap of 3·3 eV for ZnO material [333, 334].

Table 3.1 summarizes thicknesses of various layers in solar cell along with other materials' parameters [315, 330, 331, 335–337]. Here, the conduction band effective density of states (N_C) is of 2.2×10^{18} cm^{-3}; however, the valance band effective density of states (N_V) is considered as 1.8×10^{19} cm^{-3} [331, 332]. ZnTe material has electron affinity of 3.73 eV and zinc-blend crystal structure [338]. Default values for $TAUNP_0/TAUNN_0$ are kept at 1×10^{-7}s using MATERIAL statement for the simulation purpose [322].

Table 3.1. Device Dimensions and Materials' Parameters of ZnTe absorbing layer based solar cell

Parameter (units)	ZnTe	CdS	ZnO
Thickness (μm)	1.5	0.060	0.050
Bandgap (eV)	2.19	2.4	3.30
Dielectric permittivity (ε_r)	10	10	9
Acceptor/Donor Density; N_A/N_D (cm^{-3})	N_A, 10^8	N_D, 10^{15}	N_D, 10^{15}
Electron mobility (cm^2/V. s)	340	350	100
Hole mobility (cm^2/V. s)	100	40	25
Electron affinity (eV)	3.53	4.5	4.6

The device structure of ZnTe based PV cell is illustrated in Fig. 3.4 (a). Here, individual regions comprising of different materials are formed in a mesh that consists of a complex grid of triangles for entailing the calculations. Hence, reasonably high accuracy can be attained with dense meshing grids, as shown in Fig. 3.4 (b). Subsequently, the mathematical model employs a finite-element-based algorithm. This algorithm utilizes the defined meshing points to perform calculations and solve the equations governing the behaviour of the solar cells. The convergence of the algorithm is achieved by iteratively refining the solution until a high degree of accuracy is obtained.

In Fig. 3.5 (a), the current density as a function of voltage is depicted for the ZnO/CdS/ZnTe solar cell. Further, electrical characteristics and performance parameters of solar cell are analysed with aforementioned materials, dimensions, and model parameters. The maximum magnitude of this current density is observed to be 7.9 mA/cm^2 at 0 V. This current density remains relatively constant till 1.6 V and then decreases exponentially as voltage increases. The plot follows the typical current-voltage characteristics of a PV device. The photoactive

layer refers to the layer responsible for photon absorption and charge carrier generation, which are essential for solar cell operation.

The photovoltaic process starts as soon as the solar cell is illuminated with solar radiation, specifically the Air Mass 1.5 spectrum. The Air Mass 1.5 is the spectrum used for the performance calculations of solar cells in optical modelling and is representative of the actual outdoor spectral distributions. Under illumination, incident photons on surface of PV cell leads to generation of the charge carriers and flow of current in device. Further, the characteristic curve of open-circuit voltage (V_{OC}) as a function of absorber thickness is shown in Fig. 3.5 (b).

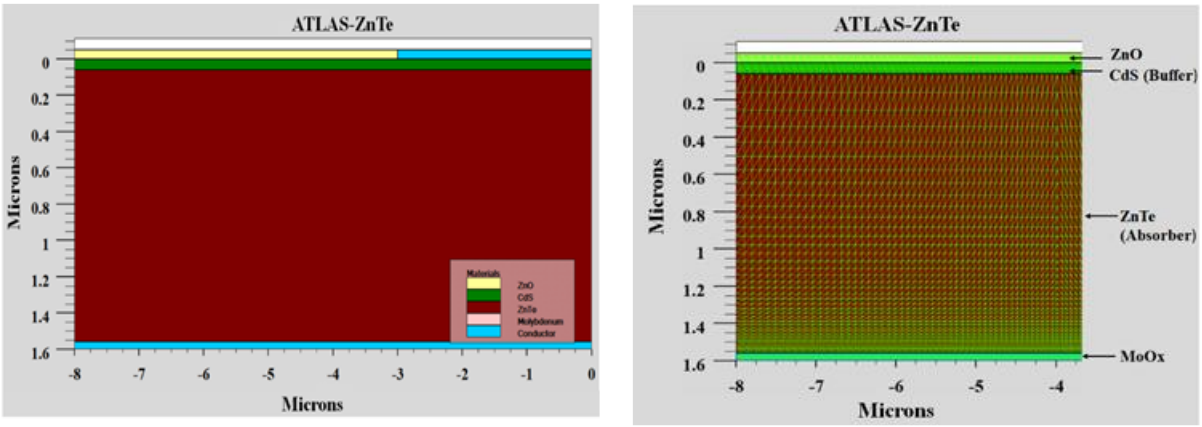

(a) (b)

Fig. 3.4. (a) Device structure and (b) Enlarged view of meshing in ZnTe Solar Cell.

In the open circuit voltage characteristic curve exhibits a linear increase as the absorber thickness is increased from 0.5 to 2.5 µm. Its maximum value is achieved as 1.87 V when the absorber thickness is 2.5 µm. This voltage is higher by 5.6% than the voltage achieved at 0.5 µm thickness. The charge carrier concentration is maximum near the buffer-absorber layer interface and thereby only slight increment is observed in V_{OC} on increasing thickness. The V_{OC} depends on lifetime of minority carriers on both sides of the junction. The linear rise in open circuit voltage with increase in absorber thickness is a result of the increasing recombination sites, particularly in the vicinity of interface. Further, J_{SC} as a function of ZnTe thickness is plotted in Fig. 3.5 (c), wherein, short circuit current density depicts a linear increment with an increase in absorber thickness. The J_{SC} of 8.3 mA/cm^2 is attained at 2.5 µm, which is higher by 15% than the current density at 0.5 µm.

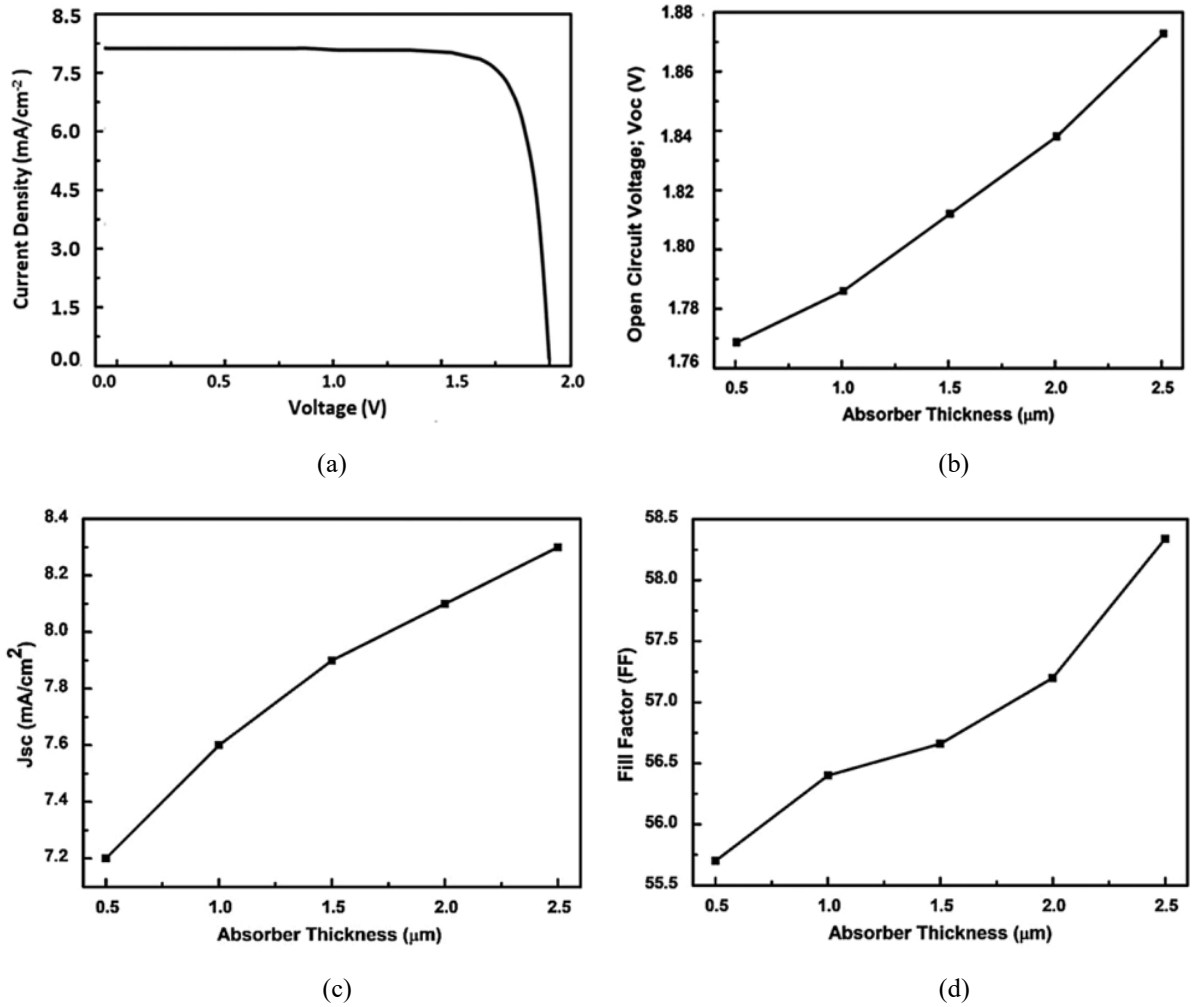

Fig. 3.5. Characteristic plots of (a) Current density vs Voltage at ZnTe layer of 1.5 μm, (b) *Voc*, (c) J_{SC} and (d) Fill Factor (in %) as a function of absorber thickness for ZnTe cell.

Fig. 3.5 (d) represents the curve between Fill Factor and absorber thickness. The Fill Factor is a parameter that indicates the quality of PV cell and represents ratio of actual power provided by PV cell under standard operating conditions to product of V_{OC} and J_{SC}. A higher FF value closer to unity (1) indicates a higher output power capability of PV cell.

The FF values are ranging from 0.55 to 0.58, as the absorber thickness scales from 0.5 to 2.5 μm, which are in agreement with the normal trend [319, 320]. Further, the solar cell is analysed internally through a horizontal cut-line within the absorber layer, specifically closer to the absorber and buffer layer junction. This exploration and understanding of the solar cell are beneficial to analyse the device physics and device behaviour in depth. The internal analysis also confirms the performance dependence of PV cell on individual layers.

Internal potential variation in each layer is shown in Fig. 3.6 (a). It is observed that the potential is primarily developed between the absorber and buffer layer, at their junction and drops as the distance increases from the junction. Further, Fig. 3.6 (b) illustrates the variation of potential with respect to *x*-coordinate, which represent the absorber layer length. The curve shows a distinct peak approximately at 5 μm, where the potential attains a value of 0.22 V and shows a rapid rise from 0.07 V. After the peak, the potential is observed to be constant, which concludes that the majority of charge carriers remain concentrated in the proximity of the electrode, located at the top of buffer layer.

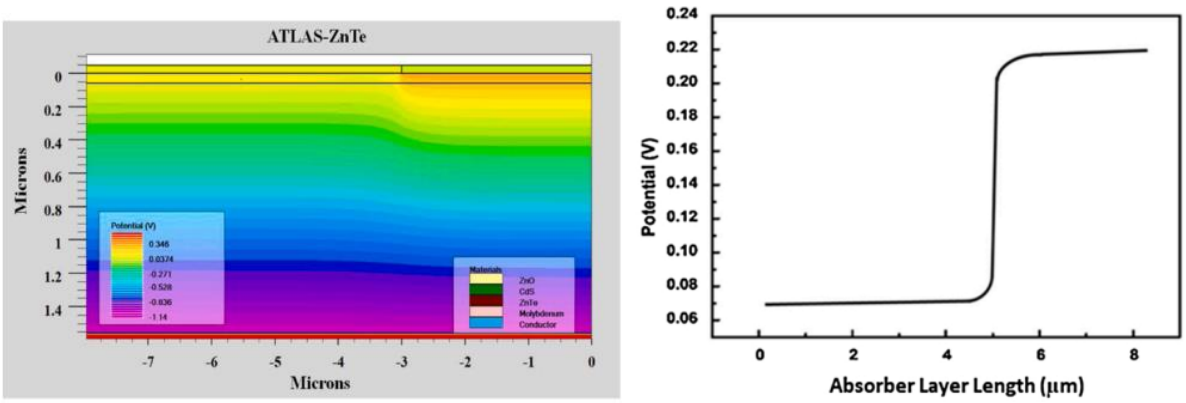

(a) (b)

Fig. 3.6. (a) Internal potential variation in ZnTe Cell and (b) Magnitude of potential as a function of absorber layer length.

Device structure depicting layer wise distribution of conduction band energy is presented in Fig. 3.7 (a). Additionally, Fig. 3.7 (b) represents the variation of the conduction band energy as a function of the *x*- coordinate, which corresponds to the length of the absorber layer. When photons incident on the device, they produce electron-hole pairs, then these charge carriers move from valance to conduction band, enabling proper current conduction. Fig. 3.7 (c) demonstrates the relative positions of conduction and valance band energies as a function of absorber layer length for ZnTe material. The black contour depicts the conduction band and red contour presents the valance band.

It can be observed that at the extreme left of the absorber layer (representing the start of the horizontal cutline), the valance band energy is approximately at -1.45 eV, and conduction band is at 0.81 eV. Therefore, the calculated band gap is 2.26 eV, which is in good agreement to the reported band gap of 2.25 eV for the ZnTe material. Upon closer examination of these figures, the characteristic band diagram of a p-n junction band is observed, with the conduction energy

level of n-side being higher than that on the p-side, thus validating solar cell operation. Fig. 3.8 (a) and (b) illustrate the profiles of hole current density and hole concentration, respectively.

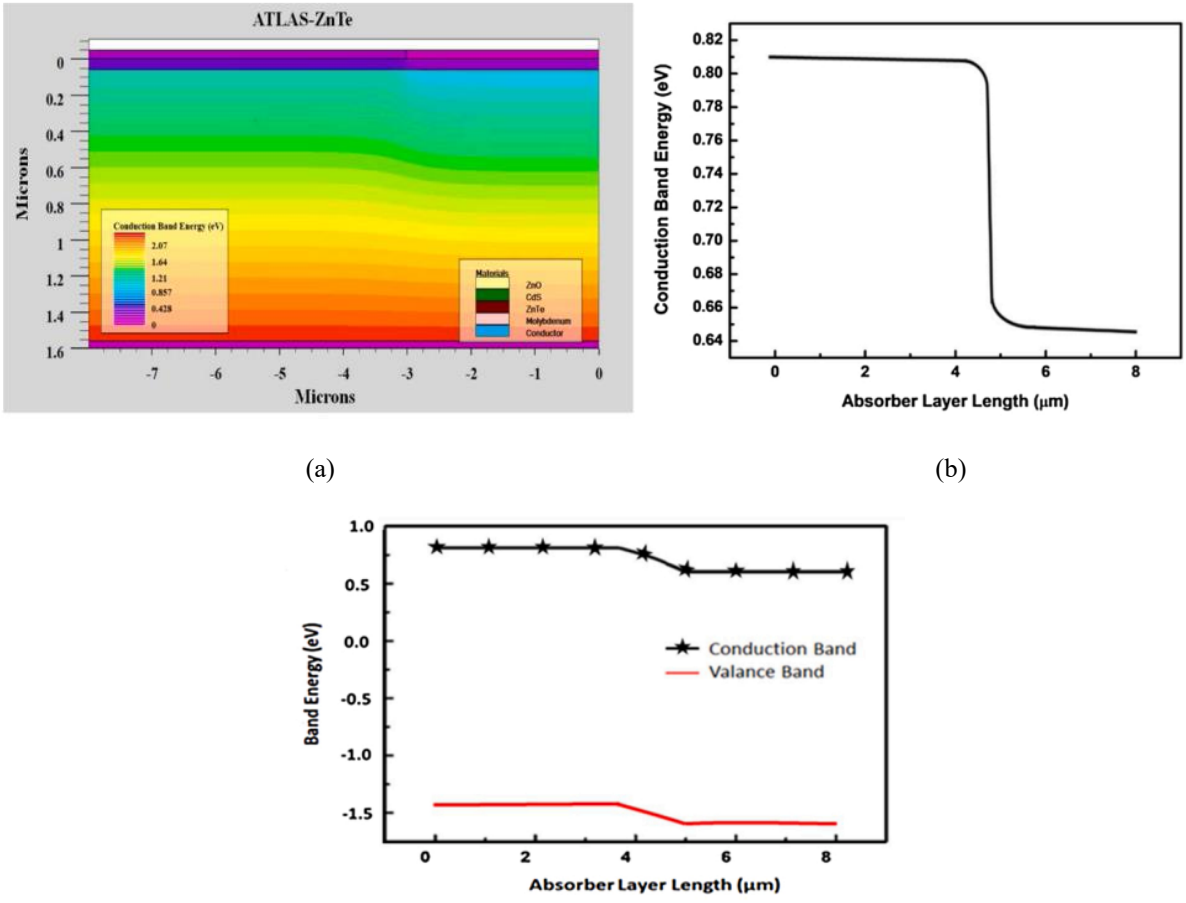

Fig. 3.7. (a) Layer-wise conduction band energy distribution in solar cell, (b) Magnitude of conduction band energy and (c) Combined plots of conduction and valance band energies as a function of ZnTe absorber layer length.

The hole current is highest at the junction of CdS and ZnTe layers. The purpose of an absorber layer in a heterojunction thin film cell is to absorb the light and generate charge carriers. Whereas, the buffer layer forms a junction with the absorber layer and facilitates the transports the photogenerated carriers. Typically, p-type semiconductor materials are used as absorber layers [339]. The main function of buffer layer is to allow maximum light penetration at the junction with minimum recombinational loss of the photogenerated carriers. It is observed from Fig. 3.8 (c) that the charge carriers are scarcely recombined in the buffer layer. This presents the fact that, a large number of charge carriers are able to freely move from absorber layer to the metal electrode.

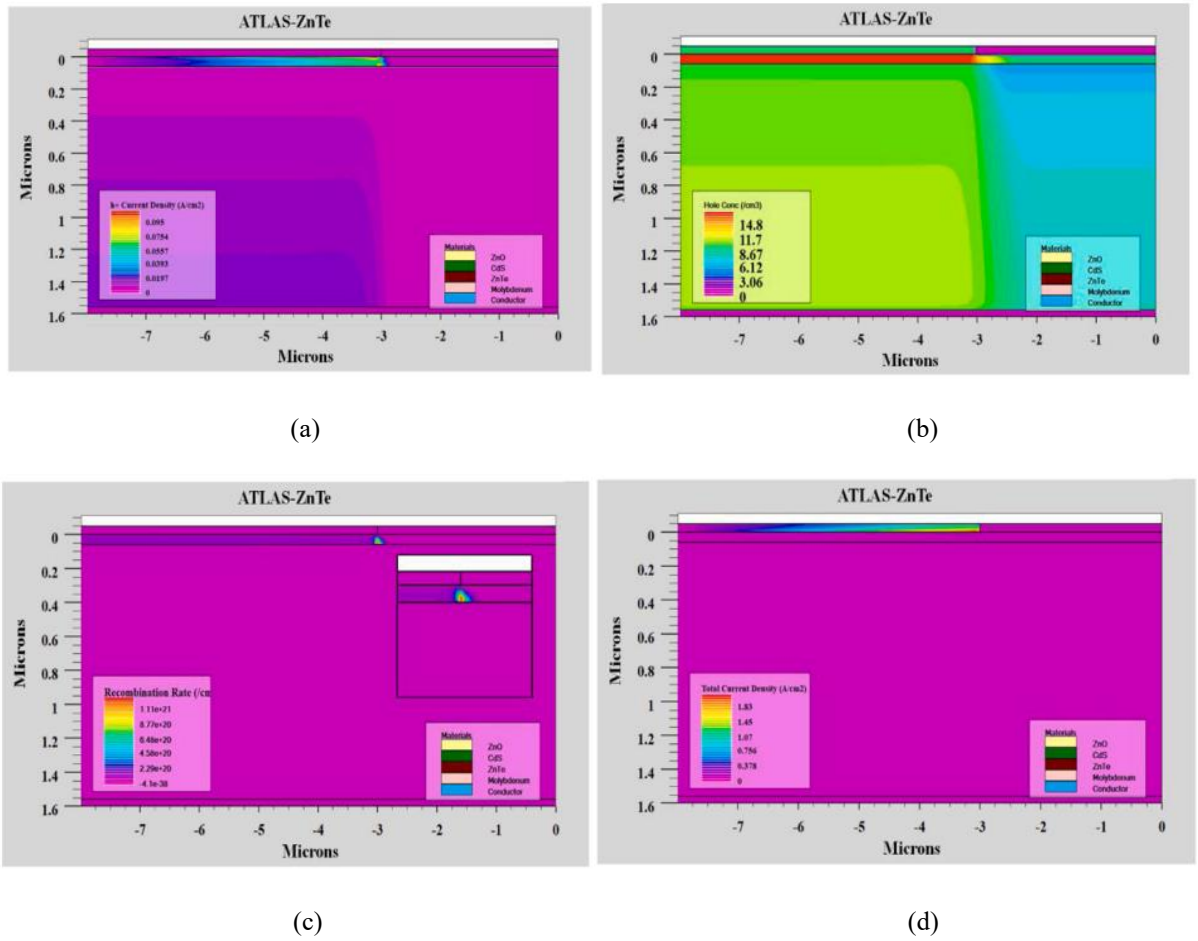

Fig. 3.8. Device structures depicting layer-wise variation of (a) Hole current density, (b) Hole concentration, (c) Recombination rate (inset shows an enlarged view) and (d) Total current density in ZnTe solar cell.

In principle, a buffer layer improves the interface between the absorber and window layers, enhancing the crystal quality on both sides. This, in turn, reduces the recombination of electrons and holes. It is worth noting that recombination is the major adversary or major challenge to the efficiency of solar cell. Window layer, is front contact of solar cell, and acts as a transparent layer to enable maximum incident radiation. The motive to put window on top of PV cell is to maximize absorption by absorption layer. Consequently, generated electron hole pairs can diffuse to the respective electrode without recombining, resulting in a potentially high solar cell efficiency.

If the window layer was positioned below the absorber layer, then the majority of photons would have been absorbed by the absorber layer near the surface. This would lead to a significant loss in efficiency. Additionally, the window layer plays a crucial role in carrying the current, as depicted by the Fig. 3.8 (d). In general, wide band gap semiconductors such as ZnO,

In_2O_3/SnO_2 are commonly used as the top layer [340, 341]. For visible light, the window layer materials are required to have a band gap of more than 3.0 eV [342].

3.4 Sn/Sb DOPED ZnTe SOLAR CELLS

Absorber layer plays a significant part in determining performance characteristic of a PV cell. Sb and Sn materials are doped in ZnTe material to achieve improved characteristics for the absorber layer. In this section, SbZnTe and SnZnTe materials are utilized for the absorber layer. The performance for both the cells is analysed by keeping other material layers (except absorber layer), device dimensions and operating conditions same as the ZnTe cell for a fair comparison among the different cell.

Absorption coefficients [315] are added in the numerical simulation (Silvaco Atlas) via. nk file. For an amorphous semiconductor, the absorption range can be divided into three levels: the low absorption tail, the exponential edge, and the strong absorption. The first level is attributed to the defects and impurities. While the second level arises because of the amorphous compounds and the last level is due to energy gap [343]. The absorption coefficient (α) as a function of photon energy (*hv*) is shown in Figs. 3.9 (a) and (b) for SbZnTe and SnZnTe layers, respectively. The absorption coefficient (α) demonstrates the increasing trend for the three materials with respect to photon energy (*hv*). Figs. 3.9 (c) and (d) illustrate the simulated structures of SbZnTe and SnZnTe absorbing material based solar cells, respectively.

Further, the current density is observed at different voltages for both the solar cells as shown in Fig. 3.10 (a). The polarity for current is observed to be positive and this aligns with the findings of previous researchers such as Tanaka *et al*. [319, 320], Khattak *et al*. [330], Mukhopadhyay *et al*. [331] and Dharmadasa *et al*. [344]. In the previous section, the maximum current density of 7.9 mA/cm^2 was observed for ZnTe (1.5 μm) solar cell. Now it is obtained as 9.0 mA/cm^2 and 20.6 mA/cm^2 for SbZnTe and SnZnTe, respectively at an absorber thickness of 1.5 μm. The improvement is of 1.1 times and 2.6 times for SbZnTe and SnZnte respectively compared to ZnTe cell. The current in SnZnte cell is enhanced significantly attributed to its smaller band gap of 1.39 eV, which is comparable to materials suitable for solar cell. [319, 320].

Figs. 3.10 (b) and (c) demonstrate the plots of V_{OC} and J_{SC}, respectively at different thickness of SbZnTe/ SnZnTe layers, ranging from 0.5 to 2.5 μm. The trend for open circuit voltage is

similar for both cells but with significant difference in the magnitudes. The V_{OC} increases from 1.67 to 1.79 Volt when SbZnTe thickness is increased from 0.5 to 2.5 µm. On the other hand, the V_{OC} increases from 0.87 to 0.93 V for SnZnTe layer in the same thickness range. This open circuit voltage is observed to be 6.1% and 50.2% lower for SbZnTe and SnZnTe cells at a thickness of 1.5 µm, respectively than that of ZnTe. There is a linear rise in the open circuit voltage values as the thickness is increased from 0.5 to 2.5 µm occurring due to limited growth in the recombination sites. The V_{OC} primarily rest on the recombination rate and Fermi splitting. A higher fermi splitting leads to an increment in V_{OC} values.

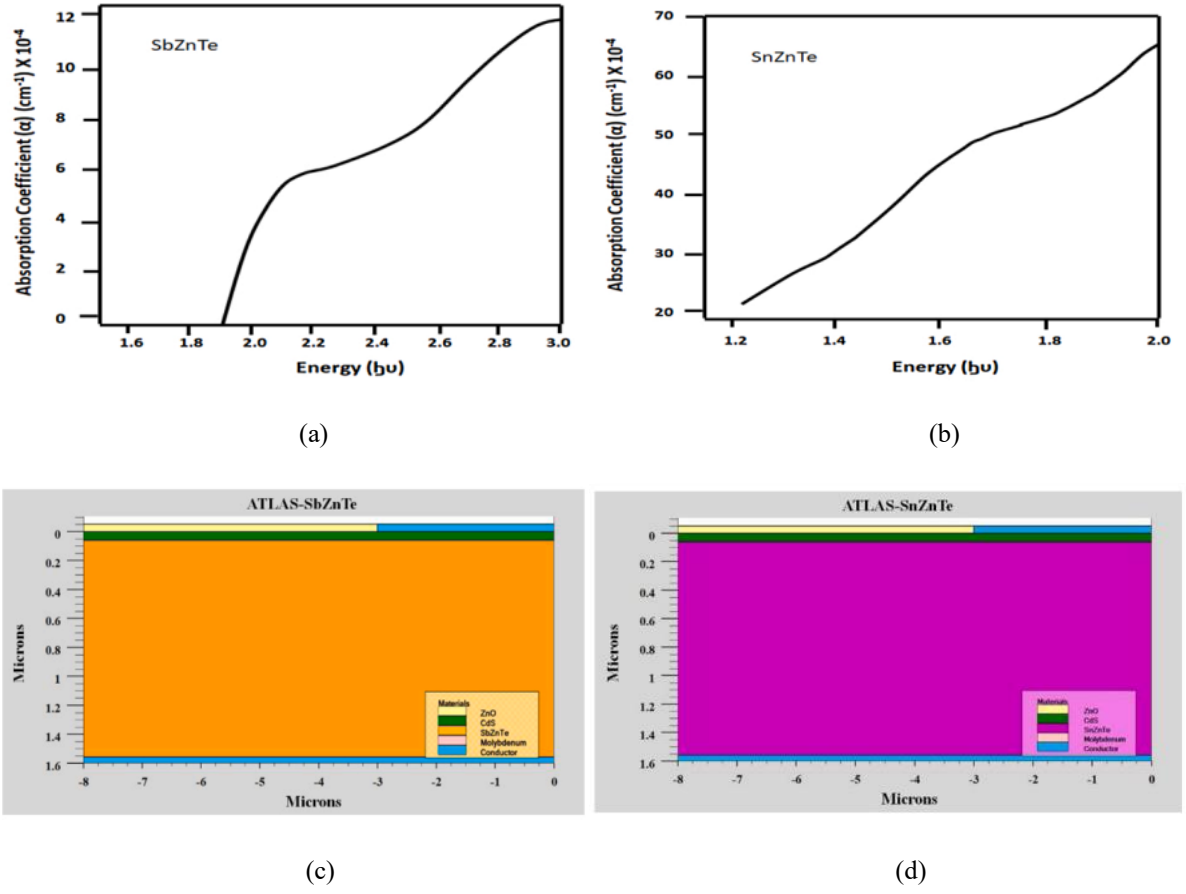

Fig. 3.9. Plots of absorption coefficients for (a) SbZnTe and (b) SnZnTe materials and device structures of (c) SbZnTe and (d) SnZnTe absorber layer based solar cells.

The J_{SC} in solar cell is calculated at electrode potential of 0 V, when solar cell is short circuited. It is more common to express short-circuit current density (*Jsc* in mA/cm^2) in place of short-circuit current (I_{SC}) to evaluate current developed per unit area of the solar cell. The J_{SC} depends on various factors, including cell's area, number of incident photons, spectrum of the incident light, optical properties and collection probability of the solar cell.

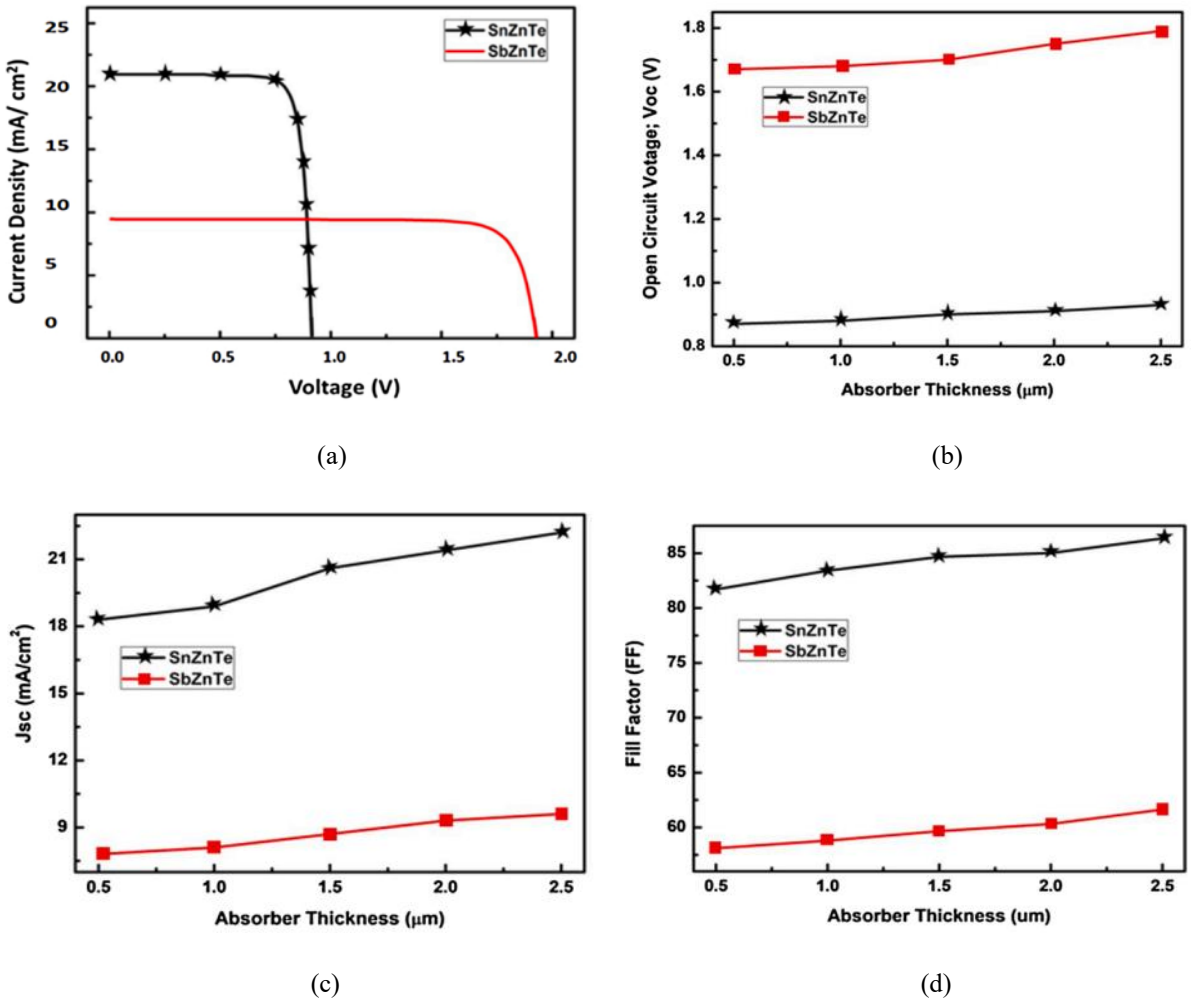

Fig. 3.10. Combined characteristics plots of (a) Current density Vs. voltage, (b) Open Circuit Voltage, (c) Short circuit current density and (d) Fill Factor as a function of absorber thickness for SbZnTe and SnZnTe cells.

Here, short circuit current shows an increment on increasing absorber thickness attributed to greater light absorption and thereby more charge carrier generation. This rise in SbZnTe and SnZnTe cell is observed as 26% and 31% respectively, when the thickness is increased from 0.5 to 2.5 μm. This trend is more prominent till 1.5 μm, as most of the carriers remain concentrated in the vicinity of interface. As the thickness increases beyond 1.5 μm, the incremental increase in short circuit current becomes slightly less proportional [310]. The current density is higher by 2.3 times for SnZnTe solar cell than SbZnTe solar cell at a 1.5 μm thickness. The current density is less in SbZnTe solar cell due to its larger band gap and lesser carrier concentration as evident from internal horizontal and vertical cutline plots (Figs. 3.13 and 3.15). Additionally, the current density is limited by the recombination of photogenerated charge carries.

The Fill factor is a crucial parameter to validate the quality of a solar cell as it determines the power conversion efficiency of the solar cell. It is a key parameter in evaluating the performance of a solar cell. The magnitude of Fill Factor as a function of absorber thickness is plotted in Fig. 3.10 (d). The obtained values of Fill Factor are 59.66% and 84.66% at the absorber thickness of 1.5 μm for SbZnTe and SnZnTe, respectively. This Fill Factor is improved by 5.3% for SbZnTe and 49% for SnZnTe than ZnTe cell. It is worth noting that the obtained Fill Factor is highest for SnZnTe as it has the lowest value of bandgap among the three cells and observed to be 1.4 times improved as compared to SbZnTe cell which ensures its higher power conversion efficiency and thereby higher quality, as well.

The Fill Factor exhibits a slight increase on increasing absorber thickness. This can be attributed to a higher number of charge carriers generated due to increased light absorbed, resulting in the generation of more electron-hole pairs. The maximum anode voltage (V_m) and maximum cathode current (I_m) as a function of absorber thickness for SbZnTe and SnZnTe cells are shown in Figs. 3.11 (a) and (b). Referring to the curves, maximum anode voltage is higher by 1.9 times for SbZnTe as compared to SnZnTe at 1.5 μm. It shows a linear rise of 1.1 times for both the cells on increasing absorber thickness from 0.5 to 2.5 μm. On the other hand, the maximum cathode current for SnZnTe is significantly higher and observed to be higher by 3.5 times than the SbZnTe at 1.5 μm thickness.

The cells are analyzed in terms of carrier concentration, potential drop, and electron/hole current density within the device to better comprehend the device physics and current carrying nature of the solar cells. To perform the internal analysis, a cutline is drawn horizontally [345] near the junction of absorber and buffer layer. Fig. 3.12 (a) presents a combined plot to depict the variation of potential in both solar cells. Further, Figs. 3.12 (b) and (c) illustrate the conduction and valance band energy plots as a function of absorber layer length ranging from 0 to 8 μm on the *x*-axis. It is observed from the plots that SnZnTe requires less energy to move the charge carriers from valance band to conduction band owing to its lower energy gap of 1.39 eV.

On the contrary, a higher bandgap of 2.14 eV is observed for SbZnTe material, indicating a higher energy requirement to move the charge carrier. Fig. 3.13 demonstrates the distribution of charge carries, both holes and electrons, within the cells and their effects on the current. It is evident from the plots that the concentration of holes and electrons is inversely related to

each other. Fig. 3.13 (a) shows that the hole concentration remains constant until approximately 4.5 μm. Afterward, a sharp decline is observed, which may be due to recombination of carriers.

Hole current density as a function of absorber layer length is illustrated in Fig. 3.13 (b) and it is significantly higher for SnZnTe material. However, the situation is reversed for electron concentration and electron current density, as can be observed from Figs. 3.13 (c) and (d), respectively. The election concentration is lower until approximately 4.5 μm, and then it shows a sudden increase. The above phenomenon occurs due to the arrangement of charge carriers and their transport to their respective electrodes, where holes travel to the cathode and electrons to the anode. The obtained values for holes and electrons concentration are higher by 9.84% and 8.96% respectively, for SnZnTe compared to the SbZnTe cell. Similarly, there is a corresponding increase of 11.86% and 35.50% in hole and electron current density, respectively.

3.5 COMPARATIVE ANALYSIS OF ZnTe, SbZnTe AND SnZnTe SOLAR CELLS

In this section, a comparative analysis of the three solar cells is performed to determine the best preforming solar cell. Based on the earlier discussion, a solar cell can be considered holistic if it exhibits adequate current density and high Fill Factor while having minimum device dimensions. A solar cell with high Fill Factor absorbs a large amount of light and results in a high current even across a broad range of wavelengths of light.

Table 3.2: Extracted performance parameters for ZnTe solar cell at absorber thickness of 1.5 μm

Parameter	Magnitude
V_{OC} (Open Circuit Voltage)	1.81 V
FF (Fill Factor)	56.66%
J_{SC} (Short Circuit Current Density)	7.9 mA/cm^2

Figs. 3.14 (a) and (b) presents combined plots of open circuit voltage and Fill Factor, respectively to facilitate a fair comparison among all three solar cells. As discussed earlier, open circuit voltage represents the maximum voltage produced by a photovoltaic cell when no load is connected. The Table 3.2 represents the Extracted performance parameters for ZnTe solar cell at absorber thickness of 1.5 μm.

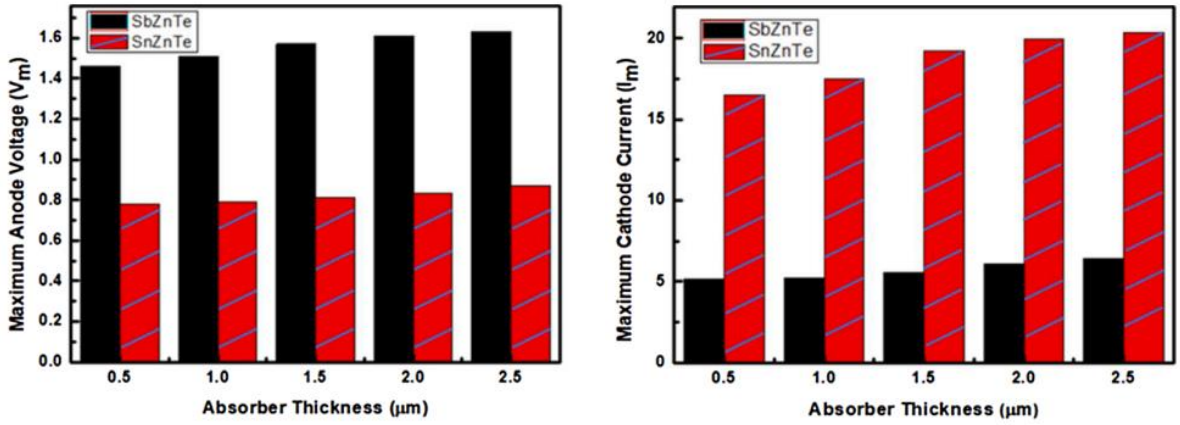

(a) (b)

Fig. 3.11. Plots of (a) Maximum anode voltage (*Vm*) and (b) Maximum cathode current (*Im*) as a function of absorber thickness for SbZnTe and SnZnTe cells.

The output voltage of the solar cell varies between 0 and open circuit voltage, depending on the impedance of the connected load. In this case, open circuit voltage is achieved as 1.81, 1.70 and 0.90 V for ZnTe, SbZnTe and SnZnTe based cells, respectively at an absorber thickness of 1.5 μm. Additionally, a small increment in open circuit voltage is observed on increasing thickness of the absorber layer. The extracted parameters for ZnTe, SbZnTe and SnZnTe cells are summarized in Table 3.3. Fill Factor is essentially a measure of the quality of a solar cell. The Fill Factor is calculated as the ratio of maximum value of actual obtainable power to the product of open circuit voltage and short circuit current [315]. In essence, the Fill Factor quantifies the "squareness" of the current voltage curve.

According to Fig. 3.14 (b), it is observed that the Fill Factor increases for all the three cells on increasing absorber thickness. The conversion efficiency of ZnTe, SbZnTe and SnZnTe is achieved to be 9.2%, 10.6% and 17.8% at an absorber thickness 2.5 μm, which are higher by 1.15 and 1.93 times in comparison to the ZnTe based solar cell. In the proposed work, the solar cell with SnZnTe as absorber layer has demonstrated a reasonable efficiency of 17.8% when compared to other reported solar cells based on amorphous absorber materials [331, 332]. Similarly, the Fill Factor is obtained as 58.34%, 61.64% and 86.34% at an absorber thickness of 2.5 μm thickness for ZnTe, SbZnTe and SnZnTe layers, respectively. These values for Fill Factor are increased by 1.05 and 1.47 times for SbZnTe and SnZnTe than that of ZnTe solar cell.

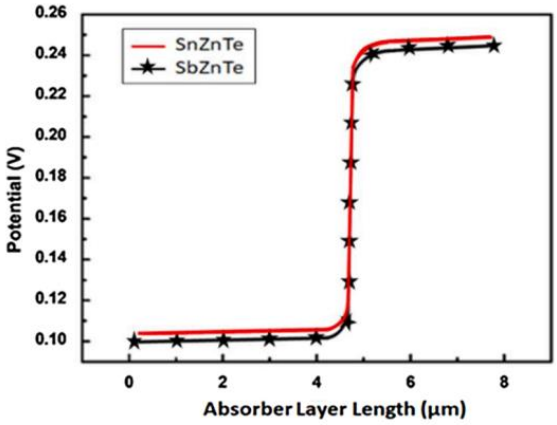

(a)

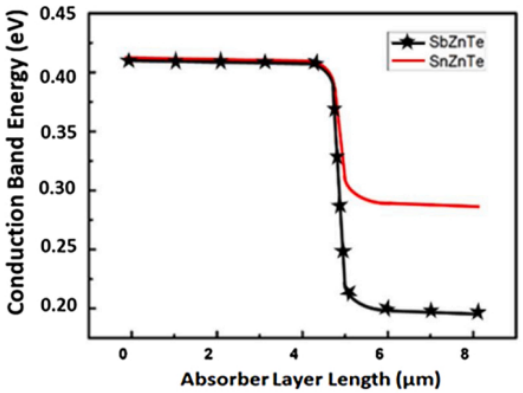

(b)

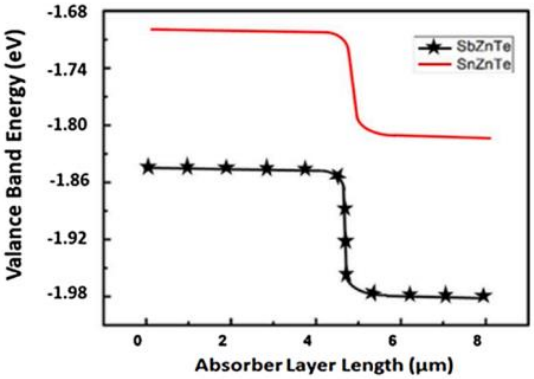

(c)

Fig. 3.12. (a) Potential distribution, (b) CB Energy and (c) VB Energy with respect to length of absorber layers.

The SnZnTe material-based cell outperforms the other cells in terms of current density, Fill Factor, and conversion efficiency due to its lowest band gap. The low band gap indicates that this cell requires least amount of energy to move the charge carriers from valance band to conduction band.

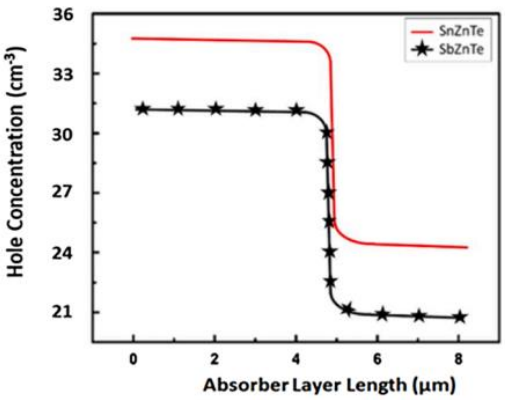

(a)

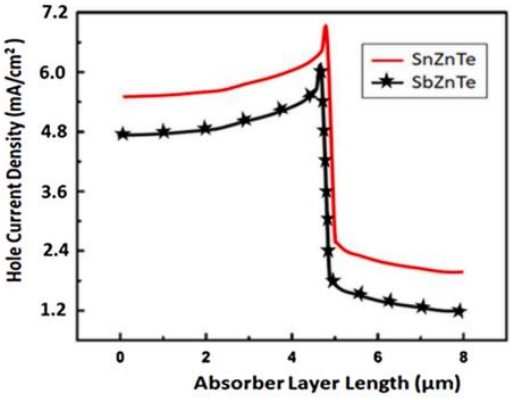

(b)

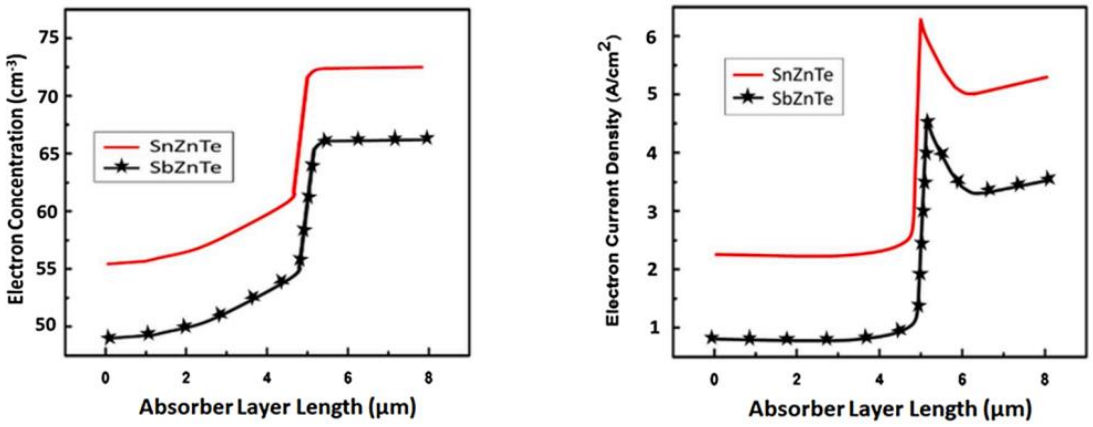

(c) (d)

Fig. 3.13. Combined Plots of (a) Hole Concentration, (b) Hole current density, (c) Electron Concentration and (d) Electron current density as a function of absorber layer length for SbZnTe and SnZnTe.

Owing to its small band gap, even photon with the smallest wavelength of incident light and minimum energy can excite a charge carrier from valance to conduction band thus, leading to maximum energy conversion. On the other hand, SbZnTe has its band gap value slightly lower than ZnTe thereby depicting small improvement in Fill Factor values. Further, an in-depth internal analysis is performed for all three solar cells by inserting a vertical cutline near the centre of solar cell along its device thickness.

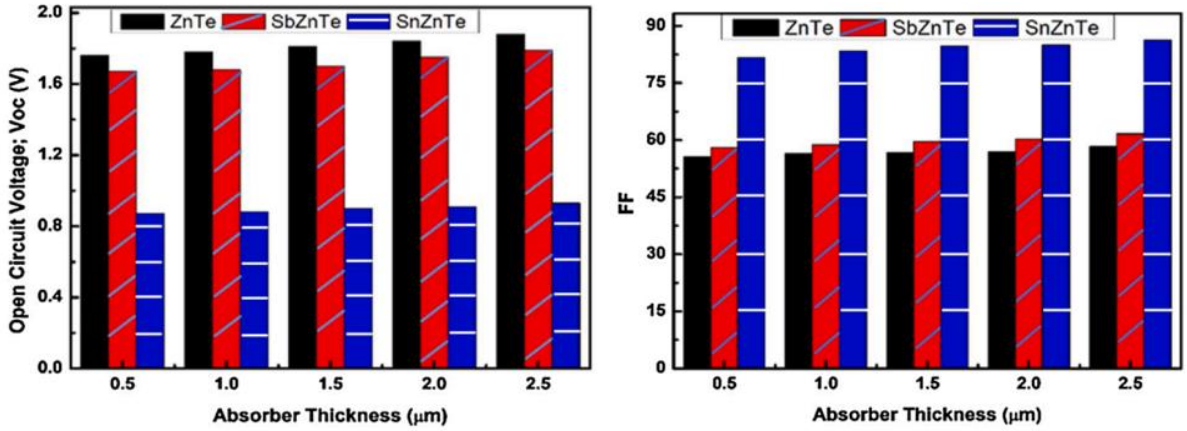

(a) (b)

Fig. 3.14. Combined plots of (a) Open circuit voltage and (b) Fill Factor as a function of respective absorber thickness for ZnTe, SbZnTe and SnZnTe layers.

The analysis of internal device physics helps to validate and explain functioning of different layers in the solar cells [346, 347]. Moreover, it is helpful to understand the variation in the open circuit voltage, Fill Factor, and other parameters. The results of cutline analysis are

presented in Fig. 3.15, where Figs. 3.15 (a) and (b) demonstrate the magnitude variation of the valance and conduction band energies across different layers.

Table 3.3. Extracted parameters for ZnTe, SbZnTe and SnZnTe cells at absorber thickness of 1.5 μm

Parameter	ZnTe	SbZnTe	SnZnTe
V_{OC} (Open Circuit Voltage)	1.81 V	1.70 V	0.90 V
FF (Fill Factor)	56.66%	59.66%	84.66%
J_{SC} (Short Circuit Current Density)	7.9 mA/cm^2	8.7 mA/cm^2	20.6 mA/cm^2
Conversion Efficiency	9.2%	10.6%	17.8%

The black contour in Fig. 3.15 represents the valance and conduction band energies of the ZnTe solar cell. Here, it can be noticed that in the vicinity of 0 μm (in the simulated solar cell the ZnO material is presented from 0 to 0.1 μm thickness) the valance band is at -3.2 eV and conduction band is at 0.2 eV, hence obtained bandgap value of ZnO stands at 3.4 eV. Similarly, at 0.15 μm (in the simulated solar cell the CdS material layer is presented from 0.1 to 0.2 μm thickness) the valance band is -2.25 eV and conduction band are 0.4 eV, resulting in a band gap of 2.6 eV for CdS. Further, for the ZnTe layer at 0.2 μm (thickness of ZnTe is from 0.2 to 1.6 μm), the valance band energy is -1.45 eV and the conduction band energy is 0.81 eV, yielding a band gap of 2.26 eV for ZnTe.

Indeed, the obtained values of energy band for ZnO, CdS and ZnTe materials are in good agreement to the reported values; 3.3, 2.4 and 2.25 eV respectively. Subsequently, valance and conduction band energies through internal cutline plots validate the reported values [8] for SbZnTe and SnZnTe layers. The internal cutline plots confirm the magnitude dissimilarity of the conduction and valance band energies across different layers, further enhancing the understanding of the functioning of solar cells.

The bandgap is highest for ZnTe and lowest for the SnZnTe material. Figs. 3.15 (c) and (d) depict the electric filed and the recombination rate, respectively. Referring to these figures, it can be observed that buffer layer shows maximum values for electric field and recombination rate due to the presence of maximum number of charge carries at the buffer and absorber layer junction. This is justified through Figs. 3.15 (e) and (f) correspondingly drawn for electron and hole concentrations.

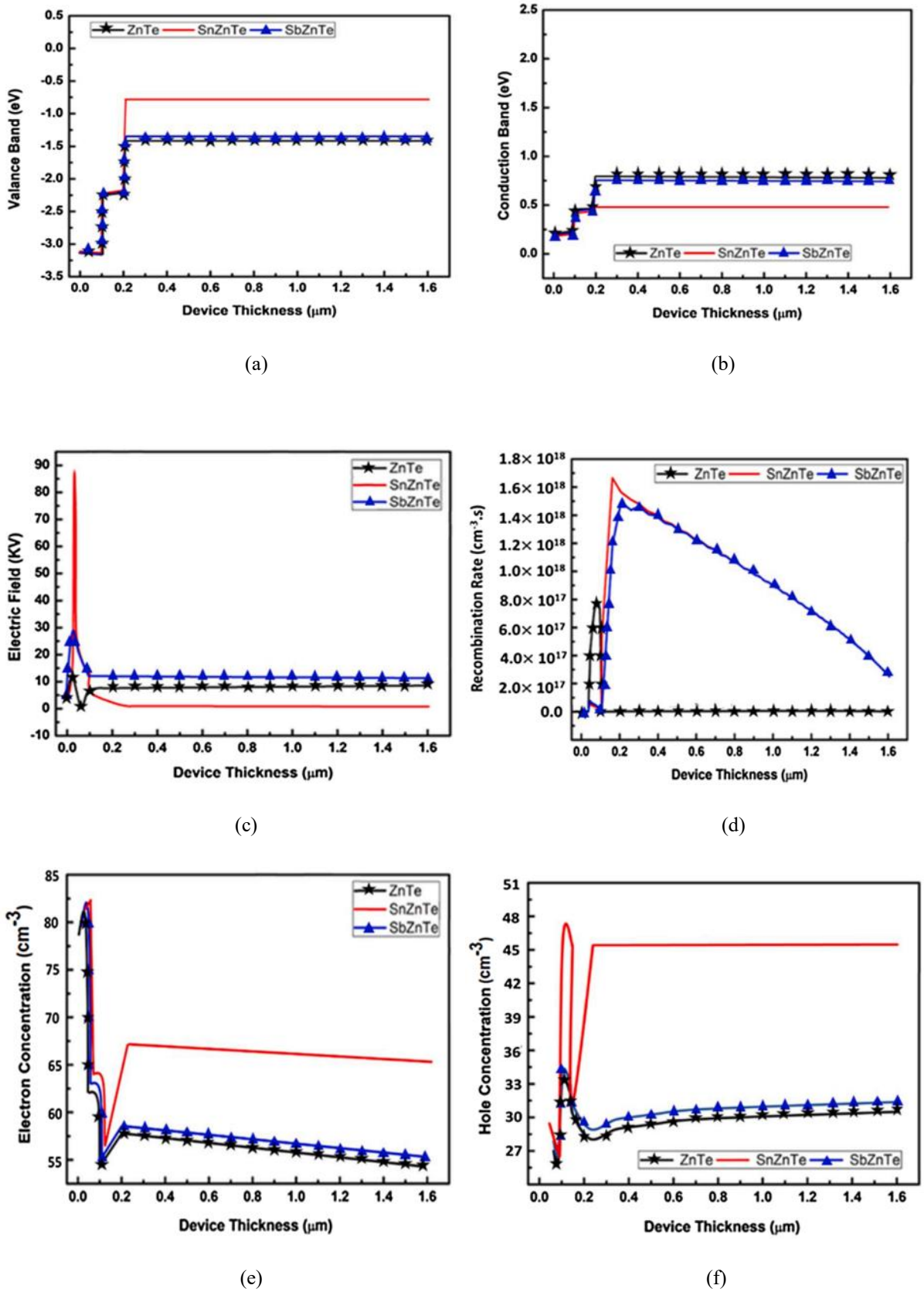

Fig. 3.15. Combined internal vertical cutline plots of (a) Valance band, (b) Conduction band, (c) Electric field, (d) Recombination rate, (e) Electron concentration and (f) Hole concentration as a function of device thickness for all three cells.

The maximum recombination of charge carriers takes place in the buffer layer. Further, a decline in the recombination rate validates the confinement of electrons and holes within the buffer layer. It is observed that there is a significant decrease in the concentration of electrons as cutline moves from window to the absorber layer. This occurs due to *p*-type nature of the absorber layer material (0.06–1.56 μm) highlighting its role as the absorber layer in the solar cell, where the charge carriers are generated after the absorption of photons. This generation of charge carriers is maximum for SnZnTe followed by SbZnTe and minimum for ZnTe material.

3.6 SUMMARY OF THE IMPORTANT RESULTS

1. The objective of this chapter is to synthesize thin films of third generation intermediate band gap solar cells. To achieve this, Sb/Sn materials are doped into ZnTe material, and further investigation and analysis are conducted on the prepared thin film solar cell to determine the most suitable absorber layer material for the solar cell.
2. Here, it is observed that SnZnTe solar cell exhibited reasonably higher hole and electron carrier concentrations compared to other solar cells, owing to its lowest band gap of 1.39 eV.
3. At an absorber thickness of 1.5 μm, the current density for SbZnTe and SnZnTe cells is improved by 1.1 times and 2.6 times respectively, as compared to ZnTe cell. This occurs due to the band gap value of the SnZnTe solar cell which is the lowest among the three cells.
4. This current density is increased by 26% and 31% when the absorber thickness is increased from 0.5 to 2.5 μm for SbZnTe and SnZnTe layers, respectively. The current density is higher by 2.3 times for SnZnTe solar cell than SbZnTe solar cell at a 1.5 μm thickness. The current density is less in SbZnTe solar cell due to its larger band gap and lesser carrier concentration.
5. The holes and electrons concentration are higher by 9.84% and 8.96% respectively for SnZnTe compared to SbZnTe solar cell.
6. The current density obtained for SnZnTe is 2.3 and 2.6 times better than SbZnTe and ZnTe, respectively, at the thickness of 1.5 μm.
7. The Fill Factor for SnZnTe cell is also significantly higher at 84.66% compared to 59.66% for SbZnTe and 56.66% for ZnTe based solar cell.
8. The highest conversion efficiency of 17.8% is achieved for SnZnTe solar cell, followed by SbZnTe with 10.6%.

9. The ZnTe solar cell exhibited the lowest efficiency of 9.2%. Indicating that the SnZnTe material is best suited as the absorber material due to its lowest band gap.
10. The conversion efficiency of SbZnTe and SnZnTe solar cells at 2.5 μm thickness are achieved as 10.6% and 17.8%, respectively, which are higher by 1.15 and 1.93 times in comparison to the ZnTe based solar cell.
11. The SnZnTe solar cell demonstrated a holistic performance owing to its lowest band-gap of 1.39 eV, The SnZnTe material leads to highest charge carrier generation, thereby hole and electron current densities are improved by 11.86% and 35.50% than the SbZnTe cell.
12. The absorber layer is found to be crucial in improving the device performance without the need for increasing the device dimensions.

CHAPTER-4

DESIGN AND PERFORMANCE ANALYSIS OF IMPROVED MULTILAYER ORGANIC SOLAR CELL

The power conversion efficiency is a vital performance parameter as it represents the ratio of power output to input solar power. A higher efficiency indicates a better performing solar cell. However, organic solar cells experience challenges of low absorption, resulting in lower PCE in comparison to inorganic solar cells. To address the issue, it is essential to optimize organic solar cells parameters by employing novel device structures and photon harvesting materials. In the case of bilayer organic solar cells, the understanding of internal device physics is still not well described due to the complexities of material science, polymers chemistry and device engineering. Nonetheless, a thorough examination of internal device physics can provide critical insight into the internal mechanism of electronic devices and help determine the optimal conditions for enhancing device performance. Therefore, the aim of this chapter is to investigate the internal device analysis of bilayer solar cells and enhance their performance. Following objective is framed to accomplish the proposed work; for which the following objective is formed:

"Design and analysis of organic materials based solar cell and further performance improvement using multi organic layers for carrier enhancement."

The methodology used to achieve framed objective involves following steps: -

- Design a bilayer organic photovoltaic cell consisting of acceptor and donor material layers.
- Analyse the bilayer organic photovoltaic cell internally through vertical cut-line for understanding complexity of the organic solar cell device physics.
- Analyse the effect of donor and acceptor layer thicknesses on solar cell performance.
- Evaluate the optimized thickness for P3HT: PCBM solar cell.
- Investigate the effect of donor material and hole/electron transport layers.
- Compare and contrast the performance of conventional and inverted solar cell structure.

The present chapter is divided into eleven different sections, starting with an introduction as first section. In the second section, the current-voltage characteristic of the solar cell is investigated. Section three focuses on the internal device physics of the solar cell. Sections four and five discuss the impact of donor and acceptor layer thicknesses on solar cell optimization. The optimized solar cell is discussed in section six. Section seven provides details on the effect of donor material. Sections eight and nine explore the effect of hole transport layer and electron transport layer respectively. Section ten and eleven discuss the conventional and inverted structure configurations of the solar cell, including the hole transport layer and electron transport layer materials. Finally, all the important outcomes are summarized in the conclusion.

4.1 INTRODUCTION

Solar Cells are clean, renewable sources of energy with tremendous potential to decrease carbon footprint [348, 349]. In past two decades, the development of Organic Solar Cells (OSCs) has made commendable progress [350-352]. Organic solar cells made of polymers are considered vital and capable substitute for presently available inorganic solar cells due to their characteristic properties, such as high mechanical flexibility, lighter weight, and lower production costs [353, 354]. However, the low power conversion efficiencies of OSCs pose challenges for their large-scale commercialization [355]. Thus, improving the efficiency of OSCs remains a primary concern of the research community.

In OSCs, incoming sunlight is converted into electric current through four stages: (a) Incoming sunlight produces electron-hole pairs known as excitons (b) exciton diffusion occurs, where the excitons move within the photoactive layer (c) dissociation of the exciton, leading to separation of charges (d) charge transportation to respective electrodes, this transportation of charge is a kinetic competition with the process of recombination. In general, OSCs consist of a photoactive layer which is sandwiched between a transparent electrode and a reflective electrode. The incident sunlight enters the organic solar cell through the transparent electrode and is reflected back inside photoactive layer by the second reflective electrode resulting in the formation of a standing wave pattern inside the OSC.

The Bilayer OSCs consist of donor layer and accepter layer materials sandwiched between two different electrodes. The solar cell structure described in this chapter comprises of transparent electrode Indium Tin Oxide (ITO). As a material ITO has excellent conductivity and transparency, making it suitable as the anode in our structure. The donor layer in the structure

is made of Poly (3-hexylthiophene-2,5-diyl) (P3HT) which acts as the electron donor. On the other hand, the acceptor layer is composed of (6, 6)-phenyl C_{61} butyric acid methyl ester (PCBM), serving as the electron acceptor. A low work function material Aluminium (Al) is utilized as a non – transparent cathode.

Organic polymer materials suffer from the issue of low absorption [356, 357], limiting the efficiency of organic solar cell. One solution to this problem is to increase the thickness of the organic solar cell's photoactive layer to an optimum level so as to absorb more quantity of incoming sunlight, leading to improved light harvesting. In this chapter, OSC is optimized to enhance its power conversion efficiency through the use of new stable device structures and photon harvesting materials. To improve the absorption of light, it is important to maximize the optical field strength with in the photoactive layer. This maximization of filed within the photoactive layer is achieved by means of introducing appropriate interfacial layers between the electrodes and photoactive layer, which will in turn result in enhanced organic solar cell performance. When the OSC is illuminated, the generated excitons (electron-hole pairs) dissociate at donor-acceptor interface. This process is driven by the differences in energy levels between the two organic semiconductors.

The then parted charge carriers drift due to the field produced by the electrodes finally being collected by corresponding electrode. The efficiency is defined as product of short-circuit current density (J_{SC}), fill-factor (FF) and open-circuit voltage (V_{OC}). The J_{SC} is related to light absorption efficiency, generation and dissociation of exciton, carrier transport and collection at electrodes. Open circuit voltage (V_{OC}) is the difference between donors highest occupied molecular orbital (HOMO) and acceptors lowest unoccupied molecular orbital (LUMO) and is calculated by the difference in-between quasi-Fermi levels of electrons and holes when kept under illumination. The nature of contact between the photoactive layer and electrode is capable of significantly influencing all the three performance parameters related to the solar cell. The modification of interfaces via introducing suitable interfacial layer could change the contact properties so as to increase the efficiency of solar cell. The present chapter represents the performance parameters, device physics and strategies to optimize and enhance the performance of an OSC.

4.2 J-V CHARACTERISTICS OF ORGANIC SOLAR CELL

A bilayer organic photovoltaic cell consists of acceptor and donor material layers which are arranged together in a planer interface, and the bilayer is sandwiched between two different electrodes. The Fig. 4.1 represents the architecture of an organic bilayer photovoltaic cell simulated using Indium Tin Oxide, P3HT, PCBM, and Aluminium as layers. The length of the photovoltaic cell is taken as 1 μm. To achieve efficient charge carrier extraction, the electrodes should match up highest occupied molecular orbital of the donor and lowest unoccupied molecular orbital of the acceptor. The transport of charge to the acceptor material from the donor material in a bilayer heterojunction is driven by the electronic affinity of the adjacent materials and the differences in their ionization potentials. In general, organic photovoltaic cells consist of a front electrode, which is transparent and a back electrode, which is opaque. The light penetrates the bilayer cell through the front transparent electrode and undergoes reflection at the opaque electrode.

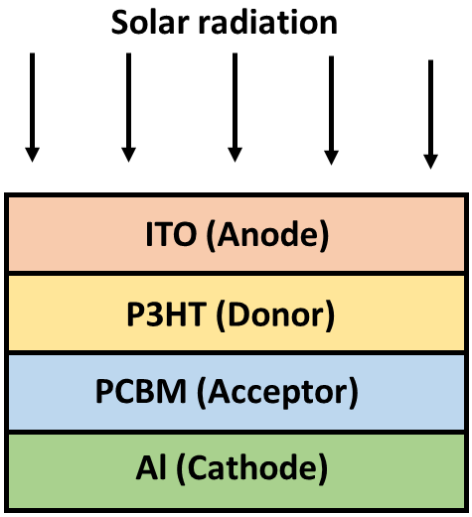

Fig. 4.1 P3HT: PCBM material based bilayer cell device architecture.

To report the internal device physics of any device is a complex task, and requires standard light sources containing appropriate filters for simulating the exterior environmental conditions indoor, to properly investigate the behaviour and characteristics of the solar cell. Typically, indoor simulations are primarily reliant on arc lamps made up with xenon, mercury, tungsten, or some other metal halides. However, these methods are extremely vulnerable to aging and require manual regulation of the arc lamps, and therefore may not essentially produce an ideal solar spectrum. Furthermore, with time the spectra of light produce by these lamps at the

starting of the experiment might not be identical to the spectra produced towards the end of the experiment. Hence, to overcome these limitations, industry standard software tool Silvaco Atlas is utilized which is capable to reproduce these solar cell devices in the computers with identical and ideal conditions without the need of continuously monitoring or controlling the incident light power from the lamps.

The excitons are created due to absorption of photon and their diffusion in the active layer according to the diffusion equation

$$D_E \frac{d^2 n_E}{dx^2} = G_E(x) - R_E(x) \tag{4.1}$$

D_E is the diffusion coefficient of the exciton, n_E is the concentration of the exciton, G_E presents the generation rate of exciton and R_E is the exciton recombination rate. The recombination rate of excitons is defined as

$$R_E(x) = \frac{n_E}{t_E} \tag{4.2}$$

where, t_E is the lifetime of exciton, n_E is excitons concentration.

$$L_E = \sqrt{D_E . t_E} \tag{4.3}$$

L_E is the diffusion length of the excitons, distance that an exciton could travel without recombination or decay.

The charge carrier transport physics in organic solar cells can be obtained by combining Poisson equation with continuity equation considering drift-diffusion model. The Poisson's equation is expressed as

$$\nabla . |\varepsilon \nabla V| = q(n - p - N_{Don}^{+} + N_{Acc}^{-} + Q_{Trap}) \tag{4.4}$$

Where, ε is permittivity, V is potential, q is charge, n and p represent free electron and hole charge densities, N_{Don}^{+} is the donor concentration, N_{Acc}^{-} is the acceptor concentration and Q_{Trap} is the trapped charges density. Hence, the Poisson's equation manages the carrier populations, trapped charges and carrier concentration. The continuity equations for free carriers, electrons and holes track the electrons in conduction band and holes in valance band and are given as following:

$$\frac{\partial n}{\partial t} = \frac{1}{q}\nabla J_e + G_e - R_e \tag{4.5}$$

$$\frac{\partial p}{\partial t} = -\frac{1}{q}\nabla J_h + G_h - R_h \tag{4.6}$$

Where, n, p are free electron and hole densities, G_e and G_h are the electron and hole optical generation rates, R_e and R_h are recombination rates for electrons and holes. J_n and J_p are the electron and hole current densities. Further, the electron and hole current densities are given as:

$$J_e = qn\mu_e\nabla V + qD_e\nabla n \tag{4.7}$$

$$J_h = qp\mu_h\nabla V + qD_h\nabla p \tag{4.8}$$

Where, μ_e and μ_p are mobilities of electron and hole and D_e and D_h are diffusion coefficients for electron and hole respectively. The equations (4.7) and (4.8) include the drift and diffusion currents resulting from the fields generated by electron affinity, density of states and bandgap. The boundary conditions for all excitons to dissociate or recombine are given as:

$$n\,(d) = n_{Al} = N_C \exp\left(-\frac{\phi_C - \chi_A}{kT}\right) \tag{4.9}$$

$$p\,(0) = p_{ITO} = N_V \exp\left(-\frac{\emptyset_a - \chi_D}{kT}\right) \tag{4.10}$$

where, ϕ_c and ϕ_a represent the cathode and anode work functions respectively, χ_D and χ_A are the lowest unoccupied molecular orbital levels for donor and acceptor, N_V and N_C are effective densities of valance and conduction band.

The device structure presented in Fig. 4.1 consists of individual layers of material substances arranged in a planer form for the P3HT: PCBM solar cell. The performance parameters and electrical characteristic of the photovoltaic device are investigated using the aforesaid material substances, device dimensions and propagation models. Table 4.1 illustrate the material parameters utilized to simulate the photovoltaic cell presented in the chapter. In a solar cell, the photovoltaic process begins immediately when the cell is illuminated by Air Mass 1.5. In general, the Air Mass 1.5 spectrum is used in optical propagation models to compute the photovoltaic cell performance, as it represents the practical and real spectral conditions present outdoor under the sunlight.

Table 4.1. Material parameters used for simulation of photovoltaic cell. [358-361]

Material parameter (units)	Default values
Mobility of holes (cm^2/V. s)	1×10^{-4}
Mobility of electrons (cm^2/V. s)	5×10^{-3}
Diffusion length of exciton [Acceptor material] (nm)	5
Diffusion length of exciton [Donor material] (nm)	20
LUMO [Acceptor material] (eV)	3.7
LUMO [Donor material] (eV)	3
HOMO [Acceptor material] (eV)	6.1
HOMO [Donor material] (eV)	4.9
Coefficient of recombination (cm^3/s)	10^{-9}
LUMO density of states (/cm^3)	10^{21}
HOMO density of states (/cm^3)	10^{21}
Anode's Work function (eV)	4.7
Cathode's Work function (eV)	3.9

The investigation of the internal device physics provides a crucial understanding of internal mechanism of organic photovoltaic cells [362, 363]. It allows us to view the concentration of electrons and holes inside the device layers using the drift-diffusion model of the photovoltaic cell. Further, internal device physics can observe the carrier concentrations flux, internal electrical filed and can provide an exclusive insight into the system performance. The internal device physics similarly aid in estimating the optimal circumstances for enhancing device performance [364]. Therefore, the internal device physics provide a comprehensive account of the operation of the photovoltaic cell.

The properties of a solar cell can be determined by material parameters and electrical nature of the contacts with electrodes [365]. The conventional physics of a p-n junction is thoroughly understood. However, the science of organic solar cells is still in a relatively early stage and continues to be an area of active investigation. The present and following sections of this chapter, seek to explore and understand the science of bilayer organic cell.

The current voltage plot is a fundamental tool utilized to evaluate the performance of photovoltaic cells. In general, the bilayer organic solar cells exhibit lower power conversion efficiency. The electron mobility within the layers performs an important role in defining

characteristics of current voltage plot. The transit time of carriers also has crucial impact on the overall device performance.

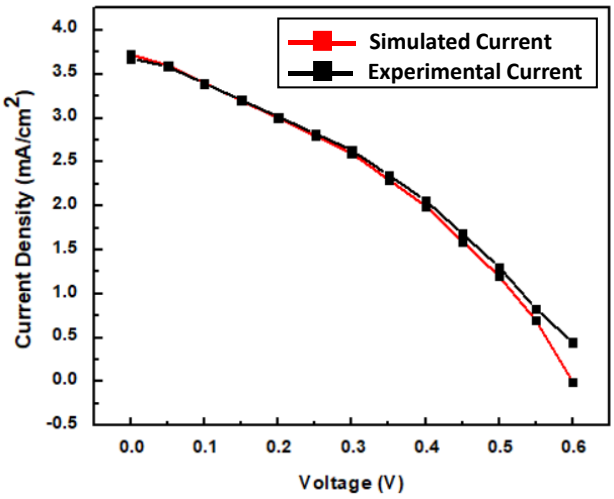

Fig. 4.2 Current density plots of P3HT/PCBM bilayer photovoltaic cell: experimental and simulated.

The Fig. 4.2 represents experimental data obtained from current-voltage measurement performed on P3HT: PCBM bilayer solar cell [366]. In the presented plot, the current density is represented as a function of the applied voltage. The simulated open circuit voltage value of 0.63 volt and current density of 3.38 mA/cm^2 aligns to the experimentally obtained open circuit value of 0.60 volt and current density of 3.72 mA/cm^2, for an acceptor thickness of 15 nm. Additionally, the plot in Fig. 4.2 also presents the comparison between simulated current and experimental current. From the plot it is evident that the experimental and simulated current align closely for the entire range of applied voltage. Further, the Table 4.2 presents the experimentally obtained parameters and corresponding parameter values extracted from the simulation. It is observed that the open circuit voltage and short circuit current density are in close agreement with a slight deviation of 9.1% and 5% respectively. Similarly, the simulation values for Fill Factor and efficiency are also in strong close agreement, with values being 37% and 0.78% respectively.

Table 4.2. Extracted parameters for photovoltaic bilayer cell and comparison with reported experimental cell [365]

Device	Open circuit voltage (V)	Short circuit current density (mA/cm^2)	Fill Factor (%)	Efficiency (%)
Experimental Cell	0.60	3.72	35	0.78
Simulated Cell	0.63	3.38	37	0.78

The performance parameters of the organic bilayer solar cell strongly depend on the choice of organic material layers. The maximum current density of 3.28 mA/cm^2 is achieved at 0 Volt. The current voltage plot follows the general current voltage pattern observed in photovoltaic cell. The plot represents the current generated by solar cell normalized by the area of the cell's photoactive layer. Thus, the strong agreement between the simulated and experimental current provides us with the opportunity to further investigate and analyse the device behaviour in order to gain a better understanding of the science behind organic bilayer solar cells.

4.3 INTERNAL DEVICE ANALYSIS

In the present section, the solar cell is internally analysed in-depth through vertical cut-line. This internal analysis is significant for exploreing and understanding the complexity of the device physics of the OSC [364]. The internal analysis represented in present section validates that distribution of electric field, photo-generated excitons, potential are concentrated at the donor and acceptor interface and has significant impact on transport of carriers and their collection [365-367]. The internal analysis also provides information about the carrier occupency and concentration in solar cell's respective layers.

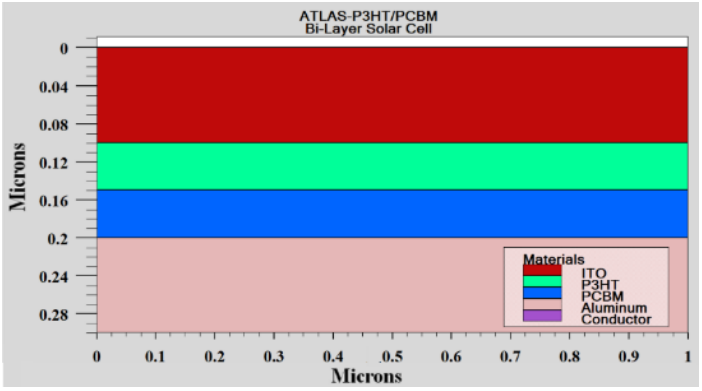

Fig. 4.3 P3HT-PCBM bilayer solar cell simulated device architecture.

The device structure of the P3HT: PCBM bilayer photovoltaic cell is illustrated in Fig. 4.3, showing the simulated structure and the individual layers comprising of different materials. The organic bilayer photovoltaic cell consists of a donor material, an acceptor material, and two electrodes: the anode and the cathode. The Indium Tin Oxide (ITO) is commonly used transparent front electrode for organic photovoltaic device. The PCBM, with its high hole mobility, serves as the electron acceptor in various organic photovoltaic cells, while P3HT acts

as the electron donor. Aluminium is utilized as the non-transparent back contact in the device structure.

The acceptor material in the bilayer photovoltaic cell is responsible for electron transport, while the donor material facilitates hole transport. The free charge carriers densities are highest at the donor-acceptor interface and gradually diminisihes in the direction of their respective electrodes. The cathode is positioned at the bottom of the device structure, while the anode is placed at the top. The device is illuminated with the Air Mass 1.5 (100 mW/cm^2) spectrum. Further, from Figs 4.4 (a) and 4.4 (c) representing internal device physics of the device through a vertical cut-line analysis, it can be observed that holes are predominantly confined to the acceptor layers and electrons are confined to the donor layer.

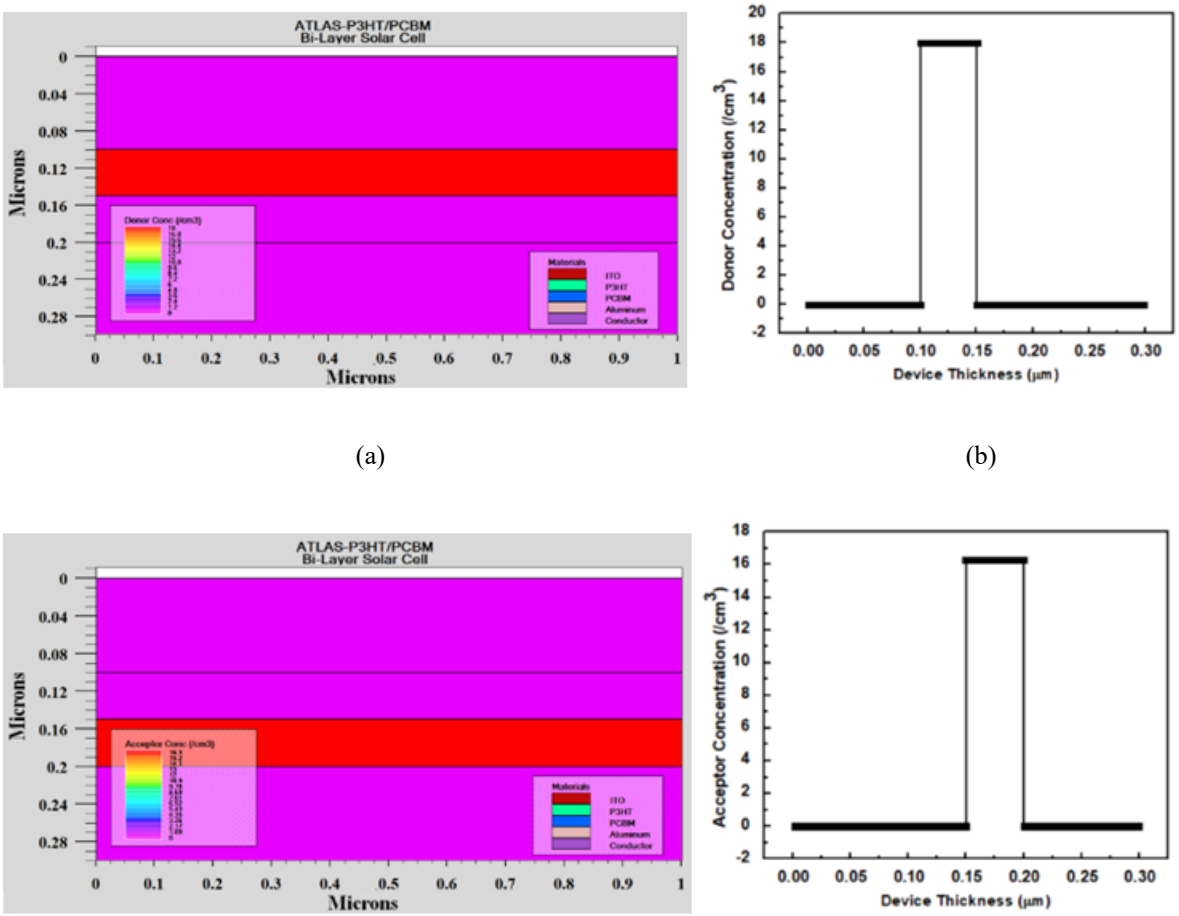

Fig. 4.4 (a) Device structure depicting electrons concentration in donor layer, (b) Donor concentration verses device thickness, (c) Device structure depicting hole concentration in acceptor layer and (d) Acceptor concentration verses device thickness.

The concentrations are graphed in Figs. 4.4 (b) and 4.4 (d) for clarity, indicating the magnitude of the respective concentration. The donor (electron) concentraton remain zero everywhere except for a constant maximum between 0.10 µm to 0.15 µm, which corresponds to the entire thickness of donor material layer, P3HT. Similarly, the acceptor (hole) concentration exhibits a contant maxium between 0.15 µm to 0.20 µm, representing the entire thickness of acceptor material layer, PCBM. The acceptor concentration is zero elsewhere in the device. These findings validate that the P3HT (donor) layer function as an electron donating layer, while the PCBM (acceptor) layer acts as an electron accepting layer. Furthermore, the electron concentrations and hole concentrations are primarily concentrated and confined to the accptor and donor materials.

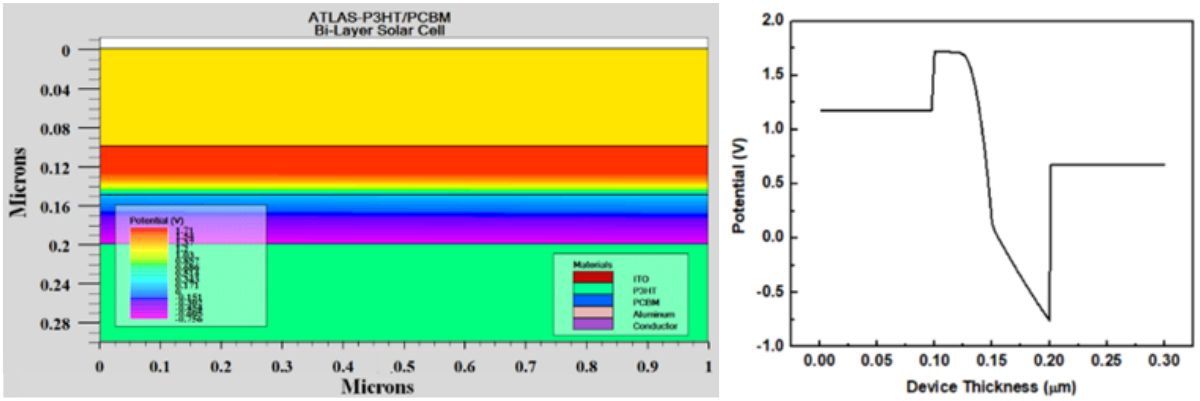

(a) (b)

Fig. 4.5 (a) Device structure depicting internal potential variation in P3HT/PCBM bilayer solar cell and (b) Potential as funciton of device thickness.

The variation in the internal potential of each individual layer is depicted in Figs. 4.5 (a) and 4.5 (b). It is evident that the maximum potential of 1.71 volts, as shown in Fig. 4.5 (a), is generated between the donor and acceptor layers, specifically in the vicinity of the donor-acceptor layer junction. The peak potential is observed at the beginning of the donor layer at 0.10 µm, while a vally is observed at 0.20 µm towards the end of the acceptor layer. Thus, indicating that the potential developed depends on the material layers and their interfaces with the electrodes. The developed potential of 1.71 volts is close to the 1.8 volts, suggesting that the longest absorbed wavelength in the device could be approximatly 650 nm [368].

As a result, the photovoltaic cell is capable of absorbing the ultraviolet portion of the light spectrum, and there is an increased absorption in the near infrared region as well. Consequently, the organic cell can also work in dark efficiently utilizing the UV energy. In Fig. 4.5 (b), a

distinct peak is observed approximately at 0.10 µm, where the potential achieves a magnitude of 1.71 volts. Afterwords, the potential rapidly decreases towards -1.0 volt. Indicating that the majority of the free charge carrier remain confined to the donor layer as represented in Fig. 4.5 (b). Further, the potential remains constant for the anode (ITO) and cathode (Aluminim) layers, as depicted in the plot.

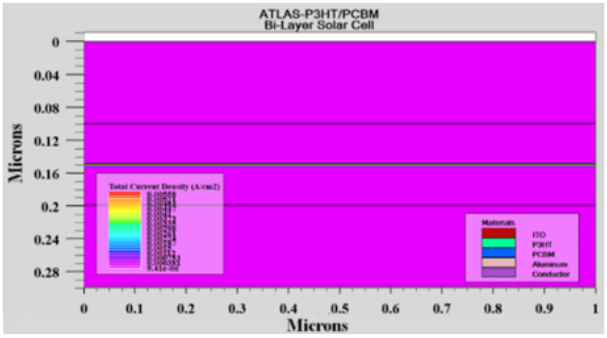

(a)

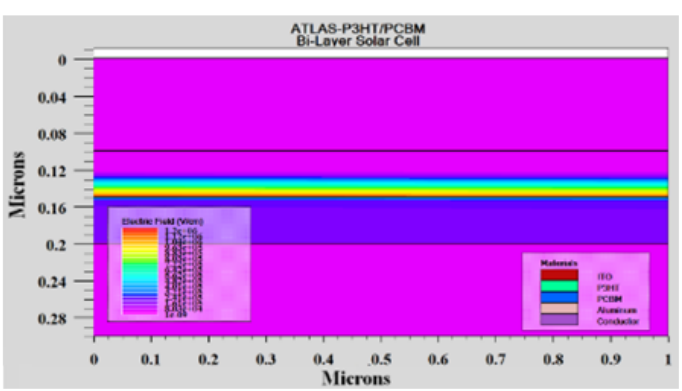

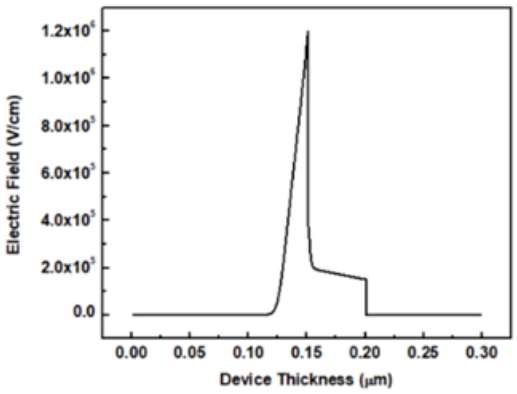

(b) (c)

Fig. 4.6 (a) Device architecture representing layer-wise distribution of total current density in an P3HT/PCBM bilayer solar cell, (b) Device structure depicting electric field variation in P3HT/PCBM bilayer solar cell and (c) Electrical field as a function of device thickness.

The donor-acceptor interface plays a critical role in the performance of the device. The electrons and holes are produced exclusively at interface. The internal device analysis reveals that the total photocurrent in the bilayer solar cell is primarily concentrated at the donor-acceptor interface. This finding demonstrates that the mechanism for photocurrent generation in organic thin photovoltaic devices is attributed to the creation of excitons resulting from light absorption in the active portions of the device, as represented by Fig. 4.6 (a). The excitons, diffuse towards the donor-acceptor interface and then local variation in electron affinity and ionization potential dissociate the excitons, separating the bound pair into free charge carriers.

Therefore, the sites of exciton dissociation are the primary points for the determination of bilayer device's efficiency. This is because the photocurrent is exclusively supplied by excitons that are able to reach and dissociate at these sites.

In Fig. 4.6 (b), it can be observed that an internal electrical field exists in the vicinity of the junctions in the device, and its magnitude is maximum there due to the thermal equlibrium of the materials in contact. Whenever two dissimilar materials possesing different work functions are brought into contact, electrons move from lesser workfunction material to the higher workfunction material until the Fermi level aligns. This process creates the internal electrical field in vicinity of the contact surfaces. This built in electric field is sufficiently high enough ($\sim 10^6$ V/cm) to facilitate the generation of the charge carriers [369]. The number of excitons generated in the device are directly influenced on the electric fields distribution which has a direct effect on the photocurrent produced by the solar cell.

The free charges (electrons and holes) are transported by internal electrical field in the direction of their respective electrodes, resulting in the generation of electric current. The Fig. 4.6 (c) is represented to illustrate the variation in the magnitude of the electric filed across the device thickness. The electric field rapidly increases and reaches its maximum value of 1.2×10^6 (V/cm) at a device thickness of 0.15 μm, precisely at the donor-acceptor interface. Subsequently, the electric field diminishes rapidly. This observation further validates the critical importance of the donor acceptor interface for the performance of the organic photovoltaic cell. Figs. 4.7 (a) to 4.7 (d) depicts the distribution of charge carriers and their respective current densities, specifically electrons and holes. It is evident from Figs. 4.7 (a) and 4.7 (b) that the concentration of holes and electrons are inversely related to each other. The donor layer exhibits a higher concentration of electrons, while the acceptor layer demonstrates a higher concentration of holes.

In Fig. 4.7 (b), the current density of electrons as a function of device thickness is presented. The electron concentration reaches its optimum at 0.10 μm, indicating that electrons are primarily concentrated in the donor layer. At the junction of the donor and acceptor layers (0.15 μm), there is a peak in electron concentration, suggesting the dominance of electrons over holes at the junction. The electron concentration gradually decreases towards the 0.20 μm.

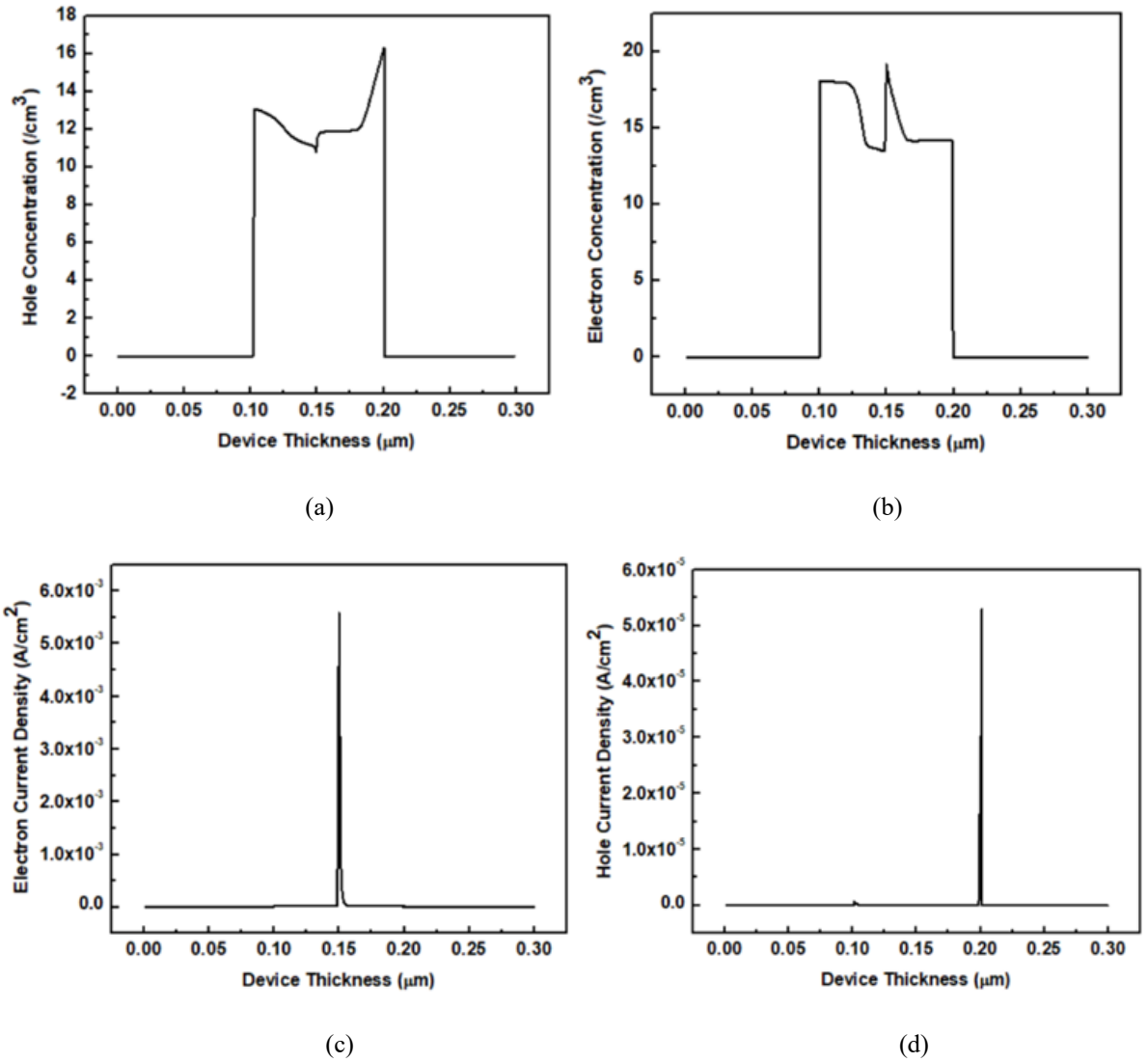

Fig. 4.7 (a) Concentration of hole, (b) Concentration of electron, (c) Current density of electrons and (d) Current density of holes verses device thickness for P3HT/PCBM bilayer photovoltaic cell.

On the other hand, the hole concentration increases from 0.10 µm towards 0.20 µm, with the maximum concentration observed at 0.20 µm, highlighting that holes are primarily concentrated in the acceptor layer. Similarly, in Fig. 4.7 (c), the corresponding electron current density has a peak value of 5.6×10^{-3} A/cm^2 at 0.15 µm, confirming that electron current is predominantly concentrated in the donor layer and zero elsewhere inside the device. In similar manner, in Fig. 4.7 (d) the current density of hole has a peak value of 5.3×10^{-5} A/cm^2 at 0.20 µm, consistently validating that hole current is primarily concentrated in the acceptor layer.

4.4 EFFECT OF P3HT (DONOR) THICKNESS ON CELL PERFORMANCE

All the charge carriers in a bilayer photovoltaic cell are produced within a few nanometers of donor-acceptor interface. This limited region of carrier generation restricts the ability to vary the thickness of individual layers while keeping the interface properties constant. However, it allows for the investigation of how the transition time of each charge carrier affects the photovoltaic cell performance. In this section, the characteristics of donor layer are studied and operational characteristics of bilayer photovoltaic cell as a function of donor layer thickness are examined.

Fill Factor is the performance parameter, it indicates the quality of photovoltaic cell, closer the value of Fill Factor to 1 extra power could be supplied by the photovoltaic cell, making it more efficient solar cell. Fill Factor is deduced by the proportion of photo-generated carriers truly reaching their respective electrodes, contributing to current and voltage output of the cell.

Here, the magnitude of Fill Factor ranges from 34.5% to 29.6% as the donor layer thickness is raised from 10 to 70 nm, which are in appropriate agreement with the conventional trend. The maximum value of Fill Factor is observed to be 37.8% at a donor thickness of 20 nm. As, organic materials have poor mobilities, increased donor layer thickness results in increased recombination of carriers, leading to a decline in the magnitude of the *FF*. However, the Fill Factor magnitude increases as the thickness is increased due to a greater amount of light being absorbed, which generates more electron hole pairs. This contributes to rise in *FF*.

Fill Factor is plotted as a function of the device thickness as illustrated in Fig. 4.8 (a). The plot demonstrates a higher value of fill factor at a donor thickness of 20 nm, while keeping the thickness of other layers constant. The Fill Factor values increase from 34.5% at device thickness of 10 nm to 37.8% at a device thickness of 20 nm. However, as the thickness of device continues to increase beyond 20 nm, Fill Factor diminishes. The device with 20 nm thickness has the highest Fill Factor because transition time of charge carriers is optimally balanced, and there is maximum photon harvesting.

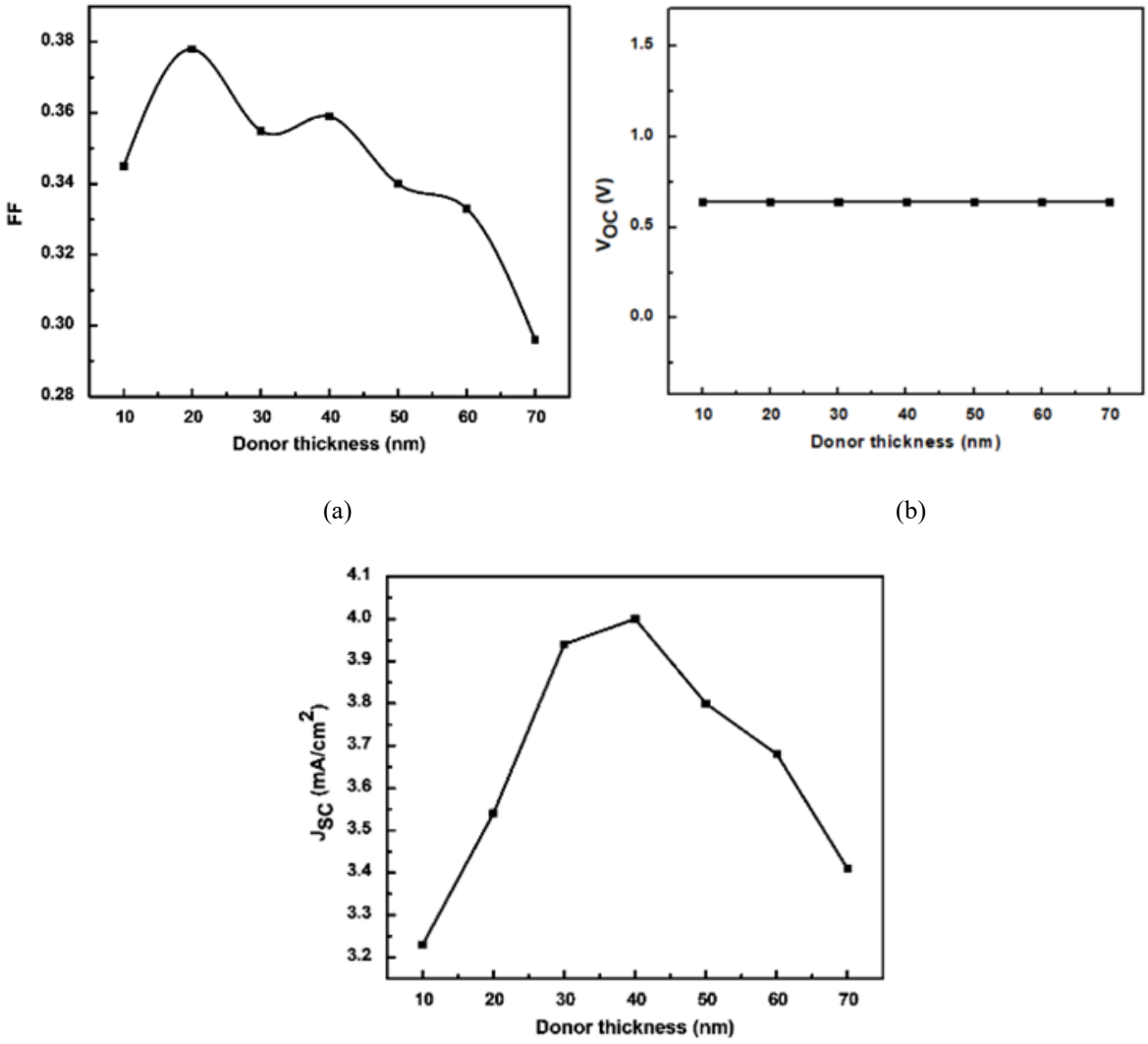

Fig. 4.8 (a) Fill Factor, (b) Open circuit voltage and (c) Short circuit current density verses donor thickness.

On the other hand, the drastic reduction in Fill Factor with an increase in thickness strongly indicates inefficient transport and collection of charge carriers. In summary, the plot illustrates that there is an optimal thickness for the donor layer that results in the highest Fill Factor. Deviating from this optimal thickness leads to decreased fill factor, indicating inefficiencies in charge transport and collection.

The imbalance in charge transport, where free charge carriers travel longer distances before getting collected at the respective electrodes, combined with the difference in mobility between holes and electrons, increases the recombination probability during their transport, resulting in decreased Fill Factor of the photovoltaic device. Moreover, increasing the thickness aggravates the condition, resulting in a substantial lowering of the Fill Factor in device with thickness 70

nm. This observation justifies the dependency of a solar cell's Fill Factor on the thickness of donor layer. As the thickness increases the recombination rate also increases, negatively impacting the fill factor.

The characteristic plot of open circuit voltage as a function of thickness of donor layer is presented in Fig. 4.8 (b). The V_{OC} is maximum magnitude of voltage generated by photovoltaic device when unconnected to external load. It remains constant at a magnitude of 0.64 volt as donor layer thickness is varied from 10 to 70 nm. In inorganic PV cells, V_{OC} is reliant on the lifetime of minority carriers present on both side of the junction, the recombination rate, and the Fermi splitting. A higher Fermi splitting leads to a rise in the value of the V_{OC}.

In organic bilayer devices, the open circuit voltage demonstrates a robust dependency on inherent characteristics and quality of the organic-organic interface. It is regulated by the energetic association amid donor and acceptor and is conventionally independent of the electrode materials, specifically the anode and cathode work functions. In particular, difference in energy between donor's HOMO and acceptor's LUMO closely present the value of V_{OC} [370, 371]. In conclusion, V_{OC} remains a function of energy levels of materials, interfaces, and contacts.

The J_{SC} is the quantity of carriers generated in a photovoltaic cell, and it depends on the generation and separation efficiency of excitons, as well as the amount of carriers collected at the respective electrodes. The I_{SC} is indeed influenced by mobility of free carriers. Organic semiconductors are materials with poor mobilities ($\approx 10^{-5}$ $cm^2/V.\ s$) which consequently restricts the active layer thickness in OSC, since after a fixed thickness free carriers would not get collected at respective electrodes. Hence, small band gap and high mobility materials are utilized for improving the I_{SC}. The J_{SC} in photovoltaic cell is well-defined at a 0-volt potential. It is prevalent to denote the short-circuit current density in mA/cm^2 instead of short circuit current in mA to calculate current produced per unit area. Short circuit current density magnitude depends on multiple factors, including the cell's area, incident light's spectrum, optical properties and the cell's collection probability.

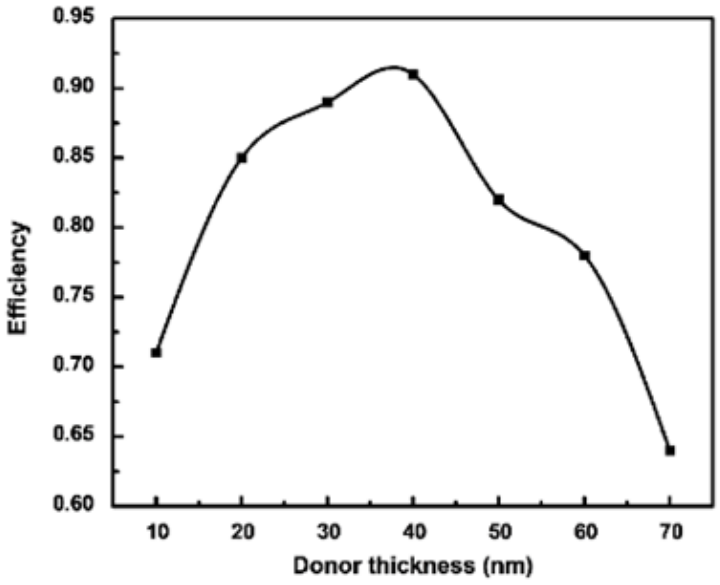

Fig. 4.9 Efficiency as a function of donor thickness for bilayer soler cell.

The Fig. 4.8 (c) represents plot of J_{SC} as a function of donor layer thickness. The plot demonstrates the shooting up of short circuit current density at a donor thickness of 40 nm, reaching a value of 4.0 mA/cm^2 compared to 3.23 mA/cm^2 at 10 nm. Subsequently, the short circuit current density exhibits a diminishing trend. The exponential rise in current density at 40 nm is attributed to the additional carrier produced, high carrier mobility, balanced transit time of the carriers and due to reduced amount of recombination. Though, as expected the thicker donor layer (from 41 nm to 70 nm) does produce a greater number of carriers but due to increased thickness the amount of recombination is also increased. As a result, the total quantity of free carriers available for collection at the respective electrodes is reduced, leading to a decline in the J_{SC}.

Efficiency is a performance parameter utilized to compare different photovoltaic cell's performance. The efficiency reflects performance of photovoltaic device and is expressed as ratio of energy produced by photovoltaic cell to energy input from the solar irradiance. As, it is observed from the plot shown in Fig. 4.9 that the V_{OC} is almost constant for entire device thickness, the power conversion efficiencies of the device are primarily determined by product of *FF* and J_{SC}. Hence, efficiency of thicker photovoltaic cell decreases because of the significant decrease in fill factor value. This decrease in efficiency can be explained and is potentially attributed to the higher thickness of P3HT layer, as the layer becomes larger than the effective diffusion length of an exciton.

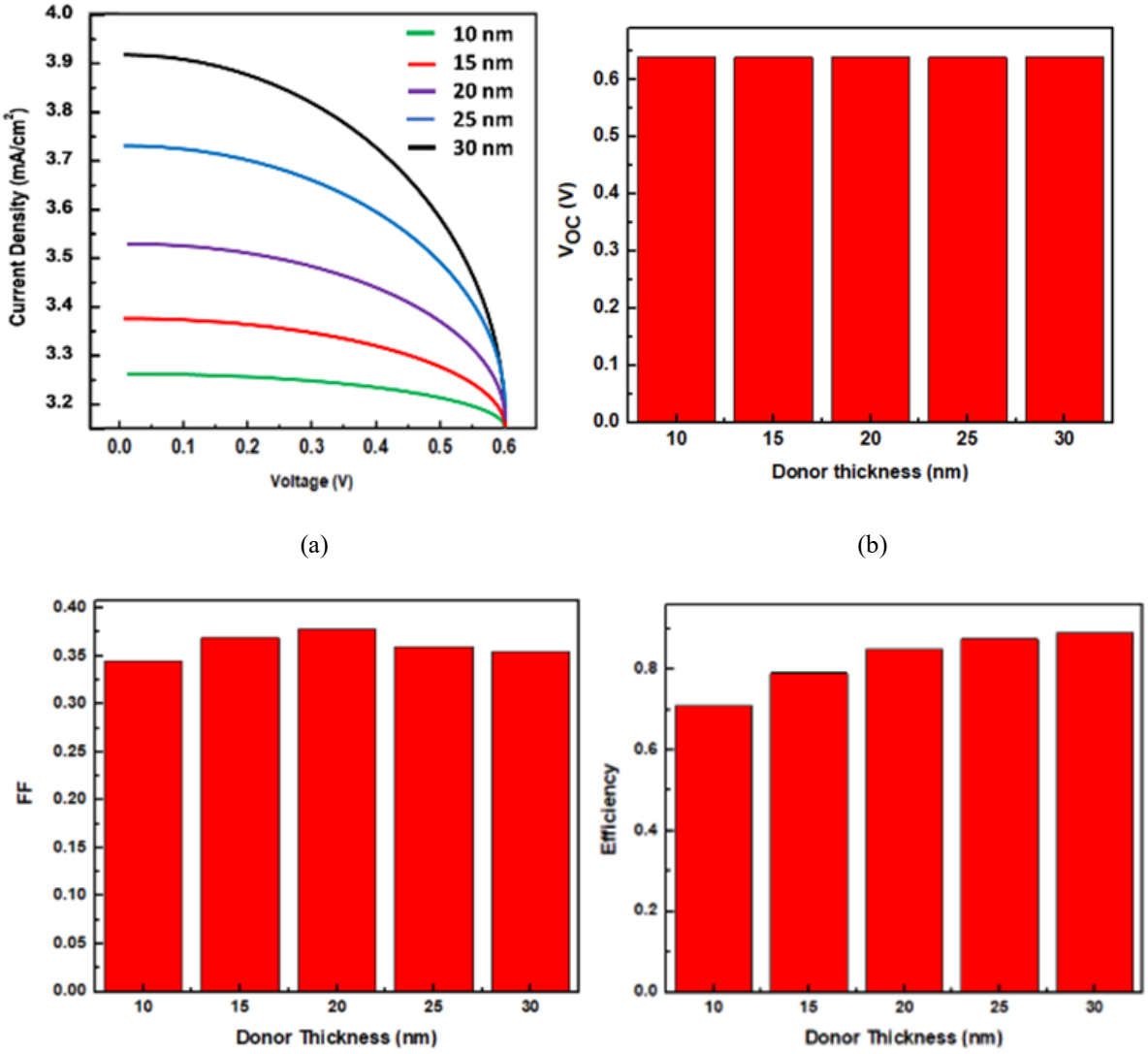

Fig. 4.10 (a) Current Voltage characteristic for multiple donor thickness from 10 to 30 nm, (b) Open Circuit Voltage, (c) Fill Factor and (d) Efficiency as a function of thickness (10 – 30 nm).

Therefore, limiting the exciton harvesting and consequently resulting in lower efficiency. In Fig. 4.10 (a), the I-V characteristic curves for various donor thickness are illustrated, with the J_{SC} being maximum at donor thickness of 30 nm. Further, the V_{OC} is observed to be constant for 10 to 30 nm range in the Fig. 4.10 (b). Additionally, Figs. 4.10 (c) and 4.10 (d) presents the fill factor and efficiency, respectively, within the 10 to 30 nm donor thickness range. The highest value of current density is observed at a donor thickness of 40 nm, which justifies the optimal donor thickness (P3HT) to be 40 nm, to achieve higher efficiency. Therefore, these results suggest that there is an optimal thickness for the donor layer in order to maximize overall efficiency of photovoltaic device.

4.5 EFFECT OF PCBM (ACCEPTOR) THICKNESS ON CELL PERFORMANCE

In this section, the characteristics of acceptor layer are studied, and the performance parameters of the photovoltaic cell are measured as a function of acceptor thickness. Increasing thickness of acceptor, it is expected that short circuit current density will improve due to more absorption and exciton generation. However, the plot in Fig. 4.11 (a) shows an increasing trend in short circuit current density until a thickness of 50 nm reached, achieving a maximum current density of 3.80 mA/cm^2 at 50 nm thickness. This significantly indicates a faster charge transfer rate, better balanced transit time, and higher exciton separation rate. Beyond 50 nm thickness, the J_{SC} exhibits a diminishing trend.

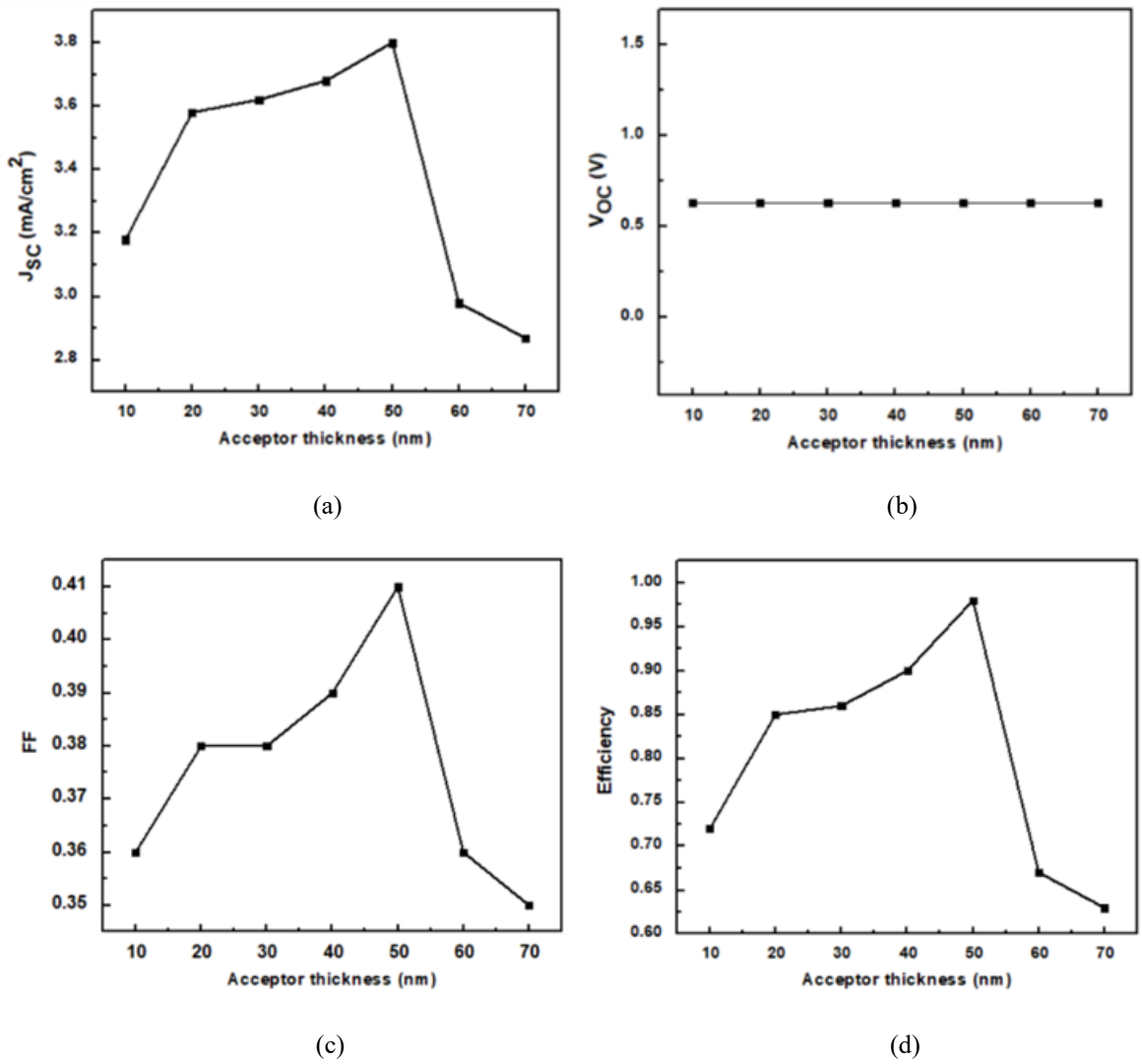

Fig. 4.11 (a) Short circuit current density, (b) Open circuit voltage, (c) Fill Factor and (d) Efficiency as a function of acceptor thickness.

This unexpected decrease in short circuit current density after 50 nm thickness is due to the poor carrier mobilities of organic semiconductors and high carrier recombination occurring in the acceptor layer, leading to lesser charge collection at the electrode. The Fig. 4.11 (b), presents the plot of open circuit voltage as a function of acceptor layer thickness variation. The V_{OC} is observed to be constant at a value of 0.63 volt, which is very close to the value of 0.64 volt reported for the donor layer thickness variation. Thus, presenting a close agreement in value of open circuit voltage.

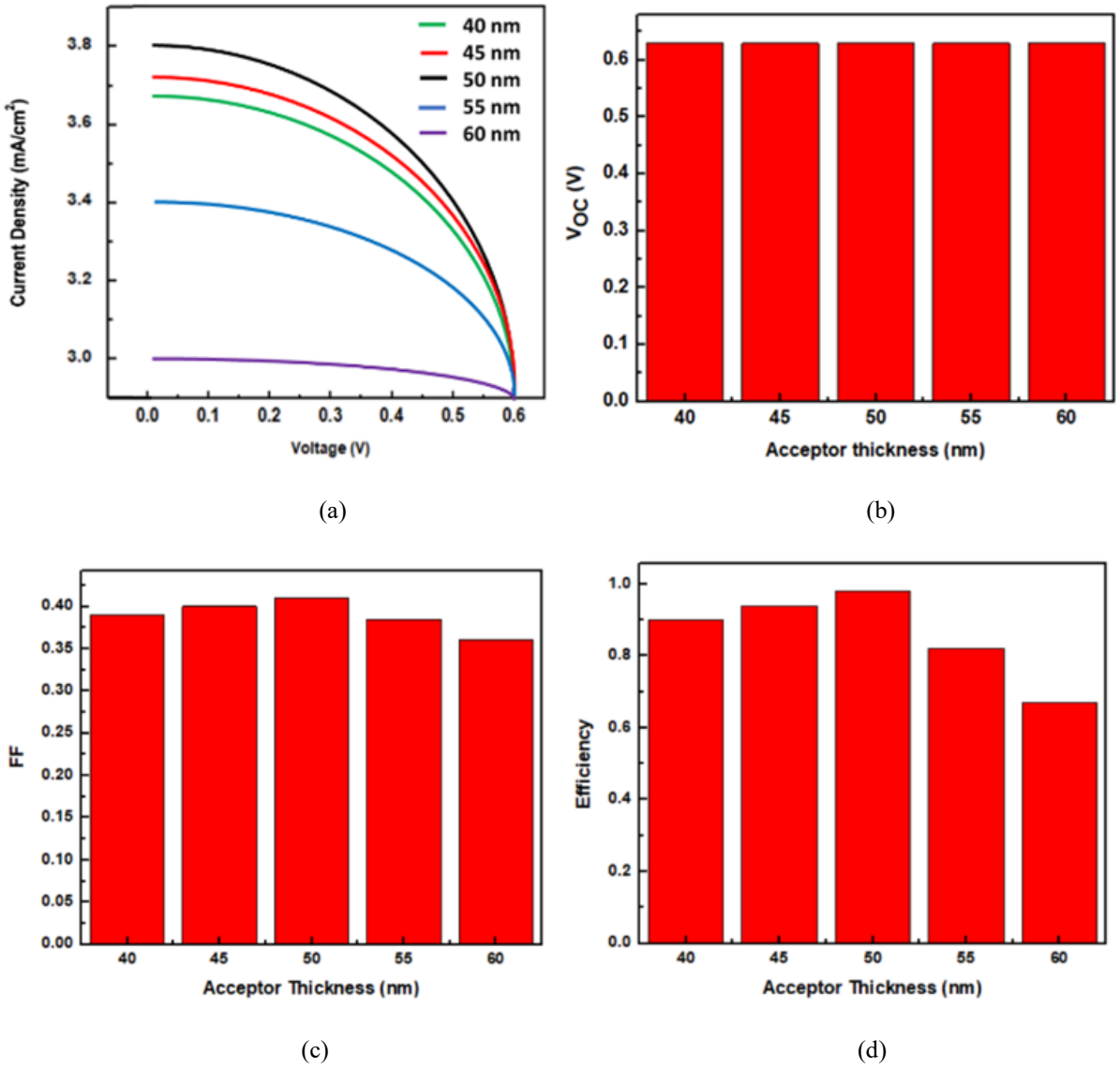

Fig. 4.12 (a) Current Voltage characteristic for multiple acceptor thickness from 40 to 60 nm, (b) Open Circuit Voltage, (c) Fill Factor and (d) Efficiency as a function of thickness (40 – 60 nm).

The magnitude of Fill Factor, as represented in Fig. 4.11 (c), increases with increasing thickness until 50 nm, attaining a maximum value of 41%. This increase could be credited to higher quantity of carriers produced. However, beyond 50 nm, the Fill Factor diminishes to a value of

35% at 70 nm. This decrease in Fill Factor is primarily caused by low mobility and unbalanced charge transport of the electrons, leading to increased recombination and inefficient transport and collection of charges at the electrodes. As mentioned earlier, open circuit voltage remains constant for all thickness, as presented in Fig. 4.11 (b). This presents that efficiency of the photovoltaic cell is reliant on fill factor and current density. Consequently, the efficiency increases till 50 nm and then drops till 70 nm, following a trend similar to the fill factor and J_{SC} as observed in Fig. 4.11 (d) As expected, while the efficiency initially increases with increased thickness due to additional generation of carriers, it subsequently diminishes due to significant charge recombination.

In Fig. 4.12 (a), the current voltage characteristic for different acceptor thickness ranging from 40 nm to 60 nm is illustrated. From the plot, it can be observed that the J_{SC} is maximum at 50 nm. Similarly, from Fig. 4.12 (b) it is noticed that V_{OC} is constant for 40 nm to 60 nm range. Additionally, Figs. 4.12 (c) and 4.12 (d) present the fill factor and efficiency for the 40 to 60 nm range. The highest value of the current density justifies the optimum thickness for acceptor (PCBM) layer to be 50 nm.

4.6 OPTIMIZED P3HT: PCBM CELL

In the present section, a solar cell with an optimized acceptor thickness of 50 nm and optimized donor thickness of 40 nm is simulated. The sections 4 and 5 have established that bilayer solar cells are highly dependent on the interface of the donor - acceptor and thickness of the donor and acceptor layers. In section 4.4 the maximum J_{SC} is achieved at a donor thickness of 40 nm and in section 4.5 maximum short circuit current density is achieved at an acceptor thickness of 50 nm, making both the thicknesses optimum thicknesses respectively. These optimized thicknesses are now used to simulate the solar cell in order to achieve improved performance.

The Fig. 4.13 (a) presents the current-voltage plot for the optimized solar cell thickness (40 nm: donor and 50 nm: acceptor layer). Maximum current density achieved is 3.66 mA/cm^2. The V_{OC} obtained is 0.63 Volts, and an *FF* of 39 % is achieved. Additionally, the efficiency obtained for the optimized solar cell thickness is 0.90%. Further, it could be observed that the experimental cell with 15 nm acceptor thickness and donor thickness of 40 nm is reported to have an efficiency of 0.78 %. Therefore, efficiency of optimized PV cell is 15.38 % higher than that of the experimental cell, demonstrating the improvement achieved by optimizing the donor and acceptor thicknesses in the bilayer solar cell.

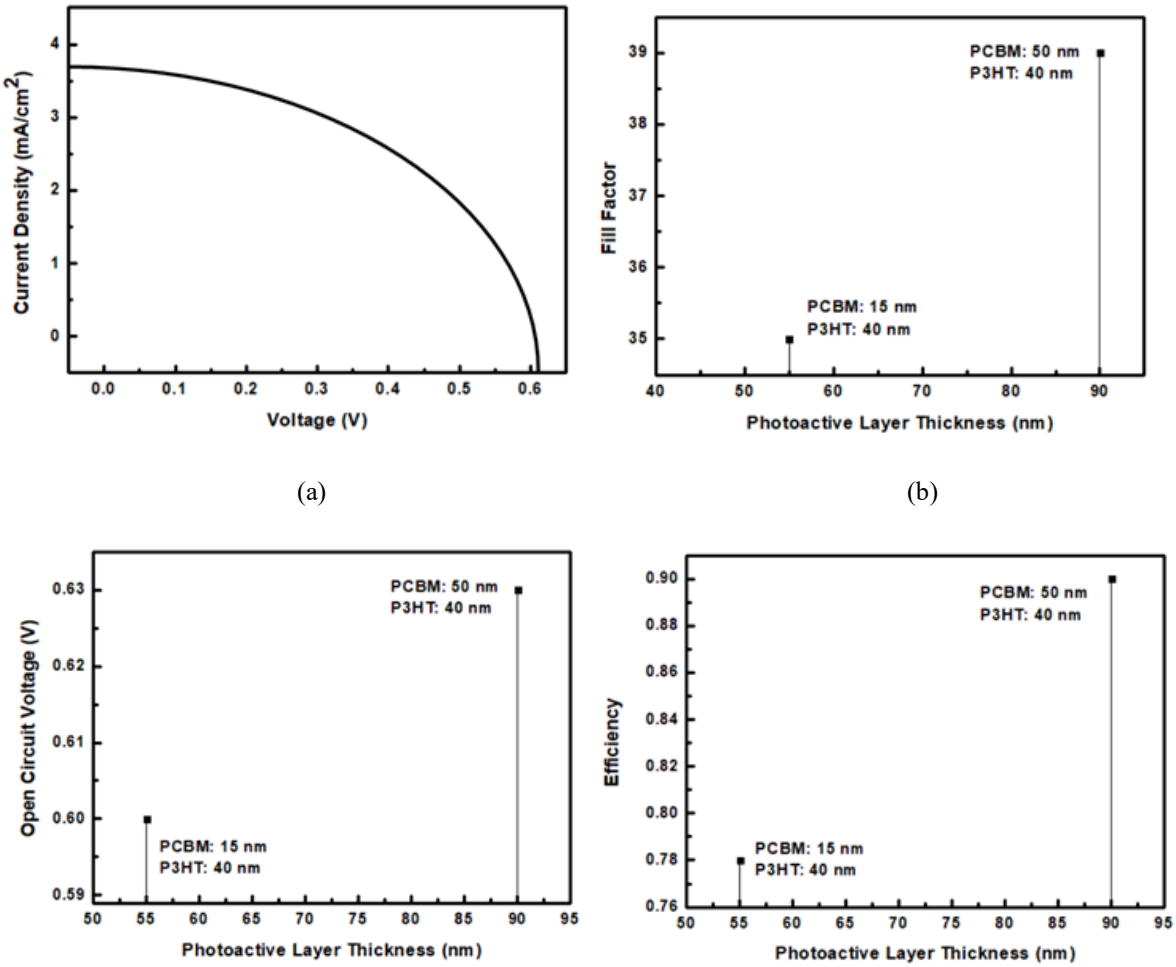

Fig. 4.13 (a) Current - Voltage curve of optimized P3HT: PCBM cell with 50 nm acceptor thickness and 40 nm donor thickness and Comparison of (b) Fill Factor, (c) Open circuit voltage and (d) Efficiency at experimental (PCBM: 15nm; P3HT: 40 nm) thickness and at optimized (PCBM: 50 nm; P3HT: 40 nm) thickness as a function of photoactive layer thickness.

The gained results confirm that the notion of increasing the photoactive layer thickness in an indiscriminate manner to achieve higher efficiency is counterintuitive. This is primarily due to increased recombination as the thickness is increased beyond a certain point, unless the carrier transit time can be effectively maintained. The Figs. 4.13 (b) to 4.13 (d), represents a comparison of different parameters between experimental and optimized thickness as a function of the photoactive layer thickness for the P3HT: PCBM cell. These plots provide a clear visualization of the improvements achieved via photoactive layer thickness optimizing in terms of these performance parameters.

Organic semiconductors have limited charge carrier transportation properties, primarily due to their low mobility which limits the photon harvesting layer's thickness in order of ~ 100 nm,

to mitigate the bimolecular recombination loss. The results obtained in the previous sections also support this observation. However, to enhance absorption of light while maintaining photoactive layer thickness to be ~ 100 nm or constant other types of light- trapping techniques are employed which are discussed in the following sections.

4.7 EFFECT OF DONOR MATERIAL

The donor materials are critical component in the development of OSCs. The donor material can affect harvesting of light and carrier transportation properties of PV cell. The present section, the donor material layer P3HT is replaced with a high performance and low bandgap polymer material called PTB7. PTB7 offers several advantages compared to P3HT, owing to its lower bandgap of 1.6 eV, which extends the absorption range for PTB7 to 550 – 750. The extended absorption range of PTB7 allows it to capture a broader range of light wavelengths, thereby enhancing light harvesting in the solar cell. Additionally, PTB7 exhibits good hole mobility, which facilitates efficient transportation of the charges within the device. Thus, all the mentioned characteristics make PTB7 a promising candidate for solar cell applications. The subsequent analysis provides the insight into the impact of using PTB7 as the donor material in enhancing the PCE of the PV cells.

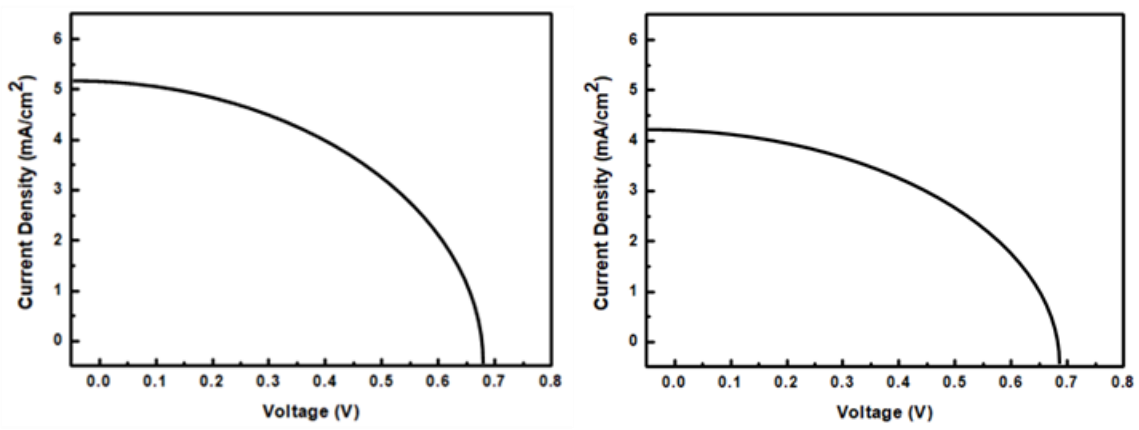

(a) (b)

Fig. 4.14 Current - Voltage curve of (a) optimized PTB7: PCBM solar cell with 50 nm acceptor and 40 nm donor thickness and (b) experimental PTB7: PCBM solar cell with 15 nm acceptor and 40 nm donor thickness.

The PTB7: PCBM solar cell, optimized donor and acceptor thickness are 40 nm and 50 nm, respectively. With this optimized thickness, the solar cell achieves a J_{SC} of 5.14 mA/cm^2, V_{OC} of 0.68 volt as represented in Fig. 4.14 (a) and an efficiency of 1.33%. The efficiency value is 47.77 % higher than the efficiency achieved with the P3HT: PCBM material (0.90 %) solar

cell. Further, when the PTB7: PCBM solar cell is simulated with 15 nm acceptor thickness and 40 nm donor thickness, thickness corresponding to experimental PV cell, the J_{SC} obtained is 4.16 mA/cm^2, as shown in Fig. 4.14 (b). The V_{OC} of 0.68 volts, and the PCE achieved is 1.16%. The efficiency value is 48.71 % higher than the efficiency achieved with P3HT: PCBM material (0.78 %).

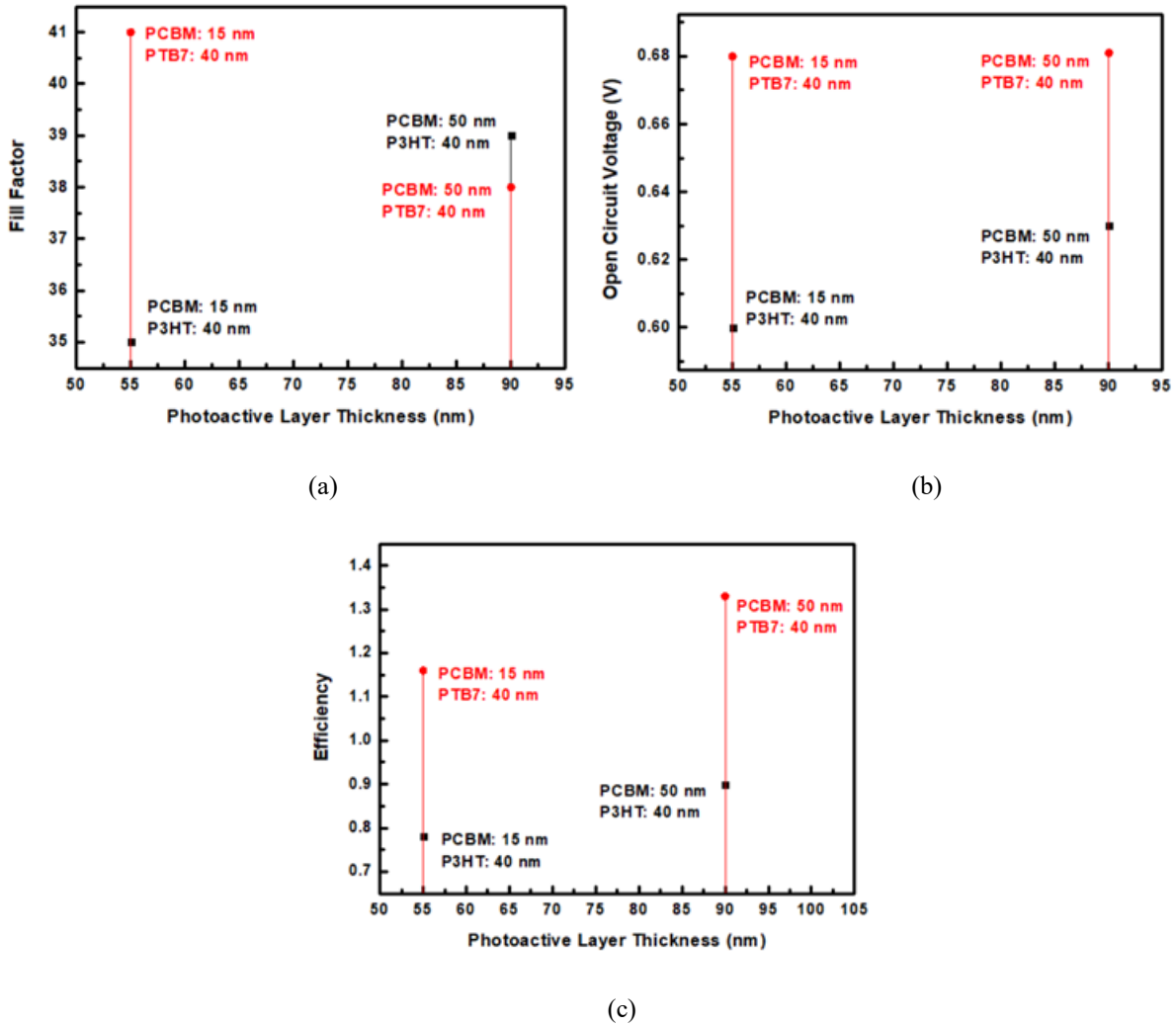

Fig. 4.15 Comparison of (a) Fill Factor, (b) Open circuit voltage and (c) Efficiency at experimental (acceptor: 15nm; donor: 40 nm) thickness and at optimized (acceptor: 50 nm; donor: 40 nm) thickness for P3HT: PCBM and PTB7: PCBM solar cell as a function of photoactive layer thickness.

The results clearly indicate that changing the donor material from P3HT to PTB7 results in a significantly improved efficiency. The PTB7: PCBM solar cell's efficiency at the optimized thickness (40 nm donor, 50 nm acceptor) is 14.65 % higher than the efficiency achieved at the experimental thickness. The Fig. 4.15 represents the comparison of different parameters at experimental and optimized thickness as a function of photoactive layer thickness for P3HT:

PCBM and PTB7: PCBM solar cell. Improved performance of PTB7: PCBM solar cell can be attributed to improved transportation of the charge carriers, lesser recombination losses, reduced space charge build-up and enhanced built-in field across the device. In summary, the improvement achieved in the efficiency by changing the donor material from P3HT to PTB7 demonstrates the crucial role of donor's chemical structure in determining performance of organic cells.

4.8 EFFECT OF HOLE TRANSPORT LAYER (HTL)

In solar cells, the photoactive layer absorbs incoming photons and generates free charge carriers. In order to attain higher efficiency, the organic solar cell should include a Hole Transport Layer (HTL) and an electron transport layer (ETL). The electron transport layer and hole transport layer are required to have apt alignment of energy levels with donor and acceptor for barrierless hole and electron extraction to anode and cathode. Additionally, the HOMO and LUMO of the transport layers should also create energy barriers to block electron and hole flow to the anode and cathode respectively. In present section, emphasis is on analysing the effect of the hole transport layer on solar cell performance. Photoactive layer of the OSC, consisting of PTB7 as donor and PCBM as acceptor, is kept fixed at a thickness of 40 nm for the donor and 50 nm for the acceptor.

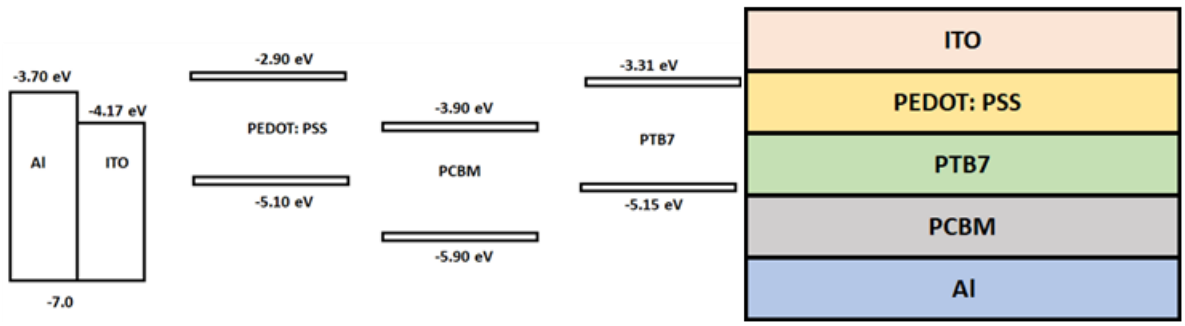

(a) (b)

Fig. 4.16 (a) Band alignment of present HTL material positioned between ITO and PTB7 layers in PTB7: PCBM organic solar cell and (b) Architecture of HTL (PEDOT: PSS) included PTB7: PCBM solar cell.

The PEDOT: PSS is used as hole transport layer material. As a HTL material PEDOT: PSS has good optical transparency, high and wide range (10^{-6} to 10^{3} S cm^{-1}) of conductivity, and is efficient transporter of holes [372]. The admirable matching between highest occupied molecular orbital level of photoactive layer and the valance band of hole transport layer forms of good ohmic contact at the interface of anode-photoactive layer, resulting in higher hole

carrier collection, reduced recombination and improved electron blocking at the interface. The Fig. 4.16 (a) presents the band alignment of OSC, illustrating the energy level positions of the different layers, including photoactive layer, HTL (PEDOT: PSS), and other components of the device.

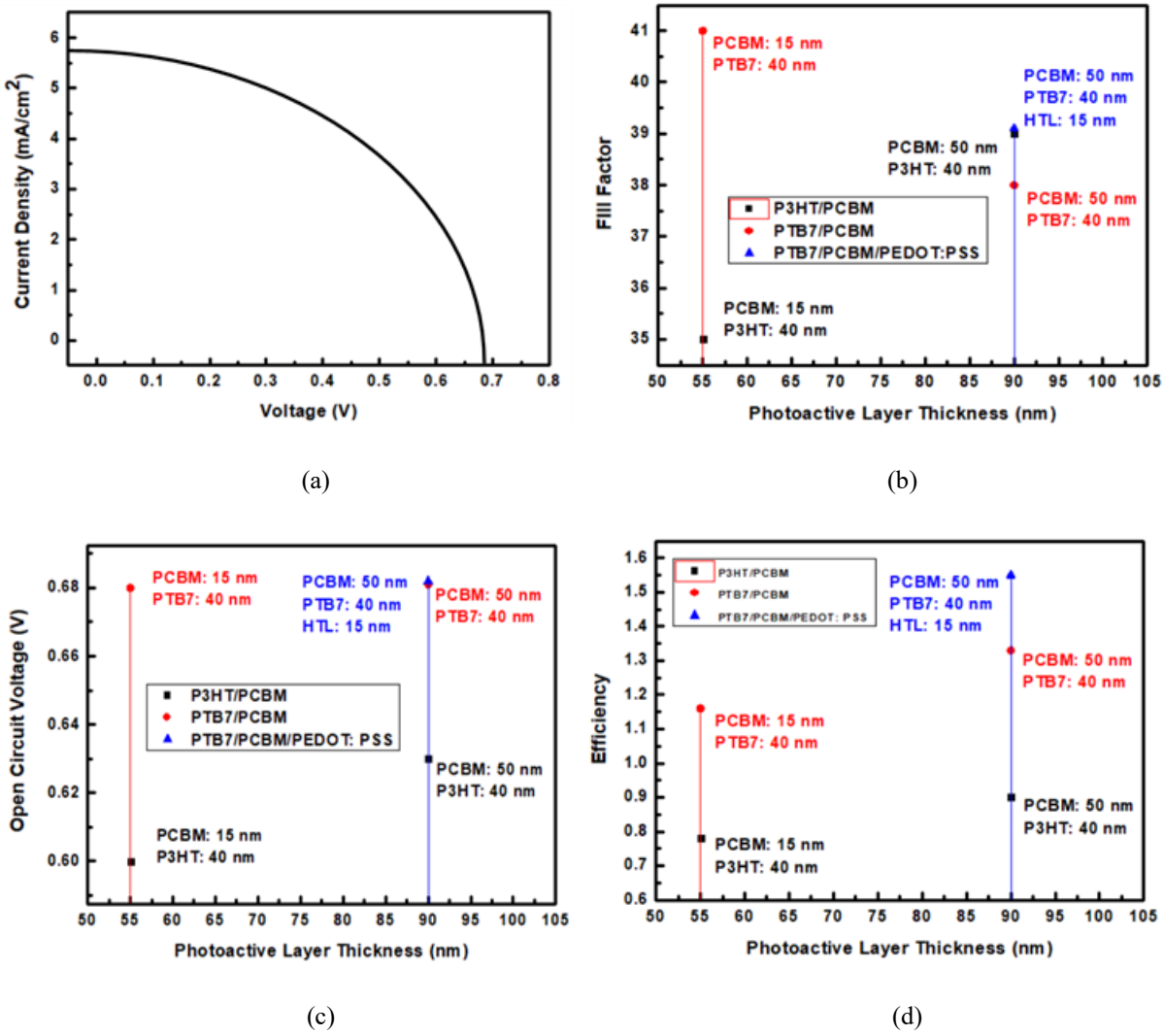

Fig. 4.17 (a) J-V characteristic curve for the HTL included PTB7: PCBM solar cell and Comparison of (b) Fill Factor, (c) Open circuit voltage and (d) Efficiency of P3HT: PCBM, PTB7: PCBM and HTL included PTB7: PCBM (optimized) solar cell at experimental and optimized thickness as a function of photoactive layer thickness.

In the present work, the performance of PTB7: PCBM solar cell with the inclusion of a hole transport layer is investigated. The hole transport layer material chosen for this analysis is PEDOT: PSS, and the considered thickness is 15 nm. The Fig. 4.16 (b) presents the layer architecture of the solar cell. A J_{SC} of 5.84 mA/cm^2, FF of 39 % and V_{OC} of 0.68 volts is achieved. The achieved efficiency for the hole transport layer included PTB7: PCBM solar cell

is 1.55 %, which is 16.54 % higher than the optimized PTB7: PCBM solar cell without the hole transport layer.

The Fig. 4.17 (a) presents the current-voltage characteristic curve for the hole transport layer included PTB7: PCBM solar cell and Figs. 4.17 (b) to (d) represent the performance parameter comparison among the optimized and experimental configurations for the P3HT: PCBM, PTB7: PCBM and HTL included PTB7: PCBM solar cells. These results highlight positive influence of incorporating the HTL on the overall performance of PTB7: PCBM solar cell, resulting in increased current density, improved fill factor, and higher efficiency.

4.9 EFFECT OF ELECTRON TRANSPORT LAYER (ETL)

In the present section, the focus is on studying the effect of the Electron Transport Layer (ETL) on the performance of the organic solar cell. The ETL serves multiple functions, including efficient electron conduction and acting as a hole blocking layer (HBL). The optimum thickness of donor and acceptor layers, determined in previous sections, is fixed at 40 nm and 50 nm respectively. The selected ETL material is Poly [(9,9-bis(3'-(N,N-dimethylamino)propyl)-2,7-fluorene)-alt-2,7-(9,9-dioctylfluorene)](PFN) with the thickness of 15 nm. The Fig. 4.18 (a) presents the layer architecture of the PTB7: PCBM solar cell with the inclusion of the ETL, and Fig. 4.18 (b) presents the band alignment diagram, illustrating the energy level alignment between the different layers.

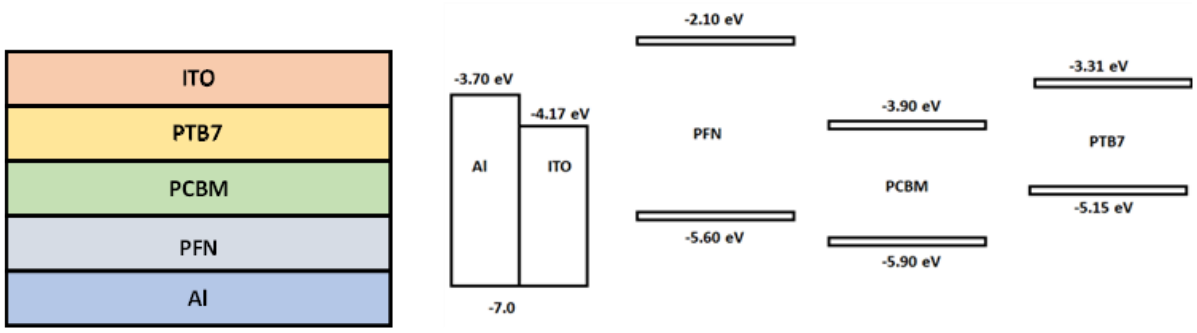

(a) (b)

Fig. 4.18 (a) Structure of ETL (PFN) included PTB7: PCBM solar cell and (b) Band alignment of present HTL material positioned between PCBM and Al in P3HT: PCBM organic solar cell.

The introduction of an Electron Transport Layer (ETL) between the photoactive layer and the cathode improves the stability of the interface. In comparison to inorganic ETLs, the use of n-type organic semiconductor material as ETL is much promising due to their tunable physical

and electrical properties resulting from their molecular design. The organic semiconductors, however, typically exhibit poor conductivity, which limits their use and results in inferior electrode electrical contacts. Therefore, to overcome this limitation, a ETL layer is introduced which improves the contact and enhances the overall device performance. The efficiency achieved for ETL included PTB7: PCBM solar cell is 1.64%, representing a 5.80 % increase from the HTL included PTB7: PCBM configuration. A Fill Factor of 40 %, open circuit voltage of 0.69 Volts and a current density of 5.94 mA/cm^2 is achieved. The Fig. 4.19 (a) presents the J-V plot of the ETL included PTB7: PCBM solar cell, illustrating the relationship between current density and voltage characteristics of the device.

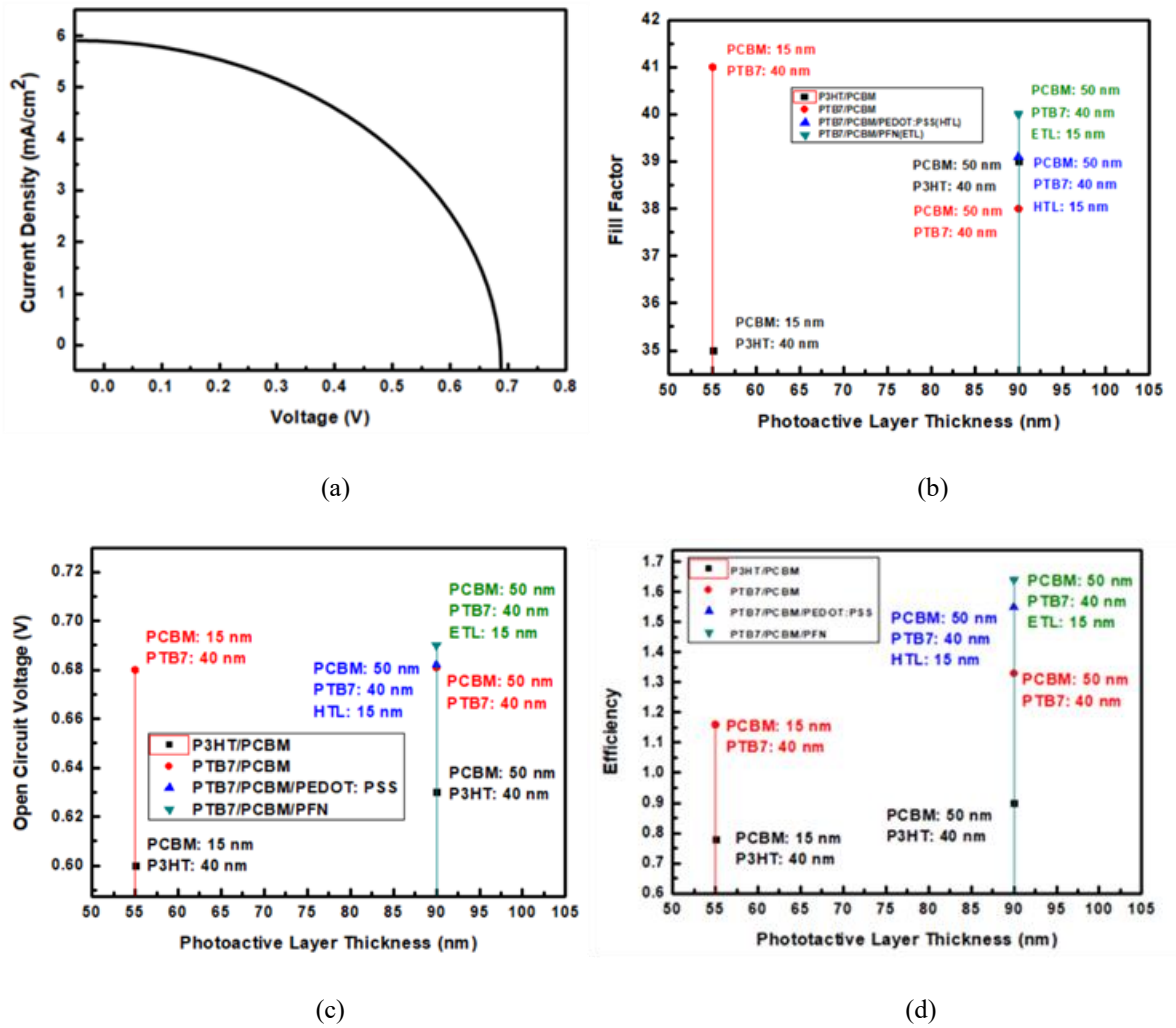

Fig. 4.19 (a) J-V plot of ETL included PTB7: PCBM solar cell and Comparison of (b) Fill Factor, (c) Open circuit voltage and (d) Efficiency at experimental and optimized thickness for P3HT: PCBM, PTB7: PCBM and ETL and HTL included optimized PTB7: PCBM solar cell as a function of photoactive layer thickness.

The Figs. 4.19 (b) to (d) presents the comparison of ETL introduced PTB7: PCBM solar with the P3HT: PCBM, PTB7: PCBM, and HTL introduced PTB7: PCBM solar cell. From the Figs.

4.19 (b) to (d) it can be observed that the organic solar cell is more sensitive to the introduction of an ETL compared to an HTL. This is because in organic solar cell the ETL is in close proximity to the cathode. Thus, facilitating better electron transport to the cathode by optimizing the light absorption within the active layer, leading to improved charge collection while providing a barrier to the flow of holes to the cathode, ultimately reducing the bimolecular recombination at the cathode. The comparison in Figs. 4.19 (b) to (d) highlights the significant impact of the ETL on the overall efficiency and performance of the PTB7: PCBM solar cell, underscoring its importance in achieving higher device performance.

4.10 ORGANIC SOLAR CELL WITH HTL AND ETL (CONVENTIONAL STRUCTURE)

The addition of suitable interfacial layers could modify the efficiency of charge extraction. The OSCs are fabricated on the basis of two types device structures which includes conventional structure and inverted structure. The conventional solar cell structure is composed of ITO/PEDOT: PSS/ PTB7/PCBM/PFN/Al. The Fig. 4.20 presents the architecture of the conventional solar cell. The PEDOT: PSS in the solar cell is functional as an HTL to improve collection of holes at anode and PFN is ETL both having thickness of 15 nm. The thickness of PTB7 and PCBM layers are 40 nm and 50 nm respectively. The structure of photoactive layer notably affects light harvesting, dissociation of exciton, transport of charge, and collection of charge in OSC.

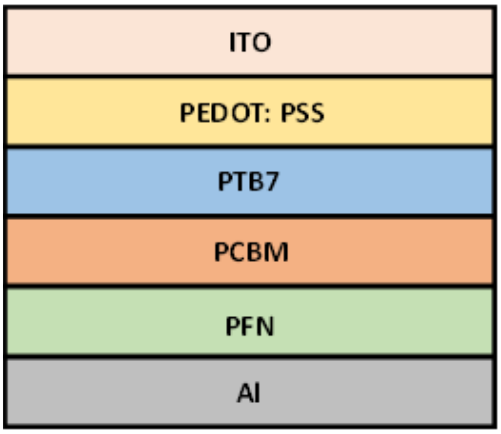

Fig. 4.20 Conventional structure of PTB7: PCBM solar cell with both HTL and ETL layers included.

The conventional OSC structure is illuminated on the transparent ITO side. The collection of electrons and holes at their respective electrode is insured by the HTL and ETL layers respectively. In the conventional approach a p-type doped conducting polymer, PEDOT: PSS

is used in general to modify the ITO so as to improve the extraction of holes from the photoactive layer, enhancing the efficiency of the hole collection at the anode. Further, to have an effective extraction of electrons, Aluminium (Al) metal with low work function is utilized as the cathode. The insertion of ETL between photoactive layer and cathode serves to improves the stability of the interface. The HTL and ETL both the layers need to have proper alignment of energy band with the acceptor and donor so that extraction of electrons and holes to anode and cathode is barrierless.

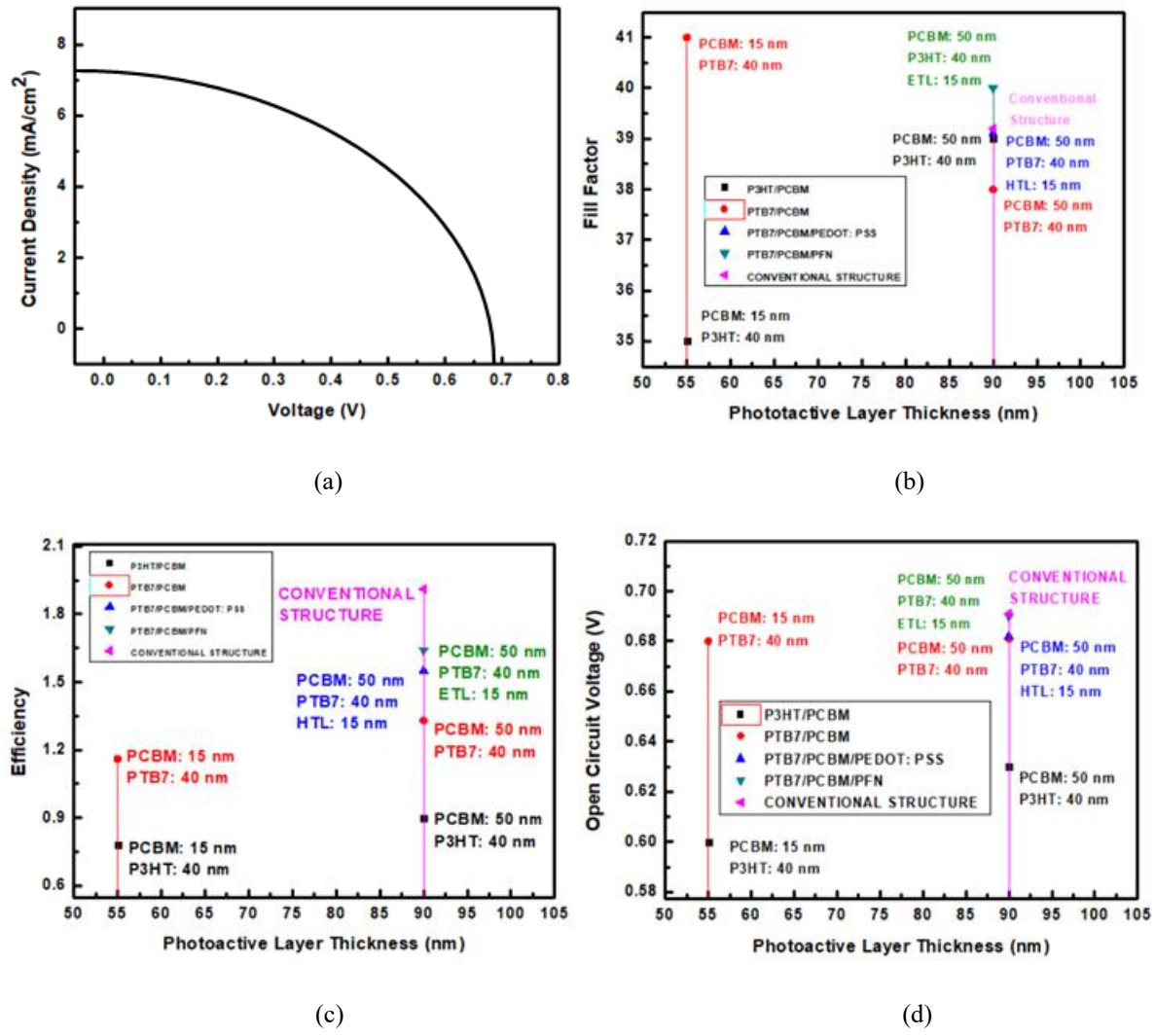

Fig. 4.21 (a) J – V characteristics for conventional PTB7: PCBM solar cell structure and comparison of different performance parameters (b) Fill Factor, (c) Open circuit voltage and (d) Efficiency at experimental and optimized thickness for P3HT: PCBM, PTB7: PCBM; HTL and ETL included optimized PTB7: PCBM solar cell with the conventional PTB7: PCBM solar cell structure as a function of photoactive layer thickness.

Further, the respective HOMO and LUMO energy levels of the hole transport layer and electron transport layer layers must offer energy barriers to block the flow of electrons and holes to the

cathode and anode, respectively. The interfacial layers with bandgaps larger than that of acceptor and donor also help in confining excitons within photoactive layer so as to increase the exciton dissociation probability and potentially also provide extra exciton dissociation interface. Fig. 4. 21 (a) presents the J-V plot of conventional solar cell structure. It achieves a short circuit current density of 7.09 mA/cm^2, fill factor of 39 % and open circuit voltage is 0.69 Volt. A efficiency of 1.91 % is achived. Further, the Figs. 4.21 (b) to (d) present the comparision of conventional structure with respect to the previously mentioned solar cell structures. From the observations it can be varified that performance of conventional structure with both the transport layers i.e., hole transport layer and electron transport layer is better compared to the previous solar cell structures.

4.11 ORGANIC SOLAR CELL WITH ETL AND HTL (INVERTED STRUCTURE)

To further enhance the performance and stability of the solar cell, the inverted structure is used with electron transport layer placed between ITO and photo-active layer for electron collection and Al metal is used as anode for collecting holes. The Fig. 4.22 presents the architecture of inverted solar cell. The PEDOT: PSS in the solar cell functions as a hole transport layer to improve collection of holes at anode and PFN is electron transport layer, both having thickness of 15 nm. The thickness of PTB7 and PCBM layers are of 40 nm and 50 nm thicknesses, respectively. The Fig. 4.23 (a) presents the current-voltage characteristic curve of the inverted solar cell, a short circuit current density of 7.93 mA/cm^2, Fill Factor of 38 % and open circuit voltage of 0.69 Volt is achieved. The achieved power conversion efficiency is 2.08 %, which is 8.90 % higher than conventional structure.

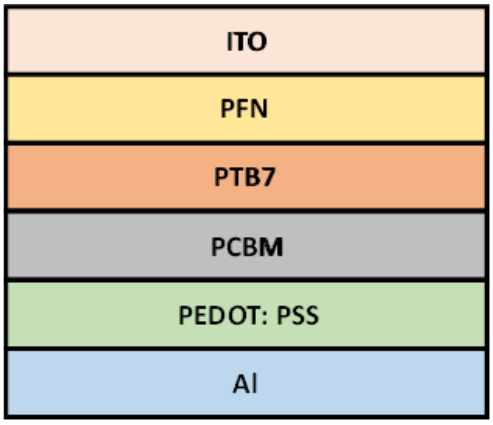

Fig. 4.22 Inverted structure of PTB7: PCBM solar cell with both HTL and ETL layers included and opposite to conventional architecture.

The inverted structure offers several advantages, including superior stability and improved compatibility. In inverted solar cells, the polarity of the device is opposite when compared to the polarity of a conventional structure. Performance of inverted solar cell is reliant upon the selection of interfacial layer and their contact properties with respect to photoactive layer and corresponding electrodes. The Figs. 4. 23 (b) to (c) present the comparison of inverted structure to the previous structures of the solar cell. As observed from the Fig. 4.23 (d), the inverted solar cell has the highest PCE when compared to any other previous structure of solar cell.

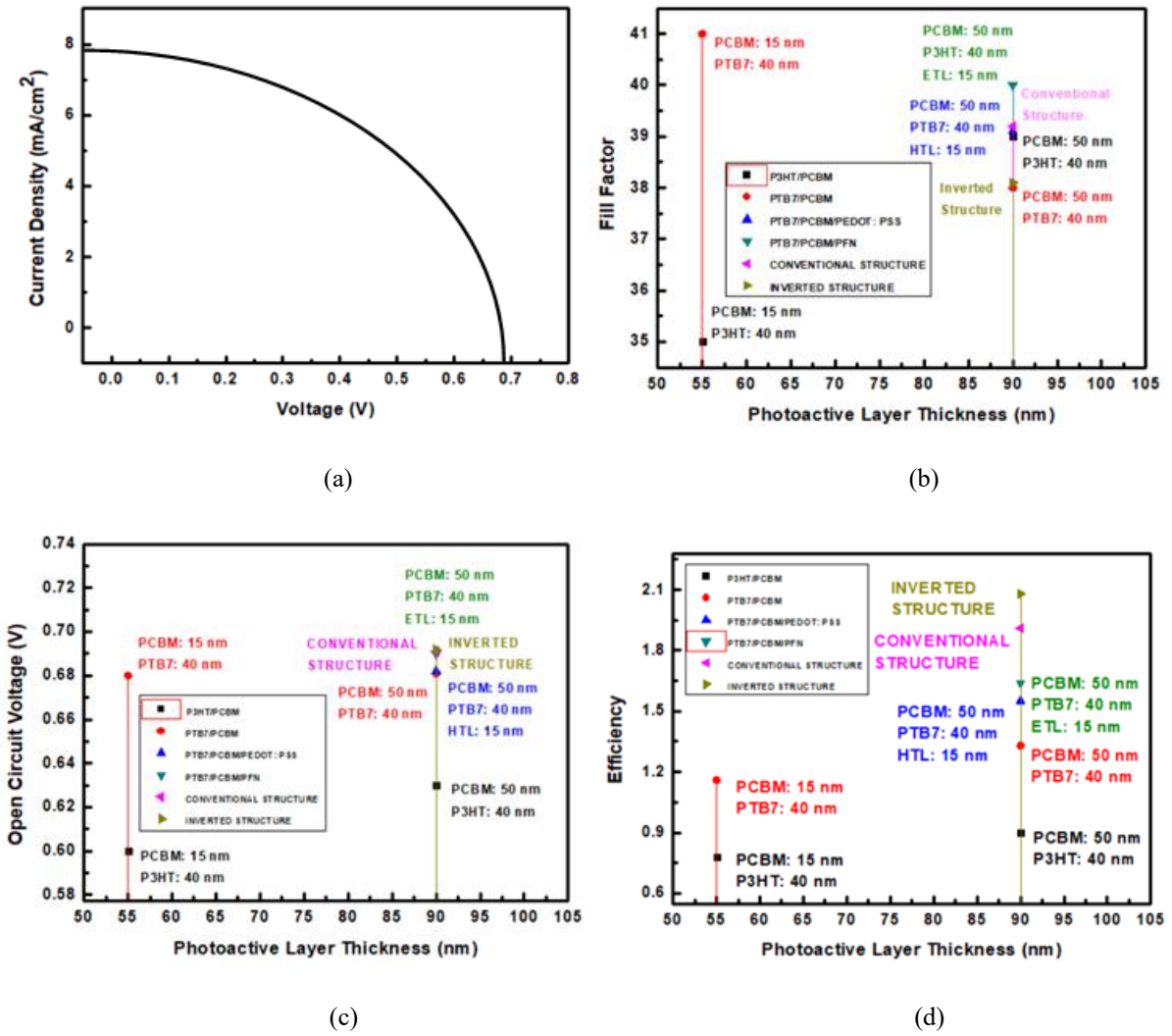

Fig. 4.23 (a) J – V characteristics for inverted PTB7: PCBM solar cell structure and comparison of (b) Fill Factor, (c) Open circuit voltage and (d) Efficiency at experimental and optimized thickness for P3HT: PCBM, PTB7: PCBM; HTL, ETL included optimized PTB7: PCBM solar cell, conventional and inverted PTB7: PCBM solar cell structures as a function of photoactive layer thickness.

This superior performance of the inverted structure can be attributed to the facilitation of Ohmic contact at the interfacial layers which correspondingly enhance charge selectivity at

photoactive layer - electrode interface. Additionally, the interfacial layers having proper charge selectivity could curtail unsought interfacial carrier recombination. Further, the performance of inverted solar cell structure demonstrations sturdy dependency on electron transport layers conductivity. This enhances the overall charge extraction and collection process, resulting in improved performance of the solar cell.

4.12 SUMMARY OF THE IMPORTANT RESULTS

1. The P3HT: PCBM solar cell outperforms with a donor and acceptor thickness of 40 nm and 50 nm, respectively.
2. The PCE of the experimental P3HT: PCBM organic solar cell with an acceptor thickness of 15 nm and donor thickness of 40 nm is 0.78 %, whereas the PCE obtained for the optimized P3HT: PCBM organic solar cell with acceptor thickness of 40 nm and donor thickness of 50 nm is 0.90%.
3. The efficiency of optimized P3HT: PCBM organic solar cell is 15.38 % higher than that of the experimental P3HT: PCBM organic solar cell. The PCE of experimental PTB7: PCBM organic solar cell with an acceptor thickness of 15 nm and donor thickness of 40 nm is 1.33%, whereas the PCE obtained for the optimized PTB7: PCBM organic solar cell is 1.16%.
4. The efficiency of PTB7: PCBM (optimized) with hole transport layer (PEDOT: PSS) is obtained as 1.55 %, a gain of 16.54 % is obtained in comparison to PTB7: PCBM (optimized) solar cell. The efficiency of PTB7: PCBM (optimized) with electron transport layer (PFN) is obtained as 1.64%, a gain of 5.80 % is obtained in comparison to PTB7: PCBM (optimized) with hole transport layer (PEDOT: PSS) solar cell.
5. A PCE of 1.91 % is achieved with the conventional structure of the solar cell. The conventional solar cell structure is composed of ITO/PEDOT: PSS/ PTB7/PCBM/PFN/Al.
6. To further enhance the performance and stability of the solar cell, the inverted structure is used. A power conversion efficiency of 2.08 % is achieved with the inverted structure of the solar cell, which is 8.90 % higher than the conventional structure, due to its superior stability and improved compatibility.
7. The inverted structure performs the best among all the other structures discussed, with the highest efficiency of 2.08 %. This achieved efficiency is 166.66% or 1.6 times higher than the 0.78 % efficiency achieved with the experimental solar cell.

CHAPTER-5

DETECTION OF BLOOD HAEMOGLOBIN FOR IDENTIFICATION OF ANAEMIA USING ORGANIC SOLAR CELL

Haemoglobin serves as a primary indicator for assessing the presence of anaemia. In developing countries like India and various African nations, significant number of people do not have access to proper diagnostic facilities. Consequently, the introduction of a portable, affordable, and non-invasive haemoglobin detector would provide a tremendous opportunity for screening populations suffering with anaemia. Existing literature suggests that the interaction of RBCs with light can be leveraged for disease detection. Additionally, it is widely known that non-anaemic blood exhibits a characteristic red colour. Therefore, the objective this chapter is to present a feasible method for the development of portable and inexpensive haemoglobin detector, targeting to address the aforementioned need the following objective is formed:

"RBC Light scattering analysis to detect compounds present in the blood for identification of disease and further utilization of organic solar cell for blood flow monitoring."

The methodology used to achieve desired objective involved following steps: -

- Analyse the current invasive haemoglobin detection technique.
- Explore the various techniques that rely on the interaction between human blood and light for disease detection.
- Determine the optical properties of haemoglobin and the materials used in photoactive layer.
- Analyse device requirements, and design of a non-invasive haemoglobin detector device based on the optical properties of haemoglobin and organic photoactive layer.
- Analyse and examine the photosensitivity of the organic solar cell to determine anaemia.

The present chapter is divided into eight sections with first section serves as an introduction, addressing the challenges associated with detection of anaemia in marginalise countries. The second section presents requirements for the design of the device. The third section focuses on the device architecture of the solar cell. In fourth section, the validations of the photoactive layer's materials are performed. The fifth section describes the optical properties of haemoglobin. The sixth section presents a detailed explanation of the sensing process. The seventh section involves calculation of the photosensitivity for anaemia detection. Finally, the chapter ends with the section number eight comprising the summary of all the important results obtained throughout the chapter.

5.1 INTRODUCTION

The scattering of light is commonly utilized in soft, condensed, and biological material applications. In the field of biomedical applications, scattering of light offers promising opportunities for non-invasive monitoring and imaging of various medical conditions [373]. Blood, is an important and attractive fluid of biological nature, which could be used for applications that involve the scattering of sunlight. The Red Blood Cells (RBCs) remain the main constituent of the human blood and is almost 45% of the blood by volume. These RBCs contain an extremely dense solution of haemoglobin. This haemoglobin is the primary component responsible for the absorption and scattering of the blue, green and UV regions of the visible light spectrum [374].

The different techniques of light scattering have already been utilized for the measurement of different RBC properties [375-377]. For instance, the light scattering has been utilised for the measurement of changes in the shape of the RBCs in case of sickle cell anaemia [378], malaria detection [375], monitoring fluctuations in the RBCs membrane [375, 376] and for studying the dynamics and metabolic characteristic of the RBCs [379, 380]. Anaemia, is a grave complication indicating deficiency of iron, and can be life-threating. More than 50% of the childbearing women in economically developing countries suffers from anaemia. In India, anaemia is a prevalent health problem and with the World Health Organisation (WHO) reporting that 52% of the population in India is anaemic.

The development of non-invasive technologies which are capable of monitoring patients' health continuously and with reliability are expected to considerably improve the quality of life and will also create new and innovative opportunities in medicine. The major benefits

associated with the use of non-invasive technologies are simplified medical practices, increased patient comfort, cost effectiveness, immediate and reliable measurement of information and monitoring, environment friendly techniques as there are no disposable biohazardous waste produced. The frequent and reliable monitoring made possible by the non-invasive methods, has the potential to revolutionize the treatment practises, especially in case of chronic disease. A perfect example of the benefit of continuous measurement and monitoring is seen in insulin delivery and glucose monitoring, which have saved and improved millions of lives worldwide over the past decade [381-383].

The absorption of light by blood in infrared (IR) and visible region is influenced by various haemoglobin derivatives [384, 385]. Haemoglobin is the primary constituent of human red blood cells. Further, the presence of haemoglobin in blood is an extremely important parameter to evaluate the medical condition, physiological status, and oxygen transportation capability of any individual. The haemoglobin is used to diagnose condition of anaemia. Anaemia presents a condition of low haemoglobin level. The existing invasive systems are capable of measuring haemoglobin [386] via spectrophotometric methods. However, these present invasive methods involve high cost and require large, specifically designed laboratories with specialized optical equipment which are not portable in nature.

Presently, the invasive methods used for determining haemoglobin involve collecting a blood sample from the patient and then analysing it. This method causes patient discomfort while collecting the blood sample and, in this method, there is a significant delay between the sample collection and sample analysis, preventing a real time or continues monitoring of the patient. In comparison to the present method of measuring haemoglobin a non-invasive method presented in this chapter offers a pain free, immediate, and reliable measurement of haemoglobin without the risk of infection. Additionally, a low-cost and portable but invasive method of haemoglobin detection known as haemoglobin colour scale method is also used for determining the haemoglobin levels, where the patient's blood is matched with a scale. However, this method suffers from high variability and inaccuracy.

The solar cell made with semiconductors of organic nature are an attractive alternate to their inorganic counterparts primarily due to their flexibility and low cost of fabrication. The organic semiconductor materials have been reported with the photoconductive properties. P. Peumans *et al.* [387] in 2000 demonstrated a high-speed multilayer photodetector. A transparent photodiode capable of detecting polarized light is reported by H. Tanaka *et al.* in 2006 [388].

In this chapter, a portable device is presented that utilizes a non-invasive, easy to use, environmentally friendly, and reliable method to detect haemoglobin deficiency in blood.

The primary motivation behind the use of proposed method is its ability to increase testing at low cost by providing immediate results without the requirement for a large setup, further as this method does not require any blood to be drawn out from the body and is completely reliant on the optical properties of the haemoglobin the organic solar cell, making it accurate and free from the risk of infection. Moreover, this method is highly reliable as the physical conditions cannot tamper with it. The method is also environmentally friendly as it creates no biohazardous waste since no chemical reagents or syringes are required, and it is reusable.

5.2 DEVICE DESIGN REQUIREMENTS

To address the vital need of improving access to health services in underdeveloped areas, the practical features which are essentially required in a haemoglobin detection device for its clinical utility are:

- It should be compact, portable, reliable, and accurate with low margin of error, replaceable and inexpensive.
- Should not require biohazardous chemicals and should be low or free on maintenance.
- Easy to use, especially in remote and resource poor settings where laboratory facilities are not available.
- Allow anaemia detection irrespective of patient gender, age, pregnancy etc. ensuring its usefulness across diverse populations.

Thus, objective of this chapter is to design and develop an inexpensive, portable, accurate, easy to use and environment friendly haemoglobin detection device by utilizing the optical properties to the haemoglobin pigment to assess the health of the RBCs and to diagnose diseases such as anaemia, sickle cell anaemia, low iron content, malaria, thalassemia. By leveraging the optical properties of haemoglobin, the device aims to provide a non-invasive and efficient method for assessing the status of RBCs and diagnosing related diseases. This approach eliminates the need for invasive procedures.

Colour can be defined as the perception of the incident sunlight on the retina of the human eye. The visible spectrum extends from violet colour at 380 nm to red colour at 750 nm as shown in Table 5.1. In the visible spectrum, different components of colour display dissimilar ranges

of reflectance. The wavelength range for colour red in visible spectrum exists from 620-740 nm.

Table 5.1. Color wise wavelength for visible light spectrum

Colour	Wavelength (nm)
Red	620 – 750
Orange	590 – 620
Yellow	570 – 590
Green	495 – 570
Blue	450 – 495
Violet	380 – 450

The haemoglobin pigment remains one of the primary chromophores of the skin which is prominent in red blood cells (RBCs). Haemoglobin comprises of optical characteristics [389-393] which when methodologically used can detect anaemia. The reflection of wavelengths at and above 600 nm by the haemoglobin pigment (oxy-haemoglobin) validates and explain the red colour appearance of the red blood cells under visible spectrum [394]. Hence, from this information about haemoglobin, it can be hypothesized that the organic photodiodes sensitive to the different colours can extract information about the health of a patient's blood sample.

The specific optical properties of haemoglobin can be utilized by organic photodiodes to potentially detect variations in the spectral characteristic of blood samples. This suggests that a device equipped with organic photodiodes sensitive to different wavelengths could provide valuable information about the health status of a patient's blood, including the presence of anaemia or other related conditions.

5.3 ORGANIC SOLAR CELL STRUCTURE

The simulations based on computer have proved to be an important and effective tool in examining and analyzing the behaviour of photovoltaic cells under different environmental conditions. These simulations are crucial as they help to accurately predict the output results of a photovoltaic device and assists in estimating their performance. Additionally, these simulations aid in determining the optimum conditions for their enhanced performance and provide a detail account of the photovoltaic cell characteristics. This present research work

utilises the industry standard Silvaco Atlas 2D numerical device simulation software. Further, the use of numerical device simulation software provides a powerful means to analyse the underlying physics and electrical behaviour of photovoltaic cells. These simulations enable to study the effects of different design choices, material properties, and external factors on the performance of the device.

The accuracy of simulation results in Silvaco Atlas arise from the combination of multiple models of propagation and accurate ray tracing techniques. This ensures that the simulated behaviour of photovoltaic devices closely matches the actual experimental results. Moreover, the Silvaco software have both the integrated spectrum Air Mass 1.5 and Air Mass 1.0 which corresponds to real outdoor solar conditions. The Silvaco also permits the user to define own materials, enabling researches to model novel materials or accurately represent specific characteristics of the materials used in the devices. The Silvaco Atlas being an industry standard device simulator relies on established analytical models and methods to envisage the performance of photovoltaic device, before it is actually realized. The Silvaco Atlas software utilizes the basic mathematical charge transport equations to comprehend the performance and behaviour of the photovoltaic device.

Table 5.2. Simulation parameters for the solar cell

Parameter (Unit)	**Coumarin 30: C_{60}**	**NN'-QA**	**ZnPc**
Hole mobility ($cm^2 V^{-1} s^{-1}$)	1.5×10^{-4}	1×10^{-3}	1.619×10^{-6}
Electron mobility ($cm^2 V^{-1} s^{-1}$)	1×10^{-5}	1×10^{-4}	1×10^{-7}
Bandgap (eV)	2.2	2.1	1.97
Dielectric permittivity	3.2	4.4	5.4
Electron affinity (eV)	2.6	3.5	3.1

In a solar cell, the process of photovoltaic carrier generation begins instantly whenever the device is illuminated by solar spectrum. Generally, the solar spectrum is utilised as an input for modelling the optical propagation and calculating the performance of a solar cell. The spectrums in Silvaco Atlas device simulator are capable of representing the real and practical environmental conditions under the natural sunlight. The Table 5.2 presents the simulation parameters used for the photovoltaic solar cell simulation performed in this chapter [395-398]. The selected device simulation parameters define the characteristics of the simulated solar cell.

In this chapter a vertically stacked Coumarin 30: C_{60}/NN'-QA/ZnPc based three-layer organic semiconductor solar cell sensitive individually to red, green, and blue light is simulated via Silvaco Atlas 2D device simulator [399-401]. This organic solar cell acts as a photodetector detecting the light transmitted through the skin tissues and hence is an extremely important component in the purposed method for haemoglobin detection. Each layer of the organic solar cell is carefully designed to exhibit satisfactory spectral selectivity, allowing it to selectively capture light of specific wavelengths. This spectral selectivity is utilised herein for the application of organic photovoltaic cell as a haemoglobin detector. The Fig. 5. 1 presents the layered structure of the multilayer organic solar cell used.

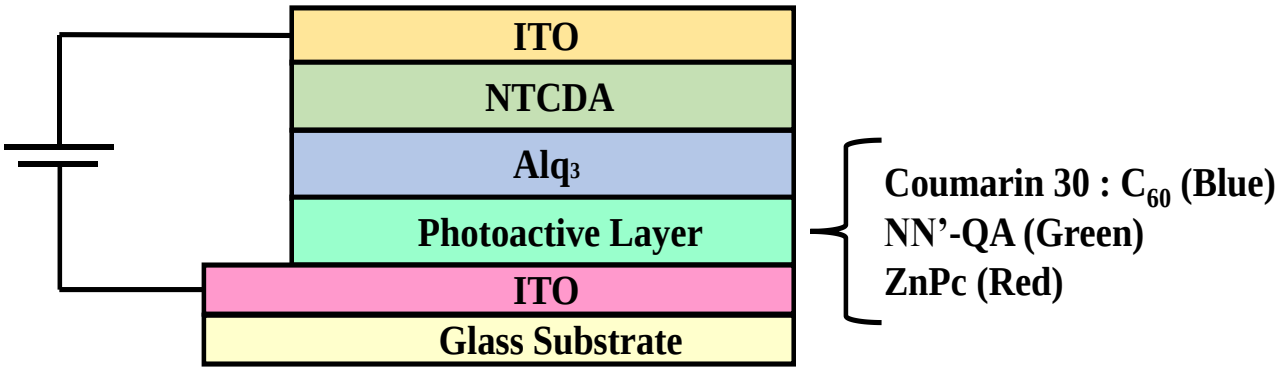

Fig. 5.1 Layered structure of simulated photovoltaic cell.

When incoming light is incident on top of organic solar cell the blue light component is absorbed by Coumarin 30: C_{60} layer of the photoactive layer. Subsequently, the green and red-light components of the incident light are absorbed by the middle NN'-dimethylquinacridone (NN'-QA) and bottom-last Zinc phthalocyanine (ZnPc) layers of the solar cell, respectively. The mentioned materials are semiconductors of organic nature. The Table 5.3 summarises the complete structure of the solar cell simulated. The length of solar cell considered is 1 μm.

The photosensitive part responsible for detecting the blue colour consists of Coumarin 30 and Fullerene (Coumarin 30: C_{60}). The Coumarin-Fullerene (60) material are highly attractive because of their broad absorption range and photostability [402-406]. The Coumarin and its derivatives are generally used in signalling applications in the sophisticated sensors, photophysical structures [407, 408] and biosensors [409]. For the green colour detection, the photosensitive part contains a layer of N, N'-dimethylquinacridone (NN'-QA). The electron affinity for NN'-QA is reported to be at 3.5 eV. Similarly, Zinc Phthalocyanine (ZnPc) is used

as a photosensitive part for the red colour detection due to its easy synthesis and non-toxic character, making it a propitious contender for photovoltaic cell applications.

Table 5.3. Thickness of the constituent layers of the simulated solar cell

Material Layers	Thickness
Glass	700 µm
ITO	0.15 µm
Coumarin 30: C_{60}	0.08 µm
NN'-QA	0.2 µm
ZnPc	0.25 µm
Alq_3	0.05 µm
NTCDA	0.3 µm
ITO	0.02 µm

Phthalocyanine (Pc) is a self-organised crystalline liquid with a bandgap of 1.97 eV and is an active part in all the organic photovoltaic cells. It is also chemically and physically very durable [410]. The various kinds of Phthalocyanines are used in variety of device application including photovoltaic cells [411, 412] and medical photodynamic healing therapy [413]. The layer of tris(8-hydroxyquinoline) aluminium (Alq_3) facilitates transportation of electrons. The deposited layer of naphthalene tetracarboxylic anhydride (NTCDA) over Alq_3 layer helps in preventing electrical short [414] caused because of the counter ITO electrode layer.

5.4 VALIDATION OF ORGANIC SOLAR CELL CONSTITUENT MATERIALS

The validation is an extremely vital part of the research as validation confirms the conclusions and findings achieved from the computational modelling software. Through the method of validation, the accuracy, applicability, and reliability of the computational model is ensured specially in open world conditions. The process of validation evaluates, if the model computed aligns with the results achieved experimentally.

The process of validation comprises of comparing or associating the simulated results with the established experimental results obtained thus, certifying the simulated results obtained. The device simulators have demonstrated their important role in picturing the concept and optimising the performance of devices before they are actually physically realised. In this section individual structures of the multilayer photovoltaic devices are simulated and their

current-voltage measurement plots obtained with Sivaco Atlas device simulator are compared with the experimentally obtained and reported data [415].

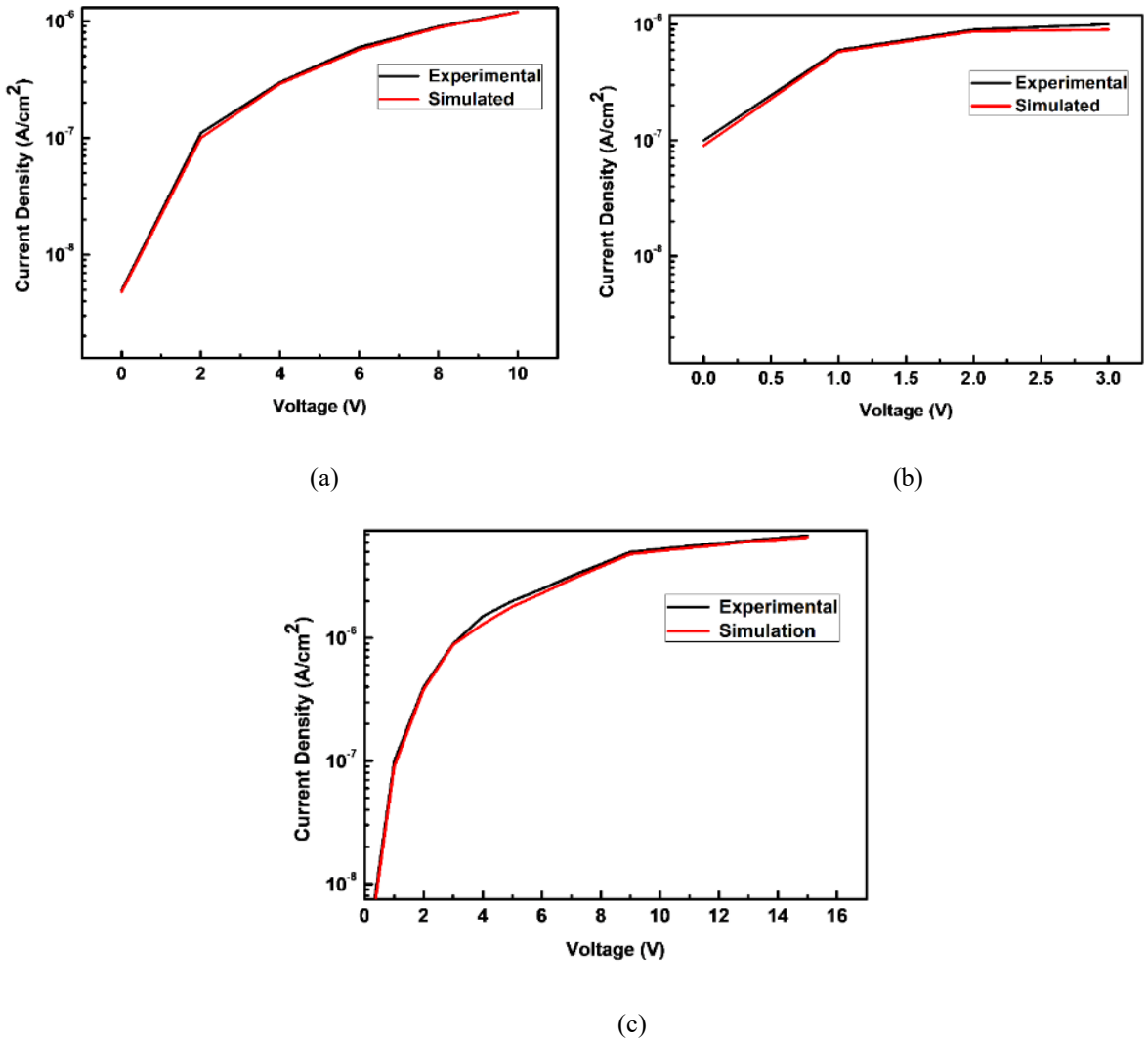

Fig. 5.2 The current voltage characteristic plots of (a) Coumarin 30: C_{60}, (b) NN'-QA and (c) ZnPc organic photovoltaic cell (black colour curve presents the experimental photo-current and red colour curve presents simulated photo-current).

The Fig. 5.2 presents photo-current characteristic of the blue, green, and red colour photosensitive organic solar cells. In all three plots, the photocurrent density increases with the increase in applied voltage. The close agreement between the simulated (presented with the red colour curve) and experimentally reported (presented with black colour curve) data enables for the further analysis of the purposed organic photovoltaic device structure for the design, development, and application in non-invasive haemoglobin detection.

5.5 OPTICAL PROPERTIES OF HAEMOGLOBIN AND ORGANIC SOLAR CELL

There are various reported papers on the absorption characteristics of the haemoglobin [416-419]. The absorption spectrum of oxy-haemoglobin is represented in Fig. 5.3 [420]. The human blood's optical characteristics are prominently determined by optical property of the haemoglobin.

The coefficients of absorption of oxygenated haemoglobin are presented in the Fig. 5.3. Further, from Fig. 5.3 it can be observed that for oxygenated haemoglobin the peak absorptions occur at 274 nm, 344 nm, 415 nm, 542 nm, and 577 nm. Oxygenated haemoglobin or oxyhaemoglobin is oxygen bound to haemoglobin present in the RBCs. One molecule of haemoglobin pigment binds to the four molecules of oxygen to form oxyhaemoglobin.

It is the primary function of oxyhaemoglobin to transport oxygen to different tissues of the body and hence is an extremely important human physiological parameter. In condition of anaemia, the oxygen affinity of the haemoglobin pigment reduced, compromising the oxygen transport mechanism in the patient's body.

This results in low oxygen levels in RBCs, leading to a condition called hypoxia in the tissues, which can be life threatening. Therefore, in this chapter, the purposed method for detecting anaemia is designed based on the optical properties of oxyhaemoglobin. The method utilises the optical properties of haemoglobin, primarily the absorption spectrum, to detect the condition of anaemia.

The detection of oxyhaemoglobin in blood indicates a patient without anaemia, as oxyhaemoglobin refers to haemoglobin combined with oxygen. Therefore, the proposed method, which is based on detecting oxyhaemoglobin, provides accurate diagnosis for anaemia. In this method, the organic solar cell absorbs transmitted wavelengths and produces a photosensitivity corresponding to an anaemia free patient. Any significant deviation in the value of photosensitivity would indicate anaemia, indicating a lack of oxygen bound to haemoglobin or the presence/detection of deoxyhaemoglobin (purple-blue colour).

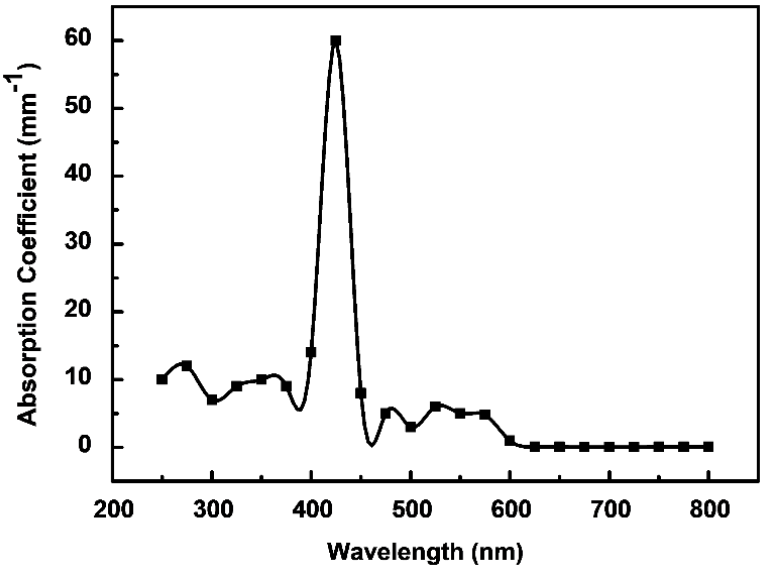

Fig. 5.3 Absorption coefficient of oxygenated haemoglobin.

Fig. 5.3 presents the plot of absorption coefficient as a function of wavelength. From the plot it can be noticed that absorption coefficients exhibit high magnitude in the wavelength range of 250 to 600 nm, with a peak around 425 nm. The magnitude of absorption coefficients starts to decrease beyond 600 nm and remains almost constant in the wavelength range of 600 to 800 nm. Thus, it can be inferred from the plot presented in Fig. 5.3 that oxygenated haemoglobin has a higher light absorption for wavelengths below 600 nm and lower absorption for wavelength ranges above 600 nm. As presented in Table 5.1 the wavelength range for blue colour is from 425 - 495 nm, for green colour it is from 500 - 540 and for red colour it's from 615 - 700 nm. Therefore, from the Fig. 5.3 it can be concluded that oxygenated haemoglobin efficiently absorbs the blue and green colour wavelength spectrum while allowing the transmission of red colour wavelengths.

The Haemoglobin, capable of absorbing wavelength ranges from 250 nm to approximately 600 nm, exhibits absorption in the Soret band (as observed from the Fig. 5.3 between 390 nm to 410 nm) and transmits (does not absorb) wavelength ranges beyond approximately 600 nm, including wavelengths corresponding to red colour in the visible spectrum. The proposed method is based on the detection of these transmitted wavelengths (620 nm to 750 nm) through the skin/blood using an organic solar cell. Therefore, though Soret band (390-410 nm) is an important peak to detect heme, the iron containing molecule which combines with globin proteins to form haemoglobin. However, the wavelengths corresponding to the Soret band (390 nm to 410 nm) will not be transmitted through the skin/blood but instead be absorbed by the

haemoglobin present in RBCs. Hence, there will be no detection of these wavelengths on the organic solar cell.

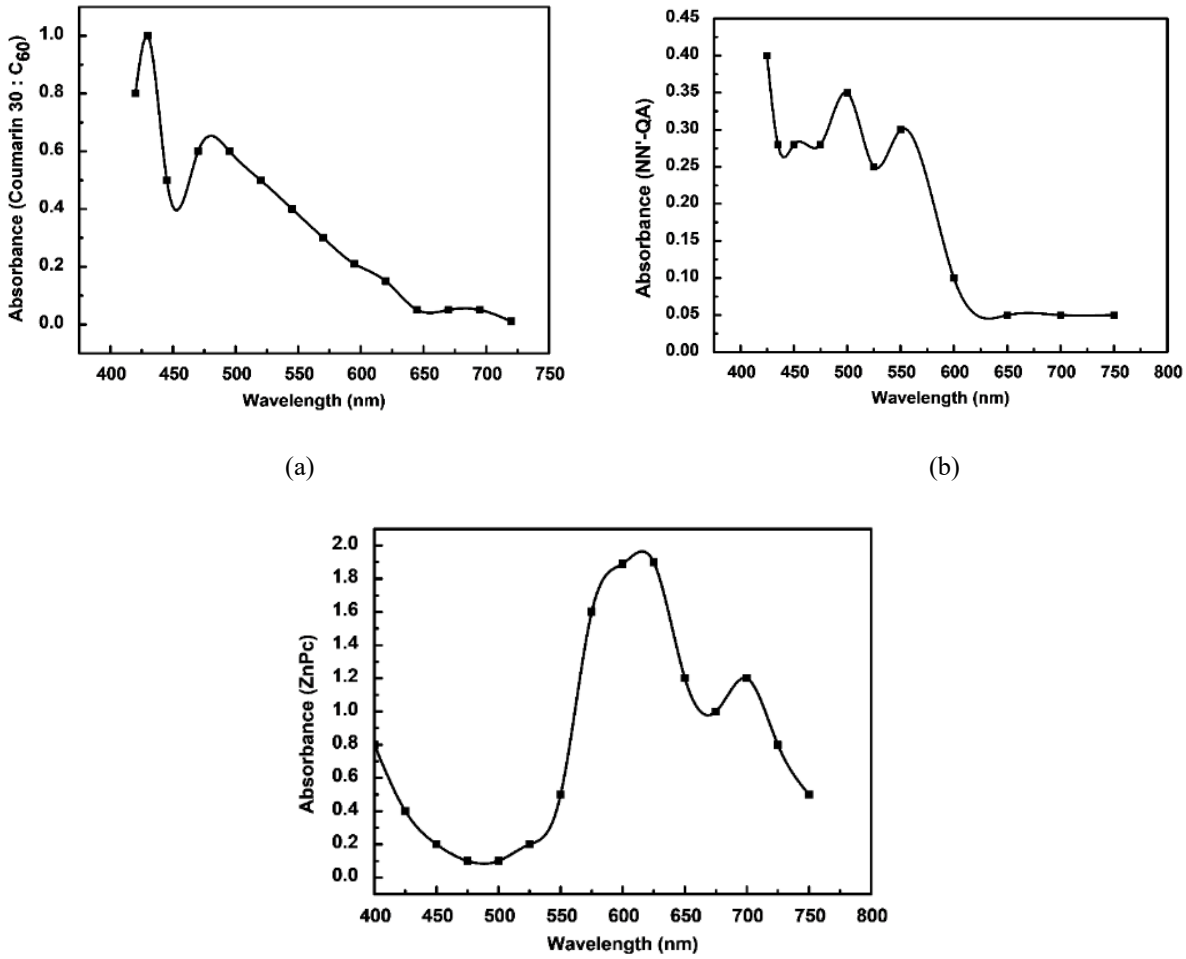

Fig. 5.4 (a) Coumarin 30: C_{60}, (b) NN'-QA and (c) ZnPc photodetectors individual (single structure) optical absorption spectrum in the wavelength range of 400 to 750 nm. The Coumarin 30: C_{60}, NN'-QA and ZnPc are blue, green and red colour photodetectors respectively.

The Fig. 5.4 (a) represents the optical absorption spectrum of the blue colour photodetector (Coumarin 30: C_{60}), the green colour photodetector (NN'-QA) and the red colour photodetector (ZnPc). From the Fig. 5.4 (a), it can be observed that the blue colour photodetector has absorption spikes around 420 nm and 540 nm. Similarly, the green colour photodetector shows absorption spikes at 500 and 540 nm. Therefore, it can also be observed from Fig. 5.4 (a) and 5.4 (b) that both the blue and green photodetectors transmit wavelengths longer than 600 nm, which corresponds to the red colour. Further, as observed from Fig. 5.4 (c), the red colour photodetector exhibits absorption spikes at 610 nm and 700 nm. The observations from Fig.

5.4 confirm that Coumarin 30: C_{60}, NN'-QA and ZnPc absorb the blue, green, and red colour light, respectively.

5.6 SENSING CONCEPT

The idea of using the colour of haemoglobin for anaemia detection dates back to 1900. Tallquist method has demonstrated that the blood colour can indicate condition of anaemia reliably. In the method, the scale used consists of a card with six red colour shades on it representing different haemoglobin levels. The blood sample of the patient after pricking is immediately matched against the one of the prearranged shades of red colour on the scale, indicating if the patient is anaemic or not. This method provides a simple and effective way to detect anaemia based on colour matching.

Modern technology has further refined and perfected this method [421-424]. Apart from being an invasive technique the primary sources of error in utilisation of these currently available haemoglobin colour scales are (i) colours of produced scales vary between different manufactures (ii) absorbent paper also show variation and are somewhat unusable due to uneven spreading of blood leading to colour dilution, also due to excessive blood absorption the paper becomes damp and translucent (iii) proper natural or artificial lighting is required for accurate interpretation of the colour scale. The purposed method in this chapter also uses the similar idea of using the red colour of blood's haemoglobin to detect the anaemia. The proposed approach overcomes the limitation associated with the haemoglobin colour scale method and offers the additional benefit of being non-invasive.

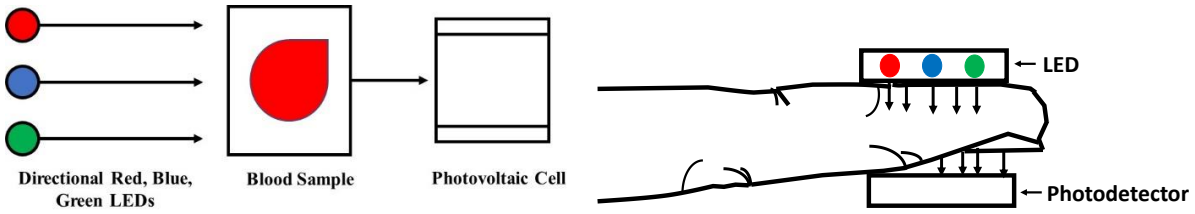

(a) (b)

Fig. 5.5 (a) The schematic representation of sensing concept and (b) organic photodetector-based haemoglobin detection device used on a finger.

The sensing method proposed in this chapter is illustrated in Figs. 5.5 (a) and 5.5 (b). The proposed method consists of three directional light emitting diodes (LED) sources which are utilised to illuminate the finger or the specimen of the blood. The appropriate wavelengths of

light passed through or transmitted through the finger's area are selected for the detection of haemoglobin. The Fig. 5.6 present the basic circuit design of the proposed device and the block diagram of the device which could be achieved through a microprocessor. A battery is connected to provides the power required for the LEDs and microprocessor to operate. The LEDs project light onto the organic solar cell (OSC), and the patient's finger is to be inserted between the LEDs and the OSC. The OSC generates current based on the wavelengths of light detected by it. Since this current is in microamperes (μA), its amplified and sent to the microprocessor, which displays the output as presented in Fig. 5.7.

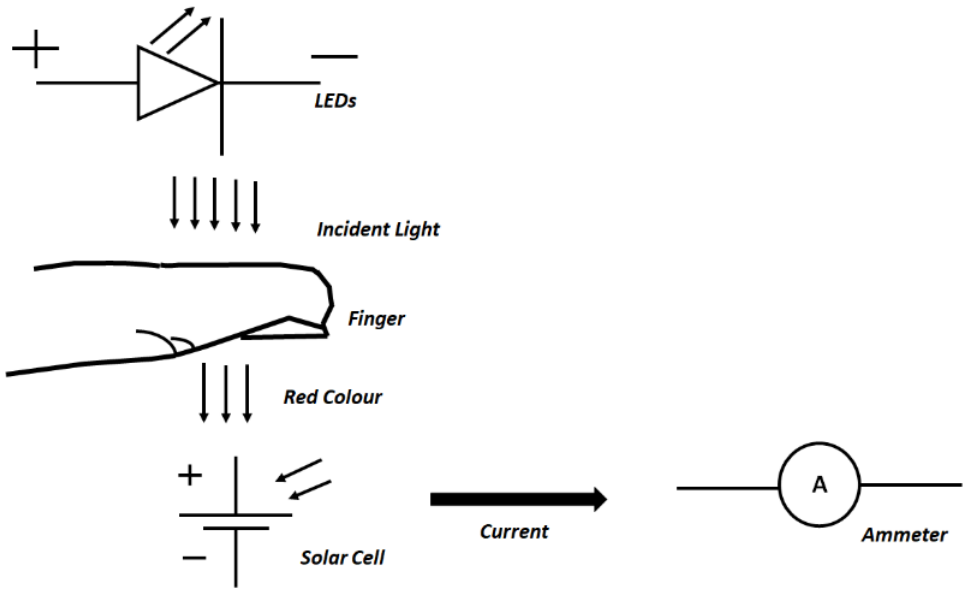

Fig. 5.6 Detection of anaemia using non-invasive method.

The purposed measurement method presented in this chapter is non-invasive and is based on the radiation of light emitted by LEDs in the wavelength rage of 450–750 nm through skin area. The method takes advantage of the absorption of light by the RBCs. The different colour wavelengths after passing through the finger are absorbed in accordance with the absorption characteristics of the blood components. The transmitted light is then detected by a non-invasive organic photovoltaic device to produce a photosensitivity value. The obtained value of photosensitivity detects the haemoglobin and determines if the patient suffers from anaemia.

The major advantages associated with the proposed non-invasive technology in comparison to other technologies are lower production cost, portability, high reliability, accuracy, and immediate and continuous measurement. Further, it does not require a large setup or trained manpower to operate, the input power required to operate it is significantly lower.

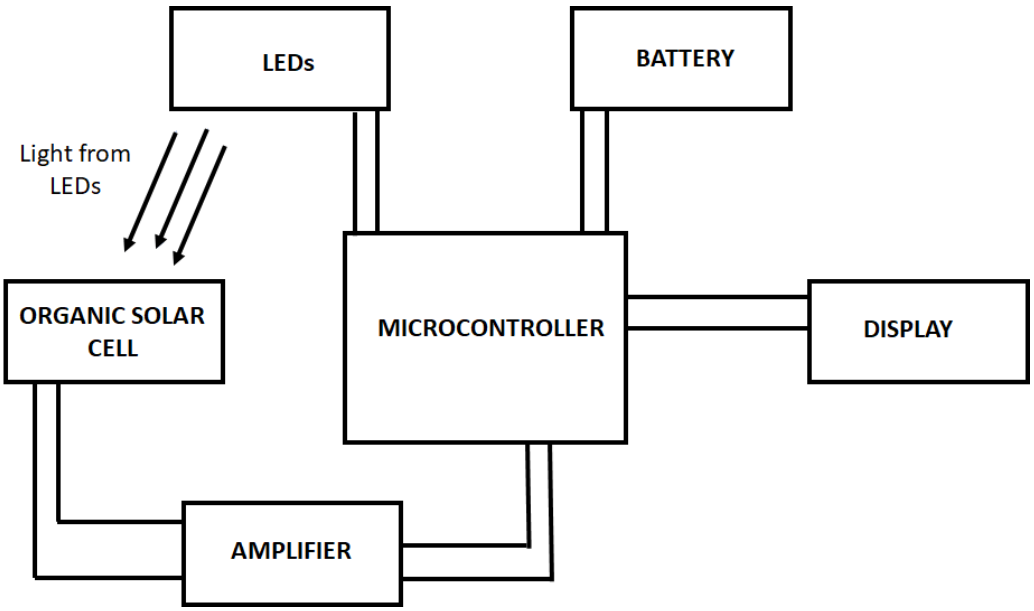

Fig. 5.7 Non-invasive anaemia detection setup.

It provides higher patient comfort, as the data is of digital nature hence patient history can be stored. Moreover, it could be integrated to the wearable electronic devices. Thus, proving beneficial for increasing testing and reducing hospital costs. On the other hand, the drawbacks associated are that to use this method the patient should be still and the skin surface on which the device is used should be contamination free so that nothing may interfere with the measurements.

5.7 EVALUATION OF THE PHOTOSENSITIVITY TO DETECT ANAEMIA

The negatives of present finger-prick technique used to determine the anaemia are complications, invasiveness and errors while reporting especially in case of younger women as haemoglobin concentration in blood capillaries are higher in comparison to the venous blood [425] and finger piercing also causes an alteration in the fluids as the pressure on fingertip increases concentration of plasma in the blood capillary thus falsifying the reading.

The Fig. 5.8 presents the characteristic spectral photo-response of the multilayer organic photovoltaic cell. The three monochromatic lights of blue, green, and red colour are irradiated from the three Light Emitting Diodes of blue, green, and red colour onto the photovoltaic device. The resultant photo-response curves of the blue, green, and red colour sensitive film layers have their spikes at the wavelengths of 420 nm, 510 nm, and 650 nm respectively. Thus, from this obtained photo-response curves it is firmly evident that the separation of colours

occurs in the purposed multilayer organic photovoltaic device. Further, from this finding it could be established that the different value of photosensitivity (A/W) are related to different wavelength ranges of colours. It is also very well known that the spectrum of wavelength for blue colour is form 425 nm to 540 nm, the wavelength spectrum for green colour is known to be from 500 nm to 540 nm and similarly the wavelength spectrum for red colour is from 615 nm to 700 nm.

The photosensitivity represents the current generated in Amperes per Watt of incoming sunlight incident on the surface of the solar cell. Photosensitivity can give the current produced by the organic photovoltaic cell according to the formula given in equation (5.1).

$$I_p = \text{Area} \times \text{Sensitivity} \times \text{Intensity} \tag{5.1}$$

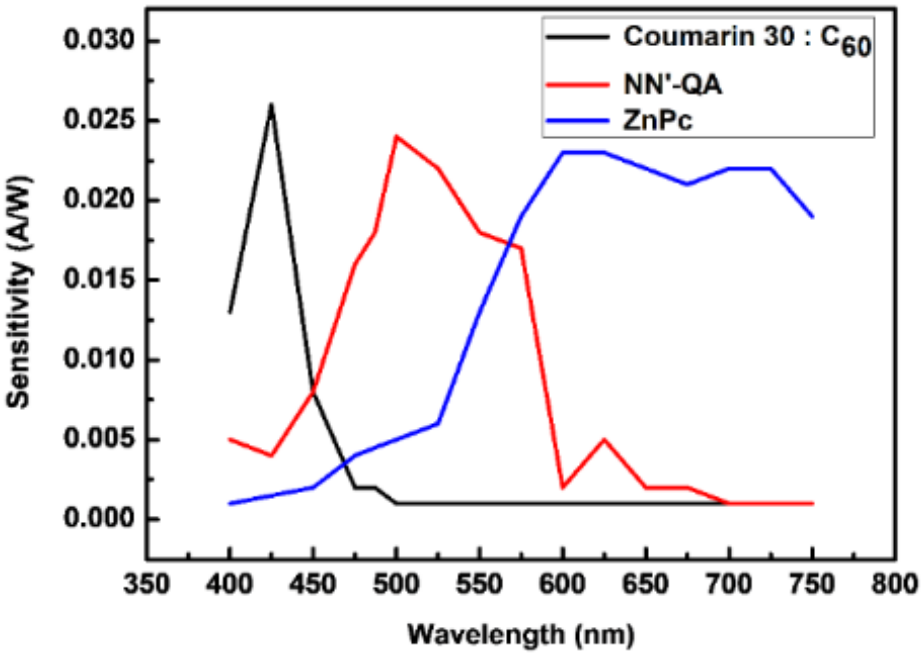

Fig. 5.8 Photosensitivity as a function of wavelength for organic photovoltaic cell.

The Fig. 5.9 represents the comparison between the sensitivity or the output current produced by the single structure red colour photo-detector and the complete multilayer photovoltaic device. From Fig. 5.9, it can be observed that the single structure device exhibits an undesirable output current signal within the blue and green colour ranges, while the multilayer photovoltaic device demonstrates a significantly reduced blue and green colour current signal as the top layer of the solar cell acts as blue colour filter and the middle layer act as a green colour filter, thereby absorbing the blue and green colours, respectively.

Thus, from the Fig. 5.9 it can be confirmed that the individual or stand-alone structure of the ZnPc material film does not possess exceptional characteristic for the separation of colours. Therefore, the use of multilayer structure arranged in blue, green, and red from top to bottom is necessarily required to achieve excellent colour separation. Additionally, from the Fig. 5.9, it can be observed that the sensitivity of the multilayer structure is approximately 0.020 A/W for the wavelength ranges of 600 nm and above.

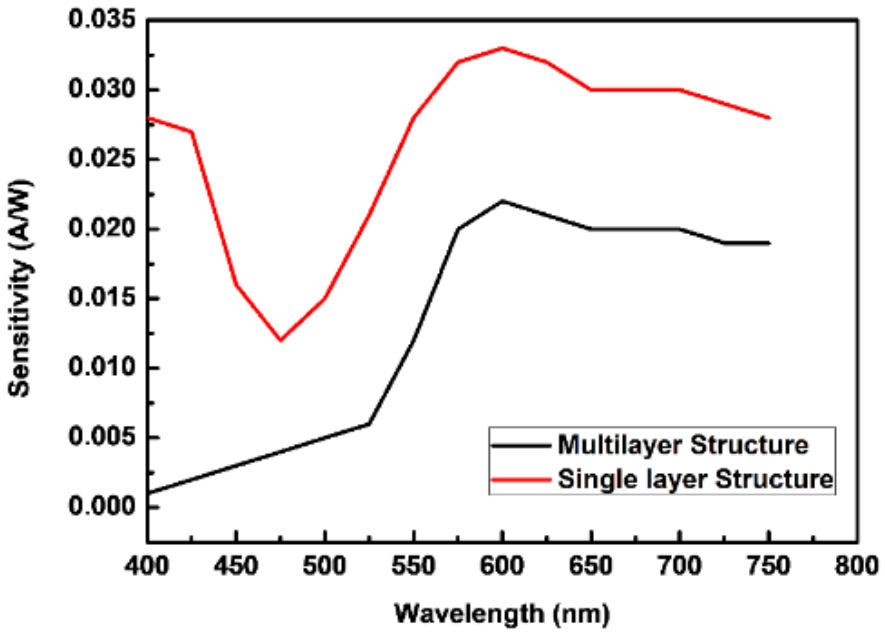

Fig. 5.9 Photosensitivity as a function of wavelength for single layer (red colour curve) and multilayer structure (black colour curve).

Hence, from the combination of Fig. 5.8 and the photosensitivity results obtained in Fig. 5.9, it can be further established that when a skin area is exposed to the three LEDs of different wavelengths, such as red, blue, and green, the blue and green colour should be completely absorbed by the skin. This means that the blood should completely absorb both the blue and green colours and should only allow the red colour to pass through. These wavelengths corresponding to the red colour spectrum (615-750 nm) that passes through the patient's blood sample should then strike the stacked organic photovoltaic cell, where they should be fully absorbed, resulting in a photosensitivity of 0.02 A/W or a current of 1 µA (considering a device area to be 1cm^2 and an intensity of 50 µW/cm^2).

The red colour light absorbed by the photodetector serves as direct evidence of the presence of Haemoglobin and indicates the absence of anaemia. This ultimately proves and establishes the fact that the sample of blood under consideration or analysis is healthy and the person is free

from anaemia. If the photosensitivity deviates from the value of 0.02 A/W, it means that the organic photovoltaic cell used as a detector has absorbed light of another colour such as blue or green, indicating that the blood sample is not completely healthy and has a lower count of red blood cells (anaemia) or iron deficiency, which require treatment. Therefore, the haemoglobin concentrations which could be detected through this technology are in the range of 18 to 12 g dl^{-1}, 18 g dl^{-1} to 14 g dl^{-1} for males and 16 g dl^{-1} to 12 g dl^{-1} for females which are the normal haemoglobin levels. If the patient's haemoglobin concentration is below the mentioned normal haemoglobin concentration range, the patient is suffering from anaemia.

5. 8 SUMMARY OF THE IMPORTANT RESULTS

1. In this chapter, a multilayer organic solar cell based on three organic photodetector layers, namely Coumarin 30: C_{60}/NN'-QA/ZnPc, are arranged in a stack, with each layer being sensitive to blue, green, and red colour light, respectively.
2. The output obtained from the purposed multilayer photovoltaic device demonstrates excellent spectral selectivity and effective colour separation within the photovoltaic cell.
3. This remarkable capability to separate colours makes the proposed organic photovoltaic cell suitable to be utilised as a photodetector, in a haemoglobin detection device by combining it with blue, green, and red colour LEDs.
4. This optical absorption characteristic of the blood yields the vital information on the composition of the blood.
5. The photodetector detects haemoglobin present in RBC by utilising the optical properties of haemoglobin to transmit or reflect red colour. This transmitted red colour wavelengths are absorbed by the ZnPc layer of the multilayer solar cell, resulting in a photosensitivity of 0.02 A/W.
6. This purposed method is cost-effective and non-invasive, making it extremely useful for screening anaemia, particularly in children and women who are suspected to be anaemic.
7. The device developed by the proposed method is portable, with minimal requirement of training and provides immediate results.
8. Thus, by leveraging the optical properties of haemoglobin, this proposed methodology proves to be highly reliable and easy to use, with the potential to reduce mortality rates, especially in marginalized and underprivileged populations around the world.

CHAPTER-6

SUBDERMAL IMPLANTABLE BIOCOMPATIBLE BULK HETEROJUNCTION SOLAR CELL FOR CARDIAC PACEMAKER

Bio-medical electronic components play a vital role in healthcare services. At present pacemakers are dependent on batteries that need to be replaced periodically through expensive and risky surgical intervention. Consequently, there is substantial demand for the biomedical electronic devices capable of harvesting and storing internal energy. Piezoelectricity and Bio-fuel cells are extensively used means for internal energy harvesting. Nevertheless, the primary issue associated with these energy harvesting methods is that of ensuring biocompatibility and flexibility, which are essential due to the complex structure of human tissues and their extreme sensitivity to foreign material. Any foreign material non-compatible with the internal tissues can lead to toxicity. Therefore, to overcome the challenge of complex periodic battery replacements, and to ensure compatibility with tissues the following objective is formulated:

"Performance optimization of fully organic and biocompatible solar cell for subdermal implants and to supply sustainable energy to pacemaker."

The methodology used to achieve desired objective involved following steps: -

- Designing a bulk heterojunction (BHJ) organic solar cell to operate modern cardiac pacemaker.
- Analysing the absorption and scattering coefficients of the skin.
- Identifying possible skin depth for implanting BHJ organic solar cell.
- Analysing generated power of designed solar cell for different skin types under illumination conditions.

The present chapter is organised into ten different sections, wherein, section 6.1 covers the introduction. Further, section 6.2 emphases on benefits of organic PV cell for energy harvesting. In section 6.3, the optical properties of the skin are explored. Afterwards, section 6.4 describes the tissue geometry for implementation of the PV cell. Validation and performance parameters extraction of PV cell is demonstrated in section 6.5. In section 6.6,

discusses the analysis of skin coefficients and skin penetration depth is mentioned. The performance of covered organic solar cell is described in section 6.7. In section 6.8, examines the relationship between the power output of the implanted organic photovoltaic cell (covered) and skin thickness is demonstrated. Further, section 6.9 presents the calculations confirming that a PV cell can effectively power a modern cardiac pacemaker. Finally, in section 6.10 a summary of all the significant results is mentioned.

6.1 INTRODUCTION

Electronic implants are widely utilized for therapeutic treatment, with cardiac pacemakers being a leading example. Pacemaker function by electrically simulating human heart to regulate its rhythm. The power required for a pacemaker is approximately 10 μW [426]. Primary batteries typically have a lifespan of about six to seven years [427] with the replacement rate of reaching up to 25% [428]. Consequently, organic PV cells are well suited for the stated purpose due to their ability to produce sufficient power, lower fabrication costs and biocompatibility, making them best technique for in body electricity generation [429-431]. Recently, organic photovoltaic (OPV) devices have gained significant attention for their commercial applications, thanks to their mechanical flexibility, inexpensive fabrication costs and semi-transparent nature. However, the operational lifetime of these devices remains a key concern.

Many research papers have reported the degradation of the best stable OPV devices within few years [432-436]. This has created an impression that organic photovoltaic devices have shorter operational lifespan making them less commercially attractive in comparison to their silicon counterparts, despite the rapid and successful acceptance of the organic light emitting devices (OLEDs) with a lifespan of million hours [437]. However, Burlingame *et. al.* [438] dispelled this impression by constructing an OPV with a T_{80} of 4.9×10^7 hours, which is equivalent to 27,000 years of outdoor use. T_{80} refers to the time required for the power conversion efficiency to reach 80% of its initial performance. Similarly, Xu *et. al.* [439] fabricated an OPV device with a T_{80} of 34,000 hours, equivalent to a lifespan of 22 years. In 2018, Du *et al.* [440] analysed a polymer solar cell device with a T_{80} of 11,000 hours, which corresponds to a lifespan of 10 years. For OPVs an estimated lifespan of 20 years can be considered commercially competitive and suitable for long term applications.

Although most of the literature on PPV: PCBM materials are focused on improving the efficiency of the PPV: PCBM organic photovoltaic cells, Krens *et. al.* [441] conducted a systematic study on the lifetime of PPV: PCBM bulk heterojunction OPV cells, considering factors such as electrodes, atmospheric conditions, and device preparation. Schuller *et. al.* [442] employed temperature accelerated lifetime measurements to PPV: PCBM bulk heterojunction solar cell. Additionally, Du *et. al.* [440] analysed the T_{80} lifetime of PCBM to be 7400 hours. Furthermore, Burlingame *et. al.* [438] in their research found that the OPV cells have potential for long operational lifespans if pure materials, apt fabrication processes, and right device structure of OPV devices are utilized.

In this chapter, the focus is on designing of organic photovoltaic cell for subdermal implantation with the purpose of powering a cardiac pacemaker. Considering various skin's optical properties from existing literature, their effect on the power of the organic cell under different skin tones is analyzed. Moreover, potential effect due to age and gender on the long-term sustainability of the organic PV device is also analysed.

6.2 FLEXIBLE ORGANIC SOLAR CELL FOR SUBDERMAL IMPLANT

The idea of integrating different types of electronically engineered devices with living organic organisms so as to achieve desired therapeutic result is defined as bioelectronic medicine [443]. To achieve reliable and effective results, it is crucial to establish an unfailing, steady, and consistent interface between a living organic tissue and the electronically active inanimate device. The materials utilized in these electronic devices requires various design aspects which are needed to be considered, as outlined in Table 6.1 [444].

Table 6.1. Characteristic of organic photovoltaic cell and in-organic inserts in evaluation to biological tissue

Characteristics	Inorganic Implants	Organic photovoltaic Cell	Tissue
Composition	Inorganic semiconductors and metals	Polymers and Organic molecules	Protein, lipids, and nucleic acid
Young's modulus	100 GPa	20KPa - 3 GPa	10 kPa
Charge transport carriers	Holes and electrons	Ions, holes, and electrons	Ions
Physical solid state	Hard	Soft	Soft

Living tissues are composed of a complex, active mix of biomolecules, lipids, proteins, and other constituents. The living tissues also possess a remarkable soft and pliable nature. In contrast, inorganic materials tend to be hard and dense. As outlined in Table 6.1, organic polymers exhibit exceptional properties that make them suitable for interfaces between abiotic electronic devices and biotic living tissues, primarily those utilised in biomedical electronic implants. The unique composition, structure, mechanical flexibility, and charge transport mechanism of organic polymers make them well-suited for such applications.

Photovoltaic cells, are designed to capture and harvest energy from external sources such as the sun [445]. These cells have the ability to utilize the incoming irradiance to generate electric current within body [446]. In bulk heterojunction (BHJ) solar cell, both the charge accepter and charge donor materials are blended together. The layer structure of a BHJ cell is illustrated in Fig. 6.1.

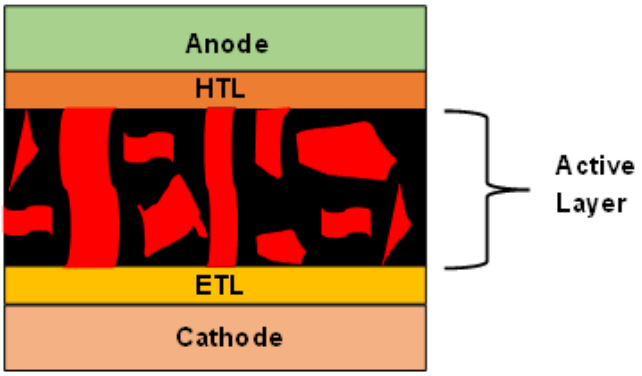

Fig. 6.1 BHJ (Bulk Heterojunction) layer structure of organic solar cell.

The subdermal organic solar have a lifespan of up to 25 years [447]. Various harvesting methods [448, 449] are considered to use energy sources inside the body for instance, electrochemical responses [450], wireless energy [451], motion [452] etc. This chapter tries to see the potentials of organic solar cell's use as a power supply source for implants to over-come restrictions of lithium batteries such as low harvested energy [453, 454], reactions [454], invasive implants [454], external power source requirement [453]. Only a small quantity of daylight is capable to penetrate the skin, predominantly in the near infrared spectrum, demonstrating decent penetrance of human skin [455].

Table 6.2. Energy harvesting methods and their advantages and disadvantages

Energy Harvesting Method	Advantages	Disadvantages	References
Piezoelectricity	Greater power production	Not easily biocompatible, Implant location issues	[456]
Electrostatic	Greater power yield	Higher output impedance	[457]
Lithium batteries	Compatibility with modern bio-medical microelectronic systems	Dimensions, Material toxicity	[458]
Electromagnetic	Unlimited implantable locations	Complex fabrication	[459]
Photo-charging	High power output	Large dimension	[460]
Thermoelectricity	Unlimited lifetime	Low power output	[461]
Nuclear battery	Extensive lifespan Continuous power production	High cost, Radioactive Risks	[458]
Bio-fuel cell	Biocompatibility with tissues	Lifespan, Lower energy production	[462]

Table 6.2 represents diverse energy harvesting practices. However, methods such as Piezoelectricity, Lithium batteries, bio-fuel cells, and nuclear batteries are toxic and non-biocompatible, and they also suffer from implant placement issues. Additionally, methods such as electrostatic, electromagnetic and thermoelectricity suffer from higher output impedance, complex fabrication, and low output power, among other limitations. In the present chapter, a comprehensive analysis is conducted to assess the potential of PPV-PCBM organic PV devices for harvesting solar energy for diverse tones of human skins at various implantation depth.

6.3 OPTICAL PROPERTIES OF HUMAN SKIN

The human skin is composed of three main layers: epidermis, dermis, and subcutaneous tissue. The subcutaneous tissue layer contains subcutaneous fat, which separates skin from underlying bone or muscle. The optical properties associated with skin include absorption (μ_a), reduced scattering coefficients (μ_s'), anisotropy factor (g) and refraction index (n). The primary function skin is to protect underlying tissues. The skin is a complex structure with various parameters and optical properties. The thicknesses and refractive index of skin layers are depicted in Fig. 6.2.

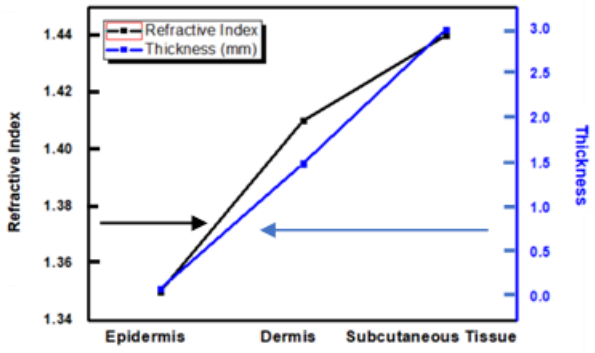

Fig. 6.2 Refractive index and thickness of skin's different layers.

The skin is composed of three layers: the epidermis, dermis, and subcutis or subcutaneous tissue. These layers exhibit distinct optical properties, including the reduced scattering coefficient (μ_s'), anisotropy factor (g), refractive index (n) and absorption coefficient (μ_a). The optical properties of each layer vary depending on the wavelength range being considered. Several works [463-465] have provided information on the optical properties of the human skin. It is important to note that human skin is not transparent. Only a portion of daylight in the range of 700 nm to 1000 nm is able to penetrate the skin, typically up to a depth of 4 mm [466].

The Absorption coefficient (μ_a) is calculated in accordance with the equation (1) [465].

$$\mu_a(\lambda) = 519\left(\frac{\lambda}{500}\right)^{-3} \tag{6.1}$$

The λ in the equation 6.1 represents the wavelength. All three skin layers are wavelength dependent and exhibit distinct optical properties. The coefficient of absorption of blood [467], water [468], and fat [469] are stated in literature.

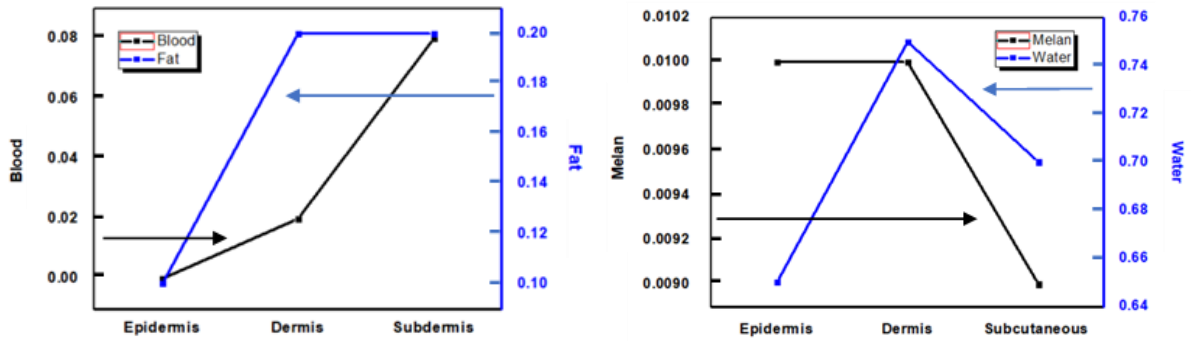

(a) (b)

Fig. 6.3 Volume fractions of skin components (a) Blood and Fat, (b) Melan and Water in the three layers [470, 471]. (Melanosome abbreviated as Melan)

Skin's coefficient of absorption is calculated via summing component's of individual absorption coefficient in harmony with volume fractions (equation 2, Fig. 6.3) [426, 465].

$$\mu_a = \sum VF_k \mu_{a,k} \tag{6.2}$$

The VF_k in equation 6.2 represent the summation of the volume fractions, while $\mu_{a,k}$ represents the summation of the absorption coefficient values. Jacques [465] presented equation for coefficients of reduced scattering for skin and subcutaneous tissue.

$$\mu_s' = a\left(\frac{\lambda}{500}\right)^{-b} \tag{6.3}$$

The μ_s' in equation 6.3 represents the reduced scattering coefficient, where the coefficient a scale the μ_s' and the coefficient b is the scattering power that adjusts the wavelength dependence of the reduced scattering coefficients. These coefficients are presented in Fig. 6.4. The values of the coefficients are adjusted to approximate the actual or real-time values of the human skin layers, aiming to obtain the most accurate real-world results.

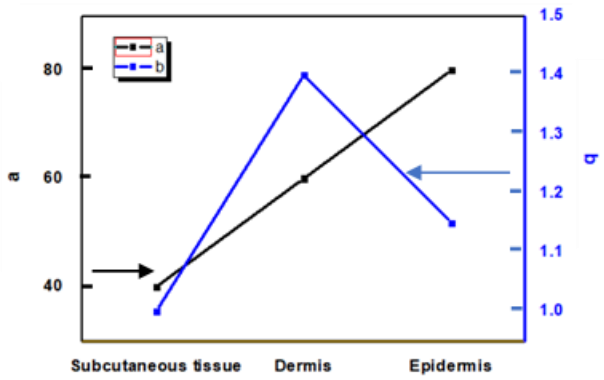

Fig. 6.4 Skin's scattering coefficients (a and b) [465].

The anisotropy in the context of human skin refer to the variation in properties of the skin in different directions or orientations. Human skin exhibits anisotropic behaviour due to the structural arrangements of its components, such as collagen fibres and cellular structure. The factor of anisotropy measured is 0.9 for entire skin layers. Furthermore, the refractive index is a measure of how much speed of light changes as it passes through a material. The refractive index of human skin is an average value, and it is considered as 1.41 for dermis and subcutaneous tissue, and 1.34 for epidermis [472].

6.4 TISSUE MODEL GEOMETRY FOR PHOTOVOLTAIC CELL IMPLANTATION

The tissue model geometry is depicted in Fig. 6.5, which illustrates the organic solar cell implantation site inside the skin. The tissue model is divided into three layers: the epidermis, dermis, and subcutaneous tissue. The Human skin can be viewed as multi-layered assembly with each layer categorized by its own different optical properties [471]. The thickness of Epidermis layer is considered to be 0.1 millimeter (mm) and that of dermis is 1.4 mm. The remaining portion of the model represents subcutaneous tissue layer, which serves as the site for photovoltaic device placement [473]. The amount of sunlight absorbed by the solar cell depends on the placement of organic PV cell (ς) and the wavelength, which can be calculated using equation (4) [474, 426].

$$\varsigma = \frac{\mathrm{N_{ABS}\ (Incident\ photons\ absorbed)}}{\mathrm{A_{TS}\ (Top\ surface\ area)}} \times \frac{\mathrm{N_{TOT}\ (Total\ projected\ photons)}}{\mathrm{A_{MS}\ (Surface\ area)}} \tag{6.4}$$

Where, N_{ABS} represents the sum of incoming photons absorbed by the PV device, A_{TS} represents the top surface area of PV device. N_{TOT} represents the sum of overall photons projected and A_{MS} represents the area of the model surface. The pure atmospheric irradiance is defined by the global standard spectrum known as Air Mass 1.5 (AM 1.5) [475]. The irradiance power associated with Air Mass 1.5 is 100 mW/cm^2.

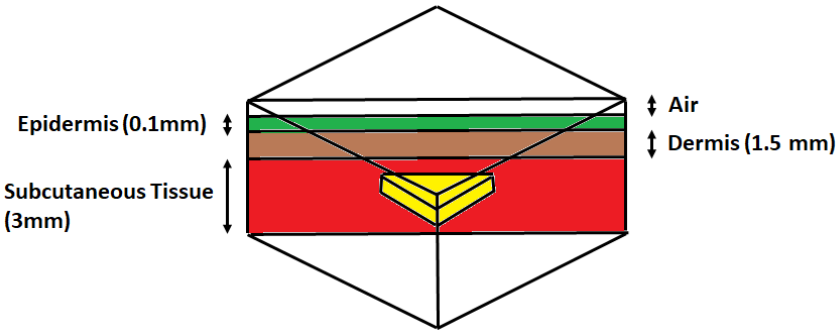

Fig. 6.5 View of the tissue model geometry illustrating organic solar cell implantation site within the skin. The organic solar cell is represented by the yellow colour. The distinct skin layers, namely the epidermis, dermis and subcutaneous tissue, are depicted in green, brown and red colours, respectively.

Photon flux (ϕ) is calculated by dividing the irradiance by the energy of photon. Each photovoltaic (PV) cell has its own External Quantum Efficiency (*EQE*), which is dependent on the wavelength of the light and represents the spectrum where the organic PV cell exhibits its

finest performance. Additionally, each PV cell is characterised by its open-circuit voltage (V_{OC}) and short-circuit current (I_{SC}) which is defined as [426]:

$$\mathrm{I_{SC}} = \int_{\lambda=400\ \mathrm{nm}}^{750\ \mathrm{nm}} \phi \times \varsigma \times \mathrm{EQE} \times \mathrm{Q} \times \mathrm{d}\lambda \tag{6.5}$$

Where, λ represents wavelength, ϕ is the photon flux, ς is the placement of organic PV cell, the *EQE* is external quantum efficiency, *Q* represents charge. The Power output of a photovoltaic cell with area of A_{TS} is stated by equation (6.6). The parameter fill factor is associated with PV cells maximum power output [426].

$$\mathrm{P_{OUT}} = \mathrm{FF} \times \mathrm{V_{OC}} \times \mathrm{I_{SC}} \times \mathrm{A_{TS}} \tag{6.6}$$

Where, P_{OUT} represents power output, *FF* is the Fill Factor, V_{OC} represents open circuit voltage, I_{SC} represents short circuit current, and A_{TS} is the PV cell area in meter square (m^2). The Fill Factor is a performance parameter of a solar cell and is associated with the maximum output power. A modern Cardiac pacemaker necessitates a normal operational power of roughly ten microwatts. The energy required to operate a pacemaker for 24 hours is approximately 0.24 milli Watthours (mWh) or 0.864 Joules.

6.5 CHARACTERISTICS ANALYSIS ORGANIC SOLAR CELL FOR IMPLANTATION

The analysis of BHJ organic solar cell arrangement is carried out using the software simulator Silvaco-Atlas-TCAD. It integrates models and mathematical equations to thoroughly and comprehensive analyze the internal physics of the device [476, 477]. By defining the material properties, new materials can be incorporated into the simulation. The biasing conditions can be applied to obtain various device parameters such as current density, electron and hole concentration, recombination rate, and more. The dimensions of the device are precisely defined, with specific material regions specified by their respective material properties such as energy levels and work function. Simulators based on computational models play a significant and crucial role in determining the accurate behaviour of the device and improving its overall performance.

The precision of the organic PV cell in the Atlas TCAD simulation software is achieved through the availability of various robust optical transmission models. In this chapter, Indium Tin Oxide (ITO); poly (3,4 ethylenedioxythiophene): poly(styrenesulfonate) (PEDOT: PSS);

PPV/PCBM; Lithium Fluoride (LiF); Aluminium (Al) BHJ organic solar cell is used. The length of the PV cell's length is considered to be 1 micrometer. Computational modelling-based device simulators are well-known for predicting and improving the performance of a device before its real-world application. The systematic simulation of the organic PV cell involves computing elementary mathematical and statistical equations to analyze the performance and internal physics of the device. These computational equations define the charge transport mechanism. The Atlas simulator is capable of demonstrating the processes that govern charge transport, charge photogeneration, and recombination in a BHJ organic PV cell.

Fig. 6.6 illustrates the design of a subdermal PV cell capable of harvesting sunlight. The proposed design for solar power harvesting consists of a BHJ organic PV cell composed of ITO/PEDOT:PSS/PPV-PCBM/LiF/Al. By examining the internal workings of the device, we gain significant insight into its internal physics. The layer thickness of the PV cell are considered as 10 nm for Al, 0.6 nm for LiF, 80nm for PPV/PCBM, 20 nm for PEDOT: PSS and 10 nm for ITO. Additionally, to accurately simulate human skin under solar illumination, three additional layers with a total thickness of 2 mm are included on top of the PPV: PCBM organic PV cell. These layers have specific optical properties of the skin such as absorption (μ_a) and scattering (μ_s) coefficients. This entire arrangement represents the skin area that covers the organic PV cell when exposed to daylight, and software simulation are performed accordingly. The average output power achieved is in the range of milliwatts (mW), while the total power consumed by modern cardiac pacemaker is approximately 10 microwatts [426].

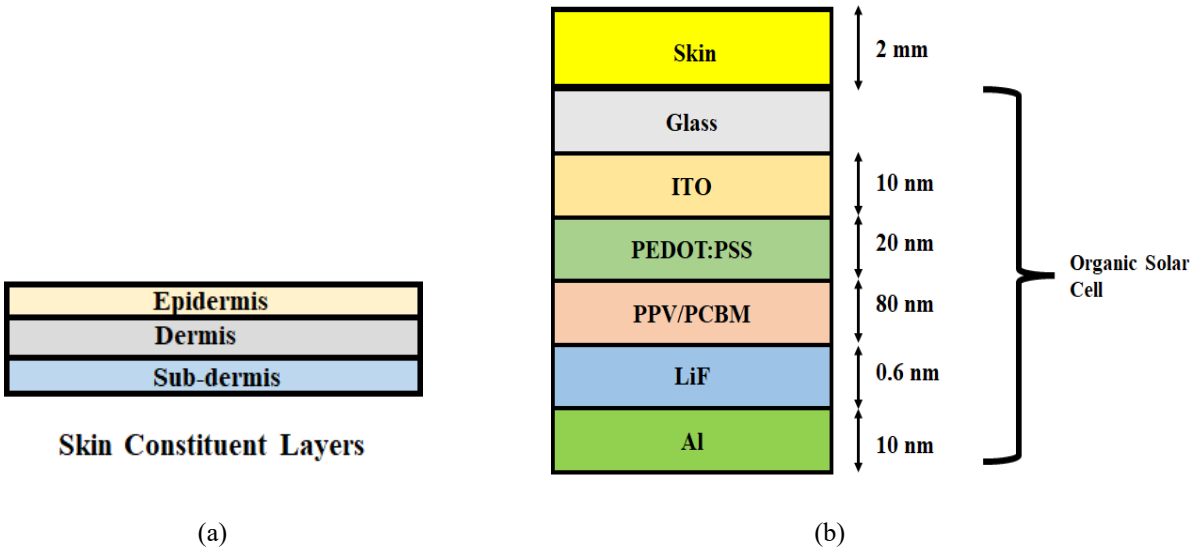

Fig. 6.6 (a) Top layer imitating skin with constituent layer optical properties and (b) Device assembly of organic solar cell when implanted beneath human skin.

The performance of the proposed organic PV cell design can be verified by measuring its characteristic I-V curve and other solar PV parameters, such as the open-circuit voltage (V_{OC}). The PPV/PCBM BHJ organic PV cell is simulated using Silvaco Atlas, which is an industry standard device software simulator [478-481]. In order to validate the performance of the proposed photovoltaic cell, it is compared with an experimentally analysed the device [482]. The simulation parameters for the device include an electron mobility of 2.5×10^{-7} m^2 V^{-1} s^{-1}, a hole mobility of 0.3×10^{-7} m^2 V^{-1} s^{-1}, an energy bandgap of 1.34 eV, a dielectric constant of 3×10^{-11} Fm^{-1}, and a density of state of 2.5×10^{25}. By simulating the device with these parameters and comparing its performance with the experimental results, the validity and accuracy of the proposed organic PV cell design could be assessed.

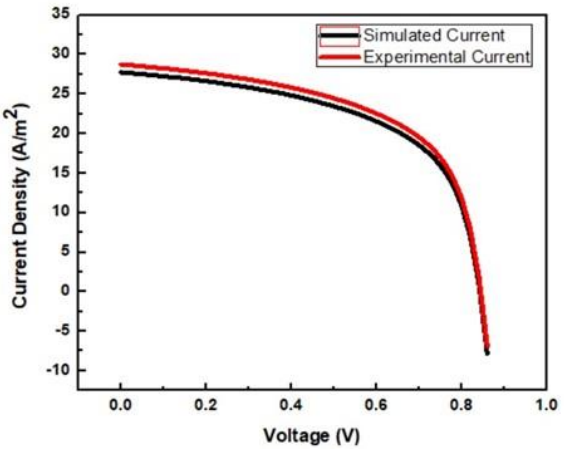

Fig. 6.7 I-V characteristics plots of the solar cells the red colour curve is experimental cell's current and black colour curve is simulated cell's current.

Fig. 6.7 represents the current-voltage curve of the simulated organic PV cell (black curve) and the experimental organic PV cell (red curve) for OCC-PPV/PCBM. The short-circuit current density (J_{SC}) obtained from the simulation is 28 A/m^2. The experimentally measured open-circuited voltage (V_{OC}) is 0.90 volts, while the simulated open circuit voltage is approximately 0.84 volts, showing a close approximation to the experimental value. The performance parameters obtained from the organic PV cell are as follows: a Fill Factor of 52.5%, an efficiency of 1.22%, short-circuit current density of 28 A/m^2, and open circuit voltage of 0.8 Volts. This excellent agreement between the simulated and experimental current-voltage characteristic curves indicates that the performance of the PPV-PCBM organic PV cell is promising for the intended application of a sub-dermal PV cell to efficiently harvest solar energy for powering a cardiac pacemaker. These results validate the suitability of the proposed

organic PV cell design and demonstrate its potential for practical implementation in the desired biomedical application.

6.6 SKIN ABSORPTION AND SCATTERING COEFFICIENTS AND ANALYSIS OF LIGHT PENETRATION DEPTH

The absorption and scattering coefficients of human skin are the main optical properties that describe how light interacts with the skin tissue. The absorption coefficient represents the rate at which light is absorbed by the skin per unit distance, indicating the fraction of light that is absorbed or transmitted through the skin. On the other hand, the scattering coefficient quantifies the scattering of light within the skin tissue, reflecting the rate at which light is redirected or scattered in various directions during its interacts with the skin.

In the following section 6.6.1, the absorption and scattering coefficients of the three different skin tones are discussed and compared. Additionally, sub-section 6.6.2 focuses on the skin penetration depth, which refers to the distance that sunlight can penetrate into the skin. This depth represents how far light can travel before it is absorbed or scattered and is influenced by the skin's absorption and scattering coefficients. Understanding the skin penetration depth is crucial in pharmaceutical research. In this case, the penetration depth determines the depth at which incoming sunlight can reach within the skin layers, aiding in determination of the optimal placement site for the organic solar cell.

6.6.1 Absorption and scattering coefficients

As one single literature source did not provide all absorption and scattering coefficients for the three types of skin (Caucasian, African and Asian) in the wavelength range of 400 to 700 nm, multiple literatures are consulted, combined, and inferred to obtain the coefficients to be used for the simulation in order to obtain accurate results. The absorption coefficients are obtained from Bashkatov *et al.* [464], and reduced scattering coefficients are obtained from Jacques [465]. Specifically, Bashkatov *et al.* [464] provided the absorption coefficients for the range of 400 to 750 nanometer (nm) and Jacques [465] provided reduced scattering coefficients for the range of 500 to 750 nm. For the range of 400 to 500 nm, the reduced scattering coefficients from Bashkatov *et al.* [464] are used, as this range of coefficients was not covered in the Jacques [465] literature.

Additionally, literature by Simpson [470] *et al.* is used to determine the absorption and scattering coefficients specifically for Caucasian and African skin types in the range of 600 to 750 nm, and for the missing coefficients in the range of 400 to 600 nm, data from literatures other relevant literature such as Bashkatov *et al.* [464], Veen *et al.* [469] are considered. It should be noted that while some literature provided the coefficient data for the dermis layer, but not for subdermal layer or subcutaneous tissues. This complicated issue of not having all the parameters related to the three skin types in one specific literature necessitated the combination of the best accepted and available literatures sources to form a consolidated dataset for simulations ensuring valid and accurate results.

Bashkatov *et al.* [464] measured the absorption and scattering coefficients of subcutaneous adipose tissue and mucous in the range of 400 to 2000 nm. The measurements were performed in vitro using the samples of skin collected from post-mortem cases and fresh subcutaneous adipose tissue which were taken from patient peritoneum area while surgery. For experimental data processing and tissue optical property determination method described in Prahl *et al.* [483] is utilized which allowed to determine absorption (μ_a) and scattering (μ_s) coefficients. Similarly, Chan *et al.* [463] measured the in vitro optical properties of the tissue for photomedicine applications, covering the visible and infrared range from 400 to 1800 nm.

The measurements were conducted using specimens of Caucasian and Hispanic donor skin obtained from a skin bank. Harvesting of tissues was done within 24 hours of post-mortem. The three specimens taken were male Caucasian donor of age 53, male Hispanic donor age 35 and female Caucasian donor age 72. The papers by Bashkatov *et al.* [464] and Chen *et al.* [463] have gained widespread acceptance and are frequently referenced in research papers related to biomedical and therapeutic treatment studies. Additionally, in 2021, Finlayson *et al.* [484] used Monte Carlo simulations to analyse light propagation through the skin in the wavelength range of 200 to 1000 nm. The deviation between the data obtained from [463, 464] and given by Finlayson *et al.* [484] is minimal.

Furthermore, Finlayson *et al.* used the equations developed by Bashkatov [464] in their simulations, confirming the widespread acceptance and reliability of the reference [463, 464] in research. Similarly, Kono *et al.* [485] conducted a study on 198 Japanese volunteers to analyse the in vivo scattering and absorption coefficients. They also analysed the effects of gender and age on these optical properties. Although the absorption and scattering coefficients vary with the gender and age, the deviations do not show a consistent trend of high variation.

In 2016, Bereuter *et al.* [474] conducted a study on subcutaneous photovoltaic energy harvesting and found that individuals above the age of 65 years achieved higher power generation in comparison to the younger individuals, due to more leisure time and spending more time under the sun. The transfer of power to biomedical implant via wired connections piercing the skin can pose a risk of infection to the patients. Therefore, generating power beneath the human skin can mitigate this risk. The organic photovoltaic cell can be implanted in areas such as inner forearm, inner or dorsal surface of hands or the neck region. The selection of implant location in the body primarily depends on the amount of incident daylight received by the specific area of the body.

In 2010, Firooz *et al.* [486] studied the variation of skin parameters with respect to age and gender by taking a sample of fifty healthy individuals both males and females in five age groups from 10 years to 60 years in Iran. The authors then reported that the gender is independent of melanin index, which is a dominant aspect in determining absorption coefficients. Therefore, it can be concluded that gender and absorption coefficients are unrelated. However, in 2019, Kono *et al.* [485] reported a slight difference (~ 0.4) in the absorption coefficients between Japanese males and females (considering 198 volunteers).

In the context of the proposed solar cell, it is capable of producing sufficient power for African skin types, generating approximately 50 microwatts (μW) with maximum absorption coefficients. Even if we consider the slight variation in absorption coefficients reported by Kono *et al.* [485] as standard, the power produced by the proposed photovoltaic cell is still approximately 5 times higher than the operational power (~ 10 μW) required by modern cardiac pacemakers.

Therefore, the proposed subdermal solar cell is capable of sustaining minor variations in absorption coefficients due to gender and age. It can provide sufficient power to a pacemaker regardless of these factors. Similarly, Mayes *et al.* [487] in accordance with the study conducted in China reported that no significant connection between pigmentation of the skin and age. Although, Kono *et al.* [485] reported slight variation in absorption coefficient with age, which can be sufficiently managed and accommodated by the proposed solar cell. Therefore, the subdermal solar cell is highly suitable for the elderly patients and even for immobile or disabled people by artificial lighting.

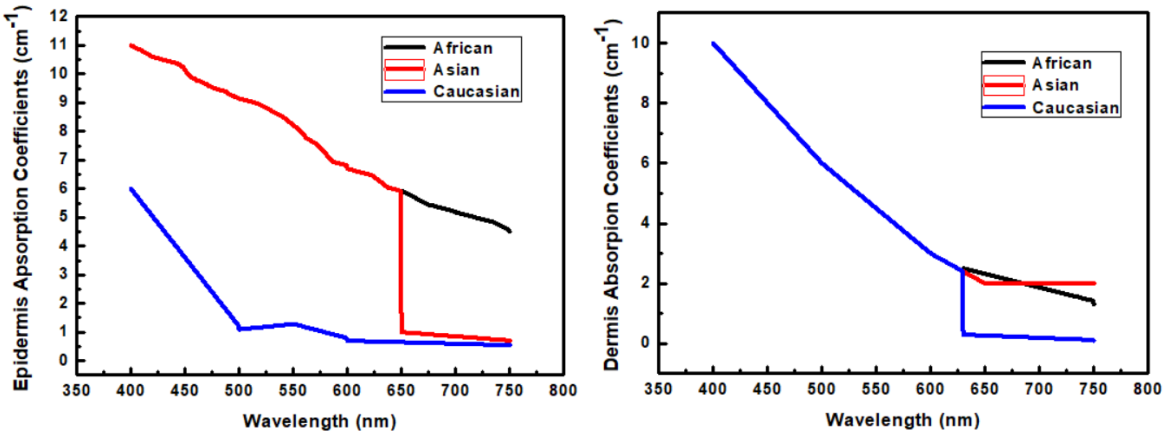

(a)

(b)

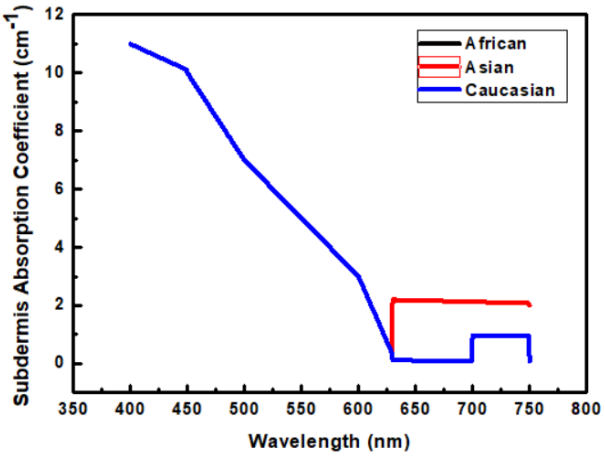

(c)

Fig. 6.8 Coefficients of absorption (μ_a) of (a) epidermis, (b) dermis and (c) subcutaneous tissue verse wavelength ranges from 400 to 750 nm.

Fig. 6.8 (a) represents the literature data for coefficients of absorption (μ_a) of the top layer human skin layer (epidermis) for Caucasian, Asian and African skin types. The data is plotted as a function of wavelength in the visible light band ranging from 400 - 750 nanometers (nm). Similarly, absorption coefficients of middle layer (dermis) and the bottom skin layer (sub-dermis tissue) of the skin as a function of wavelength are represented in Fig. 6.8 (b) and Fig. 6.8 (c) respectively for Caucasian, Asian and African skin types [470, 488].

The absorption coefficients provide information about the amount of sunlight absorbed at specific wavelengths. The absorption data for Caucasian, Asian and African skin tones are plotted as blue, red, and black colour respectively. From the plots, it can be observed that the absorption coefficients for African skin tone are generally higher in comparison to Asian and Caucasian skin tones.

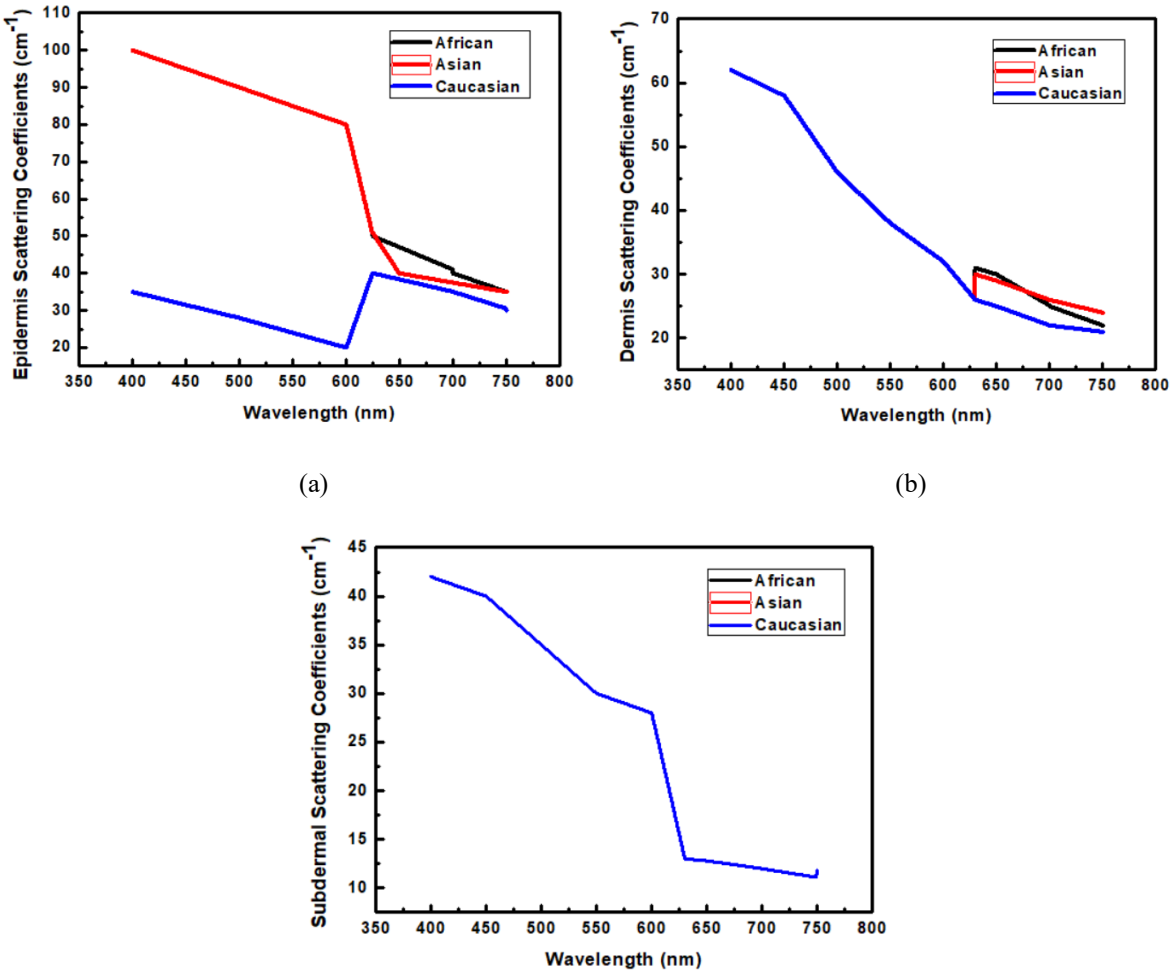

Fig. 6.9 Coefficients of reduced scattering (μ_s') of (a) epidermis, (b) dermis and (c) subcutaneous tissue as a function of wavelength range from 400 to 750 nm.

In the same manner absorption coefficient for Asian skin tone are higher than those for Caucasian skin tone in the visible spectrum, and decrease gradually as the wavelength increases [470]. The plots of absorption spectrum in Fig. 6.8 provides a precise and valuable assessment of the sunlight absorbed by human skin, which can be utilized to estimate and analyse the amount of daylight captured by the sub-dermal organic PV device.

Fig. 6.9 (a) represents the literature data for the coefficients of reduced scattering (μ_s') specially for the epidermis layer for Caucasian, Asian and African skin tones as a function of wavelength in visible light spectrum (400 to 750 nm). Similarly, scattering coefficients for middle (dermis) and bottom (sub-dermis tissue) layers as a function of wavelength are depicted in Fig. 6.9 (b) and Fig. 6.9 (c) [488] respectively.

The scattering coefficient, indicate that there are no substantial differences among the African, Asian, and Caucasian skin types [470]. The scattering spectrum exhibits a strong decline as the wavelength increases. In conclusion, while optical properties of the skin vary slightly with age and gender, these variations are minor. Therefore, the proposed organic solar cell is capable of accommodating these slight changes and can consistently provide power to pacemakers.

6.6.2 Skin penetration depth

The depth of penetration of sunlight into the human skin is determined by the equation (6.7) [489]. The assessment of penetration depth is a significant parameter for quantifying the amount of inbound solar radiation absorbed by the human skin.

$$\delta = \frac{1}{\sqrt{3\mu_a(\mu_a+\mu_s')}} \tag{6.7}$$

The Fig. 6.10 illustrates the calculated penetration depth of light based on the reduced scattering and absorption coefficients. The plot in Fig. 6.10 shows depth of light penetration as a function of wavelength in the visible range (400 to 750 nanometers). From the Fig. 6.10, it can be observed that the penetration depth increases with increasing wavelength. The highest penetration depth of 2.1 millimeters is observed at wavelength of 750 nanometers. This indicates that incident sunlight with higher energy (lower wavelength) has a shallower penetration depth in contrast to incident sunlight with lower energy. This is because lower energy sunlight or photons are not absorbed easily and therefore can penetrate deeper into the skin.

To grasp the concept of light penetration depth, the absorption of blue light, comprising higher energy and shorter wavelength, occurs primarily at the top surface. On the other hand, red light, with lower energy and longer wavelength, is absorbed to a lesser extent. For instance, in a silicon material based photovoltaic cell, blue light will be absorbed within few millimeters, whereas red light may penetrate several hundred millimeters before being fully absorbed [490].

Furthermore, Fig. 6.10 clearly indicates that the penetration depth is dependent on the wavelength of light. The highest penetration depth is observed in the range of 650 to 750 nanometers, where sunlight can penetrate up to 2.1 millimeters, exceeding the thickness of epidermis and dermis layers, reaching into the subcutaneous tissue. Consequently, this

observation provides valuable insight into selecting an appropriate implant location (depth) within the body.

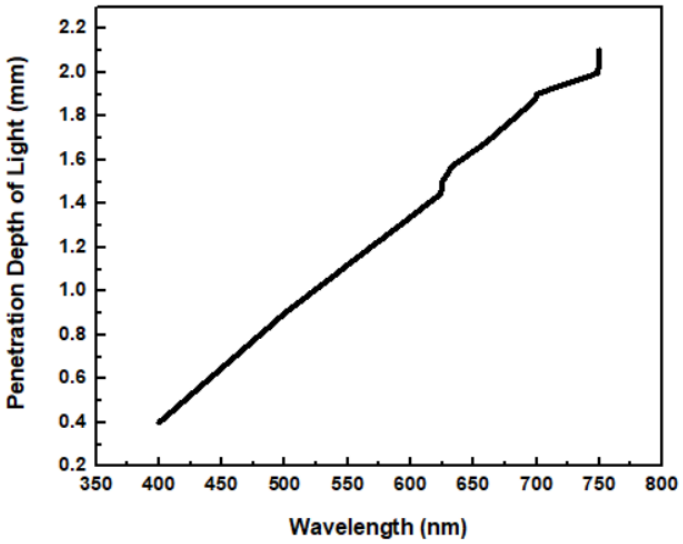

Fig. 6.10 Sunlight penetration depth inside the skin for wavelengths of 400 - 750 nm.

The photovoltaic device can be surgically implanted beneath the human skin in various locations such as the inner forearm, inner or dorsal surface of hands, the area in-between the thumb and forefinger or the neck region. The choice of implant location within the body is primarily determined by the amount of incident daylight received by that particular body area. Therefore, by selecting an appropriate location for the implant, optimal exposure to sunlight can be ensured, maximizing the efficiency of the device in harvesting solar energy.

6.7 POWER ANALYSIS FOR SOLAR CELL BASED ON PLACEMENT FOR ALL SKIN TYPES

In subcutaneously implanted organic PV cell, the harvested energy is limited by the amount of light absorbed and scattered. The characteristic of subdermally implanted organic PV cell is calculated and observed under normal daylight illumination. To validate the performance of the subdermally implanted organic PV cell, numerous characteristic graphs are plotted to measure its characteristics in various settings, such as current as a function of voltage (I-V) and power as a function of voltage (P-V) graphs.

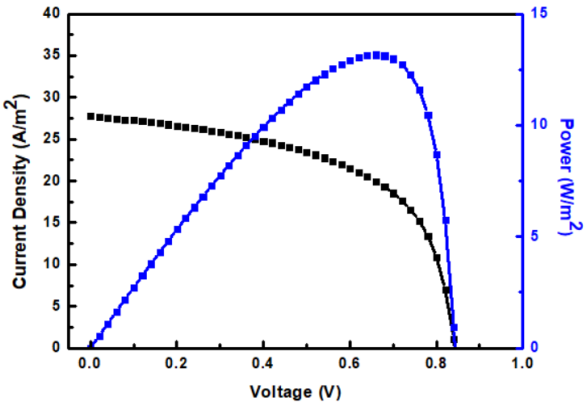
Current Density (A/m2)
Power (W/m2)
Voltage (V)

(a)

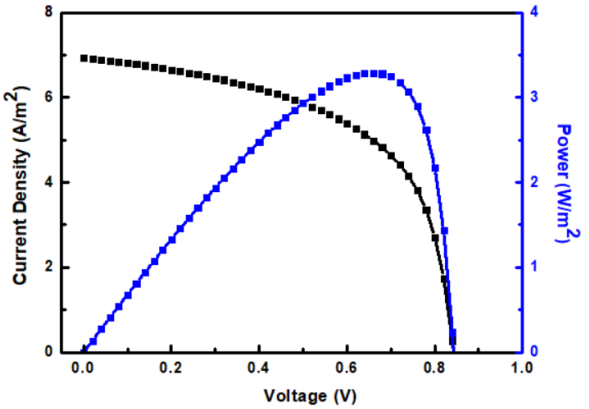
Current Density (A/m2)
Power (W/m2)
Voltage (V)

(b)

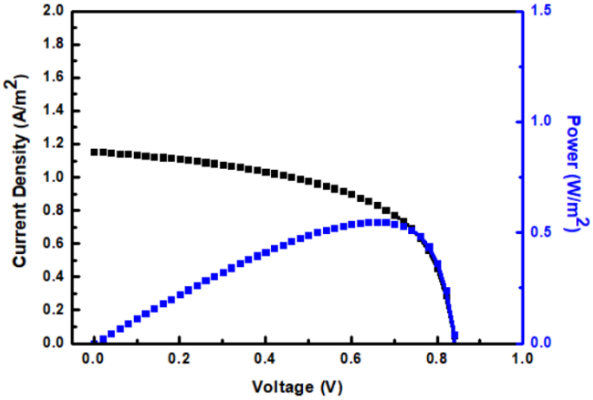
Current Density (A/m2)
Power (W/m2)
Voltage (V)

(c)

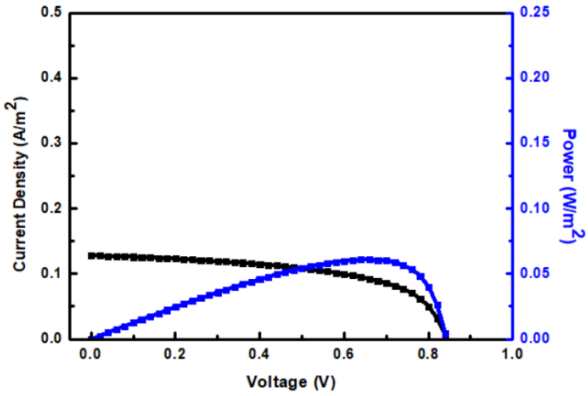
Current Density (A/m2)
Power (W/m2)
Voltage (V)

(d)

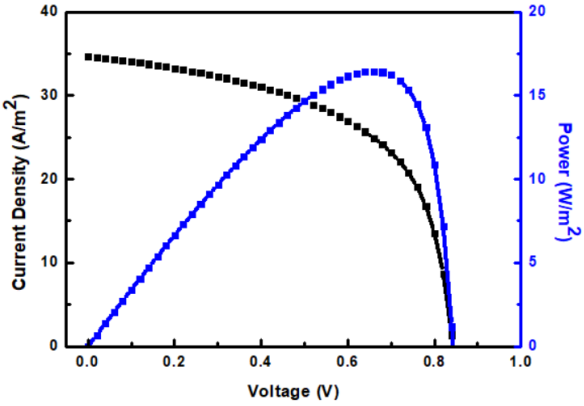
Current Density (A/m2)
Power (W/m2)
Voltage (V)

(e)

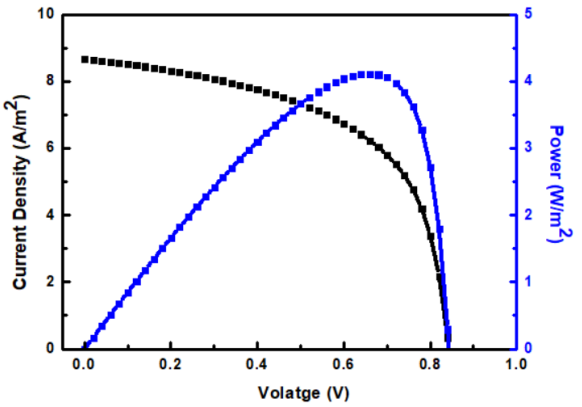
Current Density (A/m2)
Power (W/m2)
Volatge (V)

(f)

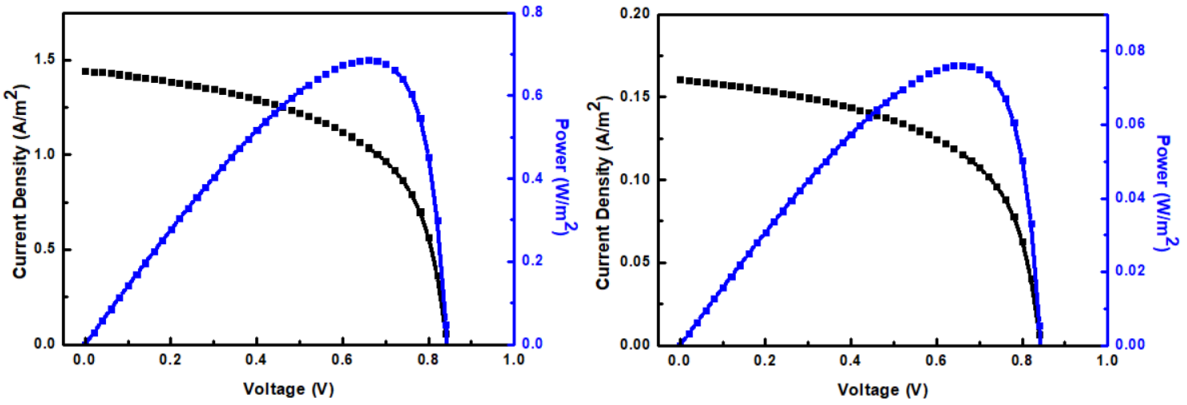

(g) (h)

Fig. 6.11 Characteristics I-V & P-V curves of organic solar device for (a) Uncovered solar cell, (b) Caucasian, (c) Asian, (d) African skin tones attained for AM 1.5 irradiance condition, (e) Uncovered solar cell, (f) Caucasian, (g) Asian and (h) African skin tones attained for AM 1.0 irradiance condition.

Fig. 6.11 depicts the simulated I-V plot obtained from a PPV-PCBM BHJ organic PV cell. The Current-Voltage plots represented in Fig. 6.11 provide a comparison of different photocurrents achieved. The highest photo-current density observed for the uncovered PV device is 28.1 A/m^2, while for enclosed (underneath the skin) PV cell (for Caucasian skin tone), it is 6.8 A/m^2 at 0 volt. Fig. 6.11 (a) displays the I-V and P-V graphs of the organic solar cell when subjected to AM 1.5 illumination (1000 W/m^2).

The plots in Fig. 6.11 depicts the characteristics of the organic photovoltaic cell for both covered and uncovered configurations. In Fig. 6.11 (a) the double Y plot shows the show current-voltage characteristic curve in black, and the power-voltage characteristic curve in blue for the organic PV cell is placed under direct incoming sunlight (uncovered PV cell). Similarly, Figs. 6.11 (b), 6.11 (c), and 6.11 (d) represent the double Y plot (black color arc for current-voltage and blue for power-voltage characteristics) for Caucasian, Asian and African skin tones, respectively, when the PV is positioned at a depth of 2 mm underneath the human skin, specifically within the subcutaneous layer beneath the epidermis and dermis skin layers.

In Fig. 6.11 (a), it can be observed that the current has a maximum magnitude of 28 A/m^2 when the organic PV device is exposed to direct daylight (uncovered solar cell). The magnitude of photocurrent decreases by approximately six folds to a magnitude of 6.8 A/m^2 when the organic PV cell is placed beneath Caucasian skin tone. Furthermore, the current magnitude decreases to 1.2 A/m^2 when the organic PV cell is placed beneath Asian skin tone, and the decrease in magnitude becomes more significant when the organic PV cell in placed beneath African skin

tone. The trend in the I-V plot can be attributed to the higher coefficients of absorption of skin layers for African skin tone compared to Asian and Caucasian skin tones. The same trend can be observed between Asian and Caucasian skin tones.

The P-V plots for different skin tone also demonstrates same trend. The P-V plot reaches its peak for the uncovered organic PV cell and decreases for Caucasian skin tone. Furthermore, the P-V plot decreases even further for the Asian and African skin tones because of their higher absorption coefficients. The higher absorption coefficients result in greater amount of incoming photons being absorbed by the skin layers, leaving a reduced quantity of photons to reach the implanted photovoltaic device for absorption and electric current generation.

In identical manner, the organic PV cell is simulated with AM 1.0 illumination settings, which has a higher irradiance power of 1376 W/m^2. Figs. 6.11 (e), 6.11 (f), 6.11 (g) and 6.11 (h) present the I-V and P-V curves for this simulation. It can be observed that the current produced by the organic photovoltaic cell under AM 1.0 illumination is notably greater than that under AM 1.5 illumination. This, confirms the fact that higher irradiance power results in greater generation of electric current in the organic solar cell, as greater amount of photons are being absorbed. This observation is further supported by comparing the P-V for AM 1.5 and AM 1.0 illumination.

6.8 IMPACT OF SKIN THICKNESS VARIATION

Fig. 6.12 illustrates the relationship between the power output of the implanted organic photovoltaic cell (covered) and skin thickness, ranging from 2 to 1 mm. The black, red, and blue colour plots correspond to the Caucasian, Asian and African skin tones, respectively. Form the curves presented in Fig. 6.12, it can be deduced that at a skin thickness of 1 mm, the power output is highest for all three tones of and begins to decrease as the skin thickness increases from 1 to 2 mm.This indicates that the power-density of the sub-dermally implanted organic PV device is inversely related to the thickness of the skin, and it depends on the amount of light reaching the subdermal PV cell through the human skin. The photovoltaic device generates more output power when exposed in bright sunlight. Furthermore, from the graphs in Fig. 6.12, it can also be inferred that different skin tones of same thickness can exhibit different power densities.

The maximum power output achieved for the Caucasian skin tone is 4.28 milliwatts at a thickness of 1 millimeter, while the lowest power output achieved is 2.2 milliwatts at a thickness of 2 millimeters. Similar, for the Asian and African skin tones, the highest output power obtained are 0.73 milliwatts (or 730 microwatts) and 0.085 milliwatts (or 85 microwatts) at a thickness of 1 millimeter, respectively. The lowest power output attained are 0.44 milliwatts (or 440 microwatts) and 0.051 milliwatts (or 52 microwatts) at 2 millimeter thickness, respectively, when the device is subjects to AM 1.5 standard global spectrum settings.

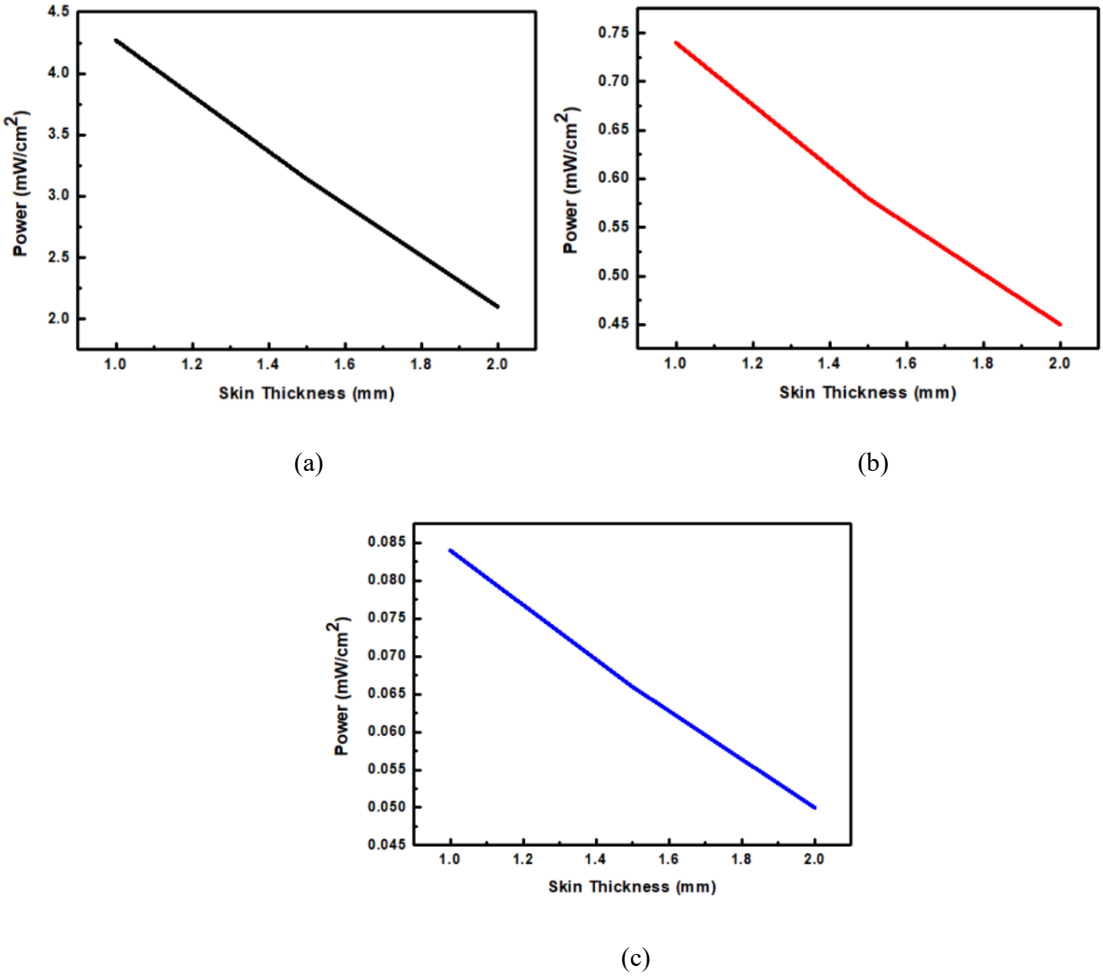

Fig. 6.12 Power output verses thickness skin for (a) Caucasian, (b) Asian and (d) African skin tones.

From Figs. 6.10 to 6.12 it can be inferred that the power generated by a sub-dermally implanted organic PV cell depends on the amount of sunlight received by it, and the amount of light reaching the PV cell through human skin depends on the skin tone and thickness in which it is positioned. Darker skin tones tend to absorb more incident sunlight, resulting in reduced

number of photons reaching the sub-dermally implanted PV cell. As a result, the photovoltaic cell generates less power even when the skin thickness is the same.

The distribution of melanin pigmentation in the epidermis layer of the skin significantly influences the skin tone. Melanin pigmentation absorbs light in visible and ultraviolet spectrum [491]. Darker skin tones have higher concentration of melanin pigmentation, which reduces the amount of sunlight reaching the sub-dermally implemented organic PV cell. Thicker skin scatters incident sunlight more, resulting in decreased sunlight reaching the sub-dermally implanted PV cell and subsequently lower power production.

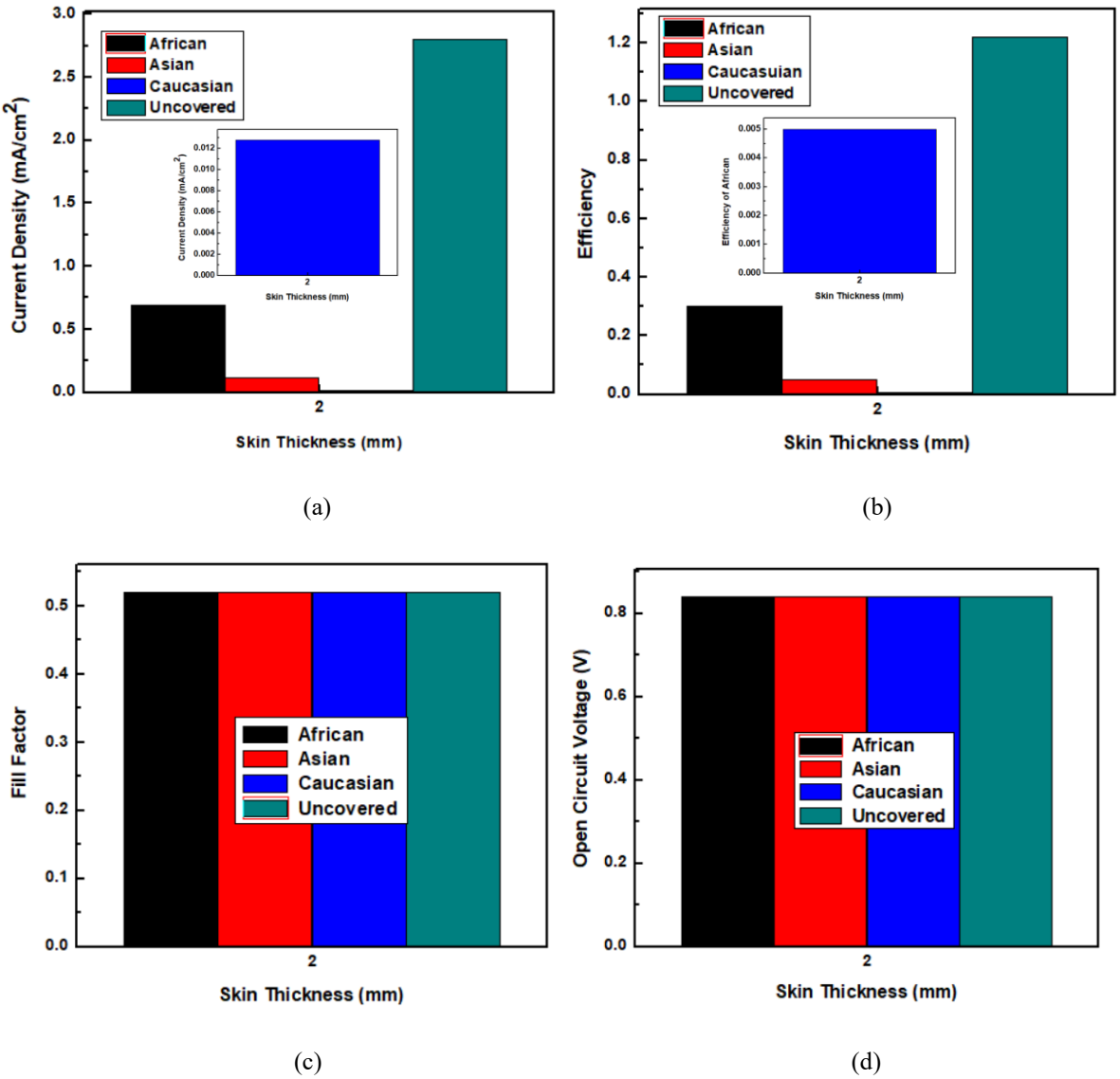

Fig. 6.13 The graphical representation of (a) Circuit density, (b) Efficiency, (c) Fill Factor and (d) Open circuit voltage at the sub-dermal skin depth of 2 millimetres.

The power generated by the sub-dermal PV cell falls within the range reported in previous studies using piezoelectric cells (0.12-0.19 μW/cm^2) [492] or glucose-based bio-fuel cell (0.2-1.2 mW/cm^2) [493]. This power output is sufficient to operate a cardiac pacemaker, which typically requires an operational power of 10 to 40 μW. In Fig. 6.13, the performance parameters of the sub-dermally implanted organic PV device are presented for both the uncovered (sea green color) and covered conditions. The different skin tones are represented by black (Caucasian), red (Asian), and blue (African) colours. Fig. 6.13 (a) shows the short-circuit current density of the PV device at a skin depth of 2 millimeter, while Fig. 6.13 (b) displays the efficiency of PV device. For the Caucasian skin tone, the short-circuit current density and efficiency of the subdermal implanted PV cell decreases from 1.21% to 0.3%, and the efficiency declines from 2.9 mA/cm^2 to 0.698 mA/cm^2.

Fig. 6.13 (c) represents Fill Factor of implanted PV device at a skin implementation depth of 2 millimetres. The Fill Factor is a measure of the efficiency of the solar cell. Similarly, Fig. 6.13 (d) presents the open circuit voltage of the PV device at the same skin implementation depth. The open circuit voltage is the maximum voltage generated by the solar cell when no external load is connected. It is primarily determined by the energy level of the materials used in the solar cell, as well as the contacts and interfaces within the device. In the plots, it can be observed that the open-circuit voltage remains constant at 0.84 volts and the Fill Factor at 52%, and both of them do not show any key deviation even after the device is implemented underneath the human skin. This specifies that both are determined by the intrinsic properties of the solar cell materials.

6.9 CHARGING TIME ANALYSIS UNDER DIFFERENT ILLUMINATION CONDITIONS

The power requirement for the functioning of a cardiac pacemaker is approximately of 10 μW over a period of twenty-four (24) hours, resulting in a total energy consumption of 0.25-milliwatt hour (mWh) or 0.86 Joules. This calculation is based on the relationship between power and energy as defined in equation (6.8).

$$\text{Energy} = \text{Power} \times \text{Time} \tag{6.8}$$

The Maximum power density achieved for the implanted sub-dermal organic PV device at a skin depth of 2 millimeter is 2.2 mW/cm^2 for Caucasian skin tone, considering the area of the solar cell to be 1 cm^2. Given that the energy required to power a cardiac pacemaker for twenty-

four hours is 0.24 milliwatt hour, by using equation (6.8) the time required to fully charge a battery could be estimated. Based on the calculation, the approximate charging time would be around six (6) minutes. From this, we conclude that the implemented organic PV device is capable of sufficiently charging a rechargeable battery of appropriate size for a pacemaker which can operate a cardiac pacemaker for twenty-four (24) hours, even in the absence of direct sunlight, at a skin depth of 2 millimeters. Therefore, the device is capable of operating in low-light or dim conditions.

Furthermore, it can be inferred that the implanted sub-dermal organic PV device directly power a cardiac pacemaker when placed under standard illumination conditions. Additionally, artificial lighting can as well be utilized to power the cardiac pacemaker indoors, as indoor lighting systems such as LEDs and halogen bulbs can generate a substantial amount of power. For example, an indoor halogen bulb emanates a spectrum ranging from 400 to beyond 1100 nm, while the spectrum of a LED light is from 400 to 700 nm [494]. Since the implanted organic PV cell presented in this chapter operates within the spectral range of 400 to 750 nm, as it has a bandgap energy of 1.34 eV, the photovoltaic cell can generate sufficient power to operate for twenty-four (24) hours using such artificial lighting sources.

Therefore, the dialogue in the previous segment strongly positions that the implanted sub-dermal solar cell can effectively power a pacemaker for a period of 25 years, considering lifetime of the organic solar cell exceeds twenty-five years. This extended lifetime of the organic solar cells correspondingly confirms use of sub-dermal implanted organic solar cells as the optimal method for operating and powering modern cardiac pacemaker compared to other power supply approaches.

6.10 SUMMARY OF IMPORTANT RESULTS

1. The objective of this chapter is to explore and analyse potential circumstances for the utilization of PVV-PCBM sub-dermal PV cell in harvesting the solar energy. This is achieved by taking into account the optical properties of the skin and considering a chosen skin thickness of 2 millimeters.
2. This chapter aims to explore how subdermal PV cell can effectively harness solar energy under different conditions and contribute to the development of efficient energy harvesting systems.

3. In this chapter, it is demonstrated that the PVV-PCBM based organic PV cell is capable of delivering power output of 0.05 milliWatts (mW), 0.45 milliWatts and 2.1 milliWatts for African, Asian and Caucasian skin tones, respectively, at a 2-millimeter implementation depth. These findings highlight the potential of subdermal organic PV cells in harnessing solar energy beneath different skin tones and their ability to generate usable power levels for various applications.
4. The power-density of sub-dermally implanted organic PV device is inversely related to the thickness of the skin, meaning that as the skin thickness increases, the power density decreases. The power density also depends on the amount of light reaching the subdermal PV cell through human skin. It is observed that photovoltaic device generates more output power when exposed to bright sunlight. This highlights the importance of optimizing the implantation depth and ensuring adequate exposure to sunlight for maximizing the output power of the organic PV device.
5. The amount of power generated by sub-dermally implanted organic PV cell depends on the amount of sunlight received by it. The volume of light acquired by the PV cell through the human skin, in turn, depends on the skin tone and skin thickness underneath which it is positioned.
6. The skin tones affect the absorption and distribution of sunlight, with darker skin tones absorbing more incident sunlight compared to lighter skin tones. Additionally, the skin thickness influences the scattering and penetration of light, affecting the amount of light reaching the PV cell.
7. The open-circuit voltage at 0.84 volts and Fill factor at 52 % of the organic PV cell do not show any significant deviations after being implemented underneath the human skin. This is because both are determined by the properties of the solar cell materials.
8. The photovoltaic cell discussed in this chapter demonstrates efficient energy harvesting capabilities, enabling direct power supply, and charging of an energy storing device to sustain a medical pacemaker for a continuous duration of twenty-four (24) hours. When exposed to daylight, the PV cell requires approximately six (6) minutes to fully charge the energy storing device, ensuring uninterrupted operation of the pacemaker, even in low light conditions.
9. The sub-dermally implanted organic PV cell has the potential to increase the lifespan of cardiac pacemaker, thereby reducing the need of complex surgeries essential for implant replacements. This technology offers the advantage of long-lasting power source, which can decrease the frequency of surgical interventions.

CHAPTER - 7

CONCLUSIONS AND FUTURE SCOPE

Solar cells play an essential role in conversion of sunlight directly into electricity through photoelectric effect. For the successful commercial application of solar cell, it is required to increase their power conversion efficiencies, especially in organic solar cells. This increase in efficiency could be achieved by developing new materials, optimizing layer thicknesses and by designing new device architectures. In this thesis, Antimony (Sb) and Tin (Sn) doped Zinc Telluride (ZnTe) solar cells are developed, and the optimization of organic solar cells is performed to enhance their power conversion efficiency. Additionally, the organic solar cells are explored for their potential biomedical applications, such as anaemia detection and powering modern cardiac pacemaker. In this chapter, the key findings of all the preceding chapters are summarized in section 7.1. Further, in section 7.2, the future scope for further research and development is elaborated.

7.1 CONCLUSIONS

This work has presented substantial advances in the solar cell technology for biomedical applications as well as energy harvesting. This research has focused on the development of Sb and Sn doped ZnTe thin films for solar cell applications, and the use of organic solar cells for non-invasive biomedical devices, notably haemoglobin detection and powering cardiac pacemakers.

This research explored the synthesis and characterisation of SbZnTe and SnZnTe thin films using a low-cost melt-quenching processes. The XRD pattern were used to characterise these thin films and their crystalline nature was determined. Additionally, these thin films were also analysed for their suitability as absorber layers in solar cells. The SbZnTe and SnZnTe solar cells were compared to a ZnTe-based solar cell. The results showed that the SnZnTe material performed the best, with enhanced current density and fill factor. The highest conversion efficiency is achieved for the SnZnTe solar cell, which was 17.8%, followed by the SbZnTe solar cell, with 10.6%. This research demonstrated the significance of the absorber layer in improving solar cell performance without increasing device dimensions.

Further the investigation and optimization of multilayer organic solar cells is performed. The research investigated the internal characteristics of a P3HT: PCBM organic solar cell. The efficiency of the solar cell was achieved by optimization of donor and acceptor layer thickness, and by adding additional electron and hole transport layers. The addition of PEDOT: PSS hole transport layer and a PFN electron transport layer, as well as the use of PTB7 as donor material significantly improved the efficiency of the solar cell. Furthermore, when conventional and inverted solar cell structures were compared, the inverted solar cell structure achieved a high-power conversion efficiency of 2.08%. These findings help to design and build high-efficiency solar cells for a variety of applications.

Furthermore, this research investigated the application of organic photovoltaic cells in non-invasive biomedical devices, notably haemoglobin detection and powering cardiac pacemakers. The idea was to develop a non-invasive approach of haemoglobin detection utilising a multilayer organic photovoltaic cell composed of Coumarin 30: C60/ NN'-QA/ ZnPc material layers. The blood haemoglobin levels could be measured simply and reliably by lighting the skin with blue, green, and red LED sources and analysing the transmitted light through the organic solar cell arrangement. This approach offered a portable and inexpensive option for screening anaemia, particularly in areas with limited access to proper diagnostic facilities. Furthermore, the incorporation of organic photovoltaic cells for powering cardiac pacemakers was explored. The results demonstrated that a subdermal organic photovoltaic device based on PPV-PCBM could generate sufficient power to operate a modern cardiac pacemaker, potentially decreasing the need for surgical procedures and improving patient comfort.

Finally, this research work has helped to enhance solar cell technology for biomedical applications and energy harvesting. The research outcomes have demonstrated the potential of SbZnTe and SnZnTe thin films as absorber materials, as well as the optimisation of multilayer organic solar cells and the usage of organic photovoltaic cells for biomedical applications. These findings may open new possibilities for the design and development of efficient solar cells for a variety of energy harvesting and healthcare applications.

7.2 FUTURE SCOPE

Based on the research conducted in this thesis and the results reported, several future scopes can be suggested for further research and development.

To begin, future research in the field of intermediate band gap thin films solar cells can focus on optimising the fabrication process to enhance the material characteristics and solar cell performance. This can involve investigating alternate deposition processes, such as sputtering or chemical vapor deposition, to obtain better control over film quality and thickness uniformity. Additionally, the impact of different dopants and their concentrations on the optical and electrical properties of the films can be explored in order to improve the efficiency of the solar cells.

Future research in the field of organic solar cells, may explore the usage of novel donor and acceptor materials to enhance the efficiency and stability of the device. New materials with increased charge carrier mobility, enhanced light absorption characteristics, and better thermal stability can be investigated. Furthermore, advanced novel device architectures and engineering methodologies, such as tandem or multi-junction structures, can be investigated to achieve higher conversion efficiencies.

Regarding biomedical applications of organic solar cells, future research can be focused on integrating these devices into implantable or wearable electronic devices. The development of biocompatible and flexible substrates can pave the way for the fabrication of conformal and stretchable electronic devices that can be smoothly incorporated into the human body. Moreover, long-term stability and biocompatibility assessments of organic materials and their interactions with biological systems should be carried out to ensure their safe and reliable operation in real world healthcare situations.

Additionally, future research can investigate the scalability and cost-effectiveness of organic solar cell technologies. Efforts could be directed towards developing large-scale manufacturing processes, utilizing printing or roll-to-roll techniques, to enable low-cost mass manufacturing of organic solar cells. Furthermore, research on the environmental impact and recyclability of organic materials used in solar cells can provide important insights for future sustainable energy solutions. Integrating energy storage solutions, assessing environmental impacts, and exploring diverse applications such as wearable and building integration will shape the research landscape. Collaborations across disciplines, incorporation of Artificial Intelligence and machine learning, and attention to policy, economics, and public outreach will collectively guide the future of organic solar cell research and their respective applications.

Finally, based on the findings of this thesis, there are several promising aspects for future investigation and development in the field of intermediate band solar cells, organic photovoltaic cells, and their biomedical applications. Addressing these future scopes can certainly result in significant advancements in solar cell technologies, bringing us closer to realizing efficient and sustainable energy solutions for variety of applications in healthcare, energy harvesting, and beyond.

REFERENCES

[1] A. L. Stanford and J. M. Tanner, "Early quantum physics," Phys. Stud. Sci. Eng., pp. 691–716, 1985.

[2] N. Amin, K. Sopian, and M. Konagai, "Numerical modelling of Cds/CdTe and Cds/CdTe/ZnTe solar cells as a function of CdTe thickness," Sol. Energy Mater. Sol. Cells, vol. 91, no. 13, pp. 1202–1208, 2007.

[3] D. Wohrle and D. Meissner, "Organic Solar Cells," Adv. Mater., vol. 3, no. 3, pp. 129-138, 1991.

[4] C. J. Brabec, N. S. Sariciftci, and J. C. Hummelen, "Plastic Solar Cells," Adv. Funct. Mater., vol. 11, no. 1, pp. 15-26, 2001.

[5] N. Behjat, N. Torabi, and F. Dossthosseini, "Improvement of light harvesting by inserting an optical spacer (ZnO) in polymer bulk heterojunction solar cells: a theoretical and experimental study," Int. J. Ophthalmic. Pract., vol. 8, pp. 3-11, 2014.

[6] H. Hoppe, N. S. Sariciftci, and D. Meissner, "Optical constants of conjugated polymer/fullerenebased bulk-heterojunction organic solar cells," Mol. Cryst. Liq. Cryst., vol. 385, no. 1, pp. 113-119, 2011.

[7] Y. H. Khattak, F. B. S. Ullah, B. Marí, S. Beg, and H. Ullah, "Enhancement of the conversion efficiency of thin film kesterite solar cell," J. Renew. Sustain. Energy, vol. 10, 033501, 2018.

[8] K. Mukhopadhyay, P. F. H. Inbaraj, and J. J. Prince, "Thickness optimization of CdS/ZnO hybrid buffer layer in CZTSe thin film solar cells using SCAPS simulation program," Mater. Res. Innov., vol. 23, 52, pp. 1–11, 2018.

[9] C. W. Tang, "Two-Layer Organic Photovoltaic Cell," Appl. Phys. Lett., vol. 48, no. 2, pp. 183-185, 1986.

[10] C. J. Brabec, A. Cravino, D. Meissner, N. S. Sariciftci, T. Fromherz, M. T. Rispens, L. Sanchez, and J. C. Hummelen, "Origin of the Open Circuit Voltage of Plastic Solar Cells," Adv. Funct. Mater., vol. 11, no. 5, pp. 374–380, 2001.

[11] M. Isik, H. H. Gullu, M. Parlak, and N. M. Gasanly, "Synthesis and temperature tuned band gap characteristics of magnetron sputtered ZnTe thin films," Physica B: Physics Condensed Matter, vol. 582, 411968, 2020.

[12] S. Negi, P. Mittal, and B. Kumar, "Analytical modelling and parameters extraction of multilayered OLED," IET Circuits Devices Syst., vol. 13, no. 8, pp. 1255–1261, 2019.

[13] P.C. Choubey, A. Oudhia, and R. Dewangan, "A review: Solar cell current scenario and future trends," Recent Research in Science and Technology, vol. 4, no. 8, pp. 88-101, 2012.

[14] Y. Chu and P. Meisen, "Review and comparison of different Solar Energy Technologies," Report of Global Energy Network Institute (GENI), Diego, 2011.

[15] S. Hegedus, "Thin film solar modules: The low cost, high throughput and versatile alternative to Si wafers," Prog. Photovoltaics, vol. 14, pp. 393–411, 2006.

[16] G.A. Chamberlain, "Organic solar cells: A review," Solar Cells, vol. 8, p. 47, 1983.

[17] D. Wöhrle and D. Meissner, "Organic solar cells," Adv. Mater., vol. 3, p. 129, 1991.

[18] C.J. Brabec, N.S. Sariciftci, and J.C. Hummelen, "Plastic solar cells," Adv. Funct. Mater., vol. 11, p. 15, 2001.

[19] J.J.M. Halls and R.H. Friend, "in Clean Electricity from Photovoltaics, edited by M.D. Archer and R. Hill (Imperial College Press, London, U.K., 2001)."

[20] J. Nelson, "Organic photovoltaic films," Curr. Opin. Solid State Mater. Sci., vol. 6, p. 87, 2002.

[21] J-M. Nunzi, "Organic photovoltaic materials and devices," C. R. Physique, vol. 3, p. 523, 2002.

[22] "Organic Photovoltaics: Concepts and Realization; Vol. 60, edited by C.J. Brabec, V. Dyakonov, J. Parisi, and N.S. Sariciftci (Springer, Berlin, Germany, 2003)."

[23] P. Peumans, A. Yakimov, and S.R. Forrest, "Small molecular weight organic thin-film photodetectors and solar cells," J. Appl. Phys., vol. 93, p. 3693, 2003.

[24] R.H. Friend et al., "Electroluminescence in conjugated polymers," Nature, vol. 397, p. 121, 1999.

[25] F. Garnier, R. Hajlaoui, A. Yassar, and P. Srivastava, "All-polymer field-effect transistor realized by printing techniques," Science, vol. 265, p. 1684, 1994.

[26] C.D. Dimitrakopoulos and P.R.L. Malenfant, "Organic thin film transistors for large area electronics," Adv. Mater., vol. 14, p. 99, 2002.

[27] C.W. Tang, "Two-layer organic photovoltaic cell," Appl. Phys. Lett., vol. 48, p. 183, 1986.

[28] G. Yu et al., "Polymer Photovoltaic Cells: Enhanced Efficiencies via a Network of Internal Donor-Acceptor Heterojunctions," Science, vol. 270, pp. 1789-1791, 1995.

[29] F. Dimroth and S. Kurtz, "High-efficiency multijunction solar cells," MRS Bull., vol. 32, p. 230, 2007.

[30] M. Grätzel, "Photoelectrochemical cells," Nature, vol. 414, p. 338, 2001.

[31] M.K. Nazeeruddin et al., "Conversion of light to electricity by cis-x2bis(2,20-bipyridyl 4,40-dicarboxylate)ruthenium(II) charge-transfer sensitizers (x ¼ Cl, Br, I, CN, and SCN) on nanocrystalline TiO2 electrodes," J. Am. Chem. Soc., vol. 115, p. 6382, 1993.

[32] W.U. Huynh, J.J. Dittmer, and A.P. Alivisatos, "Hybrid nanorod-polymer solar cells," Science, vol. 295, p. 2425, 2002.

[33] I. Gur, N.A. Fromer, M.L. Geier, and A.P. Alivisatos, "Air-stable all-inorganic nanocrystal solar cells processed from solution," Science, vol. 310, p. 462, 2005.

[34] D.J. Milliron, I. Gur, and A.P. Alivisatos, "Hybrid organic–nanocrystal solar cells," MRS Bull., vol. 30, p. 41, 2005.

[35] S. Sharma, K. Jain, and A. Sharma, "Solar cells: In research and Application- A Review," Materials Sciences and Applications, vol. 6, no. 12, pp. 1145-1155, 2015.

[36] A.M. Bagher, M.M.A. Vahid, and M. Mohsen, "Types of Solar Cells and Application," American Journal of Optics and Photonics, vol. 3, no. 5, pp. 94-113, 2015.

[37] P. Wurfel and U. Wurfel, "Physics of Solar Cells: From Basic Principles to Advanced Concepts," John Wiley & Sons, 2009.

[38] S. Dmitrijev, "Principles of Semiconductor Devices," Oxford University Press, Oxford, 2006.

[39] P. Jayakumar, "Solar Energy Resource Assessment Handbook," Renewable Energy Corporation Network for the Asia Pacific, 2009.

[40] Qusay, Noorah, and Noor Ahmed, "Effect of temperature variations on Solar Cell Efficiency," International Journal Of Engineering, Business and Enterprise Applications (IJEBEA), vol. 2, no. 4, pp. 108-112, 2012.

[41] K.L. Chopra, P.D. Paulson, and V. Dutt, "Thin-Film Solar Cells: An Overview," Progress in Photovoltaics, vol. 12, no. 2-3, pp. 69-92, 2004.

[42] P. Kamkird, N. Ketjoy, W. Rakwichian, and S. Sukchai, "Investigation on Temperature Coefficients of Three Types Photovoltaic Module Technologies under Thailand Operating Condition," Procedia Engineering, vol. 32, pp. 376-383, 2012.

[43] A.M. Barnett et al., "High current, thin silicon–on–ceramic solar cell," Solar Energy Materials & Solar Cells, vol. 66, pp. 46-50, 2001.

[44] M. Bertolli, "Solar Cell Materials," Course: Solid State II, Department of Physics, University of Tennessee Knoxville, 2008.

[45] Y.D. Goswami and F. Kreith, "Handbook of Energy Efficiency and Renewable Energy," CRC Press Boca Raton, 2007.

[46] W.A. Badawy, "A Review on Solar Cells from Si-Single Crystals to Porous Materials and Quantum Dots," Journal of Advanced Research, vol. 6, no. 2, pp. 123-132, 2015.

[47] J. Britt and C. Ferekides, "Thin-film CdS/CdTe solar cell with 15.8% efficiency," Applied Physics Letters, vol. 62, pp. 2851-2852, 1993.

[48] T. Aramoto et al., "16.0% efficient thin-film CdS/CdTe solar cells," Japanese Journal of Applied Physics, vol. 36, pp. 486-524, 1997.

[49] National Renewable Energy Laboratory (NREL), [Online]. Available: http://www.nrel.gov/. [Accessed: 2nd Feb 2019].

[50] Y. Osman et al., "J. Phys.: Conf. Ser.," vol. 1447, p. 012057, 2020.

[51] A. Benmir and M.S. Aida, "Analytical Modeling and Simulation of CIGS Solar Cells," Energy Procedia, vol. 36, pp. 618-627, 2013.

[52] M. Imamzai et al., "A Review on Comparison between Traditional Silicon Solar Cells and Thin-Film CdTe Solar Cells," Proceedings of National Graduate Conference, Tenaga Nasional Universiti, Putrajaya Campus, pp. 1-5, 2012.

[53] T.M. Razykov et al., "Solar Photovoltaic Electricity: Current Status and Future Prospects," Solar Energy, vol. 85, no. 8, pp. 1580-1608, 2011.

[54] Qusay, Noorah, and Noor Ahmed, "Effect of temperature variations on Solar Cell Efficiency," International Journal Of Engineering, Business and Enterprise Applications (IJEBEA), vol. 2, no. 4, pp. 108-112, 2012.

[55] P. Jayakumar, "Solar Energy Resource Assessment Handbook," Renewable Energy Corporation Network for the Asia Pacific, 2009.

[56] S. Dubey, J.N. Sarvaiya, and B. Seshadri, "Temperature Dependent Photovoltaic (PV) Efficiency and Its Effect on PV Production in the World: A Review," Energy Procedia, vol. 33, pp. 311-321, 2013.

[57] M. Fathi, M. Abderrezek, F. Djahli, and M. Ayad, "Study of thin film solar cells in high-temperature condition," Energy Procedia, vol. 74, pp. 1410-1417, 2015.

[58] H. Hoppe and N.S. Sariciftci, "Polymer Solar Cells," Advances in Polymer Science, vol. 214, pp. 1-86, 2008.

[59] B.N.V.S. Ganesh and Y.V. Supriya, "Recent Advancements and Techniques in Manufacture of Solar Cells: Organic solar cells," International Journal of Electronics and Computer Science Engineering, vol. 2, no. 2, pp. 565-573, 2013.

[60] S. Suhaimi, M.M. Shahimin, Z.A. Alahmed, J. Chyský, and A.H. Reshak, "Materials for Enhanced Dye-sensitized Solar Cells Performance: Electrochemical Application," International Journal of Electrochemical Science, vol. 10, pp. 2859-2871, 2015.

[61] S. Sharma, K. Jain, and A. Sharma, "Solar cells: In research and Application- A Review," Materials Sciences and Applications, vol. 6, no. 12, pp. 1145-1155, 2015.

[62] N. Ahn, D.Y. Son, I.H. Jang, S.M. Kang, M. Choi, and N.G. Park, "Highly Reproducible Perovskite Solar Cells with Average Efficiency of 18.3% and Best Efficiency of 19.7% Fabricated via Lewis Base Adduct of Lead(II) Iodide," Journal of the American Chemical Society, vol. 137, no. 27, pp. 8696-8699, 2015.

[63] Dubey S., Sarvaiya, J.N. and Seshadri, B. (2013) 'Temperature Dependent Photovoltaic (PV) Efficiency and Its Effect on PV Production in the World: A Review', Energy Procedia, Vol.33, pp.311-321

[64] B.N.V.S. Ganesh and Y.V. Supriya, "Recent Advancements and Techniques in Manufacture of Solar Cells: Organic solar cells," International Journal of Electronics and Computer Science Engineering, vol. 2, no. 2, pp. 565-573, 2013.

[65] C. Alex, Shawn R. Mayer, Brian E. Scully, Michael W. Hardin, and Michael D. McGehee, "Polymer based solar cells: A Review," Materials Today, vol. 10, no. 11, pp. 28-33, 2007.

[66] F. Wudl and Gordana Srdanov, "Conducting polymer formed of poly (2-methoxy, 5-(2'-ethyl-hexyloxy)-p-phenylenevinylene)," U.S. Patent No. 5,189,136, 23 Feb 1993.

[67] B. Srinivas, S. Balaji, M. Nagendra Babu, and Y.S. Reddy, "Review on Present and Advance Materials for Solar cells," International Journal of Engineering Research-Online, vol. 3, pp. 178-182, 2015.

[68] S. Suhaimi, M.M. Shahimin, Z.A. Alahmed, J. Chyský, and A.H. Reshak, "Materials for Enhanced Dye-sensitized Solar Cells Performance: Electrochemical Application," International Journal of Electrochemical Science, vol. 10, pp. 2859-2871, 2015.

[69] S.P. Philipps, A.W. Bett, K. Horowitz, and S. Kurtz, "Current Status of Concentrator Photovoltaics (CPV) Technology Report Version 1.2," Fraunhofer Institute for Solar Energy Systems (NREL), 2015.

[70] N.G. Park, "Perovskite solar cells: an emerging photovoltaic technology," Materials Today Elsevier, vol. 18, no. 2, pp. 65-72, 2015.

[71] T.J. Jacobsson, W. Tress, J.P.C. Baena, T. Edvinsson, and A. Hagfeldt, "Room Temperature as a Goldilocks Environment for CH3NH3PbI3 Perovskite Solar Cells:

The Importance of Temperature on Device Performance," The journal of Physical Chemistry, vol. 120, no. 21, pp. 11382–11393, 2016.

[72] D. Shi, Y. Zeng, and W. Shen, "Perovskite/c-Si Tandem Solar Cell with Inverted Nanopyramids: Realizing High efficiency by Controllable Light Trapping," Scientific Reports, no. 5, Article No. 16504, 2015.

[73] A.B. Kashyout, A.S. Arico`, P.L. Antonucci, F.A. Mohamed, and V. Antonucci, "Influence of annealing temperature on the opto-electronic characteristics of ZnTe electrodeposited semiconductors," Mater Chem Phys, vol. 51, pp. 130-134, 1997.

[74] M. Nishio, K. Hayashida, Q. Guo, and H. Ogawa, "Effect of VI/II ratio upon photoluminescence properties of aluminum-doped ZnTe layers grown by MOVPE," Appl Surf Sci, vol. 169, pp. 223-226, 2001.

[75] A.A. Ibrahim, N.Z. El-Sayed, M.A. Kaid, and A. Ashour, "Structural and electrical properties of evaporated ZnTe thin films," Vacuum, vol. 75, pp. 189-194, 2004.

[76] A.A. Ibrahim, "DC electrical conduction of zinc telluride thin films," Vacuum, vol. 81, pp. 527-530, 2006.

[77] C.-H. Hsu, C.-F. Tseng, Y.-T. Yu, P.-C. Yang, C.-H. Lai, J.-S. Lin, and H.-W. Yang, "Effect of annealing temperature on electrical properties of ZnTe layers grown by thermal evaporation," Adv Mat Res, vol. 608, pp. 1314-1317, 2013.

[78] T. Hussain, M.F.A. Kuhaili, S.M.A. Durrani, and H.A. Qayyum, "Influence of angle deposition on the properties of ZnTe thin films prepared by thermal evaporation," Ceram Int, vol. 44, pp. 10130-10140, 2018.

[79] K. Yoshino, A. Memon, M. Yoneta, K. Ohmori, H. Sato, and M. Ohishi, "Optical characterization of the ZnTe pure-green LED," Phys Status Solidi B, vol. 229, pp. 977-980, 2002.

[80] P.K. Kalita, B.K. Sarma, and H.L. Das, "Photoresponse characteristics of vacuum evaporated ZnTe thin films," Ind J Pure Appl Phys, vol. 37, pp. 885-890, 1999.

[81] E. Bacaksiz, S. Aksu, N. Ozer, M. Tomakin, and A. Özçelik, "The influence of substrate temperature on the morphology, optical and electrical properties of thermal-evaporated ZnTe thin films," Appl Surf Sci, vol. 256, pp. 1566-1572, 2009.

[82] G.K. Rao, K.V. Bangera, and G.K. Shivakumar, "The effect of substrate temperature on the structural, optical and electrical properties of vacuum deposited ZnTe thin films," Vacuum, vol. 83, pp. 1485-1488, 2009.

[83] S. Jeetendra, C.S. Naveen, P. Raghu, and H.M. Mahesh, "Optimization of thickness of ZnTe thin film as back contact for CdTe thin film solar cells," Int J Eng Res Tech, vol. 3, pp. 431-435, 2014.

[84] K.N. Raju, R.P. Vijayalakshmi, R. Venugopal, D.R. Reddy, and B.K. Reddy, "Effect of substrate temperature on the structural, optical and electrical properties of vacuum-evaporated ZnTe films," Mater Lett, vol. 13, pp. 336-341, 1992.

[85] A.M. Salem, T.M. Dahy, and Y.A. El-Gendy, "Thickness dependence of optical parameters for ZnTe thin films deposited by electron beam gun evaporation technique," Phys B, vol. 403, pp. 3027-3033, 2008.

[86] M.S. Hossain, R. Islam, and K.A. Khan, "Temperature effect on the electrical properties of undoped and vanadium-doped ZnTe thin films," Renewable Energy, vol. 33, pp. 642-647, 2008.

[87] A. Mahmood, R. Rashid, U. Aziz, A. Shah, Z. Ali, Q. Raza, and T. Ashraf, "Structural and optical properties of Zn1-xNixTe thin films prepared by electron beam evaporation technique," Prog Nat Sci, vol. 25, pp. 22-28, 2015.

[88] W. Mahmood and N.A. Shah, "Effects of metal doping on the physical properties of ZnTe thin films," Curr Appl Phys, vol. 14, pp. 282-286, 2014.

[89] A.K.S. Aqili, A.J. Saleh, Z. Ali, and S. Al-Omari, "Ag doped ZnTe films prepared by closed space sublimation and an ion exchange process," J Alloys Compd, vol. 520, pp. 83-88, 2012.

[90] T. Potlog, N. Maticiuc, A. Mirzac, P. Dumitriu, and D. Scortescu, "Structural and optical properties of ZnTe thin films," Proceedings of the International Semiconductor Conference, pp. 321-324, 2012.

[91] M.U. Farooq, M. Khan, A. Faraz, A. Maqsood, W. Ahmad, and L. Li, "Comparative study of ZnTe thin films prepared using close space sublimation (CSS) and electron beam evaporation (EBE) thin film fabrication techniques for optoelectronic applications," Mater Technol, vol. 29, pp. 29-35, 2014.

[92] G. Lastra, P.A. Luque, M.A. Quevedo-Lopez, and A. Olivas, "Electrical properties of p-type ZnTe thin films by immersion in Cu solution," Mater Lett, vol. 126, pp. 271-273, 2014.

[93] K.S. Lee, G. Oh, and E.K. Kim, "Growth of p-type ZnTe thin films by using nitrogen doping during pulsed laser deposition," J Korean Phys Soc, vol. 67, pp. 672-675, 2015.

[94] S. Beke, "A review of the growth of V2O5 films from 1885 to 2010," Thin Solid Films, vol. 519, pp. 1761-1771, 2011.

[95] Z. Zhang, J. Li, H. Zhang, X. Pan, and E. Xie, "Thickness-dependent field emission from ZnTe films prepared by magnetron sputtering," J Alloys Compd, vol. 549, pp. 88-91, 2013.

[96] H. Bellakhder, A. Outzourhit, and E.L. Ameziane, "Study of ZnTe thin films deposited by r.f. sputtering," Thin Solid Films, vol. 382, pp. 30-33, 2001.

[97] S. Mohan and R. Venkataciialam, "Brush plating - present state of art," Bull Electrochem, vol. 14, pp. 472-475, 1998.

[98] T. Mahalingam, V.S. John, S. Rajendran, and P.J. Sebastian, "Electrochemical deposition of ZnTe thin films," Semicond Sci Technol, vol. 17, pp. 465-470, 2002.

[99] T. Mahalingam, V.S. John, S. Rajendran, G. Ravi, and P.J. Sebastian, "Annealing studies of electrodeposited zinc telluride thin films," Surf Coat Technol, vol. 155, pp. 245-249, 2002.

[100] M.A. Baghchesara, R. Yousefi, M. Cheraghizade, F.J. Sheini, and A. Sa´aedi, "Photocurrent application of Cd-doped ZnTe nanowires grown in a large scale by a CVD Method," Vacuum, vol. 123, pp. 131-135, 2015.

[101] S.S. Kale, R.S. Mane, H.M. Pathan, A.V. Shaikh, O.-S. Joo, and S.-H. Han, "Preparation and characterization of ZnTe thin films by SILAR method," Appl Surf Sci, vol. 253, pp. 4335-4337, 2007.

[102] J. De Merchant and M. Cocivera, "Properties of zinc telluride containing impurities introduced during spray pyrolysis," J Electrochem Soc, vol. 143, pp. 4054-4059, 1996.

[103] G.K. Rao, K.V. Bangera, and G.K. Shivakumar, "Studies on the photoconductivity of vacuum deposited ZnTe thin films," Mater Res Bull, vol. 45, pp. 1357-1360, 2010.

[104] A. Erlacher, M. Ambrico, G. Perna, L. Schiavulli, T. Ligonzo, H. Jaeger, and B. Ullrich, "Absorption and photoconductivity properties of ZnTe thin films formed by pulsed-laser deposition on glass," Appl Surf Sci, vol. 248, pp. 402-405, 2005.

[105] A.E. Rakhshani, "Effect of growth temperature, thermal annealing and nitrogen doping on optoelectronic properties of sputterdeposited ZnTe films," Thin Solid Films, vol. 536, pp. 88-93, 2013.

[106] K.R. Murali, M. Ziaudeen, and N. Jayaprakash, "Structural and electrical properties of brush plated ZnTe films," Solid-State Electron, vol. 50, pp. 1692-1695, 2006.

[107] T. Mahalingam, V. Dhanasekaran, K. Sundaram, A. Kathalingam, and J.-K. Rhee, "Characterization of electroplated ZnTe coatings," Ionics, vol. 18, pp. 299-306, 2012.

[108] Q. Gul, M. Zakria, T.M. Khan, A. Mahmood, and A. Iqbal, "Effects of Cu incorporation on physical properties of ZnTe thin films deposited by thermal evaporation," Mater Sci Semicond Process, vol. 19, pp. 17-23, 2014.

[109] J. Pattar, S.N. Sawant, M. Nagaraja, N. Shashank, K.M. Balakrishna, G. Sanjeev, and H.M. Mahesh, "Structural optical and electrical properties of vacuum evaporated indium doped zinc telluride thin films," Int J Electrochem Sci, vol. 4, pp. 369-376, 2009.

[110] D.C. Sharma, S. Srivastava, Y.K. Vijay, and Y.K. Sharma, "Preparation and characterization of the chromium doped ZnTe thin films," Adv Mater Lett, vol. 4, pp. 68-70, 2013.

[111] Z. Ma, L. Liu, K.M. Yu, W. Walukiewicz, D.L. Perry, P.Y. Yu, and S.S. Mao, "Experimental and theoretical studies on gadolinium doping in ZnTe," J Appl Phys, vol. 103, pp. 023711, 2008.

[112] U. Pal, "Dark- and photoconductivity in doped and undoped zinc telluride films," Semicond Sci Technol, vol. 8, pp. 1331-1336, 1993.

[113] S.C. Jain, M. Willander, and V. Kumar, "Conducting Organic Materials and Devices," Academic Press, San Diego, 2007.

[114] A.K. Gosh and T. Feng, "Rectification, space-charge-limited current, photovoltaic and photoconductive properties of Al/tetracene/Au sandwich cell," Journal of Applied Physics, vol. 44, pp. 2781-2788, 1973.

[115] M. Granstrom, K. Petritsch, A.C. Arias, A. Lux, M. Andersson, and R.H. Friend, "Laminated fabrication of polymeric photovoltaic diodes," Nature, vol. 395, pp. 257-260, 1998.

[116] M.Y. Chan, S.L. Lai, M.K. Fung, C.S. Lee, and S.T. Lee, "Doping-induced efficiency enhancement in organic photovoltaic devices," Applied Physics Letters, vol. 90, pp. 23504, 2007.

[117] J.Y. Kim, K. Lee, N.E. Coates, D. Moses, T.Q. Nguyen, M. Dante, and A.J. Heeger, "Efficient tandem polymer solar cells fabricated by all-solution processing," Science, vol. 317, pp. 222-225, 2007.

[118] S.E. Shaheen, C.J. Brabec, N.S. Sariciftci, F. Padinger, T. Fromhert, and J.C. Hummelen, "2.5% efficient organic plastic solar cells," Applied Physics Letters, vol. 78, pp. 841-843, 2001.

[119] F. Padinger, R.S. Rittberger, and N.S. Sariciftci, "Effects of postproduction treatment on plastic solar cells," Advanced Functional Materials, vol. 13, pp. 85-88, 2003.

[120] J. Drechsel, B. Männig, F. Kozlowski, M. Pfeiffer, K. Leo, and H. Hoppe, "Efficient organic solar cells based on a double p-i-n architecture using doped wide-gap transport layers," Applied Physics Letters, vol. 86, pp. 244102, 2005.

[121] P. Peumans, S. Uchida, and S.R. Forrest, "Efficient bulk heterojunction photovoltaic cells using small-molecular-weight organic thin films," Nature, vol. 425, pp. 158-162, 2003.

[122] J.A. Hauch, P. Schilinsky, S.A. Choulis, R. Childers, M. Biele, and C.J. Brabec, "Flexible organic P3HT:PCBM bulk-heterojunction modules with more than 1 year outdoor lifetime," Solar Energy Materials and Solar Cells, vol. 92, pp. 727-731, 2008.

[123] F.C. Krebs and H. Spanggaard, "Significant improvement of polymer solar cell stability," Chemistry of Materials, vol. 17, pp. 5235-5237, 2005.

[124] C. Lungenschmied, G. Dennler, H. Neugebauer, S.N. Sariciftci, M. Glatthaar, T. Meyer, and A. Meyer, "Flexible, long-lived, large-area, organic solar cells," Solar Energy Materials and Solar Cells, vol. 91, pp. 379-384, 2007.

[125] S.R. Forrest, W.Y. Yoon, L.Y. Leu, and F.F. So, "Optical and electrical properties of isotype crystalline molecular organic heterojunctions," Journal of Applied Physics, vol. 66, pp. 5908-5914, 1989.

[126] H. Kumar, P. Kumar, R. Bhardwaj, G.D. Sharma, S. Chand, S.C. Jain, and V. Kumar, "Broad spectral sensitivity and improved efficiency in CuPc/Sub-Pc organic photovoltaic devices," Journal of Physics D, vol. 42, pp. 15103, 2009.

[127] M.M. Alam and S.A. Jenekhe, "Efficient solar cells from layered nanostructures of donor and acceptor conjugated polymers," Chemistry of Materials, vol. 16, pp. 4647-4656, 2004.

[128] L. Chen, D. Godovsky, O. Inganäs, J.C. Hummelen, R.A.J. Janssens, M. Svensson, and M.R. Andersson, "Polymer photovoltaic devices from stratified multilayers of donor–acceptor blends," Advanced Materials, vol. 12, pp. 1367-1370, 2000.

[129] Z.R. Hong, B. Maennig, R. Lessmann, M. Pfeiffer, K. Leo, and P. Simon, "Improved efficiency of zinc phthalocyanine/C60 based photovoltaic cells via nanoscale interface modification," Applied Physics Letters, vol. 90, pp. 203505, 2007.

[130] K.L. Mutolo, E.I. Mayo, B.P. Rand, S.R. Forrest, and M.E. Thompson, "Enhanced open-circuit voltage in subphthalocyanine/C60 organic photovoltaic cells," Journal of the American Chemical Society, vol. 128, pp. 8108-8109, 2006.

[131] S. Yoo, B. Domercq, and B. Kippelen, "Efficient thin-film organic solar cells based on pentacene/C60 heterojunctions," Applied Physics Letters, vol. 85, pp. 5427-5429, 2004.

[132] C.W. Chu, Y. Shao, V. Shrotriya, and Y. Yang, "Efficient photovoltaic energy conversion in tetracene-C60 based heterojunctions," Applied Physics Letters, vol. 86, pp. 243506, 2005.

[133] P. Peumans and S.R. Forrest, "Very-high-efficiency double-heterostructure copper phthalocyanine/C60 photovoltaic cells," Applied Physics Letters, vol. 79, pp. 126-128, 2001.

[134] J. Xue, S. Uchida, B.P. Rand, and S.R. Forrest, "4.2% efficient organic photovoltaic cells with low series resistances," Applied Physics Letters, vol. 84, pp. 3013-3015, 2004.

[135] K. Schulze, C. Uhrich, R. Schuppel, K. Leo, M. Pfeiffer, E. Brier, E. Reinold, and P. Bauerle, "Efficient vacuum- deposited organic solar cells based on a new low- bandgap oligothiophene and fullerene C60," Advanced Materials, vol. 18, pp. 2872-2875, 2006.

[136] P. Peumans, A. Yakimov, and S.R. Forrest, "Small molecular weight organic thin-film photodetectors and solar cells," Journal of Applied Physics, vol. 93, pp. 3693-3723, 2003.

[137] B.P. Rand, J. Xue, F. Yang, and S.R. Forrest, "Organic solar cells with sensitivity extending into the near infrared," Applied Physics Letters, vol. 87, pp. 233508, 2005.

[138] Y. Hirose, A. Kahn, V. Aristov, P. Soukiassian, V. Bulovic, and S.R. Forrest, "Chemistry and electronic properties of metal-organic semiconductor interfaces: Al, Ti, In, Sn, Ag, and Au on PTCDA," Physical Review B, vol. 54, pp. 13748-13758, 1996.

[139] P. Peumans, V. Bulovic, and S.R. Forrest, "Efficient photon harvesting at high optical intensities in ultrathin organic double-heterostructure photovoltaic diodes," Applied Physics Letters, vol. 76, pp. 2650-2652, 2000.

[140] J.J.M. Halls, A.C. Walsh, N.C. Greenham, E.A. Marseglia, R.H. Friend, S.C. Moratti, and A.B. Holmes, "Efficient photodiodes from interpenetrating polymer networks," Nature, vol. 376, pp. 498-500, 1995.

[141] W. Ma, C. Yang, X. Gong, K. Lee, and A.J. Heeger, "Thermally stable, efficient polymer solar cells with nanoscale control of the interpenetrating network morphology," Advanced Functional Materials, vol. 15, pp. 1617-1622, 2005.

[142] V.D. Mihailetchi, H. Xie, B.D. Bore, L.M. Popescu, J.C. Hummelen, P.W.M. Blom, and L.J.A. Koster, "Origin of the enhanced performance in poly(3-hexylthiophene):

[6,6]-phenyl C61-butyric acid methyl ester solar cells upon slow drying of the active layer," Applied Physics Letters, vol. 89, pp. 12107, 2006.

[143] Y. Liang, Z. Xu, J. Xia, S.T. Tsai, Y. Wu, G. Li, C. Ray, and L. Yu, "For the bright future-bulk heterojunction polymer solar cells with power conversion efficiency of 7.4%," Advanced Materials, vol. 22, pp. E135-E138, 2010.

[144] Y. Yao, J.H. Hou, Z. Xu, G. Li, and Y. Yang, "Effects of solvent mixtures on the nanoscale phase separation in polymer solar cells," Advanced Functional Materials, vol. 18, pp. 1783-1789, 2008.

[145] J. Peet, J.Y. Kim, N.E. Coates, W.L. Ma, D. Moses, A.J. Heeger, and G.C. Bazan, "Efficiency enhancement in low-bandgap polymer solar cells by processing with alkane dithiols," Nature Materials, vol. 6, pp. 497-500, 2007.

[146] J.Y. Kim, S.H. Kim, H.H. Lee, K. Lee, W. Ma, X. Gong, and A.J. Heeger, "New architecture for high-efficiency polymer photovoltaic cells using solution-based titanium oxide as an optical spacer," Advanced Materials, vol. 18, pp. 572-576, 2006.

[147] G. Yu and A.J. Heeger, "Charge separation and photovoltaic conversion in polymer composites with internal donor/acceptor heterojunctions," Journal of Applied Physics, vol. 78, pp. 4510-4515, 1995.

[148] F. Zhang, W. Mammo, L.M. Andersson, S. Admassie, M.R. Andersson, and O. Inganäs, "Low-bandgap alternating fluorene copolymer/methanofullerene heterojunctions in efficient near-infrared polymer solar cells," Advanced Materials, vol. 18, pp. 2169-2173, 2006.

[149] C.J. Brabec, S.E. Shaheen, C. Winder, N.S. Sariciftci, and P. Denk, "Effect of LiF/metal electrodes on the performance of plastic solar cells," Applied Physics Letters, vol. 80, pp. 1288-1290, 2002.

[150] M. Svensson, F. Zhang, S.C. Veenstra, W.J.H. Verhees, J.C. Hummelen, J.M. Kroon, O. Inganas, and M.R. Anderson, "High-performance polymer solar cells of an alternating polyfluorene copolymer and a fullerene derivative," Advanced Materials, vol. 15, pp. 988-991, 2003.

[151] S. Uchida, J. Xue, B.P. Rand, and S.R. Forrest, "Organic small molecule solar cells with a homogeneously mixed copper phthalocyanine: C60 active layer," Applied Physics Letters, vol. 84, pp. 4218-4220, 2004.

[152] J. Xue, S. Uchida, B.P. Rand, and S.R. Forrest, "A hybrid planar–mixed molecular heterojunction photovoltaic cell," Advanced Materials, vol. 17, pp. 66-71, 2005.

[153] Y. Yao, J.H. Hou, Z. Xu, G. Li, and Y. Yang, "Effects of solvent mixtures on the nanoscale phase separation in polymer solar cells," Advanced Functional Materials, vol. 18, pp. 1783-1789, 2008.

[154] G. Li, V. Shrotriya, H. Huang, Y. Yao, T. Moriarty, K. Emery, and Y. Tang, "High-efficiency solution processable polymer photovoltaic cells by self-organization of polymer blends," Nature Materials, vol. 4, pp. 864-868, 2005.

[155] M. Hiramoto, M. Suezaki, and M. Yokoyama, "Effect of thin gold interstitial-layer on the photovoltaic properties of tandem organic solar cell," Chemistry Letters, vol. 19, pp. 327, 1990.

[156] J. Xue, S. Uchida, B.P. Rand, and S.R. Forrest, "Asymmetric tandem organic photovoltaic cells with hybrid planar-mixed molecular heterojunctions," Applied Physics Letters, vol. 85, pp. 5757–5759, 2004.

[157] J. Gilot, M.M. Weink, and R.A.J. Janssen, "Double and triple junction polymer solar cells processed from solution," Applied Physics Letters, vol. 90, pp. 143512, 2007.

[158] V. Shrotriya, E.H. En Wu, G. Li, Y. Yao, and Y. Yang, "Efficient light harvesting in multiple-device stacked structure for polymer solar cells," Applied Physics Letters, vol. 88, pp. 64104, 2006.

[159] G. Dennler, H.J. Prall, R. Koeppe, M. Egginger, R. Autengruber, and N.S. Sariciftci, "Enhanced spectral coverage in tandem organic solar cells," Applied Physics Letters, vol. 89, pp. 73502, 2006.

[160] A. Colsmann, J. Junge, C. Kayser, and U. Lemmer, "Organic tandem solar cells comprising polymer and small-molecule subcells," Applied Physics Letters, vol. 89, pp. 203506, 2006.

[161] J.Y. Kim, K. Lee, N.E. Coates, D. Moses, T.Q. Nguyen, M. Dante, and A.J. Heeger, "Efficient tandem polymer solar cells fabricated by all-solution processing," Science, vol. 317, pp. 222–225, 2007.

[162] Y. Liang, Z. Xu, J. Xia, S.T. Tsai, Y. Wu, G. Li, C. Ray, and L. Yu, "For the bright future-bulk heterojunction polymer solar cells with power conversion efficiency of 7.4%," Adv. Mater., vol. 22, pp. E135–E138, 2010.

[163] G. Li, V. Shrotriya, J. Huang, Y. Yao, T. Moriarty, K. Emery, and Y. Yang, "High-efficiency solution processable polymer photovoltaic cells by self-organization of polymer blends," Nat. Mater., vol. 4, pp. 864–868, 2005.

[164] H.U. Kim, J.-H. Kim, H. Kang, A.C. Grimsdale, B.J. Kim, S.C. Yoon, and D.-H. Hwang, "Naphthalene-, anthracene-, and pyrene-substituted fullerene derivatives as

electron acceptors in polymer-based solar cells," ACS Appl. Mater. Interfaces, vol. 6, pp. 20776–20785, 2014.

[165] Y. He, M. Shao, K. Xiao, S.C. Smith, and K. Hong, "High-performance polymer photovoltaics based on rationally designed fullerene acceptors," Sol. Energy Mater. Sol. Cells, vol. 118, pp. 171–178, 2013

[166] G. Zhao, Y. He, and Y. Li, "6.5% efficiency of polymer solar cells based on poly(3-hexylthiophene) and indene-C60 bisadduct by device optimization," Adv. Mater., vol. 22, pp. 4355–4358, 2010.

[167] M.M. Wienk, J.M. Kroon, W.J. Verhees, J. Knol, J.C. Hummelen, P.A. van Hal, and R.A. Janssen, "Efficient methano[70]fullerene/MDMOPPV bulk heterojunction photovoltaic cells," Angew. Chem. Int. Ed. Engl., vol. 42, pp. 3371–3375, 2003.

[168] Y. Liu, J. Zhao, Z. Li, C. Mu, W. Ma, H. Hu, K. Jiang, H. Lin, H. Ade, and H. Yan, "Aggregation and morphology control enables multiple cases of high-efficiency polymer solar cells," Nat. Commun., vol. 5, pp. 5293, 2014.

[169] G. Zhao, Y. He, Z. Xu, J. Hou, M. Zhang, J. Min, H.-Y. Chen, M. Ye, Z. Hong, Y. Yang, et al., "Effect of carbon chain length in the substituent of PCBM-like molecules on their photovoltaic properties," Adv. Funct. Mater., vol. 20, pp. 1480–1487, 2010.

[170] M. Lenes, G.-J.A.H. Wetzelaer, F.B. Kooistra, S.C. Veenstra, J.C. Hummelen, and P.W.M. Blom, "Fullerene bisadducts for enhanced open-circuit voltages and efficiencies in polymer solar cells," Adv. Mater., vol. 20, pp. 2116–2119, 2008.

[171] J.A. Mikroyannidis, A.N. Kabanakis, S.S. Sharma, and G.D. Sharma, "A Simple and effective modification of PCBM for use as an electron acceptor in efficient bulk heterojunction solar cells," Adv. Funct. Mater., vol. 21, pp. 746–755, 2011.

[172] P.A. Troshin, H. Hoppe, J. Renz, M. Egginger, J.Y. Mayorova, A.E. Goryachev, A.S. Peregudov, R.N. Lyubovskaya, G. Gobsch, N.S. Sariciftci, et al., "Material solubility-photovoltaic performance relationship in the design of novel fullerene derivatives for bulk heterojunction solar cells," Adv. Funct. Mater., vol. 19, pp. 779–788, 2009.

[173] Y. He, H.-Y. Chen, J. Hou, and Y. Li, "Indene-C60 bisadduct: A new acceptor for high-performance polymer solar cells," J. Am. Chem. Soc., vol. 132, pp. 1377–1382, 2010.

[174] Y. He, G. Zhao, B. Peng, and Y. Li, "High-yield synthesis and electrochemical and photovoltaic properties of indene-C70 bisadduct," Adv. Funct. Mater., vol. 20, pp. 3383–3389, 2010.

[175] P.A. Troshin, H. Hoppe, J. Renz, M. Egginger, J.Y. Mayorova, A.E. Goryachev, A.S. Peregudov, R.N. Lyubovskaya, G. Gobsch, N.S. Sariciftci, et al., "Material solubility-

photovoltaic performance relationship in the design of novel fullerene derivatives for bulk heterojunction solar cells," Adv. Funct. Mater., vol. 19, pp. 779–788, 2009.

[176] Y. Liang, Z. Xu, J. Xia, S.T. Tsai, Y. Wu, G. Li, C. Ray, and L. Yu, "For the bright future-bulk heterojunction polymer solar cells with power conversion efficiency of 7.4%," Adv. Mater., vol. 22, pp. E135–E138, 2010.

[177] Y. Liu, J. Zhao, Z. Li, C. Mu, W. Ma, H. Hu, K. Jiang, H. Lin, H. Ade, and H. Yan, "Aggregation and morphology control enables multiple cases of high-efficiency polymer solar cells," Nat. Commun., vol. 5, pp. 5293, 2014.

[178] M. Lenes, G.-J.A.H. Wetzelaer, F.B. Kooistra, S.C. Veenstra, J.C. Hummelen, and P.W.M. Blom, "Fullerene bisadducts for enhanced open-circuit voltages and efficiencies in polymer solar cells," Adv. Mater., vol. 20, pp. 2116–2119, 2008.

[179] Y. He, H.-Y. Chen, J. Hou, and Y. Li, "Indene-C60 bisadduct: A new acceptor for high-performance polymer solar cells," J. Am. Chem. Soc., vol. 132, pp. 1377–1382, 2010.

[180] G. Zhao, Y. He, and Y. Li, "6.5% efficiency of polymer solar cells based on poly(3-hexylthiophene) and indene-C60 bisadduct by device optimization," Adv. Mater., vol. 22, pp. 4355–4358, 2010.

[181] T. Li, S. Dai, Z. Ke, L. Yang, J. Wang, C. Yan, W. Ma, and X. Zhan, "Fused tris(thienothiophene)-based electron acceptor with strong near-infrared absorption for high-performance as-cast solar cells," Adv. Mater., vol. 30, pp. 1705969, 2018.

[182] J. Song, L. Zhu, C. Li, J. Xu, H. Wu, X. Zhang, Y. Zhang, Z. Tang, F. Liu, and Y. Sun, "High-efficiency organic solar cells with low voltage loss induced by solvent additive strategy," Matter, vol. 4, pp. 2542–2552, 2021.

[183] Y. Cui, H. Yao, J. Zhang, K. Xian, T. Zhang, L. Hong, Y. Wang, Y. Xu, K. Ma, C. An, et al., "Single-junction organic photovoltaic cells with approaching 18% efficiency," Adv. Mater., vol. 32, pp. 1908205, 2020.

[184] Y. Lin, J. Wang, Z.-G. Zhang, H. Bai, Y. Li, D. Zhu, and X. Zhan, "An electron acceptor challenging fullerenes for efficient polymer solar cells," Adv. Mater., vol. 27, pp. 1170–1174, 2015.

[185] Y. Lin, F. Zhao, Q. He, L. Huo, Y. Wu, T.C. Parker, W. Ma, Y. Sun, C. Wang, D. Zhu, et al., "High-performance electron acceptor with thienyl side chains for organic photovoltaics," J. Am. Chem. Soc., vol. 138, pp. 4955–4961, 2016.

[186] J.-L. Wang, K.-K. Liu, L. Hong, G.-Y. Ge, C. Zhang, and J. Hou, "Selenopheno[3,2-b]thiophene-based narrow-bandgap nonfullerene acceptor enabling 13.3% efficiency

for organic solar cells with thickness-insensitive feature," ACS Energy Lett., vol. 3, pp. 2967–2976, 2018.

[187] C. Li, J. Zhou, J. Song, J. Xu, H. Zhang, X. Zhang, J. Guo, L. Zhu, D. Wei, G. Han, et al., "Non-fullerene acceptors with branched side chains and improved molecular packing to exceed 18% efficiency in organic solar cells," Nat. Energy, vol. 6, pp. 605–613, 2021.

[188] G. Chai, Y. Chang, J. Zhang, X. Xu, L. Yu, X. Zou, X. Li, Y. Chen, S. Luo, B. Liu, et al., "Fine-tuning of side-chain orientations on nonfullerene acceptors enables organic solar cells with 17.7% efficiency," Energy Environ. Sci., vol. 14, pp. 3469–3479, 2021.

[189] J. Yuan, Y. Zhang, L. Zhou, G. Zhang, H.-L. Yip, T.-K. Lau, X. Lu, C. Zhu, H. Peng, P.A. Johnson, et al., "Single-junction organic solar cell with over 15% efficiency using fused-ring acceptor with electron-deficient core," Joule, vol. 3, pp. 1140–1151, 2019.

[190] Y. Cui, H. Yao, J. Zhang, T. Zhang, Y. Wang, L. Hong, K. Xian, B. Xu, S. Zhang, J. Peng, et al., "Over 16% efficiency organic photovoltaic cells enabled by a chlorinated acceptor with increased open-circuit voltages," Nat. Commun., vol. 10, pp. 2515, 2019.

[191] W. Zhao, D. Qian, S. Zhang, S. Li, O. Inganäs, F. Gao, and J. Hou, "Fullerene-free polymer solar cells with over 11% efficiency and excellent thermal stability," Adv. Mater., vol. 28, pp. 4734–4739, 2016.

[192] W. Zhao, S. Li, H. Yao, S. Zhang, Y. Zhang, B. Yang, and J. Hou, "Molecular optimization enables over 13% efficiency in organic solar cells," J. Am. Chem. Soc., vol. 139, pp. 7148–7151, 2017.

[193] X. Xu, T. Yu, Z. Bi, W. Ma, Y. Li, and Q. Peng, "Realizing over 13% efficiency in green-solvent-processed nonfullerene organic solar cells enabled by 1,3,4-thiadiazole-based wide-bandgap copolymers," Adv. Mater., vol. 30, pp. 1703973, 2018.

[194] Y. Lin, F. Zhao, S.K.K. Prasad, J.-D. Chen, W. Cai, Q. Zhang, K. Chen, Y. Wu, W. Ma, F. Gao, et al., "Balanced partnership between donor and acceptor components in nonfullerene organic solar cells with >12% efficiency," Adv. Mater., vol. 30, pp. 1706363, 2018.

[195] Q. Liu, Y. Jiang, K. Jin, J. Qin, J. Xu, W. Li, J. Xiong, J. Liu, Z. Xiao, K. Sun, et al., "18% Efficiency organic solar cells," Sci. Bull., vol. 65, pp. 272–275, 2020.

[196] S. Li, L. Ye, W. Zhao, S. Zhang, S. Mukherjee, H. Ade, and J. Hou, "Energy-level modulation of small-molecule electron acceptors to achieve over 12% efficiency in polymer solar cells," Adv. Mater., vol. 28, pp. 9423–9429, 2016.

[197] J. Zhu, Y. Xiao, J. Wang, K. Liu, H. Jiang, Y. Lin, X. Lu, and X. Zhan, "Alkoxy-induced near-infrared sensitive electron acceptor for high-performance organic solar cells," Chem. Mater., vol. 30, pp. 4150–4156, 2018.

[198] H.N. Tran, S. Park, F.T.A. Wibowo, N.V. Krishna, J.H. Kang, J.H. Seo, H. Nguyen-Phu, S.-Y. Jang, and S. Cho, "17% Non-fullerene organic solar cells with annealing-free aqueous MoOx," Adv. Sci., vol. 7, pp. 2002395, 2020.

[199] Z. Zhang, Y. Li, G. Cai, Y. Zhang, X. Lu, and Y. Lin, "Selenium heterocyclic electron acceptor with small urbach energy for as-cast high-performance organic solar cells," J. Am. Chem. Soc., vol. 142, pp. 18741–18745, 2020.

[200] S. Li, L. Ye, W. Zhao, S. Zhang, S. Mukherjee, H. Ade, and J. Hou, "Energy-level modulation of small-molecule electron acceptors to achieve over 12% efficiency in polymer solar cells," Adv. Mater., vol. 28, pp. 9423–9429, 2016.

[201] H.N. Tran, S. Park, F.T.A. Wibowo, N.V. Krishna, J.H. Kang, J.H. Seo, H. Nguyen-Phu, S.-Y. Jang, and S. Cho, "17% Non-fullerene organic solar cells with annealing-free aqueous MoOx," Adv. Sci., vol. 7, pp. 2002395, 2020.

[202] X. Zhan, Z.A. Tan, B. Domercq, Z. An, X. Zhang, S. Barlow, Y. Li, D. Zhu, B. Kippelen, and S.R. Marder, "A high-mobility electron-transport polymer with broad absorption and its use in field-effect transistors and all-polymer solar cells," J. Am. Chem. Soc., vol. 129, pp. 7246-7247, 2007.

[203] Y. Guo, Y. Li, O. Awartani, J. Zhao, H. Han, H. Ade, D. Zhao, and H. Yan, "A vinylene-bridged perylenediimide-based polymeric acceptor enabling efficient all-polymer solar cells processed under ambient conditions," Adv. Mater., vol. 28, pp. 8483-8489, 2016.

[204] D. Mori, H. Benten, I. Okada, H. Ohkita, and S. Ito, "Low-bandgap donor/acceptor polymer blend solar cells with efficiency exceeding 4%," Adv. Energy Mater., vol. 4, 1301006, 2014.

[205] L. Gao, Z.-G. Zhang, L. Xue, J. Min, J. Zhang, Z. Wei, and Y. Li, "All-polymer solar cells based on absorption-complementary polymer donor and acceptor with high power conversion efficiency of 8.27%," Adv. Mater., vol. 28, pp. 1884-1890, 2016.

[206] Y. Shi, H. Guo, J. Huang, X. Zhang, Z. Wu, K. Yang, Y. Zhang, K. Feng, H. Y. Woo, and R. Ortiz, "Distannylated bithiophene imide: Enabling high-performance n-type polymer semiconductors with an acceptor-acceptor backbone," Angew. Chem., vol. 132, pp. 14557-14565, 2020.

[207] Y. Guo, Y. Li, O. Awartani, H. Han, J. Zhao, H. Ade, H. Yan, and D. Zhao, "Improved performance of all-polymer solar cells enabled by naphthodiperylenetetraimide-based polymer acceptor," Adv. Mater., vol. 29, 1700309, 2017.

[208] B. Fan, L. Ying, Z. Wang, B. He, X.-F. Jiang, F. Huang, and Y. Cao, "Optimisation of processing solvent and molecular weight for the production of green-solvent-processed all-polymer solar cells with a power conversion efficiency over 9%," Energy Environ. Sci., vol. 10, pp. 1243-1251, 2017.

[209] H. Fu, Y. Li, J. Yu, Z. Wu, Q. Fan, F. Lin, H. Y. Woo, F. Gao, Z. Zhu, and A. K. Y. Jen, "High efficiency (15.8%) all-polymer solar cells enabled by a regioregular narrow bandgap polymer acceptor," J. Am. Chem. Soc., vol. 143, pp. 2665-2670, 2021.

[210] W. Wang, Q. Wu, R. Sun, J. Guo, Y. Wu, M. Shi, W. Yang, H. Li, and J. Min, "Controlling molecular mass of low-band-gap polymer acceptors for high-performance all-polymer solar cells," Joule, vol. 4, pp. 1070-1086, 2020.

[211] H. Yu, Z. Qi, J. Yu, Y. Xiao, R. Sun, Z. Luo, A. M. H. Cheung, J. Zhang, H. Sun, W. Zhou, et al., "Fluorinated end group enables high-performance all-polymer solar cells with near-infrared absorption and enhanced device efficiency over 14%," Adv. Energy Mater., vol. 11, 2003171, 2021.

[212] R. Zhao, N. Wang, Y. Yu, and J. Liu, "Organoboron polymer for 10% efficiency all-polymer solar cells," Chem. Mater., vol. 32, pp. 1308-1314, 2020.

[213] Z. Luo, T. Liu, R. Ma, Y. Xiao, L. Zhan, G. Zhang, H. Sun, F. Ni, G. Chai, J. Wang, et al., "Precisely controlling the position of bromine on the end group enables well-regular polymer acceptors for all-polymer solar cells with efficiencies over 15%," Adv. Mater., vol. 32, 2005942, 2020.

[214] H. Yu, S. Luo, R. Sun, I. Angunawela, Z. Qi, Z. Peng, W. Zhou, H. Han, R. Wei, M. Pan, et al., "A difluoro-monobromo end group enables high-performance polymer acceptor and efficient all-polymer solar cells processable with green solvent under ambient condition," Adv. Funct. Mater., vol. 31, 2100791, 2021.

[215] X. Zhan, Z. A. Tan, B. Domercq, Z. An, X. Zhang, S. Barlow, Y. Li, D. Zhu, B. Kippelen, and S. R. Marder, "A high-mobility electron-transport polymer with broad absorption and its use in field-effect transistors and all-polymer solar cells," J. Am. Chem. Soc., vol. 129, pp. 7246-7247, 2007.

[216] L. Gao, Z.-G. Zhang, L. Xue, J. Min, J. Zhang, Z. Wei, and Y. Li, "All-polymer solar cells based on absorption-complementary polymer donor and acceptor with high power conversion efficiency of 8.27%," Adv. Mater., vol. 28, pp. 1884-1890, 2016.

[217] L. Zhu, W. Zhong, C. Qiu, B. Lyu, Z. Zhou, M. Zhang, J. Song, J. Xu, J. Wang, J. Ali, et al., "Aggregation-induced multilength scaled morphology enabling 11.76% efficiency in all-polymer solar cells using printing fabrication," Adv. Mater., vol. 31, 1902899, 2019.

[218] H. Sun, H. Yu, Y. Shi, J. Yu, Z. Peng, X. Zhang, B. Liu, J. Wang, R. Singh, J. Lee, et al., "A narrow-bandgap n-type polymer with an acceptor–acceptor backbone enabling efficient all-polymer solar cells," Adv. Mater., vol. 32, 2004183, 2020.

[219] T. Jia, J. Zhang, W. Zhong, Y. Liang, K. Zhang, S. Dong, L. Ying, F. Liu, X. Wang, F. Huang, et al., "14.4% efficiency all-polymer solar cell with broad absorption and low energy loss enabled by a novel polymer acceptor," Nano Energy, vol. 72, 104718, 2020.

[220] Y. Guo, Y. Li, O. Awartani, J. Zhao, H. Han, H. Ade, D. Zhao, and H. Yan, "A vinylene-bridged perylenediimide-based polymeric acceptor enabling efficient all-polymer solar cells processed under ambient conditions," Adv. Mater., vol. 28, pp. 8483-8489, 2016.

[221] D. Mori, H. Benten, I. Okada, H. Ohkita, and S. Ito, "Low-bandgap donor/acceptor polymer blend solar cells with efficiency exceeding 4%," Adv. Energy Mater., vol. 4, 1301006, 2014.

[222] Y. Shi, H. Guo, J. Huang, X. Zhang, Z. Wu, K. Yang, Y. Zhang, K. Feng, H. Y. Woo, and R. Ortiz, "Distannylated bithiophene imide: Enabling high-performance n-type polymer semiconductors with an acceptor-acceptor backbone," Angew. Chem., vol. 132, pp. 14557-14565, 2020.

[223] H. Sun, H. Yu, Y. Shi, J. Yu, Z. Peng, X. Zhang, B. Liu, J. Wang, R. Singh, J. Lee, et al., "A narrow-bandgap n-type polymer with an acceptor–acceptor backbone enabling efficient all-polymer solar cells," Adv. Mater., vol. 32, 2004183, 2020.

[224] T. Jia, J. Zhang, W. Zhong, Y. Liang, K. Zhang, S. Dong, L. Ying, F. Liu, X. Wang, F. Huang, et al., "14.4% efficiency all-polymer solar cell with broad absorption and low energy loss enabled by a novel polymer acceptor," Nano Energy, vol. 72, 104718, 2020.

[225] D. Mühlbacher, M. Scharber, M. Morana, Z. Zhu, D. Waller, R. Gaudiana, and C. Brabec, "High photovoltaic performance of a low-bandgap polymer," Adv. Mater., vol. 18, pp. 2884-2889, 2006.

[226] H.-Y. Chen, J. Hou, S. Zhang, Y. Liang, G. Yang, Y. Yang, L. Yu, Y. Wu, and G. Li, "Polymer solar cells with enhanced open-circuit voltage and efficiency," Nat. Photonics, vol. 3, pp. 649-653, 2009.

[227] Y. Liang, Y. Wu, D. Feng, S.-T. Tsai, H.-J. Son, G. Li, and L. Yu, "Development of new semiconducting polymers for high performance solar cells," J. Am. Chem. Soc., vol. 131, pp. 56-57, 2009.

[228] Y. Liang, Z. Xu, J. Xia, S.-T. Tsai, Y. Wu, G. Li, C. Ray, and L. Yu, "For the bright future-bulk heterojunction polymer solar cells with power conversion efficiency of 7.4%," Adv. Mater., vol. 22, E135-E138, 2010.

[229] H.-Y. Chen, J. Hou, S. Zhang, Y. Liang, G. Yang, Y. Yang, L. Yu, Y. Wu, and G. Li, "Polymer solar cells with enhanced open-circuit voltage and efficiency," Nat. Photonics, vol. 3, pp. 649-653, 2009.

[230] Y. Liu, J. Zhao, Z. Li, C. Mu, W. Ma, H. Hu, K. Jiang, H. Lin, H. Ade, and H. Yan, "Aggregation and morphology control enables multiple cases of high-efficiency polymer solar cells," Nat. Commun., vol. 5, 5293, 2014.

[231] S. H. Liao, H. J. Jhuo, Y. S. Cheng, and S. A. Chen, "Fullerene derivative-doped zinc oxide nanofilm as the cathode of inverted polymer solar cells with low-bandgap polymer (PTB7-Th) for high performance," Adv. Mater., vol. 25, pp. 4766-4771, 2013.

[232] G. Zhao, Y. He, and Y. Li, "6.5% efficiency of polymer solar cells based on poly(3-hexylthiophene) and indene-C60 bisadduct by device optimization," Adv. Mater., vol. 22, pp. 4355-4358, 2010.

[233] J. Zhao, Y. Li, G. Yang, K. Jiang, H. Lin, H. Ade, W. Ma, and H. Yan, "Efficient organic solar cells processed from hydrocarbon solvents," Nat. Energy, vol. 1, 15027, 2016.

[234] Y. Liang, Y. Wu, D. Feng, S.-T. Tsai, H.-J. Son, G. Li, and L. Yu, "Development of new semiconducting polymers for high performance solar cells," J. Am. Chem. Soc., vol. 131, pp. 56-57, 2009.

[235] J. Peet, J. Kim, N. E. Coates, W. L. Ma, D. Moses, A. J. Heeger, and G. C. Bazan, "Efficiency enhancement in low-bandgap polymer solar cells by processing with alkane dithiols," Nat. Mater., vol. 6, pp. 497-500, 2007.

[236] J.-D. Chen, C. Cui, Y.-Q. Li, L. Zhou, Q.-D. Ou, C. Li, Y. Li, and J.-X. Tang, "Single-junction polymer solar cells exceeding 10% power conversion efficiency," Adv. Mater., vol. 27, pp. 1035-1041, 2015.

[237] Y. Liang, D. Feng, Y. Wu, S.-T. Tsai, G. Li, C. Ray, and L. Yu, "Highly efficient solar cell polymers developed via fine-tuning of structural and electronic properties," J. Am. Chem. Soc., vol. 131, pp. 7792-7799, 2009.

[238] Z. He, C. Zhong, S. Su, M. Xu, H. Wu, and Y. Cao, "Enhanced power-conversion efficiency in polymer solar cells using an inverted device structure," Nat. Photonics, vol. 6, pp. 591-595, 2012.

[239] Y. Liu, J. Zhao, Z. Li, C. Mu, W. Ma, H. Hu, K. Jiang, H. Lin, H. Ade, and H. Yan, "Aggregation and morphology control enables multiple cases of high-efficiency polymer solar cells," Nat. Commun., vol. 5, 5293, 2014.

[240] W. Zhao, S. Li, H. Yao, S. Zhang, Y. Zhang, B. Yang, and J. Hou, "Molecular optimization enables over 13% efficiency in organic solar cells," J. Am. Chem. Soc., vol. 139, pp. 7148-7151, 2017.

[241] Y. Cui, H. Yao, J. Zhang, K. Xian, T. Zhang, L. Hong, Y. Wang, Y. Xu, K. Ma, C. An, et al., "Single-junction organic photovoltaic cells with approaching 18% efficiency," Adv. Mater., vol. 32, 1908205, 2020.

[242] L. Xue, Y. Yang, J. Xu, C. Zhang, H. Bin, Z.-G. Zhang, B. Qiu, X. Li, C. Sun, L. Gao, et al., "Side chain engineering on medium bandgap copolymers to suppress triplet formation for high-efficiency polymer solar cells," Adv. Mater., vol. 29, 1703344, 2017.

[243] R. Ma, T. Liu, Z. Luo, Q. Guo, Y. Xiao, Y. Chen, X. Li, S. Luo, X. Lu, M. Zhang, et al., "Improving open-circuit voltage by a chlorinated polymer donor endows binary organic solar cells efficiencies over 17%," Sci. China Chem., vol. 63, pp. 325-330, 2020.

[244] J. Qin, L. Zhang, C. Zuo, Z. Xiao, Y. Yuan, S. Yang, F. Hao, M. Cheng, K. Sun, Q. Bao, et al., "A chlorinated copolymer donor demonstrates a 18.13% power conversion efficiency," J. Semicond., vol. 42, 010501, 2021.

[245] Y. Lin, F. Zhao, Q. He, L. Huo, Y. Wu, T. C. Parker, W. Ma, Y. Sun, C. Wang, D. Zhu, et al., "High-performance electron acceptor with thienyl side chains for organic photovoltaics," J. Am. Chem. Soc., vol. 138, pp. 4955-4961, 2016.

[246] S. Zhang, Y. Qin, J. Zhu, and J. Hou, "Over 14% efficiency in polymer solar cells enabled by a chlorinated polymer donor," Adv. Mater., vol. 30, 1800868, 2018.

[247] Y. Cui, H. Yao, L. Hong, T. Zhang, Y. Xu, K. Xian, B. Gao, J. Qin, J. Zhang, Z. Wei, et al., "Achieving over 15% efficiency in organic photovoltaic cells via copolymer design," Adv. Mater., vol. 31, 1808356, 2019.

[248] J. Xiong, K. Jin, Y. Jiang, J. Qin, T. Wang, J. Liu, Q. Liu, H. Peng, X. Li, A. Sun, et al., "Thiolactone copolymer donor gifts organic solar cells a 16.72% efficiency," Sci. Bull., vol. 64, pp. 1573-1576, 2019.

[249] J. Yuan, Y. Zhang, L. Zhou, G. Zhang, H.-L. Yip, T.-K. Lau, X. Lu, C. Zhu, H. Peng, P. A. Johnson, et al., "Single-junction organic solar cell with over 15% efficiency using fused-ring acceptor with electron-deficient core," Joule, vol. 3, pp. 1140-1151, 2019.

[250] W. Zhao, D. Qian, S. Zhang, S. Li, O. Inganäs, F. Gao, and J. Hou, "Fullerene-free polymer solar cells with over 11% efficiency and excellent thermal stability," Adv. Mater., vol. 28, pp. 4734-4739, 2016.

[251] K. Jin, Z. Xiao, and L. Ding, "D18, an eximious solar polymer!," J. Semicond., vol. 42, 010502, 2021.

[252] H. Bin, Z.-G. Zhang, L. Gao, S. Chen, L. Zhong, L. Xue, C. Yang, and Y. Li, "Non-fullerene polymer solar cells based on alkylthio and fluorine substituted 2D-conjugated polymers reach 9.5% efficiency," J. Am. Chem. Soc., vol. 138, pp. 4657-4664, 2016.

[253] Q. Liu, Y. Jiang, K. Jin, J. Qin, J. Xu, W. Li, J. Xiong, J. Liu, Z. Xiao, K. Sun, et al., "18% Efficiency organic solar cells," Sci. Bull., vol. 65, pp. 272-275, 2020.

[254] J. Yuan, T. Huang, P. Cheng, Y. Zou, H. Zhang, J. L. Yang, S.-Y. Chang, Z. Zhang, W. Huang, R. Wang, et al., "Enabling low voltage losses and high photocurrent in fullerene-free organic photovoltaics," Nat. Commun., vol. 10, 570, 2019.

[255] S. Zhang, Y. Qin, J. Zhu, and J. Hou, "Over 14% efficiency in polymer solar cells enabled by a chlorinated polymer donor," Adv. Mater., vol. 30, 1800868, 2018.

[256] J. Min, Z.-G. Zhang, S. Zhang, and Y. Li, "Conjugated side-chain-isolated D-A copolymers based on benzo[1,2-b:4,5-b0]dithiophenealt- dithienylbenzotriazole: Synthesis and photovoltaic properties," Chem. Mater., vol. 24, pp. 3247-3254, 2012.

[257] P. E. Burrows and S. R. Forrest, "Operating lifetime of phosphorescent organic light emitting devices," Appl. Phys. Lett., vol. 76, 2493, 2000.

[258] Q. Burlingame et al., "Intrinsically stable organic solar cells under high-intensity illumination," Nature, vol. 573, pp. 394-397, 2019.

[259] X. Xu, J. Xiao, G. Zhang, L. Wei, X. Jiao, H.-L. Yip, and Y. Cao, "Interface-enhanced organic solar cells with extrapolated T80 lifetimes of over 20 years," Sci. Bull., vol. 65, pp. 208-216, 2019.

[260] W. Qiu, R. Müller, E. Voroshazi, B. Conings, R. Carleer, H.-G. Boyen, M. Turbiez, L. Froyen, P. Heremans, A. Hadipour, "Solvent Annealing Effect in Sequentially Deposited Polymer: Fullerene Photovoltaic Devices," ACS Appl. Mater. Interfaces, vol. 7, pp. 3581-3587, 2015.

[261] E. Voroshazi, I. Cardinaletti, G. Uytterhoeven, A. Hadipour, B. P. Rand, T. Aernouts, "Device Stability of Flexible Organic Solar Cells," in 2013 IEEE 39th Photovoltaic Specialists Conference (PVSC), IEEE, 2013, pp. 3212-3216.

[262] N. Chaturvedi, S. K. Swami, A. Kumar, V. Dutta, "High Performance Solar Cell with Polymer Blend as Electron Acceptor," Sol. Energy Mater. Sol. Cells, vol. 126, pp. 74-81, 2014.

[263] M. Corazza, F. C. Krebs, S. A. Gevorgyan, "R2R slot die-coated organic solar modules: techniques to achieve 1.2 cm2/second coating speed," Sol. Energy Mater. Sol. Cells, vol. 130, pp. 99-105, 2014.

[264] J.-H. Huang, K.-C. Lee, "Effects of polymer molecular weight on performance of polymer solar cells," ACS Appl. Mater. Interfaces, vol. 6, pp. 7680-7686, 2014.

[265] M. T. Lloyd, D. C. Olson, J. J. Berry, N. Kopidakis, M. O. Reese, K. X. Steirer, D. S. Ginley, "Accelerated Lifetime Measurements of Organic Photovoltaic Materials," in 2010 35th IEEE Photovoltaic Specialists Conference, IEEE, 2010, pp. 001060-001063.

[266] X. Du et al., "Efficient polymer solar cells based on non-fullerene acceptors with potential device lifetime approaching 10 years," Joule, vol. 3, pp. 215-226, 2019.

[267] F. C. Krebs, J. E. Carlé, N. Cruys-Bagger, M. Andersen, M. R. Lilliedal, M. A. Hammond, and S. Hvidt, "Lifetimes of organic photovoltaics: photochemistry, atmosphere effects and barrier layers in ITO-MEHPPV:PCBM-aluminium devices," Sol. Energy Mater. Sol. Cells, vol. 86, pp. 499-516, 2005.

[268] S. Schuller et al., "Determination of the degradation constant of bulk heterojunction solar cells by accelerated lifetime measurements," Appl. Phys. A, vol. 79, pp. 37-40, 2004.

[269] Q. Burlingame et al., "Intrinsically stable organic solar cells under high-intensity illumination," Nature, vol. 573, pp. 394-397, 2019.

[270] E. Ravishankar, R. E. Booth, C. Saravitz, H. Sederoff, H. W. Ade, and B. T. O'Connor, "Achieving net zero energy greenhouses by integrating semitransparent organic solar cells," Joule, vol. 4, pp. 490-506, 2020.

[271] D. Wang et al., "High-performance and eco-friendly semitransparent organic solar cells for greenhouse applications," Joule, vol. 5, pp. 945-957, 2021.

[272] C. Sun, R. Xia, H. Shi, et al., "Heat-insulating multifunctional semitransparent polymer solar cells," Joule, vol. 2, pp. 1816-1826, 2018.

[273] M. Ninck, M. Untenberger, T. Gisler, "Diffusing-wave spectroscopy with dynamic contrast variation: disentangling the effects of blood flow and extravascular tissue

shearing on signals from deep tissue," Biomed Opt Express, vol. 1, pp. 1502-1513, 2010.

[274] M. C. Meinke, M. Friebel, and J. Helfmann, "Optical properties of flowing blood cells," in Advanced Optical Flow Cytometry: Methods and Disease Diagnoses, V. V. Tuchin, Ed. Wiley-VCH Verlag GmbH & Co.KGaA, 2011, pp. 95–132.

[275] Y. K. Park, M. Diez-Silva, D. Fu, G. Popescu, W. Choi, I. Barman, et al., "Static and dynamic light scattering of healthy and malaria-parasite invaded red blood cells," J. Biomed. Opt., vol. 15, p. 020506, 2010.

[276] Y. K. Park, C. A. Best-Popescu, R. R. Dasari, and G. Popescu, "Light scattering of human red blood cells during metabolic remodeling of the membrane," J. Biomed. Opt., vol. 16, p. 011013, 2011.

[277] J. Lim, H. Ding, M. Mir, R. Zhu, K. Tangella, and G. Popescu, "Born approximation model for light scattering by red blood cells," Biomed. Opt. Express, vol. 2, pp. 2784–2791, 2011.

[278] Y. Kim, J. M. Higgins, R. R. Dasari, S. Suresh, and Y. K. Park, "Anisotropic light scattering of individual sickle red blood cells," J. Biomed. Opt., vol. 17, p. 040501, 2012.

[279] Y. K. Park, C. A. Best, T. Auth, N. S. Gov, S. A. Safran, G. Popescu, et al., "Metabolic remodeling of the human red blood cell membrane," Proc. Natl. Acad. Sci. USA, vol. 107, pp. 1289–1294, 2010.

[280] H. Turlier, D. A. Fedosov, B. A. Audoly, T. Auth, N. S. Gov, C. Sykes, et al., "Equilibrium physics breakdown reveals the active nature of red blood cell membrane fluctuations," Nat. Phys., vol. 12, pp. 513–519, 2016.

[281] S. S. Yang, Z. C. Hsieh, M. L. Keshtov, G. D. Sharma, and F. C. Chen, "Toward high-performance polymer photovoltaic devices for low-power indoor applications," Sol RRL, vol. 1, p. 1700174, 2017.

[282] S. Mori, T. Gotanda, Y. Nakano, M. Saito, K. Todori, and M. Hosoya, "Jpn. J. Appl. Phys.," vol. 54, p. 071602, 2015.

[283] C. L. Cutting, M. Bag, and D. Venkataraman, "J. Mater. Chem. C," vol. 4, pp. 10367–10370, 2016.

[284] Y. S. Hsiao, Y. H. Liao, H. L. Chen, P. L. Chen, and F. C. Chen, "Organic photovoltaics and bioelectrodes providing electrical stimulation for PC12 cell differentiation and neurite outgrowth," ACS Appl. Mater. Interfaces, vol. 8, pp. 9275–9284, 2016.

[285] J. Choi, D. Kwon, B. Kim, K. Kang, J. M. Gu, J. Jo, et al., "Wearable self-powered pressure sensor by integration of piezo-transmittance microporous elastomer with organic solar cell," Nano Energy, vol. 74, p. 104749, 2020.

[286] S. Park, S. W. Heo, W. Lee, D. Inoue, Z. Jiang, K. Yu, et al., "Self-powered ultraflexible electronics via nano-grating-patterned organic photovoltaics," Nature, vol. 561, pp. 516–521, 2018.

[287] L. Lu et al., "Biodegradable monocrystalline silicon photovoltaic microcells as power supplies for transient biomedical implants," Adv. Energy Mater., vol. 8, pp. 1–8, 2018.

[288] J. N. Hoover, D. L. Singer, P. Pahwa, and K. Komiyama, "Clinical evaluation of a light energy conversion toothbrush," J. Clin. Periodontol., vol. 19, pp. 434–436, 1992.

[289] J. F. Maya-Vetencourt et al., "A fully organic retinal prosthesis restores vision in a rat model of degenerative blindness," Nat. Mater., vol. 16, pp. 681–689, 2017.

[290] S. Park et al., "Self-powered ultra-flexible electronics via nanograting-patterned organic photovoltaics," Nature, vol. 561, pp. 516–521, 2018.

[291] Y. S. Hsiao et al., "Organic photovoltaics and bioelectrodes providing electrical stimulation for PC12 cell differentiation and neurite outgrowth," ACS Appl. Mater. Interfaces, vol. 8, pp. 9275–9284, 2016.

[292] S. Park et al., "Self-powered ultraflexible electronics via nano-grating-patterned organic photovoltaics," Nature, vol. 561, pp. 516–521, 2018.

[293] D. Ghezzi et al., "A polymer optoelectronic interface restores light sensitivity in blind rat retinas," Nat. Photonics, vol. 7, pp. 400–406, 2013.

[294] D. Khodagholy et al., "NeuroGrid: Recording action potentials from the surface of the brain," Nat. Neurosci., vol. 18, pp. 310–315, 2015.

[295] S. Bonetti et al., "A lysinated thiophene-based semiconductor as a multifunctional neural bioorganic interface," Adv. Healthc. Mater., vol. 4, pp. 1190–1202, 2015.

[296] E. Bystrenova et al., "Neural networks grown on organic semiconductors," Adv. Funct. Mater., vol. 18, pp. 1751–1756, 2008.

[297] S. M. Richardson-Burns et al., "Polymerization of the conducting polymer poly(3,4-ethylenedioxythiophene) (PEDOT) around living neural cells," Biomaterials, vol. 28, pp. 1539–1552, 2007.

[298] N. Zaquen et al., "Profluorescent PPV-Based Micellar System as a Versatile Probe for Bioimaging and Drug Delivery," Biomacromolecules, vol. 17, pp. 4086–4094, 2016.

[299] G. Kim et al., "Bacterial adhesion, cell adhesion and biocompatibility of nafion films," J. Biomater. Sci. Polym. Ed., vol. 20, pp. 1687–1707, 2009.

[300] N. Li, X. Zhang, Q. Song, R. Su, Q. Zhang, T. Kong, L. Liu, G. Jin, M. Tang, and G. Cheng, "The promotion of neurite sprouting and outgrowth of mouse hippocampal cells in culture by graphene substrates," Biomaterials, vol. 32, pp. 9374–9382, 2011.

[301] T. J. Rivers, T. W. Hudson, and C. E. Schmidt, "Synthesis of a novel, biodegradable electrically conducting polymer for biomedical applications," Adv. Funct. Mater., vol. 12, pp. 33–37, 2002.

[302] S. Kamalesh, P. Tan, J. Wang, T. Lee, E. T. Kang, and C. H. Wang, "Biocompatibility of electroactive polymers in tissues," J. Biomed. Mater. Res., vol. 52, pp. 467–478, 2000.

[303] D. Khodagholy, J. N. Gelinas, T. Thesen, W. Doyle, O. Devinsky, G. G. Malliaras, and G. Buzsáki, "NeuroGrid: Recording action potentials from the surface of the brain," Nat. Neurosci., vol. 18, pp. 310–315, 2015.

[304] Y. Wang, W. Zhang, L. Huang, Y. Ito, Z. Wang, X. Shi, Y. Wei, X. Jing, and P. Zhang, "Intracellular calcium ions and morphological changes of cardiac myoblasts response to an intelligent biodegradable conducting copolymer," Mater. Sci. Eng. C, vol. 90, pp. 168–179, 2018.

[305] S. Kamalesh, P. Tan, J. Wang, T. Lee, E. T. Kang, and C. H. Wang, "Biocompatibility of electroactive polymers in tissues," J. Biomed. Mater. Res., vol. 52, pp. 467–478, 2000.

[306] D. Ghezzi, M. R. Antognazza, M. Dal Maschio, E. Lanzarini, F. Benfenati, and G. Lanzani, "A hybrid bioorganic interface for neuronal photoactivation," Nat. Commun., vol. 2, p. 166, 2011.

[307] A. Mazzatenta, M. Giugliano, S. Campidelli, L. Gambazzi, L. Businaro, H. Markram, M. Prato, and L. Ballerini, "Interfacing neurons with carbon nanotubes: Electrical signal transfer and synaptic stimulation in cultured brain circuits," J. Neurosci., vol. 27, pp. 6931–6936, 2007.

[308] A.L. Stanford and J.M. Tanner, "Early quantum physics," Phys. Stud. Sci. Eng., pp. 691-716, 1985.

[309] N. Amin, K. Sopian, and M. Konagai, "Numerical modelling of Cds/CdTe and Cds/CdTe/ZnTe solar cells as a function of CdTe thickness," Sol. Energy Mater. Sol. Cells, vol. 91, no. 13, pp. 1202-1208, 2007.

[310] S. Negi, P. Mittal, B. Kumar, and P. Juneja, "Organic LED based light sensor for detection of ovarian cancer," Microelectron. Eng., vol. 218, pp. 111154-111164, 2019.

[311] M.B. Rabha and B. Bessaïs, "Enhancement of photovoltaic properties of multicrystalline silicon solar cells by combination of buried metallic contacts and thin porous silicon," Sol. Energy, vol. 84, no. 3, pp. 486-491, 2010.

[312] T. Mahalingam, V.S. John, S. Rajendran, and P.J. Sebastian, "Electrochemical deposition of ZnTe thin films," Semicond. Sci. Technol., vol. 17, no. 5, pp. 465-470, 2002.

[313] W. Tao, M. Jurkovic, and W.I. Wang, "Doping of ZnTe by molecular beam epitaxy," Appl. Phys. Lett., vol. 64, pp. 1848-1849, 1994.

[314] P.R. Nikam, P.K. Baviskar, J.V. Sali, K.V. Gurav, J.H. Kim, and B.R. Sankapal, "CdS surface encapsulated ZnO nanorods: synthesis to solar cell application," J. Alloys Compd., vol. 689, pp. 394-400, 2016.

[315] N. Pandey, B. Kumar, and D.K. Dwivedi, "Synthesis and characterization of pure and Sb/Sn doped ZnTe for solar cell application," Mater. Res. Express, vol. 6, no. 9, 096425, 2019.

[316] H. Benelmadjat, B. Boudine, O. Halimi, and M. Sebais, "Fabrication and characterization of pure and Sn/Sb-doped ZnO thin films deposited by sol-gel method," Opt. Laser Technol., vol. 41, no. 5, pp. 630-633, 2009.

[317] H. Bayad, A.E. Manouni, B. Marí, Y.H. Khattak, S. Ullah, and F. Baig, "Influence of P+ ZnTe back surface contact on photovoltaic performance of ZnTe based solar cells," Opt. Quantum Electron., vol. 50, no. 6, p. 259, 2018.

[318] O.I. Olusola, M.L. Madugu, N.A. Abdul-Manaf, and I.M. Dharmadasa, "Growth and characterisation of n- and p-type ZnTe thin films for applications in electronic devices," Curr. Appl. Phys., vol. 16, pp. 120-130, 2016.

[319] T. Tanaka, M. Miyabara, K. Saito, Q. Guo, M. Nishio, K.M. Yu, and W. Walukiewicz, "Development of ZnTe-based solar cells," Mater. Sci. Forum, vol. 750, pp. 80-83, 2013.

[320] T. Tanaka, K.M. Yu, P.R. Stone, J.W. Beeman, and O.D. Dubon, "Demonstration of homojunction ZnTe solar cells," J. Appl. Phys., vol. 108, 024502, 2010.

[321] R. Sharma, N.S. Saxena, S. Kumar, and T.P. Sharma, "Optical band gap studies on Zn-Te pellets," Indian J. Pure Appl. Phys., vol. 44, pp. 192-195, 2006.

[322] ATLAS, "ATLAS User's Manual Device Simulation Software," Silaco International Ltd, Santa Clara, 2014.

[323] Q. Gul, M. Zakriab, T.M. Khan, A. Mahmood, and A. Iqbal, "Effects of Cu incorporation on physical properties of ZnTe thin films deposited by thermal evaporation," Mater. Sci. Semicond. Process., vol. 19, pp. 17-23, 2014.

[324] M. Isik, H.H. Gullu, M. Parlak, and N.M. Gasanly, "Synthesis and temperature tuned band gap characteristics of magnetron sputtered ZnTe thin films," Physica B: Physics Condensed Matter, vol. 582, 411968, 2020.

[325] J.D. Lopez, J.D. Lopezab, L. Tirado-Mejíaa, H. Ariza-Calderona, H. Riascosc, Fde Andad, and E. Mosquerabe, "Structural and Optical Properties of Gadolinium Doped ZnTe Thin Films," Materials Letters, vol. 268, 127562, 2020.

[326] R. Zarei, M.H. Ehsani, and H.R. Dizaji, "An investigation on structural and optical properties of nanocolumnar ZnTe thin films grown by glancing angle technique," Mater. Res. Express, vol. 7, 026419, 2020.

[327] J. Meija, T.B. Coplen, M. Berglund, W.A. Brand, P. De Bièvre, M. Gröning, N.E. Holden, J. Irrgeher, R.D. Loss, T. Walczyk, and T. Prohaska, "Atomic weights of the elements 2013 (IUPAC Technical Report)," Pure Appl. Chem., vol. 88, no. 3, pp. 265-291, 2016.

[328] M. Witkowska-Baran, A. Mycielski, D. Kochanowska, A.J. Szadkowski, R. Jakiela, B. Witkowska, W. Kaliszek, J. Domagala, E. Lusakowska, V. Domukhovski, and K. Dybko, "Contacts for high-resistivity (Cd, Mn) Te crystals," IEEE Trans. Nucl. Sci., vol. 58, no. 1, pp. 347-353, 2011.

[329] N. Pandey, B. Kumar, and D.K. Dwivedi, "Influence of thermal annealing on structural and optical properties of Sb doped ZnTe thin film," Adv. Sci. Eng. Med., vol. 12, no. 1, pp. 100-104, 2020.

[330] Y.H. Khattak, F.B.S. Ullah, B. Marí, S. Beg, and H. Ullah, "Enhancement of the conversion efficiency of thin film kesterite solar cell," J. Renew. Sustain. Energy, vol. 10, 033501, 2018.

[331] K. Mukhopadhyay, P.F.H. Inbaraj, and J.J. Prince, "Thickness optimization of CdS/ZnO hybrid buffer layer in CZTSe thin film solar cells using SCAPS simulation program," Mater. Res. Innov., vol. 23, 52, pp. 1-11, 2018.

[332] D.E. Aimouch, S. Meskine, Y.B. Cherif, A. Zaoui, and A. Boukortt, "Effect of sodium p-type doping on the structural, electrical and optical properties of zinc oxide," Optik, vol. 130, pp. 1320-1326, 2017.

[333] W. Qarony, M.I. Hossain, M.K. Hossain, M.J. Uddin, A. Haque, A.R. Saad, and Y.H. Tsang, "Efficient amorphous silicon solar cells: characterization, optimization, and optical loss analysis," Results Phys., vol. 7, pp. 4287-4293, 2017.

[334] Z. Yu, X. Zhang, H. Zhang, Y. Huang, Y. Li, X. Zhang, and Z. Gan, "Improved power conversion efficiency in radial junction thin film solar cells based on amorphous silicon germanium alloys," J. Alloys. Compd., vol. 803, pp. 260-264, 2019.

[335] F.A. Jhuma and M.J. Rashid, "Simulation study to find suitable dopants of CdS buffer layer for CZTS solar cell," J. Theor. Appl. Phys., vol. 14, pp. 75-84, 2020.

[336] B. Singh, J. Singh, R. Kaur, R.K. Moudgil, and S.K. Tripathi, "Quantitative measurement of transport properties: Ag-doped nanocrystalline CdS thin films," R. Soc. Chem., vol. 7, pp. 53951-53962, 2017.

[337] H.H.A. Safe, M. Hossain, H. Naseem, W. Brown, and A.A. Dhafiri, "Chlorine-doped CdS thin films from CdCl2-mixed CdS powder," J. Electron. Mater., vol. 33, no. 2, pp. 128-134, 2004.

[338] A. Kaneta and S. Adachi, "Photoreflectance study in the E-1 and E-1+Delta 1 transition regions of ZnTe," J. Phys. D Appl. Phys., vol. 33, no. 8, pp. 901-905, 2000.

[339] W. Shockley and H.J. Queisser, "Detailed balance limit of efficiency of p-n junction solar cells," J. Appl. Phys., vol. 32, no. 3, pp. 510-519, 1961.

[340] S. Hussain, C. Cao, G. Nabi, W.S. Khan, M. Tahir, M. Tanveer, and I. Aslam, "Optical and electrical characterisation of ZnO/Cuo heterojunction solar cells," Optik, vol. 130, pp. 372-377, 2017.

[341] D.E. Aimouch, S. Meskine, Y.B. Cherif, A. Zaoui, and A. Boukortt, "Effect of sodium p-type doping on the structural, electrical and optical properties of zinc oxide," Optik, vol. 130, pp. 1320-1326, 2017.

[342] C.A. Gupta, A. Mishra, S. Mangal, and U.P. Singh, "Study of Al and Ga doped and co-doped ZnO thin film as front contact in CIGS solar cell, physics of semiconductor devices," Environ. Sci. Eng., vol. 80, pp. 319-322, 2014.

[343] S. Feng, R.P. Li, L. Tian, and K. Zou, "Investigation on the properties of Sb-doped CdTe thin films," Appl. Mech. Mat., vols. 275-277, pp. 2018-2022, 2013.

[344] I.M. Dharmadasa, Y. Rahaq, A.A. Ojo, and T.I. Alanazi, "Perovskite solar cells: a deep analysis using current-voltage and capacitance-voltage techniques," J Mater Sci: Mater. Electron., vol. 30, pp. 1227-1235, 2019.

[345] S. Negi, P. Mittal, and B. Kumar, "Analytical modelling and parameters extraction of multilayered OLED," IET Circuits Devices Syst., vol. 13, no. 8, pp. 1255-1261, 2019.

[346] S. Negi, P. Mittal, and B. Kumar, "Impact of different layers on performance on performance of OLED," Microsyst. Technol., vol. 24, no. 12, pp. 4981-4989, 2018.

[347] P. Mittal, Y.S. Negi, and R.K. Singh, "A depth analysis for different structures of organic thin film transistors: modeling of performance limiting issues," Microelectron. Eng., vol. 150, pp. 7-18, 2016.

[348] S. Heo, Sk. Lee, and Y.S. Yang, "An efficient energy and power manager for autonomous systems based on energy harvesting," Analog Integr Circ Sig Process, vol. 81, pp. 299–311, 2014.

[349] S. Amirtharaj, L. Premalatha, and D. Gopinath, "Optimal utilization of renewable energy sources in MG connected system with integrated converters: an AGONN Approach," Analog Integr Circ Sig Process, vol. 101, pp. 513–532, 2019.

[350] D. Wohrle and D. Meissner, "Organic Solar Cells," Advanced Materials, vol. 3, no. 3, pp. 129-138, 1991.

[351] C.J. Brabec, N.S. Sariciftci, and J.C. Hummelen, "Plastic Solar Cells," Advanced Functional Materials, vol. 11, no. 1, pp. 15-26, 2001.

[352] J.M. Nunzi, "Organic Photovoltaic Materials and Devices," Comptes Rendus Physique, vol. 3, no. 4, pp. 523-542, 2002.

[353] H.-Y. Chen, J. Hou, S. Zhang, Y. Liang, G. Yang, Y. Yang, L. Yu, Y. Wu, and G. Li, "Nat. Photonics," vol. 3, pp. 649–653, 2009.

[354] Y.J. Cheng, S.-H. Yang, and C.-S. Hsu, "Chem. Rev.," vol. 109, pp. 5868–5923, 2009.

[355] C.J. Brabec, "Organic photovoltaics: technology and market," Sol. Energy Mater. Sol. Cells, vol. 83, pp. 273–292, 2004.

[356] J. Gilot, I. Barbu, M.M. Wienk, and R.A. Janssen, "The use of ZnO as optical spacer in polymer solar cells: theoretical and experimental study," Appl. Phys. Lett., vol. 91, 113520, 2007.

[357] Behjat, N. Torabi, and F. Dossthosseini, "Improvement of light harvesting by inserting an optical spacer (ZnO) in polymer bulk heterojunction solar cells: a theoretical and experimental study," Int. J. Ophthalmic. Pract., vol. 8, pp. 3-11, 2014.

[358] H. Hoppe, N.S. Sariciftci, and D. Meissner, "Optical constants of conjugated polymer/fullerene based bulk-heterojunction organic solar cells," Molecular Crystals and Liquid Crystals, vol. 385, no. 1, pp. 113-119, 2011.

[359] V.S. Gevaerts, L.J.A. Koster, M.M. Wienk, and R.A.J. Janssen, "Discriminating between bilayer and bulk heterojunction polymer: fullerene solar cells using the external quantum efficiency," ACS Applied Materials and Interfaces, vol. 3, pp. 3252-3255, 2011.

[360] A.D. Rakic, "Algorithm for the determination of intrinsic optical constants of metal films: application to aluminum," Applied Optics, vol. 34, no. 22, pp. 4755-4767, 1995.

[361] G.A. Buxton and N. Clarke, "Predicting structure and property relations in polymeric photovoltaic devices," Physical Review B, vol. 74, pp. 085207-1-085207-5, 2006.

[362] P. Chamola and P. Mittal, "Impact of ZnTe, SbZnTe and SnZnTe absorber materials for multi-layered solar cell: Parametric extraction and layer wise internal analysis," Optik, vol. 224, 165626, 2020.

[363] P. Mittal, Y.S. Negi, and R.K. Singh, "An analytical approach for parameter extraction in linear and saturation regions of top and bottom contact organic transistors," Journal of Computational Electronics, vol. 14, no. 3, pp. 828–843, 2015.

[364] W.D. Leon-Salas and X. Fan, "Solar Cell Photo-Luminescence Modulation for Optical Frequency Identification Devices," IEEE Transactions on Circuits and Systems I, vol. 66, no. 5, pp. 1981 – 1992, 2018.

[365] X. Lin, J. Seok, S. Yoon, T. Kim, B.S. Kim, and K. Kim, "Morphological Investigation of P3HT/PCBM Heterojunction and its Effects on the Performance of Bilayer Organic Solar Cells," Synthetic Metals, vol. 196, pp. 145-150, 2014.

[366] S. Negi, P. Mittal, and B. Kumar, "Modeling and Analysis of High-Performance Triple Hole Block Layer Organic LED Based Light Sensor for Detection of Ovarian Cancer," IEEE Transaction on Circuits and Systems I, vol. 68, no. 8, pp. 3254-3264, 2021.

[367] Y. Zang, X. Gao, X. Lu, Q. Xin, J. Lin, and J. Zhao, "Improved Performance of Polymer Solar Cells Using PBDTT-FTT:PC71BM Blend Film as Active Layer," Applied Surface Science, vol. 376, pp. 138-144, 2016.

[368] J. Zou, H.L. Yip, Y. Zhang, Y. Gao, S.C. Chien, K. O'Malley, C.C. Chueh, H. Chen, and A.K.Y. Jen, "High Performance Inverted Polymer Solar Cells: Device Characterization, Optical Modeling, and Hole-Transporting Modifications," Advanced Functional Materials, vol. 22, no. 22, pp. 2804-2811, 2012.

[369] T. Kobori, T. Fukuda, "Effect of Optical Intensity Distribution on Device Performances of PTB7-Th:PC71BM Based Organic Photovoltaic Cells," Organic Electronics, vol. 51, pp. 76-85, 2017.

[370] S. Cook, R. Katoh, and A. Furube, "Ultrafast Studies of Charge Generation in PCBM:P3HT Blend Films following Excitation of the Fullerene PCBM," Journal of Physical Chemistry C, vol. 113, no. 6, pp. 2547-2552, 2009.

[371] C.W. Tang, "Two-Layer Organic Photovoltaic Cell," Applied Physics Letters, vol. 48, no. 2, pp. 183-185, 1986.

[372] C.J. Brabec, A. Cravino, D. Meissner, N.S. Sariciftci, T. Fromherz, M.T. Rispens, L. Sanchez, and J.C. Hummelen, "Origin of the Open Circuit Voltage of Plastic Solar Cells," Advanced Functional Materials, vol. 11, no. 5, pp. 374-380, 2001.

[373] M. Ninck, M. Untenberger, and T. Gisler, "Diffusing-wave spectroscopy with dynamic contrast variation: disentangling the effects of blood flow and extravascular tissue shearing on signals from deep tissue," Biomed. Opt. Express, vol. 1, pp. 1502-1513, 2010.

[374] M. C. Meinke, M. Friebel, and J. Helfmann, "Optical properties of flowing blood cells," in Advanced Optical Flow Cytometry: Methods and Disease Diagnoses, V. V. Tuchin, Ed. Wiley-VCH Verlag GmbH & Co.KGaA, 2011, pp. 95-132.

[375] Y. K. Park, M. Diez-Silva, D. Fu, G. Popescu, W. Choi, I. Barman, et al., "Static and dynamic light scattering of healthy and malaria-parasite invaded red blood cells," J. Biomed. Opt., vol. 15, 020506, 2010.

[376] Y. K. Park, C. A. Best-Popescu, R. R. Dasari, and G. Popescu, "Light scattering of human red blood cells during metabolic remodeling of the membrane," J. Biomed. Opt., vol. 16, 011013, 2011.

[377] J. Lim, H. Ding, M. Mir, R. Zhu, K. Tangella, and G. B. Popescu, "Approximation model for light scattering by red blood cells," Biomed. Opt. Express, vol. 2, pp. 2784-2791, 2011.

[378] Y. Kim, J. M. Higgins, R. R. Dasari, S. Suresh, and Y. K. Park, "Anisotropic light scattering of individual sickle red blood cells," J. Biomed. Opt., vol. 17, 040501, 2012.

[379] Y. K. Park, C. A. Best, T. Auth, N. S. Gov, S. A. Safran, and G. Popescu, et al., "Metabolic remodeling of the human red blood cell membrane," Proc. Natl. Acad. Sci. USA, vol. 107, pp. 1289-1294, 2010.

[380] H. Turlier, D. A. Fedosov, B. A. Audoly, T. Auth, N. S. Gov, and C. Sykes, et al., "Equilibrium physics breakdown reveals the active nature of red blood cell membrane fluctuations," Nat. Phys., vol. 12, pp. 513-519, 2016.

[381] A. H. Aly, et al., "Theoretical study of hybrid multifunctional one-dimensional photonic crystal as a flexible blood sugar sensor," Phys. Scr., vol. 95, 035510, 2020.

[382] R. Hovorka, "Closed-loop insulin delivery: from bench to clinical practice," Nat. Rev. Endocrinol., vol. 7, p. 385, 2011.

[383] A. H. M. Almawgani et al., "Detection of glucose concentration using a surface plasmon resonance biosensor based on barium titanate layers and molybdenum disulphide sheets," Phys. Scr., vol. 97, 065501, 2022.

[384] V. C. Roberts, "Photoplethysmography - fundamental aspects of the optical blood in motion," Trans. Inst. Meas. Control, vol. 4, pp. 101-106, 1982.

[385] A. Roggan, M. Friebel, K. Dörschel, A. Hahn, and G. Müller, "Optical properties of circulating human blood," J. Biomed. Opt., vol. 4, pp. 36-46, 1999.

[386] I. Fine and A. Finarov, "Probe for use in non-invasive measurements of blood related parameters," ed: Google Patents, 2006.

[387] P. Peumans, V. Bulovic, and S. R. Forrest, "Appl. Phys. Lett.," vol. 76, pp. 3855, 2000.

[388] H. Tanaka, T. Yasuda, K. Fujita, and T. Tsutsui, "Adv. Mater.," vol. 18, pp. 2230, 2006.

[389] S. D. Cotton and E. Claridge, "Developing a Predictive Model of Human Skin Colouring," Proceedings of SPIE Medical Imaging, vol. 2708, pp. 814-825, 1996.

[390] N. Tsumura, H. Haneishi, and Y. Miyake, "Independent Component Analysis of Skin Colour Image," J. Society of America, vol. 16, Issue 9, pp. 2169-2176, 1999.

[391] S. Cotton, E. Claridge, and P. Hall, "A Skin Imaging Method Based on a Colour Formation Model and its Application to the Diagnosis of Pigmented Skin Lesions," Proceedings of Medical Image Understanding and Analysis, Oxford: BMVA, pp. 49-52, 1999.

[392] E. Claridge, S. Cotton, P. Hall, and M. Moncrieff, "From Colour to Tissue Histology: Physics Based Interpretation of Images of Pigmented Skin Lesions," MICCAI 2002, LNCS 2488, pp. 730-738, 2002.

[393] N. Tsumura, H. Haneishi, and Y. Miyake, "Independent Component Analysis of Skin Color Images," The Sixth Color Imaging Conference: Color Science, Systems, and Applications, 1999.

[394] K. P. Nielsen, L. Zhao, J. J. Stamnes, K. Stamnes, and J. Moan, "The Optics of Human Skin: Aspects Important for Human Health," Photodermatology, Photoimmunology & Photomedicine, vol. 24, no. 1, pp. 35-46, 2008.

[395] M. J. Brites, C. Santos, S. Nascimento, B. Gigante, H. Luftmann, A. Fedorov, and Mario N. Berberan-Santos, "Synthesis and fluorescence properties of [60] and [70] fullerene-coumarin dyads: Efficient dipole-dipole resonance energy transfer from coumarin to fullerene," New J. Chem., vol. 30, pp. 1036-1045, 2006.

[396] D. S. Leem, K. H. Lee, K. B. Park, S. J. Lim, K. S. Kim, Y. W. Jin, and S. Lee, "Low dark current small molecule organic photodetectors with selective response to green light," Appl. Phys. Lett., vol. 103, 043305, 2013.

[397] S. senthilarasu, S. velumani, R. sathyamoorthy, A. subbarayan, J. A. ascencio, G. canizal, P. J. Sebastian, J. A. Chavez, R. perez, "Characterization of zinc

phthalocyanine (ZnPc) for photovoltaic applications," Appl. Phys. A, vol. 77, pp. 383-389, 2003.

[398] R. M. L. Kitaneh, M. M. Abu-Samreh, S. M. Musameh, S. M. Hraibat, A. M. Saleh, "Dielectric characterization of semiconducting ZnPc films sandwiched between Gold or Aluminum electrodes," Appl Phys A, vol. 114, pp. 1267-1275, 2014.

[399] ATLAS, "ATLAS User's Manual Device Simulation Software," Silvaco International Ltd., Santa Clara, 2014.

[400] S. Negi, P. Mittal, and B. Kumar, "Analytical Modelling and Parameters Extraction of Multilayered OLED," IET Circuits Devices Syst., vol. 13, issue 8, pp. 1255-1261.

[401] P. Chamola and P. Mittal, "Flexible organic solar cell to power modern cardiac pacemakers: Versatile for all age groups, skin types and genders," Phys. Scr., vol. 98, 035018, 2023.

[402] R. M. Christie and C. Lui, "Dyes Pigm.," vol. 42, pp. 85–93, 1999.

[403] R. M. Christie and C. Lui, "Dyes Pigm.," vol. 47, pp. 79–89, 2000.

[404] S. R. Trenor, A. R. Shultz, B. J. Love, and T. E. Long, "Chem. Rev.," vol. 104, pp. 3059–3077, 2004.

[405] B. Kovac and I. Novak, "Spectrochim. Acta, Part A," vol. 58, pp. 1483–1488, 2002.

[406] X. Zhou, J. Blochwitz-Nimoth, M. Pfeiffer, B. Maenning, J. Drechsel, A. Werner, and K. Leo, "Synth. Met.," vol. 138, pp. 193–196, 2003.

[407] K. Hara, K. Sayama, Y. Ohga, A. Shinpo, S. Suga, and H. Arakawa, "Chem. Commun.," pp. 569–570, 2001.

[408] K. Hara, Y. Tachibana, Y. Ohga, A. Shinpo, S. Suga, K. Sayama, H. Sugihara, and H. Arakawa, "Sol. Energy Mater. Sol. Cells," vol. 77, pp. 89–103, 2003.

[409] C. Jiao, C. Niu, L. Chen, G. Shen, and R. Yu, "Sens. Actuators, B," vol. 94, pp. 176–183, 2003.

[410] S. senthilarasu, S. velumani, R. sathyamoorthy, A. subbarayan, J. A. ascencio, G. canizal, P. J. Sebastian, J. A. Chavez, R. perez, "Characterization of zinc phthalocyanine (ZnPc) for photovoltaic applications," Appl. Phys. A, vol. 77, pp. 383–389, 2003.

[411] P. A. Lane, J. Rostalski, C. Giebeler, S. J. Martin, D. D. C. Bradley, and D. Meissner, "Sol. Energy Mater. Sol. Cells," vol. 63, no. 3, 2000.

[412] D. Wrobel and A. Boguta, "J. Photochem. Photobiol. A: Chem.," vol. 6045, no. 1, 2002.

[413] K. Oda, S. I. Ogura, and I. Okura, "J. Photochem. Photobiol. B: Biol.," vol. 59, no. 20, 2000.

[414] K. Suemori, T. Miyata, M. Yokoyama, and M. Hiramoto, "Appl. Phys. Lett.," vol. 85, no. 6269, 2004.

[415] H. Seo, S. Aihara, T. Watabe, H. Ohtake, T. Sakai, M. Kubota, N. Egami, T. Hiramatsu, T. Matsuda, M. Furuta, and T. Hirao, "A 128 × 96 Pixel Stack-Type Color Image Sensor: Stack of Individual Blue-, Green-, and Red-Sensitive Organic Photoconductive Films Integrated with a ZnO Thin Film Transistor Readout Circuit," Japanese Journal of Applied Physics, vol. 50, 024103, 2011.

[416] M. Friebel and M. Meinke, "Determination of the complex refractive index of highly concentrated hemoglobin solutions using transmittance and reflectance measurements," J. Biomed. Opt., vol. 10, 064019, 2005.

[417] O. Assendelft, "Spectrophotometry of Hemoglobin Derivates," Royal Vangorcum, 1970.

[418] S. Prahl, "Tabulated data from Various Sources Compiled by S. Prahl," [Online]. Available: http://omlc.ogi.edu/spectra/ (accessed 2009).

[419] A. N. Rohen et al. "On the effective refractive index of blood," Phys. Scr., vol. 91, 015503, 2016.

[420] R. R. Anderson and J. A. Parrish, "The Optics of Human Skin," Journal of Investigative Dermatology, vol. 77, no. 1, pp. 13-19, 1981.

[421] G. Stott and S. M. Lewis, "A simple and reliable method for estimating haemoglobin," Bulletin of the World Health Organization, vol. 73, pp. 369-73, 1995.

[422] M. Miinster et al. "Field evaluation of a novel haemoglobin measuring device designed for use in rural setting," South African Medical Journal, vol. 87, pp. 1522-26, 1997.

[423] P. E. Beales, "Anaemia in malaria control: a practical approach," Annals of Tropical Medicine & Parasitology, vol. 91, pp. 713-8, 1997.

[424] S. M. Lewis, G. J. Stott, K. J. Wynn, "An inexpensive and reliable new haemoglobin colour scale for assessing anaemia," Journal of Clinical Pathology, vol. 51, pp. 21-4, 1998.

[425] A. J. Patel, R. Wesley, S. F. Leitman, B. J. Bryant, "Capillary versus venous haemoglobin determination in the assessment of healthy blood donors," Vox Sang, vol. 104, pp. 317-23, 2013.

[426] M.V. Tholl, H.G. Akarçay, H. Tanner, T. Niederhauser, A. Zurbuchen, M. Frenz, A. Haeberlin, "Subdermal solar energy harvesting – A new way to power autonomous electric implants," Appl Energy, vol. 269, 114948, 2020.

[427] D. Katz, T. Akiyama, "Pacemaker longevity: The world's longest lasting VVI pacemaker," Ann Noninvasive Electrocardiol, vol. 12, 223, 2007.

[428] H. G. Mond, A. Proclemer, "The 11th world survey of cardiac pacing and implant cardioverter-defibrillators: Calendar year 2009-a world society of arrhythmia's project," Pacing Clin Electrophysiol, vol. 34, 1013, 2011.

[429] S. Arora et al., "Role of donor–acceptor domain formation and interface states in initial degradation of P3HT:PCBM-based solar cells," Phys. Scr., vol. 83, 035804, 2011.

[430] D. Qin et al., "Electron injection via doped p–n heterojunction for inverted organic light emitting diodes," Phys. Scr., vol. 89, 015802, 2014.

[431] H. Cheng and N. Yi, "Dissolvable tattoo sensors: from science fiction to a viable technology," Phys. Scr., vol. 92, 013001, 2017.

[432] C. H. Peters et al., "High efficiency polymer solar cells with long operating lifetimes," Adv. Energy Mater., vol. 1, pp. 491–494, 2011.

[433] D. Baran et al., "Reducing the efficiency-stability-cost gap of organic photovoltaics with highly efficient and stable small molecule acceptor ternary solar cells," Nat. Mater., vol. 16, pp. 363-369, 2017.

[434] N. Gasparini et al, "Burn-in free nonfullerene-based organic solar cells," Adv. Energy Mater., vol. 7, 1700770, 2017.

[435] Q. Burlingame et al., "Reliability of small molecule organic photovoltaics with electron-filtering compound buffer layers," Adv. Energy Mater., vol. 6, 1601094, 2016.

[436] S. B. Sapkota, A. Spies, B. Zimmermann, I. Dürr and U. Würfel, "Promising long-term stability of encapsulated ITO-free bulk-heterojunction organic solar cells under different aging conditions," Sol. Energy Mater. Sol. Cells, vol. 130, pp. 144–150, 2014.

[437] P. E. Burrows and S. R. Forrest, "Operating lifetime of phosphorescent organic light emitting devices," Appl. Phys. Lett., vol. 76, 2493, 2000.

[438] Q. Burlingame, X. Huang, X. Liu et al., "Intrinsically stable organic solar cells under high-intensity illumination," Nature, vol. 573, pp. 394–397, 2019.

[439] X. Xu, J. Xiao, G. Zhang, L. Wei, X. Jiao, H-L. Yip, Y. Cao, "Interface-enhanced organic solar cells with extrapolated T80 lifetimes of over 20 years," Science Bulletin, vol. 65, pp. 208-216, 2019.

[440] X. Du et al., "Efficient Polymer Solar Cells Based on Non-fullerene Acceptors with Potential Device Lifetime Approaching 10 Years," Joule, vol. 3, pp. 215-226, 2018.

[441] F. C. Krebs, J. E. Carlé, N. Cruys-Bagger, M. Andersen, M. R. Lilliedal, M. A. Hammond, S. Hvidt, "Lifetimes of organic photovoltaics: photochemistry, atmosphere

effects and barrier layers in ITO-MEHPPV:PCBM-aluminium devices," Solar Energy Materials and Solar Cells, vol. 86, pp. 499-516, 2005.

[442] S. Schuller, P. Schilinsky, J. Hauch et al., "Determination of the degradation constant of bulk heterojunction solar cells by accelerated lifetime measurements," Appl. Phys. A, vol. 79, pp. 7–40, 2004.

[443] K. Birmingham, V. Gardinaru, P. Anikeeva, W.M. Grill, V. Pikov, B. McLaughlin, P. Pasricha, D. Weber, K.A. Ludwig, and K. Famm, "Bioelectronic medicines: a research roadmap," Nat. Rev. Drug Discov., vol. 13, pp. 399–400, 2014.

[444] D.C. Martin, "Molecular design, synthesis, and characterization of conjugated polymers for interfacing electronic biomedical devices with living tissue," MRS Communications, vol. 5, pp. 131–152, 2015.

[445] S. C. Chang, Y. J. Hsiao, T. S. Li, "Improving the Power Conversion Efficiency of Organic Solar Cell by Blending with CdSe/ZnS Core–Shell Quantum Dots," J. Electron. Mater., vol. 43, 3077, 2014.

[446] M. Scholdt, H. Do, J. Lang, A. Gall, A. Colsmann, U. Lemmer, J. D. Koenig, M. Winkler, H. Boettner, "Organic Semiconductors for Thermoelectric Applications," J. Electron. Mater., vol. 39, 1589, 2010.

[447] D. C. Jordan, S. R. Kurtz, "Photovoltaic degradation rates - an analytical review," Prog Photovoltaics Res Appl, vol. 21, no. 12, 2011.

[448] K.T. Settaluri, H. Lo, R.J. Ram, "Thin Thermoelectric Generator System for Body Energy Harvesting," J. Electron. Mater., vol. 41, 984, 2012.

[449] M. Thielen, G. Kara, I. Unkovic, et al., "Thermal Harvesting Potential of the Human Body," J. Electron. Mater., vol. 47, 3307, 2018.

[450] C. Agnes, M. Holzinger, A. Le Goff, B. Reuillard, K. Elouarzaki, S. Tingry, S. Cosnier, "Supercapacitor/biofuel cell hybrids based on wired enzymes on carbon nanotube matrices: autonomous reloading after high power pulses in neutral buffered glucose solutions," Energy Environ. Sci., vol. 7, pp. 1884, 2014.

[451] S. Kim, J. S. Ho, L. Y. Chen, A. S. Poon, "Wireless power transfer to a cardiac implant," Appl. Phys. Lett., vol. 101, 073701, 2012.

[452] P. Bai, G. Zhu, Z. H. Lin, Q. Jing, J. Chen, G. Zhang, J. Ma, Z. L. Wang, "Integrated multilayered triboelectric nanogenerator for harvesting biomechanical energy from human motions," ACS Nano, vol. 7, pp. 3713, 2013.

[453] E. Miyako, C. Hosokawa, M. Kojima, M. Yudasaka, R. Funahashi, I. Oishi, Y. Hagihara, M. Shichiri, M. Takashima, K. Nishio, Y. Yoshida, "A photo-thermal-

electrical converter based on carbon nanotubes for bioelectronic applications," Angew Chem Int Ed Engl, vol. 50, pp. 12266, 2011.

[454] P. Roberts, G. Stanley, J. M. Morgan, "Harvesting the energy of cardiac motion to power a pacemaker," Circulation, vol. 118, pp. 679, 2008.

[455] International Commission on Non-Ionizing Radiation Protection, "ICNIRP statement on far infrared radiation exposure," Health Phys, vol. 91, pp. 630, 2006.

[456] P. Niu, P. Chapman, R. Riemer, X. Zhang, "Evaluation of Motions and Actuation Methods for Biomechanical Energy Harvesting," In Proceedings of the IEEE 35th Annual Power Electronics Specialists Conference, Aachen, Germany, pp. 2100, 2004.

[457] R. Tashiro, N. Kabei, K. Katayama, Y. Ishizuka, F. Tsuboi, K. Tsuchiya, "Development of an electrostatic generator that harnesses the motion of a living body (Use of a resonant phenomenon)," JSME Int. J. Ser. C, vol. 43, pp. 916, 2000.

[458] X. Wei, J. Liu, "Power sources and electrical recharging strategies for implantable medical devices," Front. Energy Power Eng. China, vol. 2, pp. 1, 2008.

[459] A. Irani, M. Bianco, D. Tran, P. D. Deyoung, M. L. R. Wyld, T. H. Li, "Energy Generating Systems for Implanted Medical Devices," U.S. Patent US20090171404 A1, July 2, 2009.

[460] K. Goto, T. Nakagawa, O. Nakamura, S. Kawata, "An implantable power supply with an optically rechargeable lithium battery," IEEE Trans. Biomed. Eng., vol. 48, pp. 830, 2001.

[461] I. Stark, M. Stordeur, "New Micro Thermoelectric Devices Based on Bismuth Telluride-Type Thin Solid Films," In Proceedings of the Eighteenth International Conference on Thermoelectrics, Piscataway, NJ, USA, pp. 465, 1999.

[462] N. Mano, F. Mao, A. Heller, "Characteristics of a miniature compartment-less glucose-O2 biofuel cell and its operation in a living plant," J. Am. Chem. Soc., vol. 125, pp. 6588, 2003.

[463] E. Chan, B. Sorg, D. Protsenko, M. O'Neil, M. Motamedi, A. Welch, "Effects of compression on soft tissue optical properties," IEEE J Sel Top Quantum Electron, vol. 2, pp. 943, 1996.

[464] A. N. Bashkatov, E. A. Genina, V. I. Kochubey, V. V. Tuchin, "Optical properties of human skin, subcutaneous and mucous tissues in the wavelength range from 400 to 2000nm," J Phys D: Appl Phys, vol. 38, pp. 2543, 2005.

[465] S. L. Jacques, "Optical properties of biological tissues: a review," Phys Med Biol, vol. 58, pp. R37, 2013.

[466] D. Barolet, "Light-emitting diodes (LEDs) in dermatology," Semin. Cutan. Med. Surg., vol. 27, pp. 227, 2008.

[467] N. Bosschaart, G. J. Edelman, M. C. G. Aalders, T. G. van Leeuwen, D. J. Faber, "A literature review and novel theoretical approach on the optical properties of whole blood," Lasers Med Sci, vol. 29, pp. 453, 2013.

[468] G. Yoon, A. Welch, M. Motamedi, M. Gemert, "Development and application of three-dimensional light distribution model for laser irradiated tissue," IEEE J Quantum Electron, vol. 23, pp. 1721, 1987.

[469] R. L. Van Veen, H. Sterenborg, A. Pifferi, A. Torricelli, R. Cubeddu, "Determination of VIS- NIR absorption coefficients of mammalian fat, with time- and spatially resolved diffuse reflectance and transmission spectroscopy," Biomedical topical meeting OSA, vol. 2004.

[470] C. R. Simpson, M. Kohl, M. Essenpreis, M. Cope, "Near-infrared optical properties of exvivo human skin and subcutaneous tissues measured using the monte carlo inversion technique," Phys Med Biol, vol. 43, pp. 2465, 1998.

[471] I. V. Meglinski, S. J. Matcher, "Quantitative assessment of skin layers absorption and skin reflectance spectra simulation in the visible and near-infrared spectral regions," Physiol Meas, vol. 23, pp. 741, 2002.

[472] G. J. Tearney, M. E. Brezinski, J. F. Southern, B. E. Bouma, M. R. Hee, J. G. Fujimoto, "Determination of the refractive index of highly scattering human tissue by optical coherence tomography," Opt Lett, vol. 20, pp. 2258, 1995.

[473] Y. Lee, K. Hwang, "Skin thickness of korean adults," Surg Radiol Anat, vol. 24, pp. 183, 2002.

[474] L. Bereuter, S. Williner, F. Pianezzi et al., "Energy Harvesting by Subcutaneous Solar Cells: A Long-Term Study on Achievable Energy Output," Ann Biomed Eng, vol. 45, pp. 1172–1180, 2017.

[475] ATLAS, ATLAS User's Manual Device Simulation Software, Silvaco International Ltd., Santa Clara, 2014.

[476] P. Mittal, Y. S. Negi, R. K. Singh, "A Depth Analysis for Different Structures of Organic Thin Film Transistors: Modeling of Performance Limiting Issues," Microelectronics Engineering, vol. 150, pp. 7, 2016.

[477] S. Negi, P. Mittal, and B. Kumar, "Analytical Modelling and Parameters Extraction of Multilayered OLED," IET Circuits, Devices and Systems, vol. 13, pp. 1255, 2019.

[478] P. Mittal, Y. S. Negi, R. K. Singh, "An analytical approach for parameter extraction in linear and saturation regions of top and bottom contact organic transistors," Journal of Computational Electronics, vol. 14, pp. 828, 2015.

[479] S. Negi, P. Mittal and B. Kumar, "Numerical Modeling and Parameters Extraction of Novel Triple Hole Block layer based Organic Light Emitting Diode for Display," Journal of the Society for Information Display, vol. 22, pp. 956, 2020.

[480] S. Negi, P. Mittal and B. Kumar, "In-Depth analysis of structures, materials, models, parameters and applications of organic light emitting diodes," Jou Of Ele Mat, vol. 49, pp. 4610, 2020.

[481] S. Negi, P. Mittal and B. Kumar, "Modeling and Analysis of High-Performance Triple Hole Block Layer Organic LED Based Light Sensor for Detection of Ovarian Cancer," in IEEE Trans. Circuits Syst. I: Reg. Papers, vol. 68, pp. 3254, 2021.

[482] V. D. Mihailletchi, P. W. M. Blom, J. C. Hummelen, M. T. Rispens, "Cathode dependence of the open circuit voltage of polymer: fullerene bulk heterojunction solar cells," Journal of Applied Physics, vol. 94, pp. 6849, 2003.

[483] S. A. Prahl, M. J. C. Van Gemert and A. J. Welch, "Determining the optical properties of turbid media by using the adding–doubling method," Appl. Opt., vol. 32, pp. 559–568, 1993.

[484] L. Finlayson, I. R. M. Barnard, L. McMillan, S. H. Ibbotson, C. T. A. Brown, E. Eadie, K. Wood, "Depth Penetration of Light into Skin as a Function of Wavelength from 200 to 1000 nm," Photochem. Photobiol., 2021.

[485] T. Kono, J. Yamada, "In Vivo Measurement of Optical Properties of Human Skin for 450–800 nm and 950–1600 nm Wavelengths," Int J Thermophys, vol. 40, pp. 51, 2019.

[486] A. Firooz, B. Sadr, S. Babakoohi, M. S. Yazdy, F. Fanian, A. K. Timsar, M. N. Kashani, M. M. Naghizadeh, Y. Dowlati, "Variation of Biophysical Parameters of the Skin with Age, Gender, and Body Region," The Scientific World Journal, vol. 2012, pp. 386936, 2012.

[487] A. E. Mayes, P. G. Murray, D. A. Gunn et al., "Ageing appearance in China: biophysical profile of facial skin and its relationship to perceived age," Journal of the European Academy of Dermatology and Venereology, vol. 24, no. 3, pp. 341–348, 2010.

[488] S. H. Tseng, A. Grant, A. J. Durkin, "In vivo determination of skin near-infrared optical properties using diffuse optical spectroscopy," J Biomed Opt, vol. 13, pp. 014016, 2008.

[489] J. P. Ritz, A. Roggan, C. Isbert, G. Muller, H. Bhur, C. T. Germer, "Optical properties of native and coagulated porcine liver tissues between 400 and 2400 nm," Lasers Surg. Med., vol. 29, pp. 205, 2001.

[490] H. R. Philip, E. A. Taft, "Optical constants of silicon in the region 1 to 10 eV," Phys. Rev., vol. 120, pp. 37, 1960.

[491] T. Igarashi, K. Nishino, S. K. Nayar, "The appearance of human skin: A survey," Found. Trends Comput. Graph. Vis., vol. 3, pp. 1, 2007.

[492] C. Dagdeviren, B. D. Yang, Y. Su et al., "Conformal piezoelectric energy harvesting and storage from motions of the heart, lung, and diaphragm," Proc. Natl. Acad. Sci., vol. 111, pp. 1927, 2014.

[493] A. Zebda, S. Cosnier, J. P. Alcaraz, M. Holzinger, A. Le Goff, C. Gondran, F. Boucher, F. Giroud, K. Gorgy, H. Lamraoui, P. Cinquin, "Single glucose biofuel cells implanted in rats power electronic devices," Sci. Rep., vol. 3, pp. 1, 2013.

[494] G. Grandi, A. Ienina, and M. Bardhi, "Effective low-cost hybrid LED-halogen solar simulator," IEEE Transactions on Industry Applications, vol. 50, pp. 3055, 2014.

LIST OF PUBLICATIONS

SCI/SCIE Indexed Journal Papers Published

1. Paritosh Chamola and Poornima Mittal, "Impact of ZnTe, SbZnTe and SnZnTe absorber materials for multi-layered solar cell: Parametric extraction and layer wise internal analysis," Optik. vol. 224, 165626, 2020. (**I.F. - 2.84, Elsevier**).
2. Paritosh Chamola, Poornima Mittal, "PPV–PCBM bulk heterojunction organic solar cell to power modern pacemakers," Journal of Materials Research, vol. 38, pp. 1304-1316, 2023. (**I.F. - 2.909, Springer**).
3. Paritosh Chamola and Poornima Mittal, "Flexible organic solar cell to power modern cardiac pacemakers: Versatile for all age groups, skin types and genders," Physica Scripta, vol. 98, 035018, 2023. (**I.F. - 3.081, IOP Publishing**).
4. Paritosh Chamola and Poornima Mittal, "Parametric Extraction and Internal Analysis of Fullerene-based Polymer Bulk Heterojunction Solar Cell," Main Group Chemistry, vol. 22, pp. 155-166, 2023. (**I.F. – 1.5, IOS Press**).
5. Paritosh Chamola and Poornima Mittal, "A non-invasive optical method for anaemia detection," Physica Scripta, vol. 98, 065023, 2023. (**I.F. - 3.081, IOP Publishing**).

Revised Paper Submitted in SCI/SCIE Indexed Journals

1. Paritosh Chamola and Poornima Mittal, "Internal Analysis and Performance Parameter Optimization of Bilayer Organic Solar Cell," Analog Integrated Circuits and Signal Processing (**I.F. - 1.321, Springer**).

Paper Under-Process for Submission in SCI/SCIE International Journal

1. Paritosh Chamola and Poornima Mittal, "Effect of Different Layers on the Performance of Multilayer Organic Solar Cell."
2. Paritosh Chamola and Poornima Mittal, "A Comprehensive Review on Advancement of Flexible Organic Solar Cells: Structural Diversity, Role of Layers and Applications."
3. Paritosh Chamola and Poornima Mittal, "Zinc Telluride Material Properties for Solar Cell Application: Absorber Layer"

Scopus Indexed International Conference Papers

1. Paritosh Chamola and Poornima Mittal, "Cut-line Analysis and Parameters' Extraction of Zinc Telluride Absorber Material based Multi-layer Solar Cell," *International Conference on Smart and Intelligent Learning for Information Optimization (CONSILIO 2020)*, organized by Consilio Intelligence Research Lab, Neida and Jaypee University of Engineering and Technology, Guna at Goa, India during 24 – 25 October, 2020, Journal of Physics: C. Series (ISSN: 1742-6596), Vol. 1714, pp. 012020, Jan – 2021, (Published by IOP Sciences, Scopus Indexed).
2. Paritosh Chamola and Poornima Mittal, "Analysis of Performance Diversity in OTFT Utilizing La0.850Nb0.150O4 as Gate Dielectric," *International Conference on Electrical and Electronics Engineering (ICE3-2020)*, organized by MMMUT, Gorakhpur, UP, India, 14-15 Feb, 2020, pp. 601-605 (Published by IEEE, Scopus Indexed).
3. Paritosh Chamola and Poornima Mittal, "Performance Parameter Extraction of SnZnTe Absorber Layer Photovoltaic Cell," *3rd International Conference on Functional Materials, Manufacturing and Performances (ICFMMP-2022)*, organized by Division of Research and Development, Lovely Professional University, Punjab, India, 29-30 July, 2022, (Accepted, to be published by AIP, Scopus Indexed).